Optimizing Critical Current Density Through Composition and Microstructure in Mechanically Alloyed Magnesium Diboride

by

Ben James Senkowicz

A dissertation submitted in partial fulfillment of
the requirements for the degree of

Doctor of Philosophy
(Materials Science)

at the
University of Wisconsin-Madison
2007

ABSTRACT

Optimizing Critical Current Density Through Composition and Microstructure in Mechanically Alloyed Magnesium Diboride

Ben James Senkowicz

under the supervision of Professor Eric E. Hellstrom and Professor David C Larbalestier
at the University of Wisconsin-Madison

Carbon doped MgB_2 is an emerging superconductor with potential for operation in the 0-10 Tesla range at 4.2 K or 3-4 T up to ~25 K. In order to be a viable conductor option, mid to high-field J_c(H) must be improved from J_c(8T,4.2K) ~ 3×10^4 A/cm^2 typical of conductors made by in-situ powder in tube reaction. J_c(H) is controlled by H* (a function of H_{c2} and flux pinning), flux pinning itself (largely a function of grain size), and connectivity. Current in-situ wires are limited by a trade-off between connectivity and grain size because aggressive sintering heat treatments grow grains. In order to escape this dilemma, this work examines bulk C-doped MgB_2 made by sintering pre-reacted powder. An engineering approach was adopted, studying the effect of processing parameters on our primary metric, J_c(H). In this work we used high energy ball milling to simultaneously do the following: 1) Alloy MgB_2 with C, 2) refine grains, 3) break up oxide sintering barriers on particle surfaces, and 4) disperse second phases on a fine scale. By this method we obtained extremely fine 20-30 nm grains even after heat treatment at 1000°C – probably due to dispersed second phases retarding grain growth. Heat treatment optimization revealed a temperature window between 900°C and 1000°C (depending on composition and milling time) which was sufficiently hot for sintering, but did not result in excessive grain growth. In this way (combined with hot isostatic pressing) we were able to repeatedly obtain J_c(8T,4.2K) = $7\text{x}10^4$ A/cm^2 or higher – within a factor of 2 of optimized NbTi. An additional benefit of this work is the discovery that C-solubility in MgB_2 is a strong function of T for T < 1150°C, which could open the door for further processing strategies.

Approved:

Date

Professor Eric E. Hellstrom

Acknowledgements

First I would like to thank my advisors David Larbalestier and Eric Hellstrom, for their guidance, and their tireless efforts to help me improve my level of achievement. I would also like to thank my committee, Mark Rzchowski, Chang-Beom Eom, and Paul Voyles for their sage counsel over the last few years. I have benefited tremendously from association with Peter Lee, Alex Gurevich, Anatolii Polyanskii, Lance Cooley, and Jianyi Jiang. Makoto Takayasu and Joe Minervini taught me a lot about experimentation, including my first taste of the magnet lab. Bruce Strauss gave me lots of good advice. Melinda Menard, Jenne Orr, Kate Liu, and Connie Linville smoothed many things out for me. Alex Squitieri was always available to explain the intricacies of cryogenic measurements, or the latest governmental outrage. Bill Starch did a great job getting things in Tallahassee running as I needed them. Without his efforts, I would still be making samples. Jonathan Giencke and Ye Zhu helped me with x-ray and TEM measurements which were particularly valuable to this work. Much of the labor in this work was done by undergraduates especially Richard Mungall, Jonathan Hedstrom, and Jason Mantei. I could not have asked for a better team.

I would like to thank Raymond and Anne Herb for funding me during my first year, and the US Department of Energy Fusion Energy Sciences Fellowship program for three years of support. DOE funded this work through a fusion grant, and NSF also funded it through the Focused Research Group in magnesium diboride.

On a less professional level, I would like to acknowledge my comrades in arms – Matt Jewell, Zhijun Chen, Zu-Hawn Sung, Jian Zhou, and Sang-Il Kim as well as those

who have moved on to greater things: Mike Naus, Chad Fischer, Yongwen Yuan, Sandy Liao, Jermal Chandler, Albertus (Arno) Godeke, and Valeria Braccini – and one who has moved on in a different sense.

And most of all I would like to thank my family. My parents Bill and Joan always believed in me and encouraged my dreams – and still do. My wife Rebecca has been unflagging in her support, and has been my source of strength. My boys Sam and Brian have kept me mindful of what is really important in life.

Table of Contents

Symbols, Acronyms and Their Meanings

Å	Angstroms
α	A constant
σ	Denotes sigma band, also conductivity
σ_0	Low temperature conductivity
π	3.14159, also denotes pi band
ξ	Superconducting coherence length
ξ_0	Superconducting coherence length in clean limit
ξ_{dirty}	Superconducting coherence length in dirty limit
γ	Surface energy per unit area, also Sommerfeld coefficient
λ	Penetration depth, wavelength
θ	Bragg angle
ε	Charge on an electron
Θ_D	Debye temperature
Φ_0	Superconducting flux quantum
Φ_B	Magnetic flux
ρ	Resistivity, pore radius of curvature
ρ_A	Adjusted resistivity
ρ_n	Normal-state resistivity
ρ_{def}	Defect component of resistivity

ρ_{Ph}	Phonon component of resistivity
$\Delta\rho$	ρ(300 K) – ρ(40 K)
$\Delta\rho_{ideal}$	Ideal $\Delta\rho$
//c	Parallel to c-axis
//ab	Parallel to ab-plane
A	Area, also used as a constant
A_F	Active area fraction
a	a-axis lattice parameter, sample dimension, spacing
B	Magnetic field ($B=\mu_0H$), XRD peak breadth (FWHM)
b	a length
c	c-axis lattice parameter, also used as a constant
C_0	Concentration in grain
C_B	Concentraion at grain boundary
CIP	Cold isostatic press
D	Diffusivity, height displacement
D_0	A constant
D_{RL}	Rate limiting diffusivity
d	Grain size, length, sample dimension, interplanar spacing
d_A	Average grain size
d_0	Grain size prior to heat treatment
e	Charge of an electron
E	Electric field
f	Function of, volume fraction

F_P	Pinning force
F_L	Lorentz force
G	Gibbs free energy
ΔG_γ	Excess surface energy per mol powder
H	Magnetic field
H*	Irreversibility field (also B*)
H_K*	Irreversibility field obtained by Kramer extrapolation
H_{loop}*	Irreversibility field obtained by loop closure
H_{c2}	Upper critical field (also B_{c2})
H_P	Field of full flux penetration
H_a	Applied field
h	Reduced field h = H/H*, Planck's constant
H_V	Vickers hardness
HIP	Hot isostatic press
I	Current
J	Current density
J_c	Critical current density
J_d	Depairing current density
k	A constant
K	Kelvins, also a constant
L	Length
l	mean free path
M	Atomic mass, grain boundary mobility, volumetric magnetization

m	magnetic moment, mass of electron, also used as a constant
m*	Effective mass
N	Number of turns in a coil
n	Number of free electrons per unit volume, also used as a constant
P	Pressure, Packing fraction, Restraining force to grain boundary motion
P_{HIP}	Pressure of hot isostatic press
$P_{Capillary}$	Capillary pressure
Q	Activation energy
Q_s	Activation energy for surface diffusion
Q_{gb}	Activation energy for grain boundary diffusion
Q_l	Activation energy for lattice diffusion
R	Electrical resistance, radius, also a constant
r	particle radius, pin radius
RRR	Residual resistivity ratio
T	Temperature, Tesla
T_c	Critical Temperature
T_{HIP}	Temperature of hot isostatic press
T_{HT}	Heat treatment temperature
T_m	Melting temperature
t	time, grain size in Scherrer formula
t_{mill}	milling time
t_{HIP}	time in hot isostatic press
V	Volume, voltage

V_F	Velocity at Fermi surface
v_A	Average grain boundary velocity
X	Carbon content $Mg(B_{1-X}C_X)_2$
x	neck radius
z	An integration term
AC	Alternating current
ACMS	Alternating current measurement system
CVD	Chemical vapor deposition
DC	Direct current
ex situ	Made from pre-reacted MgB_2
FWHM	Full Width Half Maximum
HTS	High Temperature Superconductor
in situ	Mg and B reacted in the wire
LTS	Low temperature superconductor
MgB_2	Magnesium diboride
MO	Magneto-Optical
PIT	Powder in tube
PPMS	Physical property measurement system
SEM	Scanning electron microscope
SQUID	Supercondcuting Quantum Interferometer Device
TEM	Transmission electron microscope
XRD	X-ray diffraction
VSM	Vibrating sample magnetometer

VTI	Variable temperature insert

Introduction

Most superconducting magnets are currently made with Nb based low temperature superconductors (LTS) NbTi and Nb_3Sn. These conductors are limited to operation at 4.2 K or colder, and fields no greater than ~10 T for NbTi and 16 T for Nb_3Sn at 4.2 K. High temperature cuprate superconductors (HTS), most notably YBCO, can operate at much higher temperatures and magnetic fields. But they suffer from large anisotropy and grain boundary orientational weak links. HTS tapes and coated conductors are also flat, and therefore present additional challenges to magnet builders.

MgB_2 was only discovered to be superconducting in 2001[Nagamatsu01] so its full potential is not yet known, but already it has been shown to have sufficient upper critical field (in C-doped form) for potential high field magnet application at 4.2 K. It could also be used at fields ~ 5 T at 20 K, which is suitable for MRI application. Furthermore, its raw materials are potentially cheap and it can be made into round wire.

In order to find application in magnets, the critical current density (J_c(H)) of MgB_2 must be increased. Critical current density is determined by composition and microstructure. In 2004 we found [Senkowicz01] that high energy ball milling pre-reacted MgB_2 to mechanically alloy with carbon resulted in then-record J_c(8 T, 4.2 K) ~ 5 x 10^4 A/cm^2, but the reasons for this success were unclear.

As a result, we launched a line of experimentation designed to further optimize J_c(H) based on our initial process. The result is this thesis. The goal of this work was to understand how to use our processing tools (carbon content, ball milling, and heat treatment) to maximize J_c(H) in bulk MgB_2 made from pre-reacted powder. We found that J_c(H) depends mainly on composition, grain size, and electrical connectivity, and we determined how those properties evolve as a result of processing. This thesis is dedicated to explaining those findings in detail.

Chapter 1- Basic Properties of MgB_2.

The understanding of any material begins with the basic properties. This chapter will briefly discuss basic physical, thermodynamic, and superconducting properties of MgB_2 as well as common processing routes and challenges. Particular attention will be paid to connectivity. This will frame later discussion of the effects of carbon doping (Ch. 2), our own synthesis and analysis methods (Ch. 3) and our efforts to advance MgB_2 technology (Ch. 4-8).

1.1 - Basic physical properties

1.1.1 - Structure and Bonding

MgB_2 has a hexagonal lattice, with a basis consisting of alternating boron and magnesium sheets running parallel to the a-b plane similar to AlB_2 (P6/mmm). This structure is shown if Figure 1.1. Lattice parameters of pure MgB_2 are a = 0.3083 nm and c = 0.35213 nm [Lee01] The graphitic boron planes have strong in-plane SP2 hybridized σ bonding, and more isotropic π bonding connects the planes.[Karpinski01] Many properties are therefore anisotropic, but not as strongly as in HTS such as YBCO or BiSCCO where c is much larger than a. The unusual bonding arrangement of MgB_2 results in two distinct superconducting bands that in the ideal case have little connection, as discussed below in section 1.2. Alloying can strain the lattice, altering the band structure. Most notably, adding carbon causes a contraction of the a-axis lattice parameter without any significant change to the bulk c-axis parameter. In films, carbon addition actually expands the c-axis parameter – a fact that may be related to the higher H_{c2} values obtainable in the films compared to the bulks, as discussed later.

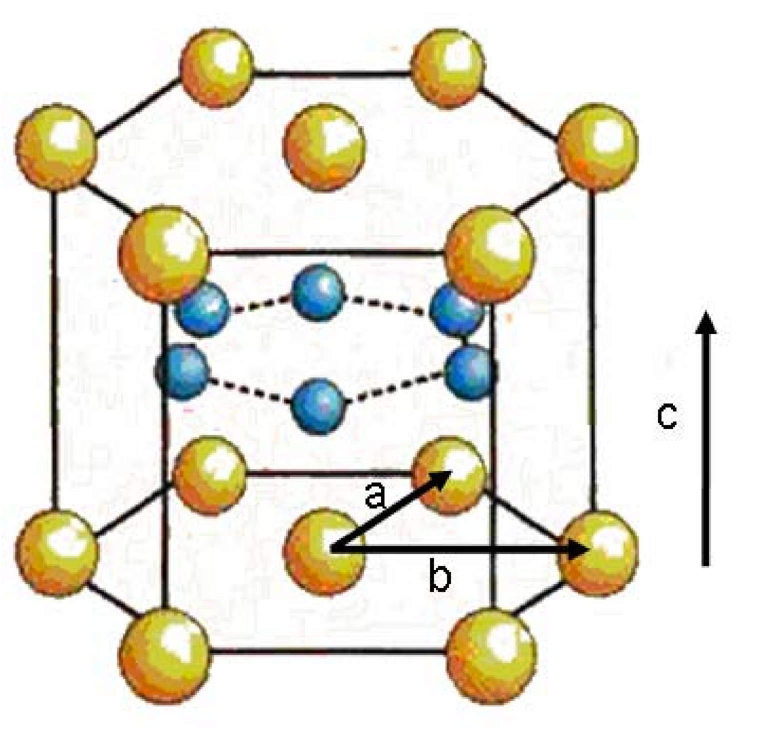

Figure 1.1 - MgB_2 Structure adapted from Canfield and Crabtree [Canfield01]. Mg is light yellow. B is dark blue.

Mechanically, MgB_2 is similar to other hard, strongly bonded intermetallics such as Nb_3Sn. MgB_2 has hardness similar to that of WC cutting tools ($H_V \sim 1500$), and has a dark bronze metallic luster, shading to black when doped with carbon. MgB_2 is brittle and oxidizes easily.

1.1.2 - Thermodynamics and Kinetics

Thermodynamic data on the Mg – B system is still neither abundant nor well accepted for two reasons. First, until 2001 none of the Mg-B phases was commercially important. Second, there are experimental difficulties working with the system since both B and Mg are highly reactive, and MgB_2 actually decomposes at less than half its own theoretical melting temperature and ambient pressure. Most people argue that Mg-B is a system of line compounds with practically no mutual solubility anywhere in the system. This is the case in the phase diagram shown in figure 1.2.

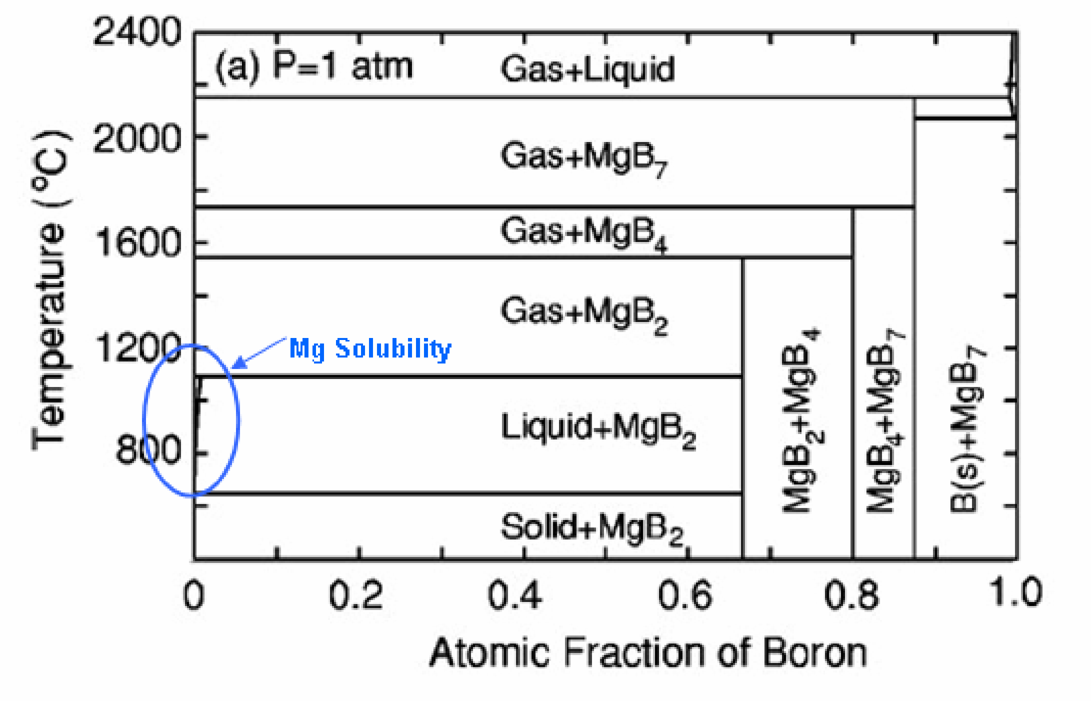

Figure 1.2 - MgB_2 phase diagram adapted from [Liu01].

This phase diagram was obtained by simulation, and is frequently consulted by the community. It has been argued [Bellingeri01,Braccini01] that MgB_2 can exist with a small magnesium deficiency, but this argument has fallen out of favor in the last few years. This diagram shows small but important B solubility in Mg, which occurs to a much larger extent in Karpinski's high pressure phase diagram.[Karpinski01] The emergence of this solubility seems to correlate with the T range for the onset of sintering observed elsewhere[Braccini02,Braccini04] and in this work (Ch. 7). Therefore, sintering in MgB2 could be facilitated by the presence of liquid Mg. In our samples with high $T_{HIP} > 1150^{o}C$ (Ch. 7) free Mg existed, and was found to disrupt supercurrent flow.

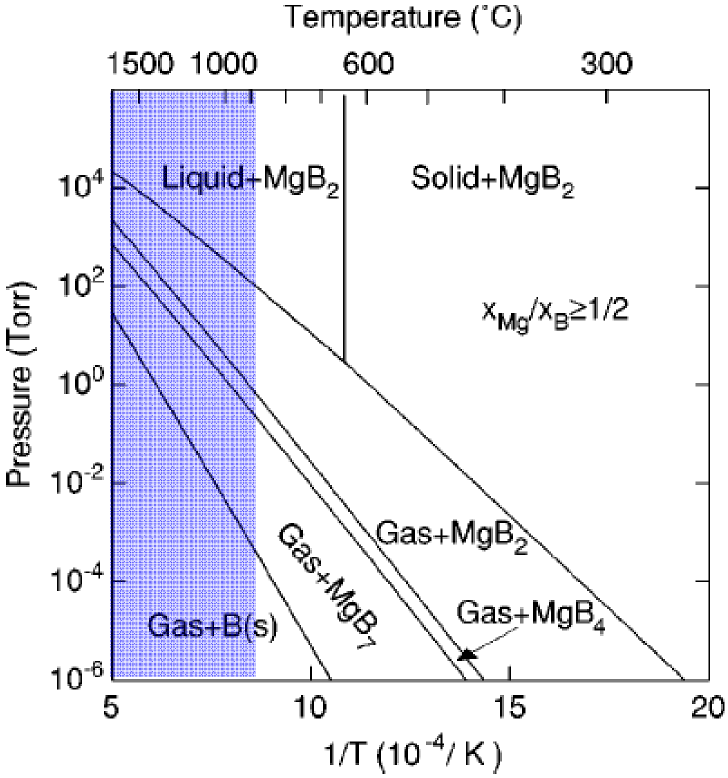

Figure 1.3 - P-T diagram adapted from [Liu01] Based on simulation.

It can be seen from the compositional phase diagram that MgB_2 is the most Mg-rich intermetallic phase in the system. Therefore, if Mg is present in sufficient quantities, MgB2 will occur in reacted samples. Since Mg is the mobile species in the Mg-B reaction we expect that MgB_2 first forms on the surface of B particles where MgB_4 and higher borides are already present. Some difficulty arises in keeping the Mg activity high enough to maintain MgB_2 at elevated temperatures > about 900°C because Mg develops a high vapor pressure that requires containment. This is expressed in the P-T diagram shown in Figure 1.3, adapted from Liu et al[Liu01] in which the approximate region of necessary Mg containment has been shaded. This diagram is a product of simulation, so it may contain some quantitative error, but we see that during heat treatments at 1500°C, a Mg partial pressure of about 10^4 Torr (~1 MPa) develops. At single crystal growth temperatures ~1700-2200°C [Karpinski01, Kazakov01] Mg pressure is not shown in Figure 1.3 but could be on the order of 0.2 GPa – the limit of many hot isostatic presses. Uniaxial pressing with BN anvils is typically used for MgB_2 single crystal work, with pressure up to several GPa. Karpinski [Karpinski01] published a phase diagram at 3 GPa showing a Mg-MgB_2 eutectic at 840 K and MgB_2 melting point around 2500 K.

Many challenges to MgB_2 wire makers stem from the radically different character of Mg and B, as alluded to above in the phase diagram showing their respective melting temperatures. Mg is ductile, melts at 650°C and is easily vaporized (Boiling Point 1050°C). Boron is a hard, brittle solid with T_m > 2000°C and very high boiling temperature. For laboratory purposes vaporous B does not exist (although B_2O_3 is a glass former which can evaporate). The melting temperature of MgB_2 is nearly twice the boiling temperature of Mg. Doping is very difficult because at the temperatures necessary to achieve reasonable diffusion kinetics in B or MgB_2, a very high Mg pressure is necessary to prevent loss of Mg. Similarly, large chunks of B react very slowly with Mg because the reaction is limited by diffusion of Mg through MgB_2. As a result, in order to beneficially dope the material, the dopant element must be well mixed and diffusion distances must be very short. That is accomplished in this work by mechanical alloying.

Although C-doping in bulk MgB_2 has been reported for heat treatment temperatures as low as 600°C [Matsumoto01], such low temperature reactions result in poorly connected material. Generally, for the formation of MgB_2 a reaction temperature of 650-900°C is used [Sumption01] and for sintering pre-reacted MgB_2 at least 800-900°C is necessary.[Braccini02]

1.2 Basic superconducting properties

Bud'ko et al. [Budko01, Budko02] showed that MgB_2 made with ^{10}B as opposed to ^{11}B or to natural B does in fact show a T_c shift due to the isotope effect predicted by the relationship

$$T_c = cM^{-\alpha} \tag{1.1}$$

Where c is a constant, M is the atomic mass of the superconductor and α~0.5.[Evetts01] This behavior is consistent with MgB_2 being a phonon mediated BCS superconductor.

Larbalestier et al. [Larbalestier01] placed MgB_2 closer to LTS than HTS when they showed that unlike HTS cuprates, MgB_2 does not suffer from orientational grain boundary weak links, implying that texturing the material is not necessary to make a high quality conductor. In that way, it can be considered the highest T_c member of the LTS group. Unfortunately, dH_{c2}/dT of pure MgB_2 is less than 0.5 T/K. Canfield [Canfield02] and Bud'ko [Budko02] showed for pure MgB_2, H_{c2}(0 K) is only 16 T with H//ab-plane and ~2.5 T with H//c-axis. These values are far inferior to that of Nb_3Sn (H_{c2}(0 K) ~ 32 T).[Godeke01] Even though NbTi has H_{c2}(0 K) only about 12 T, H*(4.2 K) of NbTi is typically higher than that of randomly oriented unalloyed MgB_2 where H* is limited by the unfavorably oriented crystals. H*(4.2K) of pure MgB_2 is typically less than 7 T, far too low to challenge the Nb based LTS technologies.

Fortunately, alloying MgB_2 can have a profound impact on H_{c2}, as first shown in thin films fabricated by Eom et al. [Eom01], which Gurevich et al. [Gurevich01] demonstrated had H_{c2} (0 K) of nearly 50 T. Perhaps even more significant was the shape of the H_{c2} curve, which had an upward curvature near 0 K, rather than leveling off as expected from the WHH (Werthamer, Helfand, Hohenberg) model. The best of those films – CB2 – contained both O and C impurities. At the time, it was suspected that the increased H_{c2} was due to oxygen doping. It is still unknown to what extent O doping affected H_{c2}, but later work by the group at Penn State University obtained even higher H_{c2} by carbon doping their HPCVD thin films [Braccini03]. These H_{c2} results fit the model of Gurevich [Gurevich02] in terms of electron scattering rates within each band, as discussed below.

Prior to Gurevich's work, it had already been shown [Kortus01] that MgB_2 has two weakly coupled superconducting bands. The σ band having the larger gap ($\Delta_\sigma(0) \sim 7.2$ mV) and being confined to the B sheets, and the smaller gap ($\Delta_\pi(0) \sim 2.3$ mV) in the nearly isotropic π band. The σ band actually has both a higher T_c (~39 K) and a higher $H_{c2}(0\ K)$ (16 T in the pristine state) than the π band. As a result, in a randomly oriented bulk, we would expect both T_c and H_{c2} to be controlled by the properties of the σ band. Because the bands are only weakly coupled, it is possible to exploit differential scattering rates within each band to alter the properties, especially to improve $H_{c2}(T)$ without significant T_c reduction. Figure *** shows how the measured H_{c2} is actually a combination of the two bands. For each band acting separately, H_{c2} is determined by the coherence length, and the total H_{c2} is therefore determined by the properties of the dirtier band. By preferentially scattering electrons in the σ band, $H_{c2}(T)$ can be made to curve upward as T approaches 0 K, as shown in Figure 1.4. Interband scattering decouples the bands, causing T_c to decrease with no H_{c2} benefit.

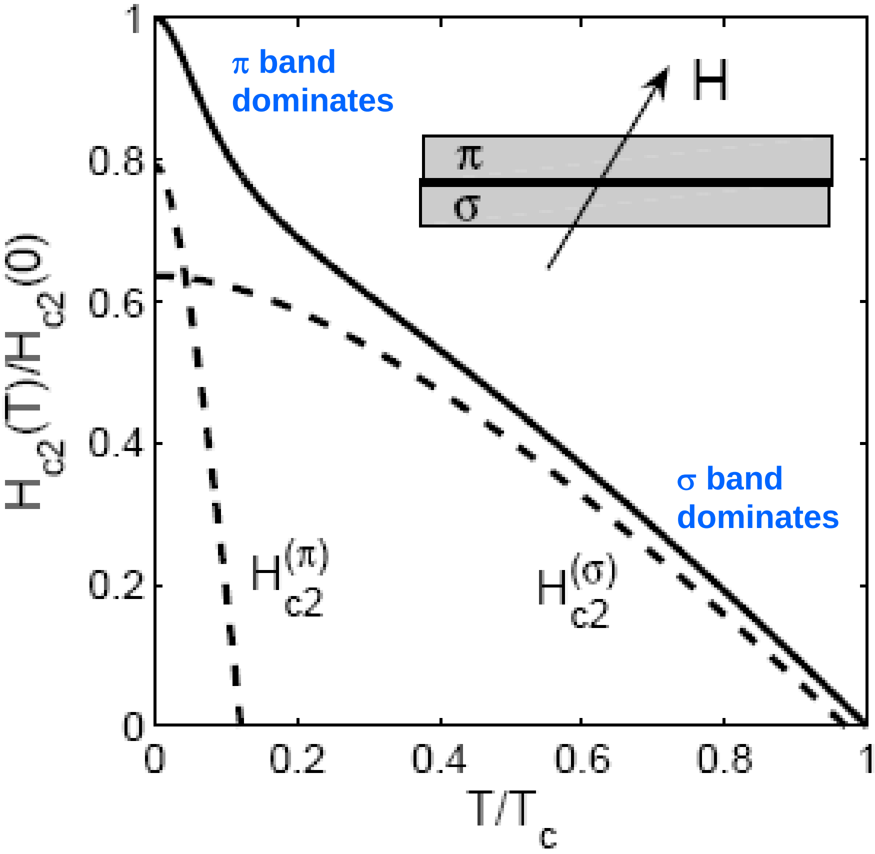

Figure 1.5 - Relative H_{c2} lines predicted theoretically for each band, and the actual H_{c2} curve of MgB_2 according to the Gurevich "toy" model. Adapted from Gurevich.[Gurevich03]

According to the Gurevich model, the source of electron scattering is non-specific. In practice, it can be the result of defects, disorder (such as neutron scattering [Putti01,Zhetmayer01,Wilke01,Wilke02]), strain, or alloying. In the case of high H_{c2} films, carbon alloying occurs, but lattice buckling has also been observed which could be responsible for the favorable combination of scattering parameters yielding the high H_{C2}.[Zhu01]

Bulks have also benefited from doping with carbon or C-containing species [Dou01,Matsumoto01,Sumption01,Senkowicz01,Senkowicz02,Ma01] but not to the extent of the films. Bulk MgB_2 has rarely (#Matsumoto) exceeded $H_{c2}(0\ K) = 40$ T. The study of H_{c2} by C-doping is one of the thrusts of this thesis.

Electron scattering is observable as increased normal state resistivity because resistivity in metals originates from scattering the charge carriers, electrons or holes. Electrons can be scattered either by lattice defects or by interaction with phonons. The relative contributions to resistivity from defect and phonon scattering is approximately described by Matthiesen's rule, expressed as:

$$\rho = \rho_{def} + \rho_{ph}(T)). \tag{1.2}$$

Here we see that the defect contribution is temperature independent below the annealing temperature of the metal. The phonon contribution is a strong function of temperature because the phonon frequency is a function of temperature. Near 0 K the phonon contribution is generally close to zero and so $\rho \sim \rho_{def}$, and the measured ρ value is known as the residual resistivity. For low temperatures where $T < \Theta_D / 12$, (Θ_D is the Debye Temperature) the phonon contribution to resistivity is given by the Bloch-Gruneisen expression [Sumption02]

$$\rho_{ph}(T) \approx \rho(0) + A\left(\frac{T}{\Theta_D}\right)^5 \int_0^{\frac{\Theta_D}{T}} \frac{e^z z^5}{\left(e^z - 1\right)^2} dz \tag{1.3}$$

Where A is a metal specific constant. At $T > \Theta_D / 12$, the phonon contribution to resistivity increases approximately linearly. The net result of these behaviors is to produce a curve similar to that shown in Figure 1.6.

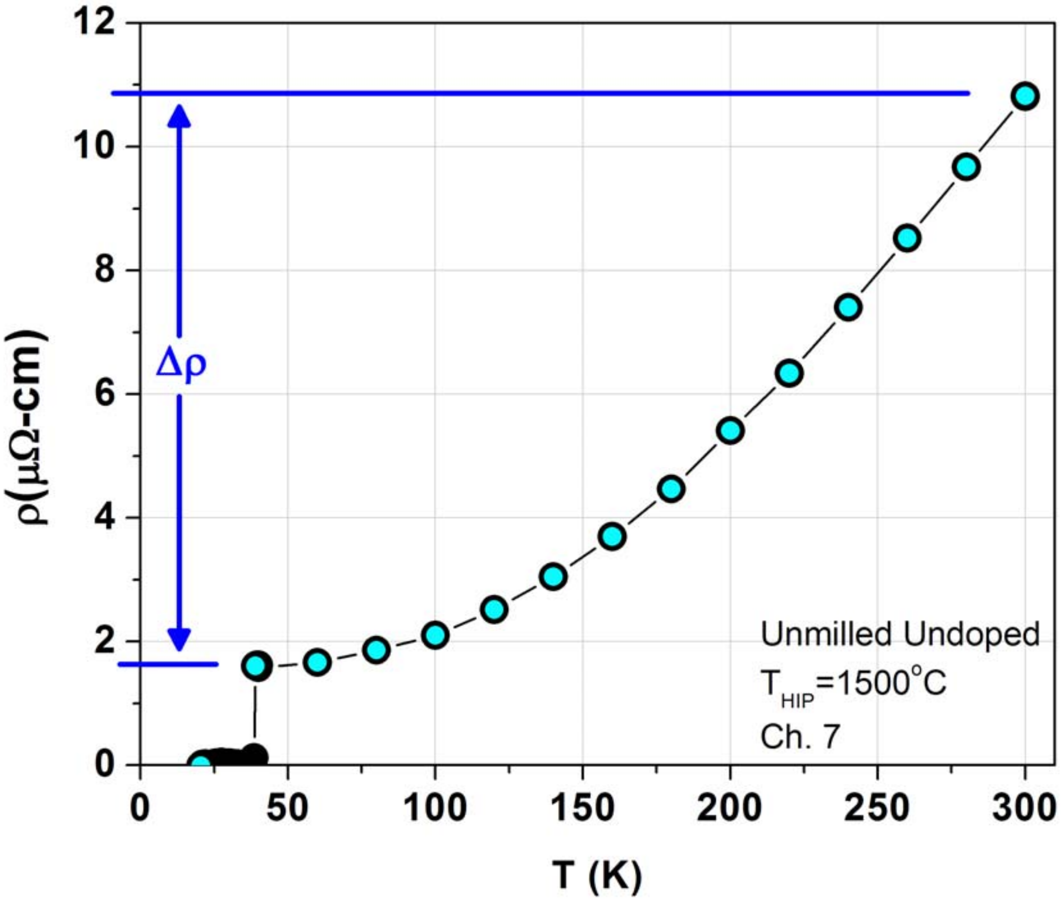

Figure 1.6 – ρ(T) for a well connected MgB_2 bulk sample.

As defect scattering increases, both ρ(40 K) and ρ(300 K) increase. To first approximation ρ_{ph} is unaffected by changes in defect scattering, so Δρ = ρ(300 K) -

ρ(40 K) remains roughly constant despite the fact that the residual resistivity ratio (RRR = ρ(300 K) / ρ(40 K)) decreases, approaching 1 for very high defect concentrations.

Early in the study of MgB_2, there was much confusion over the resistivity curve. Numerous groups measured curves with the general shape shown in the figure above, and often with high RRR > 4 or 5, but with a wide variety of ρ(40 K) values ranging from < 1 μΩ-cm to hundreds of μΩ-cm. These ρ variations were often unaccompanied by changes in T_c or $H_{c2}(T)$ Rowell [Rowell01,Rowell02] explained those seemingly unphysical findings by proposing that Δρ is approximately equal for all pure MgB_2, but the wide range of measured Δρ is actually due to variations in connectivity. When connectivity is incomplete the portion of the sample cross section carrying current is smaller than the measured sample cross section. Since

$$R = \frac{\rho L}{A} \tag{1.4}$$

(where R is the resistance, A is the cross sectional area perpendicular to current transport, and L is the length of current flow), an artificially low A gives a high measured R and thus an artificially high calculated ρ.

By assuming a universal value of Δρ (for example $\Delta\rho_{ideal}$ = 7.3 μΩ-cm),[Rowell03] based on measurements of samples thought to be fully connected, it is then possible to calculate the active current carrying cross sectional area (A_F) simply by scaling the measured Δρ to $\Delta\rho_{ideal}$ as follows:

(1.5) $$A_F = \frac{\Delta\rho_{ideal}}{\Delta\rho}$$

And when A_F is known, it is then possible to estimate the true residual resistivity of the fully connected portion (which we call the adjusted resistivity, ρ_A) according to:

(1.6) $$\rho_A = \rho_{measured}(40\ K) \times A_F$$

For polycrystalline bulk MgB_2, A_F is typically less than 0.5, indicating incomplete connectivity.

Early work by Larbalestier et al. [Larbalestier01] indicated that MgB_2 behaves more like Nb-based LTS than HTS cuprates in that MgB_2 does not suffer orientational weak link behavior at grain boundaries, however they noted that their sample was porous and not fully reacted and therefore J_c was low due to incomplete connectivity. Achieving good connectivity is a critical issue in order to achieve high J_c. This point was made by Iwasa et al. [Iwasa01] who point out that most engineering superconductors reach J_c(0 K) ~ 0.1 J_d where J_d is the depairing current density. In MgB_2, that value is achieved by only a few very well connected films. Bulks are far behind with typical J_c(0 K) < 0.02 J_d. Since the well-connected, high J_c films do not appear to have markedly stronger flux pinning properties than the bulks, the difference is probably due to connectivity.

Connectivity can be limited by several considerations. The reaction Mg + 2B → MgB_2 is accompanied by a 34% volume loss,[Yamamoto02] implying that wires made with Mg + B cores and reacted *in-situ* can be expected to contain a minimum of ~34% porosity. In reality, they are usually closer to 50% porous [Matsumoto02] although the use of very strong sheath materials has been shown to improve core density through the mechanism of residual compression of the core by the sheath.[Goldacker01] In wires made from MgB_2 powder already reacted *ex-situ* prior to the PIT process, reaction shrinkage is not an issue but sintering is very important. *Ex-situ* samples may have high bulk densities (especially after drawing or pressing) but very low connectivity results from heat treatments lower than about $800^{o}C$, as demonstrated by Braccini et al. [Braccini04] and by this work.

Current flow can be blocked by amorphous regions with in the sample, or by non-superconducting grain boundary phases. Song et al. [Song01] found grain boundary coating phases even in otherwise very pure MgB_2, which could be related to the fact that B_2O_3 is a glass forming compound with melting point $\sim 800^{o}C$. Chen et al [Chen02] found that starting boron source had a large effect on final MgB_2 properties. Jiang et al. [Jiang01] discovered that current blocking MgO phases could be largely eliminated by removing adsorbed oxygen from the surface of the starting boron powder. Using our "boron purification" method we were able to roughly double A_F when using commercial B as a starting material.

High connectivity MgB_2 filaments [Canfield03,Wilke03] made by a CVD process have supplied the MgB_2 community with most of the data on fully-connected polycrystalline bulk properties. Good results have also been achieved by hot isostatic pressing [Serquis01] but the HIP method alone does nothing to alleviate current blocking by second phases, and at $T_{HT} = 1000^{o}C$ there is sometimes up to 10% retained porosity, particularly in heavily C-doped material. Milling does alleviate current blocking by second phases, as described in Ch.3.

Artificial introduction of flux pinning centers such as Dy_2O_3 [Chen03] and Si compounds [Xu01] has resulted in increased J_c, but MgB_2 is primarily a grain boundary flux pinner, as demonstrated by Kitaguchi et al. [Kitaguchi01] who performed J_c measurements as a function of orientation on films with columnar grains. Like Nb_3Sn [Rodrigues01], MgB_2 (particularly ball milled MgB_2) obeys a Kramer scaling relationship [Evetts01] in which the plot of $J_c^{0.5}H^{0.25}$ as a function of H is close to linear.

1.3 - Bulk Processing

This document focuses on bulk materials, with particular emphasis on MgB_2 made from powder precursors which are adaptable to powder-in-tube (PIT) wire making. There are two competing PIT wire making strategies currently employed for commercial MgB_2 strand. These are the *in-situ* process (filling the tube with pre-reacted powder) and the *ex-situ* process (reacting Mg and B powders inside the wire). Both have been used to produce long lengths of high quality strand, resulting in > 1T coils [Sumption03,Serquis02,Braccini02]. Each method has its own suite of advantages, but the eventual best route will probably be determined by the balance between flux pinning (grain refinement), connectivity, and doping achievable by each method.

The *in situ* method involves formation of MgB_2 inside the final-sized conductor – usually by direct reaction of Mg and B. Using *in situ* reaction method, small grains can only be obtained by using very low heat treatment temperatures, in many cases below T_m of Mg (650°C), but then it is very difficult to get good connectivity. Matsumoto et al. [Matsumoto02] obtained < 50 nm grains in SiC doped tapes made using MgH_2 as a Mg source with T_{HT} = 600°C. Unfortunately, A_F was less than 0.2 and so while J_c in those samples is very good, it is less than that obtained by some other bulks [Senkowicz02,Ma01] – none of which approach the best fully connected films.[Chen04]

The *ex-situ* method is simpler in concept. Pre-reacted MgB_2 is obtained, often commercially, and then packed into a metal tube (generally Fe, Ni, or Nb-lined) which is then drawn into wire or rolled into tape. Grasso et al. [Grasso01] showed that even in the absence of heat treatment $J_c \sim 10^5$ A/cm^2 could be obtained in as-rolled tapes provided high-strength sheath material was used. Unfortunately, in order to improve on that result, MgB_2 must be sintered with approximately T_{HT} > 800°C and preferably T_{HT} > 900°C.[Braccini02,Braccini04] These high temperatures limit the choice of sheath material to avoid extensive reaction with the core. In particular, there is a eutectic reaction in the Cu-Mg phase diagram around 725°C that can cause melting of the sheath. Furthermore, Al (which is desirable for fusion applications) cannot be used as a sheath material because of its low melting point and its propensity to detrimentally alloy MgB_2.

The advantages of the *ex-situ* method are more subtle than those if *in situ*. Reaction shrinkage is not an issue, so the core density can be high. Mixing of Mg and B is not required, so the possibility of microstructural inhomogeneity due to poor mixing does not apply. In the author's opinion, the most important advantage of the *ex-situ* method is that using pre-reacted powder allows us to introduce a processing variable which does not exist for the *in-situ* method – mechanical work. Through high energy milling, we have refined grain size to ~10 nm in pre-reacted powder. Although the grains grow during sintering, final grain size for samples with T_{HT} = 1000°C is only ~50 nm.[Senkowicz02] In this way we can achieve very strong pinning in a homogeneous sample.

The basic physical and superconducting properties have now been summarized. Processing-related challenges have been identified to be minimizing grain size while maximizing connectivity, and the two main powder-in-tube wire making processes have been identified. Unfortunately, the basic properties of MgB_2 are not good enough for widespread application. In particular, J_c(H) must be improved. This can occur by raising H_{c2}(T) through increased carrier scattering, as will be further discussed in the next chapter.

Chapter 2 – Effects on upper critical field and other properties by carbon doping and electron scattering.

As shown in Ch.1, H_{c2}(H//ab plane) of large grained, undoped MgB_2 is only 16 T, and H_{c2}(H//c-axis) < 5 T. These values are too low for most magnet applications, even if J_c(0 T) were very high. As a result, much attention has been devoted to increasing upper critical field in MgB_2. This is most commonly achieved through C-doping, but non-compositional effects can also be important. Since the main thrust of this thesis is the understanding and optimization of medium to high field (using a benchmark 8 T, 4.2 K) J_c, it is critically necessary to understand the effects of C-doping on superconducting and normal state (lattice parameter, resistivity) properties. These effects are discussed below. We then compare some of the best J_c(H) results for in-situ MgB_2 bulks doped by different forms of C and see that the J_c(H) curves are almost the same – indicating that the achievable J_c in in-situ MgB_2 is not controlled by the way C is introduced, but is limited by other considerations such as connectivity, flux pinning, and possibly dopant homogeneity. Present in-situ conductors are limited because connectivity and flux pinning are difficult to co-optimize. High T_{HT} gives good connectivity, but grows grains. Ex-situ conductors have not yet been optimized and may be capable of higher J_c(H). This discussion will establish context for later chapters where we will focus on the co-optimization of composition, connectivity and flux pinning in ex-situ C-doped bulks. This chapter does not explain in detail the physics associated with various electron scattering effects, but does seek to provide the reader with sufficient information about the effects of disorder and doping (especially C-doping) on superconducting properties to thoughtfully interpret the results in subsequent chapters.

In a single band superconductor, upper critical field goes as:

(2.1) $$B_{c2} = \frac{\phi_0}{2\pi\xi_0 l}\left(1 - \frac{T}{T_c}\right)$$

Where ϕ_0 is the superconducting flux quantum, l is the mean free path, and ξ_0 is the coherence length at 0 K.

Upper critical field can be manipulated by changing the coherence length, such as by shortening the electron mean free path within each superconducting band (and between the bands), either by non-compositional means (disorder, possibly grain boundaries) or by introducing impurities, according to:

(2.2) $$\xi_{dirty} = 0.85(\xi_o l)^{0.5}$$

Where l is the electron mean free path and $l < \xi$. As a result, upper critical field increases with more electron scattering, and is proportional to the normal state resistivity

(2.3) $$H_{c2} = 3110\rho_n \gamma T_c$$

Where γ is the Sommerfeld coefficient (around 3-6) and ρ_n is the residual resistivity. In MgB_2 the presence of two superconducting bands makes the relationship between resistivity and upper critical field more complicated, as described by Gurevich[Gurevich02,Gurevich03]. In practice, this relationship is unreliable in MgB_2 because under some conditions H_{c2} is determined by the cleaner band, so H_{c2} could be controlled by one band and measured ρ could be dominated by the other band.

Another way to roughtly estimate $H_{c2}(0\ K)$ as a function of ρ by calculating the mean free path, assuming free electrons and a single band. This allows the use of the Sommerfeld equations:

(2.4) $$n = \frac{8\pi}{3}\left(\frac{mV_F}{h}\right)^3$$

And

(2.5) $$\sigma_0 = \frac{n\varepsilon^2 l}{mV_F}$$

Where σ_0 is the low-temperature conductivity, n is the number of free electrons per unit volume, V_F is the electron velocity at the Fermi surface, h is Planck's constant, ε is the charge of an electron, and m is the mass of an electron. To be accurate, we should use the effective mass (m^*) for m. A value $m^* \sim 0.5\ m_e$ was determined by Cooper et al [Cooper01] using the de Haas – van Alphen effect. Obtaining $V_F \sim 4.8 \times 10^5$ m/s and $n \sim 6.7 \times 10^{28}$ e/m^3 from Bud'ko et al [Budko01] and applying the relationship $\rho = 1 / \sigma$, we arrive at the following approximation:

(2.6) $$l \approx \frac{1}{7.9 \times 10^{15} \rho}$$

Where l is in meters, and ρ is in Ω-m. Thus for $\rho = 0.4$ μΩ-cm, $l \sim 32$ nm which is within a factor of 2 of Bud'ko et al's similar calculation.[Budko01] According to this equation it requires ρ on the order of 3 μΩ-cm to obtain $l \sim \xi$. We can combine the equation for l with the equation for B_{c2} (equation 2.1), which then yields:

(2.7) $$B_{c2}(0K) = 5.2 \times 10^{8} \rho$$

With ρ in Ω-m or

(2.8) $$B_{c2}(0K) = 5.2 \rho$$

With ρ in μΩ-cm. So for $\rho = 3$ μΩ-cm, we estimate B_{c2}(0 K) ~ 15.6 T which is very close to the experimental 0 K value B_{c2}(B//ab) ~ 16 T.[Budko02] Furthermore, $\rho = 10$ μΩ-cm (a conservative value for ρ_A in C-doped bulks) should yield $B_{c2} > 50$ T. This value is higher than given by equation (2.3). In practice, B_{c2} falls short of any of these predictions, since for bulks B_{c2} almost never exceeds 40 T. The reasons for this discrepancy probably lie in the two band nature of MgB_2 which was briefly discussed in Ch.1.[Gurevich03]

We therefore see that shortening the mean free path (*l*) by scattering charge carriers (in this case electrons) should increase H_{c2}, whether the scattering derives from alloying or from non-compositional factors such as defects or grain boundaries, but the 2 band nature of MgB_2 makes it difficult to predict the magnitude of the effect without detailed knowledge of the type of electron scattering, and which band(s) it affects.

2.1. Non-compositional electron scattering

Disorder can be produced by ball milling and can raise H_{c2} in some circumstances. Defects in MgB_2 scatter electrons and influence the superconducting and normal state properties. The effects of disorder have been studied by neutron irradiation [Zhetmayer01,Putti01,Wilke01,Wilke02,Karkin01] and are qualitatively similar to those of C-doping. Those effects include reduction of T_c, increase of normal state resistivity, and changes in H_{c2}. Small amounts of neutron irradiation (< about 10^{18} n/cm^2) generate point defects which scatter electrons, shorten the electron mean free path, reduce T_c, increase normal state resistivity, and increase H_{c2}.[Zhetmayer01,Putti01] Fluences greater than about 10^{18} n/cm^2 cause strong disordering which probably results in a drop in the density of states at the Fermi surface $N(E_F)$ as in LTS.[Karkin01] H_{c2} degrades for fluences above about 10^{18} n/cm^2.[Wilke01]

Annealing neutron irradiated (~10^{19}n/cm^2) bulks[Wilke01] largely reversed the effects of irradiation. After annealing undoped MgB_2 for 24 hours at 500 - 700°C, T_c and H_{c2} can be restored nearly to their unirradiated values. This result establishes a temperature scale for defect annealing, and suggests that disorder should not be a significant factor influencing ex-situ samples heat treated at $T > 900^oC$.

Ball milling of Mg + B powders [Wu01,Gumbel01,Gumbel02,Lorenz01] has produced high J_c MgB_2 by in-situ mechanical alloying. These studies all observed decreased T_c and increased H_{c2} and $J_c(H)$ compared with unmilled MgB_2. Gumbel et al[Gumbel01,Gumbel02] reported some recovery of T_c with hot pressing at 700°C, from 33 K to 34.6 K after 90 minutes of pressing. Lattice parameter measurements showed a~0.3085 nm indicating little or no carbon substitution, and other impurities were unlikely. They attributed the decreased T_c to defects or crystalline disorder, but the possibility of grain boundaries scattering effects on T_c cannot be ruled out in their fine grained (40-100 nm) samples (see also Ch. 6,7).

2.2 Doping

The two elements best known to substitutionally dope MgB_2 are Al for Mg, and C for B.[Angst01] Both are electron donors, and both result in similar T_c decreases per additional electron in the unit cell. C-doping can increase H_{c2}(0 K) by more than a factor of two, but Al substitution reduces $H_{c2}(T)$. C-substitution on the B lattice contributes electrons primarily to the σ band, which also decreases the anisotropy of the Fermi surface (and thus of H_{c2}).[Karpinski01]

Li can be substituted for Mg,[Li01,Karpinski01] resulting in hole doping on the π band, which reduces T_c. No improvement in properties critical to $J_c(H)$ was reported due to Li doping. Monni et al. [Monni01,Monni02] concluded that structural distortion due to the dopant atoms resulted in pair breaking and suggested that interband scattering is more important than lattice compression or band filling in determining T_c. The observation that no dopant has been known to increase T_c in MgB_2 supports that suggestion. Li doping does not seem to produce the sort of intraband scattering thought to result in high H_{c2}.

Other elements for which there is some evidence of doping are Zr,[Chen01,Bhatia01] Mn, V, Ca, [Karpinski01,Sun01] and O.[Eom01] Bhatia et al.[Bhatia01] reported increased H_{c2} through doping by a variety of metal diborides including Zr and Nb but that result has not been widely confirmed. Ti addition has been shown [Wilke06, Shen01] to produce excellent flux pinning, but there is no evidence that it alloys the lattice or increases H_{c2}.

The only dopant well known to increase H_{c2} or high-field $J_c(H)$ is carbon. H_{c2} increase has been achieved through addition of a number of C-containing species such as graphite, SiC [Senkowicz01,Dou01,Matsumoto02], or organic compounds [Yamada01,Xu02]. Bulk H_{c2} of MgB_2 above 40 T has been reported twice: due to SiC addition[Matsumoto01] which resulted in $H_{c2}(1.8\ K) \sim 45$ T and later by addition of carbon nanotubes [Serquis03] which resulted in $H_{c2}(1.8K?) \sim 44$ T, but the mechanism is not yet understood. Some of these C-sources have decomposition products that enhance flux pinning, but often at the expense of connectivity.[Wang01]

Moderate C-doping raises H_{c2} and $J_c(H)$ in both bulks and films. In bulks increased carbon content results in a contraction of the a-axis lattice parameter and no significant effect on the c-axis lattice parameter. Furthermore, bulks *almost* universally have maximum $H_{c2} \sim 35$ T. This limit appears to be related to strong interband and σ

scattering and weak π band scattering. Quantitative dependencies of structural and superconducting properties as a function of carbon concentration in bulk MgB_2 are shown in Figure 2.1.

Most films behave similarly to the bulk, but some C-doped films[Braccini03] have expanded a-axis *and* c-axis lattice parameters. Such films have been found to have H_{c2}(//ab) > 50 T and H_{c2}(//c) > 30 T with only a few K depression of T_c. These high H_{c2} values may be due to fine-scale (~20 nm) carbon-induced C-axis tilting, which could disrupt the p_z orbitals and cause strong π band scattering.[Zhu01,Gurevich01]

2.2.1 Effects of Carbon Doping on bulk and single crystal MgB_2

C-doped MgB_2 single crystals were grown by both the S. Lee group at ISTEC, Japan [Lee02], and the J. Karpinski group at ETH, Switzerland [Kazakov01,Karpinski01] Both groups used high temperature uniaxial pressing with BN media. Lee used T_{max} ~ 1700°C with P = 5 GPa. Kazakov used higher T_{max} = 1950°C with the exact pressure unspecified. Both studies found that actual lattice carbon content was generally higher than nominal carbon content of the precursor powder mixtures, probably due to contamination. Lee et al. used Auger Electron Spectroscopy (AES) to determine their carbon concentration within a stated error of about X=0.015 or less. In most of their data analysis, they used their nominal carbon content rather than the Auger peak intensity ratio, assuming that AES was detecting carbon not incorporated into the MgB_2 lattice. The author of this thesis prefers to use the AES intensity ratio for the Lee samples instead of the nominal composition, because the Lee data then agrees with Kazakov and Avdeev et al.[Avdeev01]

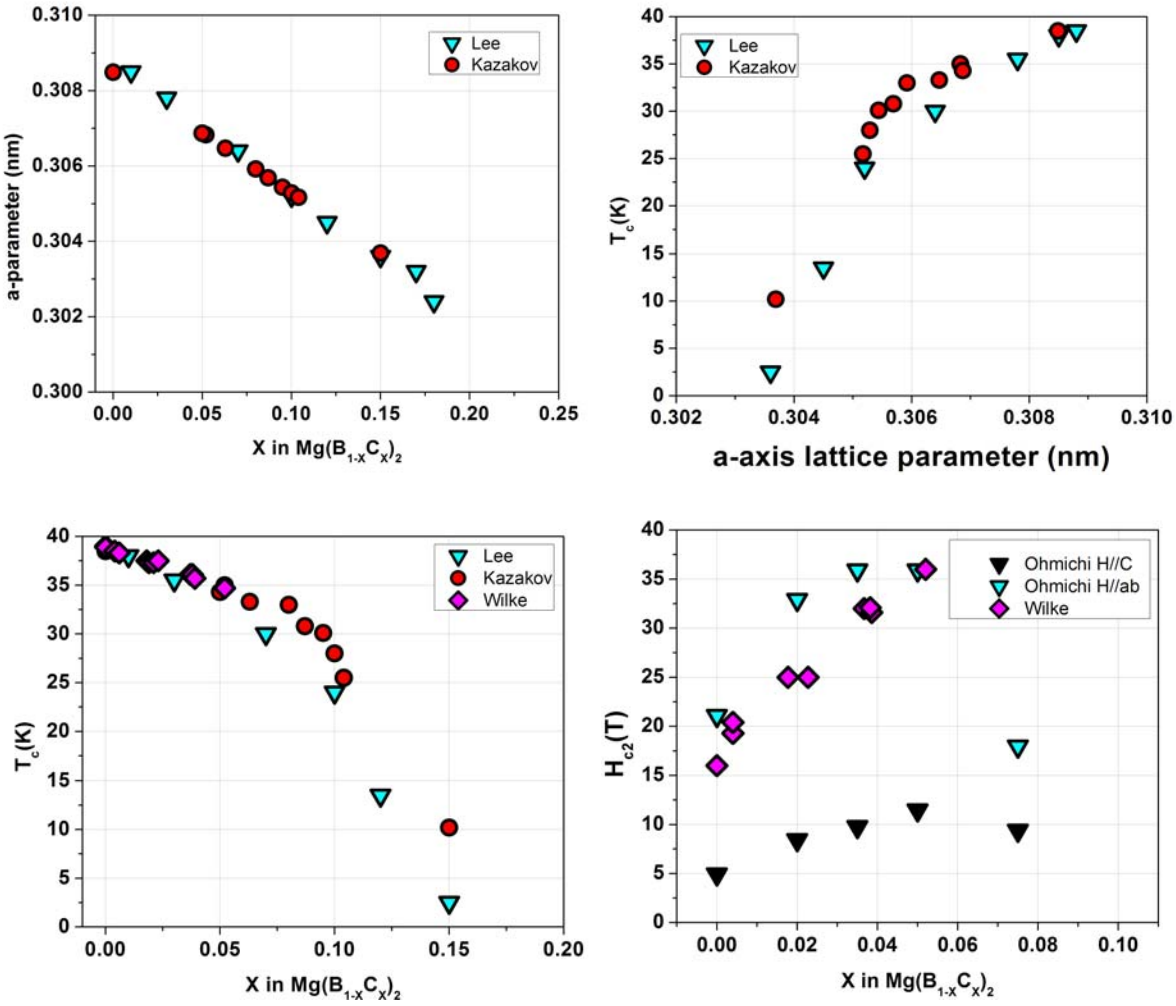

Figure 2.1 – Properties of C-doped single crystals and CVD filaments.

As shown in Figure 2.1, the a-axis lattice parameter contracts linearly with increasing C-content, as established by Lee et al. The two sets of single crystals agree well with the polycrystalline CVD filament data from Wilke et al. [Wilke03] for which X was calculated from lattice parameters using data from polycrystals of Avdeev et al.[Avdeev01] The Kazakov data show slightly higher T_c than the Lee data, possibly because Kazakov et al. obtained T_c from resistivity measurements while Lee et al. used magnetic measurements. These C-content relationships, particularly the lattice parameter dependence on X, apply generally for bulk $Mg(B_{1-X}C_X)_2$.

H_{c2} in bulks and single crystals benefits from carbon alloying. Figure 2.1 shows data from Ohmichi et al. single crystals [Ohmichi01] (resistive transition midpoints) and Wilke et al. CVD filaments [Wilke03] (resistive transition 99% of normal state ρ). Differences between the data sets may result from uncertainty in lattice carbon content.

The highest X points obtained in the single crystals (see fig 2.1 and 2.2) (X ~ 0.15 to 0.18) represent what Lee et al. [Lee02] refer to as the C solubility limit for the system, given their synthesis temperature of 1600°C - 1700°C. That number can be compared to apparent solubility limits of X(600°C) ~ 0.015 [Zhu02] in SiC-doped tapes, as well as the milled ex-situ bulks described in Chapters 4-7 of this thesis. The result is shown in figure 2.2. Compositions with X exceeding the solvus defined by Figure 2.2 should result in $Mg(B_{1-X}C_X)_2$ in equilibrium with MgB_2C_2. Commonly, MgB_2C_2 is absent and the excess C occurs as one or more unknown (possibly amorphous) phases. Here we see that C-solubility is strongly T dependent. This opens up additional possibilities for processing.

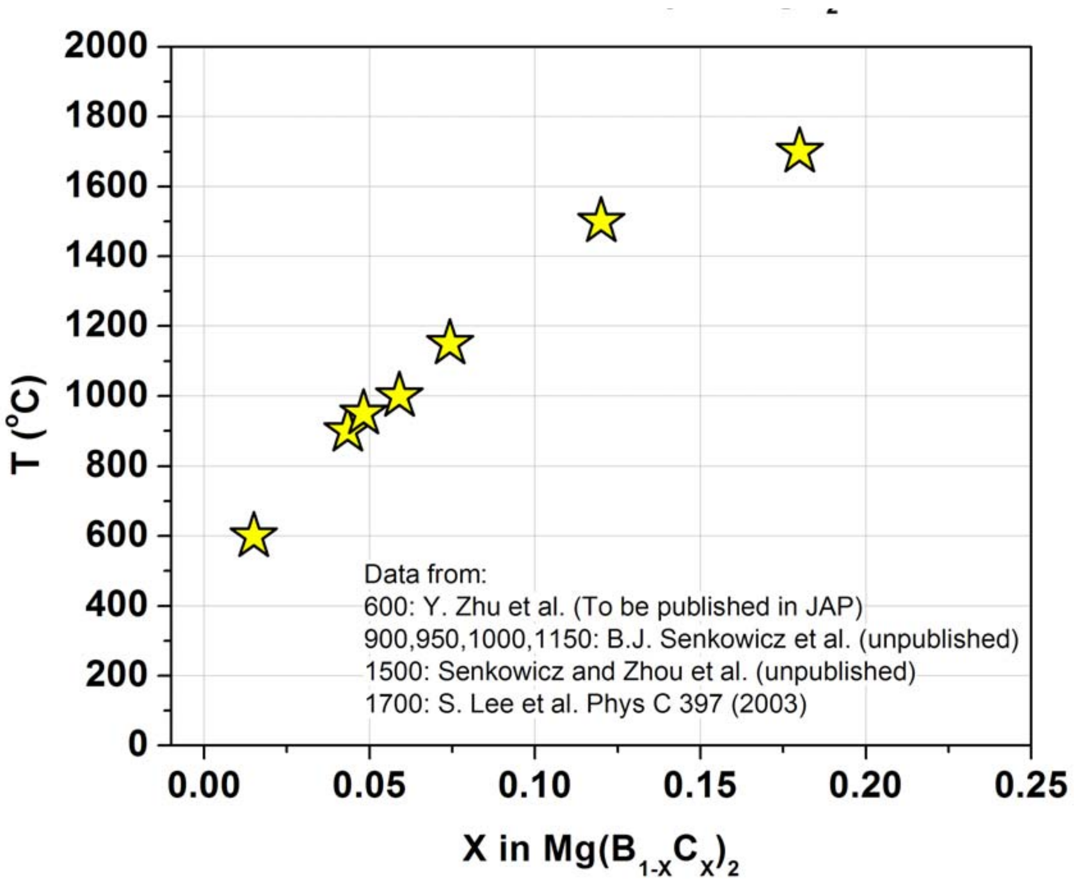

Figure 2.2 – Apparent carbon solubility in MgB_2 as a function of temperature.

2.2.1.1 Effect of carbon doping on normal state resistivity of bulk and single crystal MgB_2.

It is important to understand the dependence of normal state resistivity on C-content in order to extend the Rowell connectivity analysis to C-doped samples. The principal difficulty in applying the Rowell analysis to carbon doped MgB_2 is in choosing a suitable $\Delta\rho_{ideal}$ value. There are very few fully connected C-doped sample sets to use as a reference. In single crystals, c-axis resistivity data is only available in undoped crystals. Resistivity values in the ab-plane are shown for undoped crystals in figure 2.3a. Normal state restivity increases strongly with carbon addition. $\Delta\rho$ increases more gradually.

The $\Delta\rho$ values of the CVD filaments (shown in figure 2.3b) are higher than those of the ab-plane oriented single crystals due to the c-axis resistivity contribution. In undoped crystals, $\Delta\rho$ in the c-direction can exceed ab-plane $\Delta\rho$ by a factor of 3, as shown in Table 2.I.[Eltsev01]

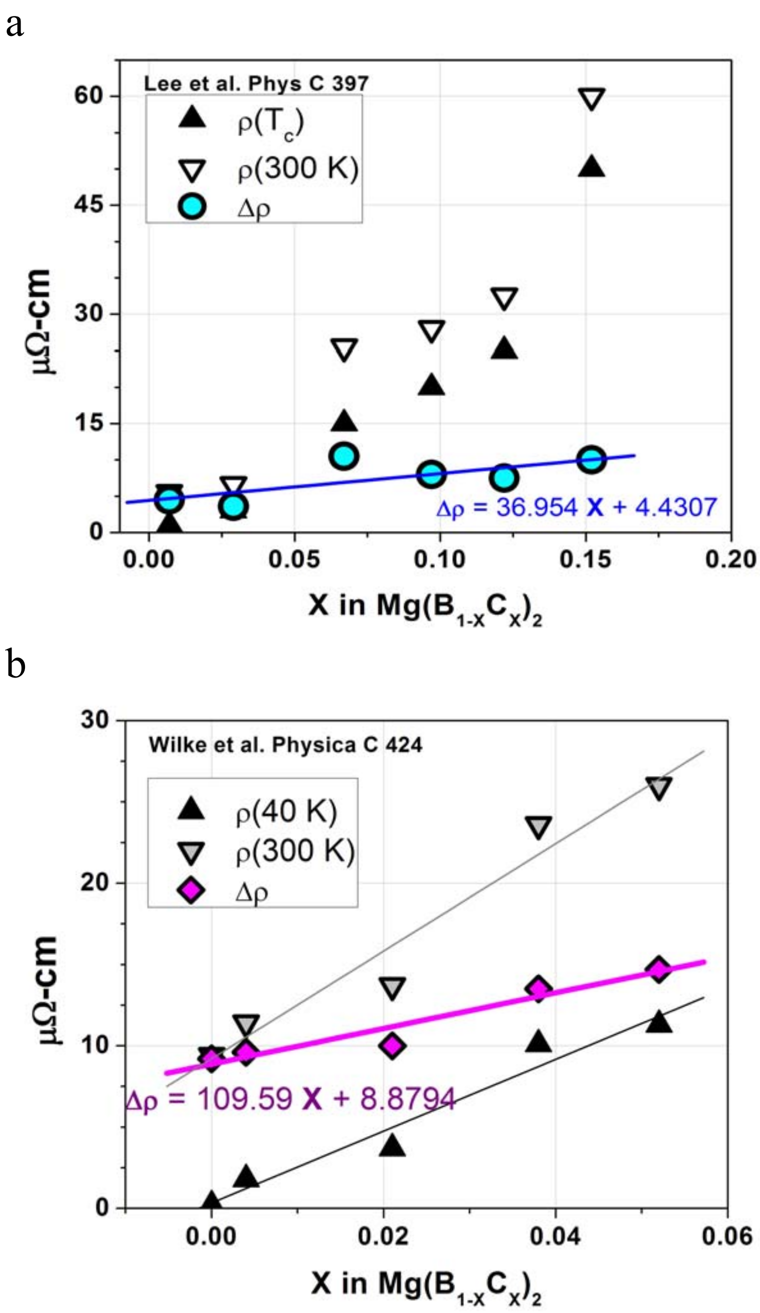

Figure 2.3 – Resistivity in a) ab plane of C-doped single crystals and b) polycrystalline CVD filaments. Δρ=ρ(300 K)-ρ(40 K)

For undoped material, J. Rowell's recommended value [Rowell03,Matsumoto02] of $\Delta\rho_{ideal} = 7.3$ μΩ-cm is empirical. The Wilke filaments yield a value of $\Delta\rho = 9.2$ μΩ-cm. Rowell – type calculations on C-doped samples that appear later in this thesis must be viewed as only semi-quantitative for three reasons: 1) lack of appropriate $\Delta\rho_{ideal}$ standards, 2) the phenomenological nature of the Rowell analysis itself, and 3) the fact that matching the C-content between our milled samples and the CVD filaments neglects any non-compositional effects on $\Delta\rho_{ideal}$.

Table 2.I – anisotropic single crystal resistivity from Eltsev. et al.[Eltsev01]. 300 K values are extrapolated from 275 K. All values are in μΩ-cm.

Pure crystals (ISTEC)		
	a-b plane	c-axis
ρ(300)	5.34	17.53
ρ(40)	0.79	2.68
Δρ(300-40)	4.55	14.85
RRR	5.77	5.54

2.3 Effects of C-doping on bulk J_c(H)

Carbon doping is often used to increase J_c(H) because it increases H_{C2} and H*. Results for some of the best in-situ bulks are shown in figure 2.5. The similarity of the curves indicates that optimized C-content can be obtained with a variety of C-sources, but changing the carbon source results in only minor improvements to flux pinning and connectivity. Some carbon sources such as solvents and oils result in worse J_c than that shown [Kim01,Hossain01,Wang01,Yeoh01,Yamada01] – probably because of connectivity loss.

In order to further optimize C-doped MgB_2 bulks, further improvements in flux pinning and connectivity must be made. Matsumoto et al. [Matsumoto02] and Zhu et al. [Zhu02] showed that grain size can be minimized by reacting in-situ tapes at T as low as 600°C, but connectivity was poor. Higher heat treatment T resulted in larger grains and less flux pinning.

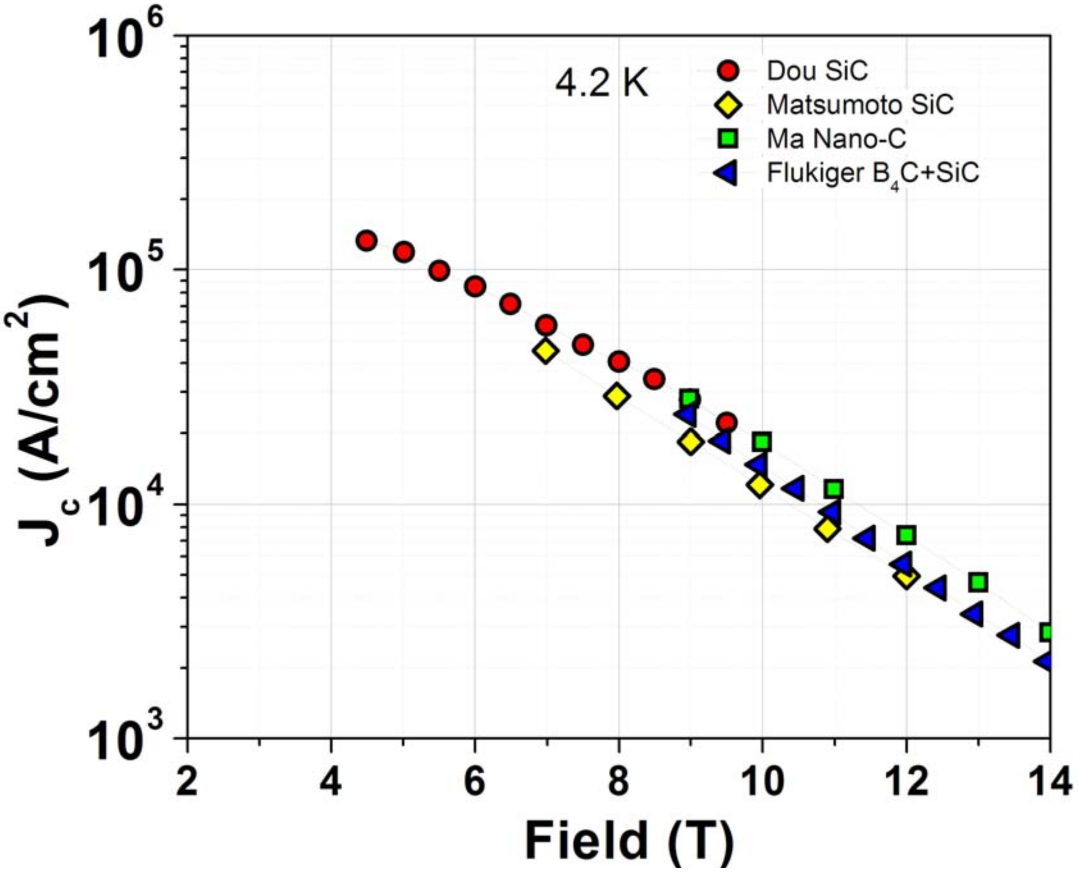

Figure 2.5 – C-doped bulk MgB_2 J_c(H). All curves are at 4.2 K unless otherwise specified.

2.4 Summary

Increased H_{c2} and $J_c(H)$ are always valuable for magnet applications. That can be obtained by introducing electron scattering centers such as defects, grain boundaries, or impurities. Point defect or disorder scattering is probably not relevant for samples heat treated above 500-700°C. Grain boundaries can remain dense at 1000°C. In bulks, C-doping has predictable effects on a-axis lattice parameter and positive effects on H_{c2} at a small expense in T_c. Effects of C doping on normal state resistivity are less well established. The best in-situ wires have similar $J_c(H)$ because connectivity and grain size (flux pinning) are difficult to co-optimize. Significant in-situ $J_c(H)$ improvement may require a breakthrough in obtaining fine, well connected grains. As discussed in later chapters, ex-situ processing combined with high-energy milling presents an alternate route to higher $J_c(H)$

Chapter 3 - Synthesis and Analysis Techniques.

The experiments described later in this thesis all involved the synthesis and analysis of pellets made from ball-milled prereacted MgB_2 by hot isostatic pressing. Understanding many of the results in this thesis requires a clear idea of the synthesis procedure and the characterization methods. The purpose of this chapter is to provide this background so that judgments about inhomogeneity, non-uniformities, and the effects of milling and alloying are well founded.

The analytical methods are of particular importance because much of the data presented in this thesis is derived from more basic measurements. For instance, connectivity, H_{c2}, and normal state adjusted resistivity are all derived from the same 4-point resistance measurement, and all require some data analysis to obtain.

3.1 – Synthesis and sample preparation

3.1.1 -- Properties of the starting MgB_2

Several experiments in the literature [Chen02,Jiang01] highlight the fact that starting powder selecting strongly affects the properties of sintered MgB_2. The most desirable powder would be 1) cheaply available in large quantities, 2) phase pure, 3) free from contaminants, and 4) homogeneous. Of course, no powder has all those qualities. The powder we used (as shown below) contained small amounts of WC, MgO, and unreacted B and it was contaminated with enough C to yield X~0.008 in $Mg(B_{1-X}C_X)_2$.

As a result, all of the samples in this thesis are slightly carbon doped and any statements to the contrary refer to nominal composition.

All MgB_2 powders used in chapters 4-7 were purchased from Alfa-Aesar. Powder size was 325 mesh, and average particle size was stated by the supplier's analysis to be 4 μm. That analysis of lot H01R038 gave the data shown in figure 3.I. The Alfa-Aesar analysis gives a ratio at%B / at%Mg = 1.995. 0.2 wt% C corresponds to about 0.26 at% C. Given sufficient Mg, that could produce $Mg(B_{1.996}C_{0.004})_2$ which would have expected properties (see Ch.2) of $T_c \sim 38.6$ and $H_{c2}(0\ K) \sim 20\ T$. As will be described later, those values represent an upper bound for T_c and a lower bound for H_{c2} in Ch. 4-7.

Table 3.I – Compositional analysis of commercial MgB_2 from Alfa-Aesar.

Element	Wt%
Boron	45.7
Mg	51.5
C	0.2
Fe	0.1
Sum	97.5

An x-ray diffraction pattern taken from Alfa-Aesar powder is shown in figure 3.1. Small amounts of MgO and WC were identified in this as-received pattern. Therefore W and O probably comprised most of the 2.5 wt% not accounted for in Table 3.I. SEM by Peter Lee on heat treated samples found WC and unreacted B. Rietveld Analysis [Rodrigues02] on as-received powder gave an a-axis lattice parameter of 3.088 Å with estimated grain size of 97 nm. This lattice parameter indicates no detectable carbon in the MgB_2 lattice in as-received powder. Since the powders are known to contain C, suggest the C may be present on powder surfaces (See Ch.4).

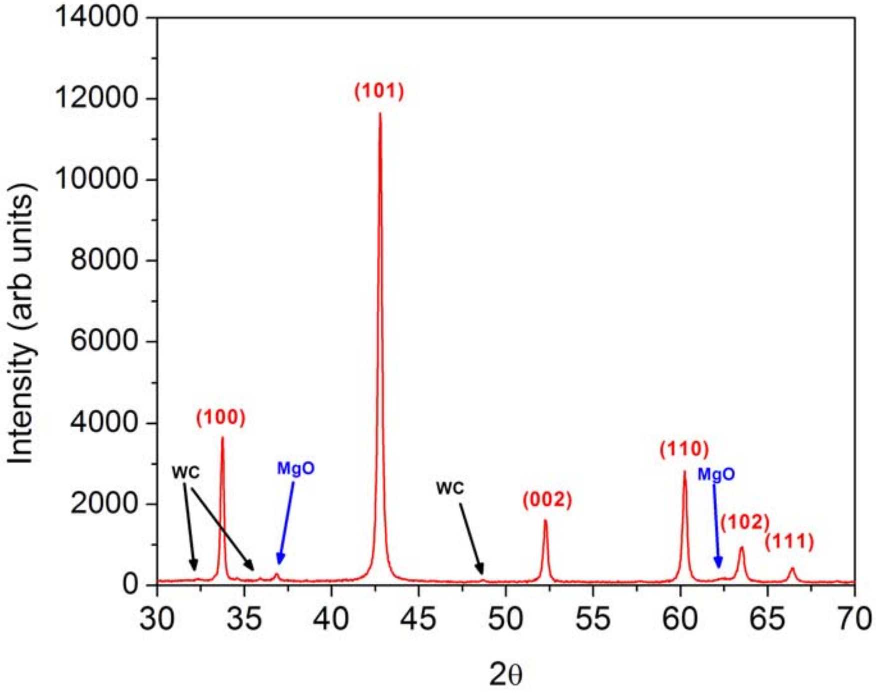

Figure 3.1 – X-ray diffraction pattern of MgB_2 powder as-received from Alfa-Aesar.

Heat-treated samples made from this as-received Alfa-Aesar powder show typical C-doping effects (T_c, H_{c2}, resistivity, a-axis lattice parameter) corresponding to $0 < X < 0.01$ in $Mg(B_{1-X}C_X)_2$. Usually X~0.008, slightly higher than that given by the Alfa-Aesar chemical analysis.

This information is extremely important to the later chapters for the following reasons: 1) Enough C was available in the starting powder for nominally undoped samples to have X~0.008. 2) This initial C was not incorporated into the lattice of the as-received powders and was therefore probably present on powder surfaces. 3) Our heat-treated sample properties typically correspond to X~0.008, which is double the C-content specified by Alfa-Aesar. Therefore C-content of powder surfaces may have increased after Alfa-Aesar powder analysis. 4) If powder surfaces were contaminated with C, then they were probably also heavily contaminated with O. We will see later (Ch.8) that this may have resulted in improved flux pinning of milled and sintered samples.

The work presented in Ch. 4 (atmospheric doping study) indicates that this additional surface carbon could have accumulated during storage and handling after chemical analysis but before receipt of the powder.

The presence of these surface contaminants is of great concern because they affect sample properties, sometimes (such as with O) in ways that are not fully understood. This is one cause of uncertainty in the results. Even if these effects are beneficial to J_c(H) they can complicate data interpretation and cause sample-to-sample variation. In order to minimize further air exposure, as-received containers of powder were opened and stored in an inert gas-filled glove box equipped with active oxygen and water scavenging. Handling of powders was carried out in the same inert gas atmosphere, except where noted.

3.1.2 – Milling

One of the main thrusts of this work is demonstrating and understanding the (mostly beneficial) effects of high-energy ball milling. It is useful here to understand not only the general milling configuration, but the specific effects of the process, and contaminants that could be introduced. In this work, ball milling was usually carried out in a SPEX 8000M Mixer/Mill (shown in figure 3.2).

Figure 3.2 – Photograph of SPEX 8000M mixer/mill located in inert gas glove box, and holding WC milling jar.

The SPEX mill is a high-energy mill suitable for mechanical alloying. The SPEX mill shakes the milling vial (milling jar) in such a way that the media and charge impact alternate ends of the vial at a rate of several shakes per second. Particle attrition is by fracture under the impact of the milling media. This action reduces 325 mesh MgB_2

powder to <1 μm in < 15 min and causes the x-ray diffraction pattern to weaken and broaden, as shown in Figure 3.3.

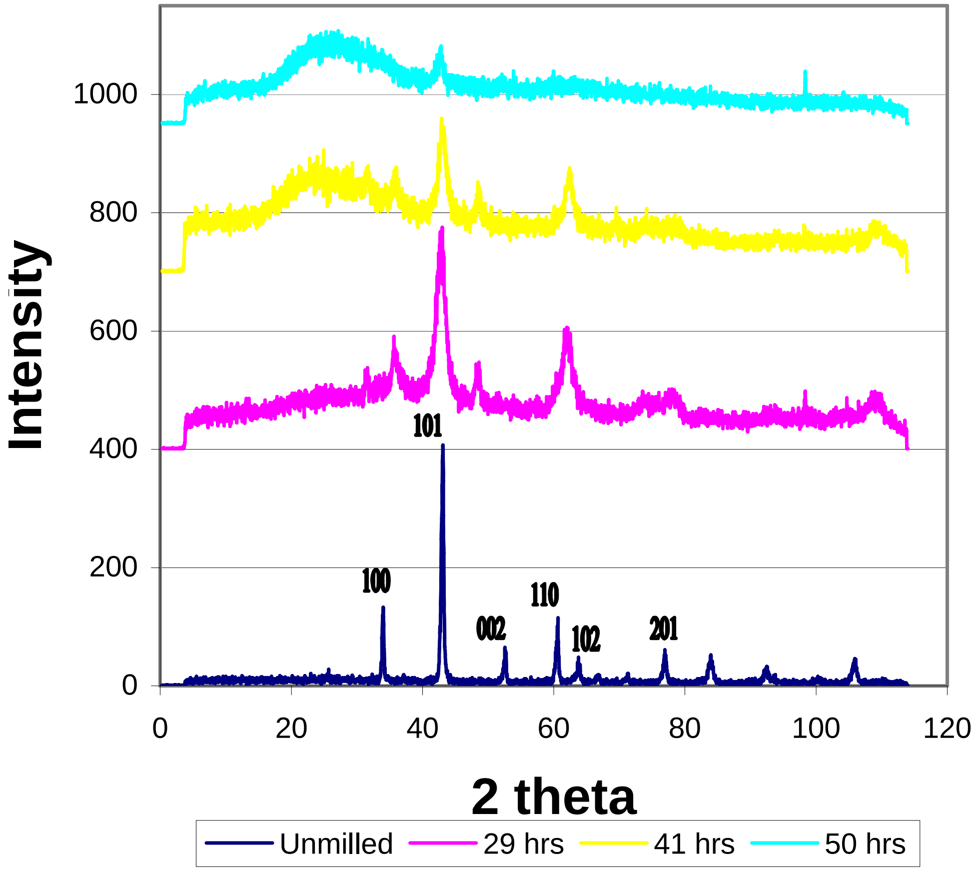

Figure 3.3 – X-ray diffraction patterns from undoped MgB_2 with varied milling times. XRD by Ely Colon.

Figure 3.4 is a TEM micrograph by Ye Zhu showing MgB_2 powder after 20 hrs milling. Grain size was ~10 nm.

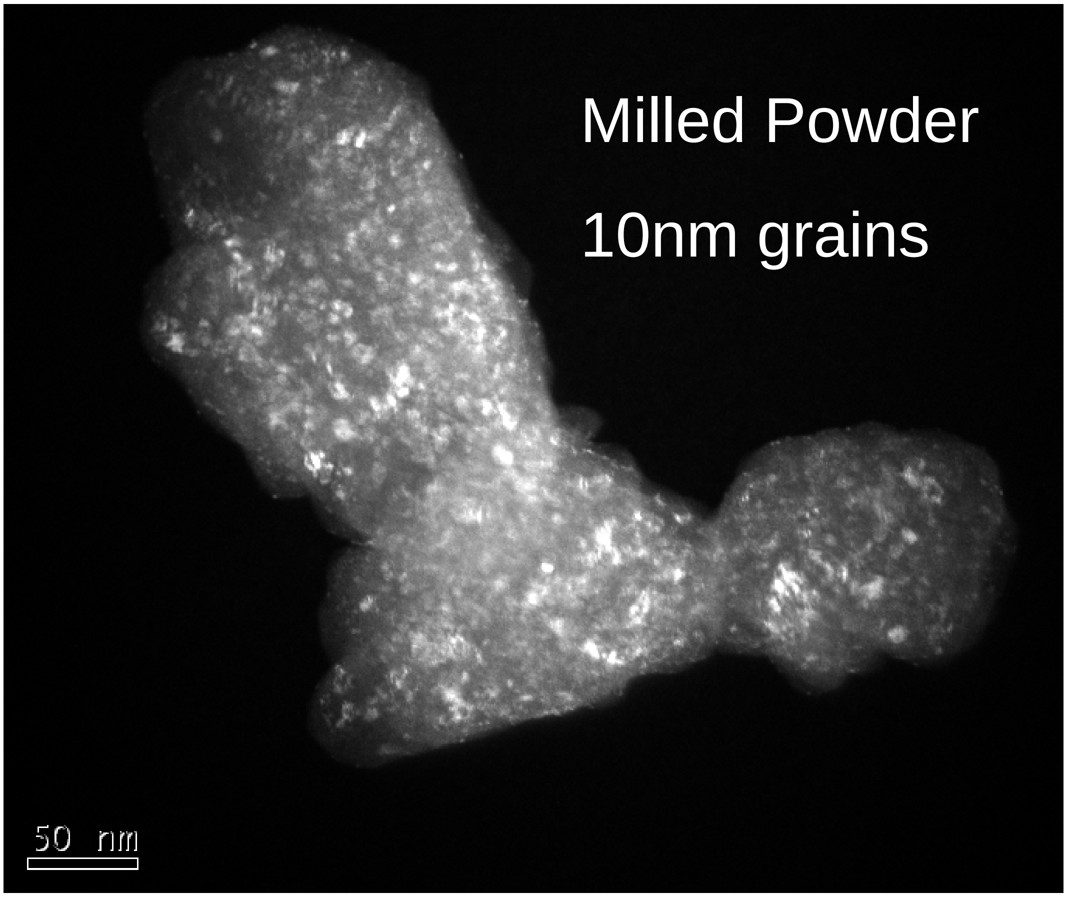

Figure 3.4 – TEM micrograph by Ye Zhu showing MgB_2 powder milled 20 hours.

Milling vials are available in WC (visible in Figure 3.2) and steel. WC was chosen for this work because MgB_2 is extremely hard ($H_V > 9.8$ GPa) and can severely abrade steel which would the sample. Entrainment of steel could introduce magnetic impurities into the sample, which may have deleterious effects on superconducting properties. Despite its durability, WC powder is entrained in the powder during milling. After 20hrs of milling 10 g of powder, about 5 wt% of the charge is WC. Given that the mol wt. of WC = 195.851 g and mol wt. MgB_2= 45.927 g, full decomposition of WC and reaction with sufficient free Mg would give $Mg(B_{0.9939}C_{0.0061})_2$. Entrained WC does not appear (Ch.7) to react much below 1000°C, but has been observed to form WB and MgB_2C_2 at 1000°C (Ch.4). At 1500°C, WC is entirely dissolved in an MgB_2 + Mg mixture (Ch.7). WC milling media contain small quantities of Co as a binder, as shown in Figure 3.5. As mentioned in Ch.5, there is no evidence of Co entering the MgB_2 lattice during heat treatment. Powder charges had a typical mass of 5-10 g, and the combined mass of the 5 WC balls was about 20 g.

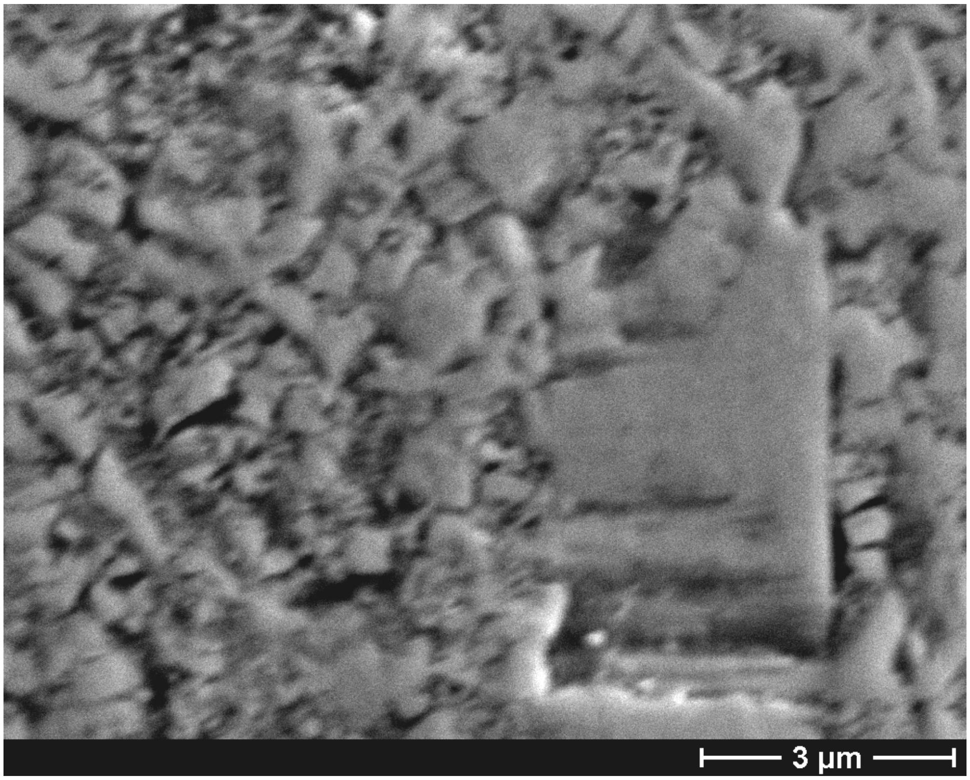

Figure 3.5 – Scanning electron micrograph of WC-Co. WC is light gray – SEM by J. Hedstrom

Rubber O-rings were used to form a gas-tight seal at each end of the milling vial. These O-rings abrade very slowly during milling and contribute a negligible amount of C to the powder. The author has used the O-ring sets since 2003 on two WC jars and although they do show some wear, they are still fully serviceable. Each set of o-rings therefore has an estimated milling life time on the order of thousands of hours. The SPEX mill was located inside the same glove box that was used for powder handling. Due to the generation of fresh MgB_2 surfaces during milling, milled powder oxidation outside the glove box could be rapid. In one case a charge becoming red hot when the SPEX milling jar was opened in air. No such heating was observed during handling in the glove box.

A further source of potential contamination (and thus uncertainty in properties and sample to sample variation) stems from the necessity of cleaning the milling jar. During milling, a coating of powder adheres to the inside of the milling jar. While most of the milled charge was removed from the jar by scraping with a spatula, that method was not able to remove all of the residual powder from the jar inner surface. In most cases (especially when varying composition) the jar had to be removed from the glove box and cleaned thoroughly washed with water. Additional cleaning was sometimes necessary, was sometimes accomplished by loading the jar (containing balls and some alcohol) into a paint shaker and milling. Clean WC milling jars have a bright metallic luster. Exposure to water for tens of minutes can cause the finish to become dull grey, probably indicating oxidation, and certainly indicating a potential source of sample contamination. We tried to avoid this condition, but jar surface contamination was difficult to quantify.

This process is highly significant to all of the results in Ch. 5-8. Disruption of the oxide surface layers, combined with extreme grain refinement resulted in significant benefits to sintered samples. The investigation of those benefits is a major thrust of this thesis. The possibility of unintentional doping during this process (by WC/Co or jar surface oxides) must also be kept in mind later both as a source of sample-to-sample variation and in considering the high T_{HIP} samples of Ch. 7.

3.1.3 – Cold isostatic pressing and sealing methods

A cold isostatic press (CIP) was used to form milled powders into pellets. Working in the glove box, powders were loaded into CIP molds consisting of short (2.5”) sections of rubber tubing sealed at the ends with rubber plugs. A typical pellet mass was 1-2g. Filled molds were encapsulated in latex balloons before removal from the glove box and then CIP treated at 40 kpsi. This configuration is known as “wet bag” CIP. The balloons were then dried in air and inserted into the glove box to be opened. The green strength of the CIPed pellets is primarily the result of particle interlocking, since MgB_2 is not believed to deform except at elevated temperature.

After CIP treatment, pellets were welded into evacuated metal tubes for hot isostatic pressing (HIP). The tube material was selected based on the following criteria: 1) low reactivity with Mg, 2) low reactivity with B, 3) sufficiently high melting temperature so that $T_m > T_{HIP}$, and 4) cost. These factors effectively limit tubing selection to Fe and its alloys, Ni and its alloys, Nb, and Ta. It is possible [Indrakanti01] to use pyrex glass as a HIP can but pyrex was not used in this work due to the low success rate we experienced with pyrex. 304 stainless steel tubing was used as a HIP can in Ch. 4-7. Pure Nb was used for high temperature (>1150°C) heat treatments, and in some cases (Ch. 7, all $T_{HIP} \leq 1150^{o}C$) Nb foil was used to line SS tubes.

The starting tube length was > 6". One end was welded closed prior to loading. Loaded tubes were evacuated using an apparatus consisting of a valve and a short section of rubber hose. Evacuated tubes (still attached to the valve and hose assembly) were hammered flat above the sample and then squeezed in a vise between metal bars to preserve vacuum during the cutting step. Flattened and clamped tubes were cut with tin snips and then immediately welded using a TIG system. In the case of Nb tubes, extremely high Ar flow rates were used to prevent embrittlement by O, which leads to cracking on subsequent deformation during the HIP process. Thermal expansion issues also complicated Nb welding because temperature gradients near the arc caused tubes to warp. The thermal expansion issues were mitigated by cutting the tube as close as possible to the vise seal.

Vacuum integrity after cutting and before welding was entirely dependent on the quality of the vise seal which was difficult to verify. Leakage of this seal is the only point in the fabrication process when samples might have come in direct contact with air, and this could be another potential source of sample to sample variation. Furthermore, exposure to the air during this stage might have a much larger detrimental effect on sintering (and ultimately connectivity) than air exposure before milling, because after sealing there is no subsequent process which creates fresh surface.

These stages of powder handling were carried out with the aim of preventing air exposure, mainly because oxidation of powder surfaces after milling could hinder sintering and connectivity. As described, all of these powder handling steps involved the samples in inert gas or vacuum. The only reasonable possibility for direct air exposure was when the HIP can tubes were clamped in the vise, after cutting and before welding. If this method were to be improved, the author would suggest spot welding the hammered tube, which would eliminate the necessity of the temporary pressure seal (in the vise).

3.1.4 – Sintering and grain growth

Sintering is the process by which porosity is eliminated from a powder compact, and good connectivity is developed. This is the heat treatment process by which powder is converted into bulk superconductor. The subtleties of this process have a dramatic impact on bulk properties – because heat treatment influences both connectivity and grain size. First, sintering in the absence of applied pressure will be explained. Grain growth will be discussed. Then the effects of hot isostatic pressing on sintering will be described.

3.1.4.1 – Sintering

Pressureless sintering operates on the principle that particle free surfaces have a higher free energy than grain boundaries. Therefore the free energy of the system can be minimized by a fully dense state, as determined by the Gibbs-Thompson (capillarity) relationship. The excess surface energy per mol of powder (ΔG_γ) (compared to full density) is given by

(3.1) $$\Delta G_{\gamma} = \frac{2\gamma V_m}{r}$$

where γ is the particle surface energy per unit area, r is the particle radius, and V_m is the molar volume.[Porter01] This energy can be 1 J/m^2 surface area. [Chiang01]

Concave particle surfaces have a lower chemical potential than convex surfaces. Two powder particles brought into contact establish a concave surface with a small radius of curvature around the point of contact (a neck). Diffusion processes will move atoms down the chemical potential gradient into the neck, which increases the radius of curvature of the concave surface. This is the first stage of sintering, known as *neck growth*, during which the interparticle contact area increases from zero to ~0.2 of the particle cross-sectional area. It is followed by *intermediate sintering* which is characterized by formation of a grain boundary network, grain growth, and pinching-off of open porosity. *Final stage* sintering involves the collapse of closed porosity.[Coble01]

There are three diffusive paths involved in sintering: surface diffusion, grain boundary diffusion, and lattice diffusion. All are thermally activated, with diffusion coefficients of the form:

(3.2) $$D = D_o e^{\frac{-Q}{RT}}$$

Where D is the diffusivity, D_o and R are constants and Q is an activation energy. $Q_s < Q_{gb} < Q_l$ so that surface diffusion dominates at low T and lattice diffusion dominates at very high T.

Neck formation is primarily a surface diffusion effect. Surface diffusion results in grain coarsening as material is transported from small to large grains and also to necks, but surface diffusion does not bring particle centers closer together and therefore does not result in densification. Bulk and grain boundary diffusion move atoms to the free surface from the particle interior and therefore close pores and decrease particle separation. In order to maximize density while minimizing grain growth, a material can be rapidly heated to a temperature regime (0.6 - 0.7 T_m which ~ at least 1250°C in MgB_2) where grain boundary or lattice diffusion is more active than surface diffusion. This is known as "fast firing".[Chiang01] For the early stage of sintering (x/r < 0.3 where x is the neck radius and r is the particle radius), the rate equations for densification and coarsening go as:

(3.3) $$\left(\frac{x}{r}\right)^n = \left(\frac{\beta t}{r}\right)^m$$

Typically $\beta \propto 1/(kT)$ and n and m vary depending on the diffusion mode.[Chiang01,German01] Figure *** shows neck growth in an MgB_2 sample (Ch.7).

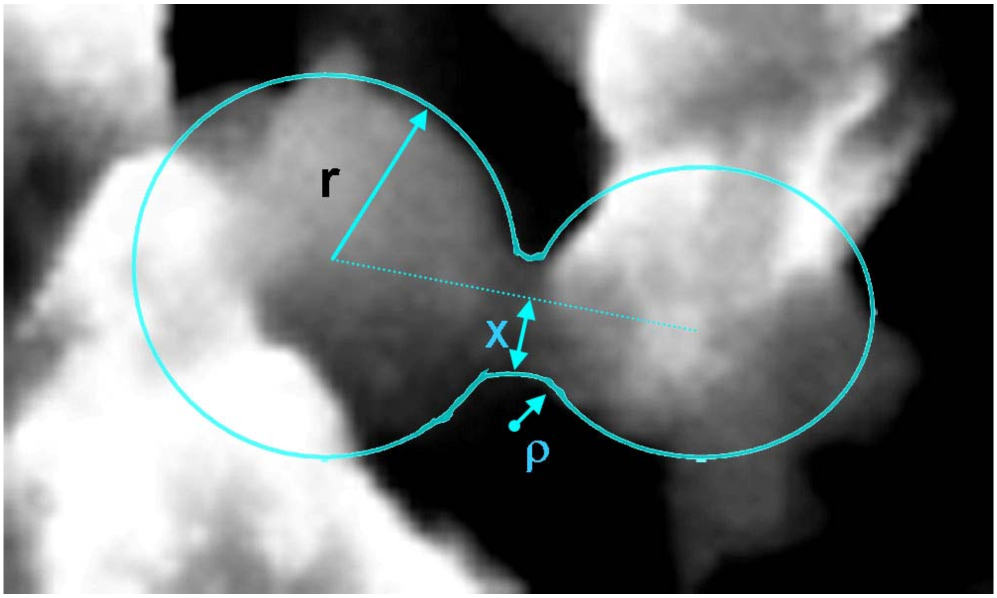

Figure 3.6 - Scanning electron micrograph of MgB_2 particles involved in neck growth (see Ch. 7).

The driving force to close an isolated spherical pore can be expressed as a pressure in the form $p=2\gamma/\rho$ where ρ is the pre radius. For γ~1 J/m^2 and pore radius of 1 μm, p~300 psi. For a pore radius of 10 nm, p~30,000 psi. This pressure pulls the particle surfaces toward the center of curvature of the pore, eventually eliminating the pore. In order to accelerate sintering, an external pressure can be applied to supplement the effect of capillarity, which facilitates pushing the particle centers together, as in hot pressing or hot isostatic pressing.

3.1.4.2 Grain Growth

Grain growth refers to the thermally activated motion of grain boundaries toward their centers of curvature. During sintering it has been shown that grain size for porous solids goes as: [German01]

$$(3.4) \qquad d^n = d_0^n + Kte^{\frac{-Q_s}{kT}}$$

Where d is the grain size, d_0 is an initial grain size, K is a constant, Q_s is an activation energy for grain growth, and the kinetic grain growth exponent (n) is between 3 and 5 depending on diffusion mechanism, and n = 3 for coarsening in a dense material with liquid present (such as MgB_2 + Mg). Typically n is extracted from isothermal heat treatments at variable time. Both the time and temperature relations to grain size were previously shown to be accurate in $BaTiO_3$.[Park01] For a set of isochronal heat treatments at different T, final grain size would be expected to follow an Arrhenius relationship. We will verify this for MgB_2 in Ch. 7.

Grain growth is driven by the reduction of free energy associated with decreased grain boundary density and therefore decreased grain boundary energy according to: [Chiang01]

$$(3.5) \qquad \Delta G = \int_{A_1}^{A_2} \gamma dA = \gamma(A_2 - A_1)$$

Where ΔG is the free energy, γ is the grain boundary free energy per unit area and A is the total grain boundary area.

Grain boundary motion is driven toward the center of curvature of each grain boundary, thus large grains tend to consume smaller grains. If the radius of curvature for all grain boundaries is proportional to the average grain diameter d_A (round grains) then the mean driving force for grain growth is proportional to $2\gamma/ d_A$ and the average grain boundary velocity (v_A) is given by: [Porter01]

(3.6) $$v_A = \alpha M \frac{2\gamma}{d_A}$$

Where γ is the grain boundary energy, α is a proportionality constant and M is the grain boundary mobility, which is diffusion limited. In practice, several factors act to retard grain boundary motion. These include pinning by pores or second phases, and solute drag. The restraining force per unit grain boundary area (P) due to an array of spherical pins having volume fraction f and radius r is:

(3.7) $$P = \frac{3f\gamma}{2r}$$

If P becomes large enough to equal the driving force, it can cause grain growth to stagnate and a maximum grain size d_{max} is reached:

(3.8) $$d_{\max} = \frac{4r}{3f}$$

Where r is pin radius and f is the pin volume fraction. The grain boundary mobility (M) is controlled by diffusion so that [Chiang01]

(3.9) $$M \propto \frac{D_{RL}}{kT}$$

where D_{RL} is the rate limiting diffusivity associated with grain boundary motion, k is a constant, and T is temperature. In many cases, D_{RL} is simply the diffusivity across the boundary of one of the species comprising the phase of interest, but in the presence of a solute, the rate limiting diffusivity can be the solute diffusivity. This phenomenon is known as solute drag, and occurs because solubility at grain boundaries is generally higher than in the matrix. For low concentrations (C_0) the equilibrium grain boundary enrichment ratio (C_B/C_0) is given by: [Porter01]

(3.10) $$\frac{C_B}{C_0} \cong \exp\frac{Q_B}{RT}$$

where Q_B is the binding interaction energy between the solute and the grain boundary. Movement of the grain boundary tends to pull the excess solute atoms through the material, exerting a drag force which slows grain boundary motion. While there is no definite evidence of solute drag effects in MgB_2, they are certainly possible.

Furthermore, the solute causing the drag effect would not need to be C but could be some other less soluble impurity (perhaps even such as W or Co).

Some materials have an inhomogeneous distribution of grain boundary pins. While grains in strongly pinned regions may reach d_{max} and cease to grow, grains in poorly pinned regions can grow with less restriction, eventually consuming the finer grains. This phenomenon is known as discontinuous (or abnormal) grain growth. It results in a bimodal grain size distribution, such as we will observe in Ch.6.

In later chapters we will find that fine grains and good connectivity are extremely important to J_c(H) in MgB_2. The relationships described above show that grain growth and sintering are controlled by some of the same diffusional mechanisms, and thus can be expected to progress concurrently. But the driving force for sintering is stronger for smaller particles. Furthermore, we can predict (and will verify) that grain size increases exponentially with T_{HIP}, but that heat treated grain size also depends on initial grain size. Therefore we would expect the following: 1) Reduction of particle size (by milling) facilitates sintering. 2) Reduction of grain size (by milling) results in smaller heat treated grain size for low enough T_{HIP}. So extreme particle size refinement could reduce the T_{HIP} necessary to achieve good connectivity, and if T_{HIP} can be made low enough then grain refinement by milling could carry over into the sintered samples. We seem to have achieved that in Ch. 6 and 7.

There are two other tools which could help maintain fine grains through heat treatment, but which were not systematically studied in this thesis: grain boundary motion pinning by second phases such as pulverized remnants of powder surface oxides, and solute drag by additional alloying elements present as impurities.

3.1.4.3 Hot Isostatic Pressing (HIP)

Pressing at elevated temperature is widely used in the aluminum, aerospace, cutting tool, and powder metallurgy industries to achieve sintering and densification. At ambient pressure, sintering is driven by thermodynamic effects relating to surface curvatures. In both hot pressing and hot isostatic pressing, an external pressure provides an additional driving force for volume reduction by densification. Applied pressure is typically in the range of 5,000 to 50,000 psi for both methods. For this work P_{HIP} ~ 30,000 psi (~0.2 GPa). For pores with r~10 nm, the applied P_{HIP} increases the driving force for densification by a factor of ~2, but for a pore with r~10 μm, $P_{HIP}/P_{Capillarity}$ can be 1000. Thus HIP is very effective in initial densification. The primary effect of HIP is therefore to promote rapid densification by dramatically increasing the driving force to remove large pores. Because HIP uses a gas as a pressure-transmission medium, any surface-connected porosity is equivalent to an extension of the sample surface and will not be removed. This necessitates the use of a HIP can to encapsulate the powder compact except in the special case of sinter-HIP procedures. [Richerson01] The use of a HIP can makes all porosity in the powder compact equivalent to closed porosity.

Hot isostatic pressing was used in this work in preference to uniaxial pressing largely because of the volatility of Mg and the lack of die materials for hot pressing that are inert with Mg or B at high temperature. Additionally, the HIP process can be adapted to any shape work piece including wound coils, which offers an advantage in applying the process. The HIP unit consisted of a furnace within a pressure vessel containing inert gas (N_2 or Ar), as shown in Figure 3.7.

Figure 3.7 - HIP unit with Hoskins furnace (inset)

For T > 1000^{o}C, Ar gas was used rather than N_2 to avoid N reacting with the possible Nb HIP cans. For some work at 1000^{o}C (Ch. 4-6), N_2 gas was used. Maximum sustained T and P of the HIP unit were ~1800^{o}C and 30,000 psi. MgB_2 samples were not prepared at T > 1500^{o}C due to excessive reaction of B with the Nb HIP cans.

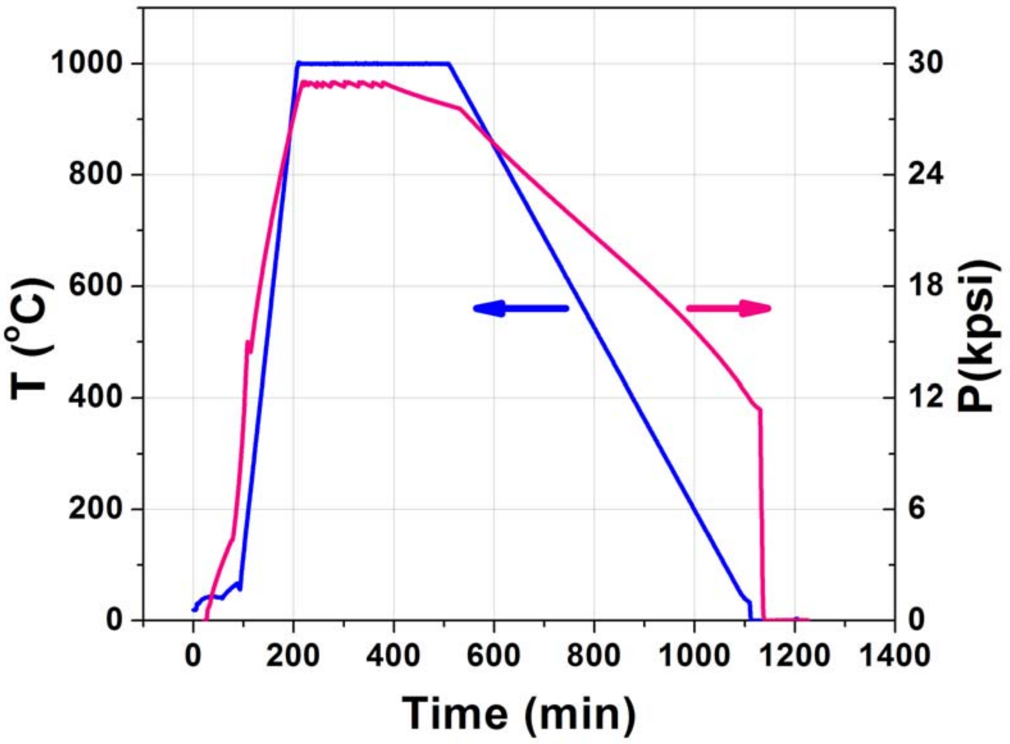

Figure 3.8 – Typical HIP T(t) and P(t) profiles.

P and T profiles for a typical HIP cycle are shown in Figure 3.8. The HIP unit was partially pressurized before heating. Full pressure was attained as a result of heating the gas. Samples were allowed to cool before pressure was released in order to prevent sample decomposition in a low-pressure, high-temperature state. The thermal ramp rate varied from experiment to experiment, within the range of about 100°C – 500°C per hour for the ramp up, with generally 100 – 250°C per hour ramping down. Most of the samples in this work were held at the maximum temperature 200 min or 300 min.

A small fraction of HIP samples failed due to HIP can leakage at high pressure. With care, the failure rate can be reduced below 10%, even for thin walled tube. Failed samples are easily identifiable because the MgB_2 is not sintered. If a tube has a very small leak, it may inflate due to rapid reduction of pressure at the end of the HIP cycle. HIP processing typically results in MgB_2 sample density 80-100% of theoretical density (depending on composition, T_{HIP} and milling status, see Ch. 7), with hardness $H_v>10$ GPa, depending on T_{HIP} and sample composition.

The use of HIP rather than ambient pressure processing has an important advantage besides improved sintering. As described in Ch.1, at $T > 800\text{-}900^oC$, MgB_2 seeks to establish a significant Mg vapor pressure over the solid. If the sample is in a large container, this results in loss of Mg, formation of MgB_4, and undesirable properties (particularly poor connectivity). HIPing ensures that the free volume around the sample is extremely small. This permits heat treatment at very high temperature (1500^oC) without significant Mg loss. In practice, (Ch. 7) high temperature heat treatment results in *excess* Mg because B is consumed by reaction with the HIP can. Excess Mg can block supercurrent flow.

3.1.5 – Sintered sample preparation

HIPed samples were very dense and hard, so cutting was difficult, but they were resistant to atmospheric degradation. Due to their high strength, they could be shaped into regular geometries with well-defined dimensions, which were desirable for measuring properties such as J_c, ρ, and mass density.

Sintered samples were typically sectioned with a diamond saw. For poorly sintered samples (such as those with $T_{HIP} < 900^oC$) no lubricant was used. The high hardness of some well-sintered samples necessitated the use of lubricant. Lubricant was typically used only where dry cutting was expected to take hours to days. Lubricant was typically water-based, but oil was occasionally used. Although water oxidizes MgB_2, those samples that required lubricant were dense enough that oxidation was limited to a surface layer typically a few microns thick. The oxide surface layer appears white in Figure 3.9.

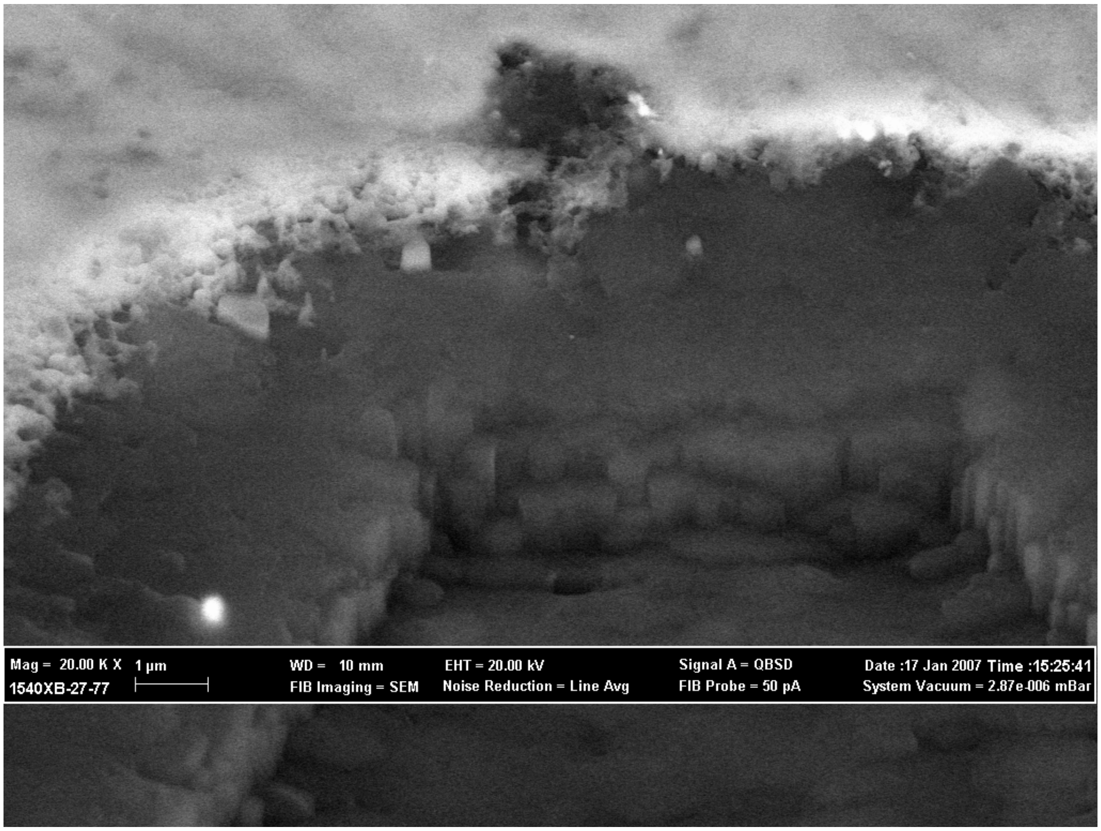

Figure 3.9- Backscattered electron micrograph showing surface oxide layer in bulk MgB_2. Scale bar is 1 µm.

To facilitate resistivity and magnetization measurements in the PPMS and VSM, (described below) samples were shaped into rectangular section bars by either fracturing with cutting pliers, grinding with sandpaper, or a combination of both. Grinding was preferred due to its reduced potential for undesired cracks and the difficulty in obtaining regular geometry by fracturing. Rectangular bars are shown wired to a PPMS puck in Figure 3.10. Typical dimensional uncertainty after grinding is assumed to be 0.01 mm, due to a combination of measurement uncertainty and deviations from regular shape. For a resistivity sample with square cross section 1 mm on each side, this would produce ~2% uncertainty in cross sectional area. For a VSM sample with dimensions 0.5 x 0.5 x 1 mm the uncertainty in volume would be about 5%. In practice, the dimensional % uncertainty is probably higher in very small samples than in large ones, because of the difficulty in obtaining regular geometries.

3.2 Characterization

Samples were characterized by a number of methods. The most important characterization methods for this work are described in this section, along with the approximations made in analyzing the data from each technique.

3.2.1 – Physical Property Measurement System (PPMS) resistivity curves

Much of the data in subsequent chapters is based on these small current $\rho(T,H)$ measurements, from which we can extract $\rho(T)$, A_F, ρ_A, T_c, and H_{c2}(H//ab plane) by analysis. The main limitation of these measurements is that they tend to measure the highest (T, H) superconducting pathways, and thus the T_c and H_{c2} data are representative of only the "best bit" within the sample. In a randomly oriented sample, only H_{c2}(H//ab) can be measured, not H_{c2}(H//c). In inhomogeneous samples the T_c and H_{c2} values thus obtained over report those of the average crystals.

The Quantum Design Physical Property Measurement System (PPMS) consists of a variable temperature insert (VTI) in a superconducting magnet. The base of the VTI contains a plug that can accommodate any of several inserted devices designed to measure normal state resistivity, heat capacity, magnetic moment, or AC susceptibility. All measurements can be made at T from 4 K to 300 K and magnetic fields up to 9 T. In this thesis, PPMS resistivity measurements are the primary source for normal state ρ(T) from which we deduce connectivity and ρ_A by the Rowell analysis (which are important parameters in this work). These measurements also allow us to determine H_{c2}(H//ab) and T_c (although magnetic T_c is presented more frequently in this work). In order to interpret those data, it is desirable to understand how the measurements are made.

Figure 3.10 shows three MgB_2 bars mounted on a PPMS resistivity puck for 4-point resistivity measurement. The Puck diameter was ~1". Samples were mounted on a sapphire substrate and secured with GE varnish. The sapphire was held in thermal contact with the Cu puck surface by a thin layer of silicone grease. Fine (~100 μm) Cu wires were attached to the samples with silver paint. In order to achieve low contact resistance (typically ~1 Ω) the oxidized layer on the sample surface was mechanically disrupted by scratching with a diamond scribe.

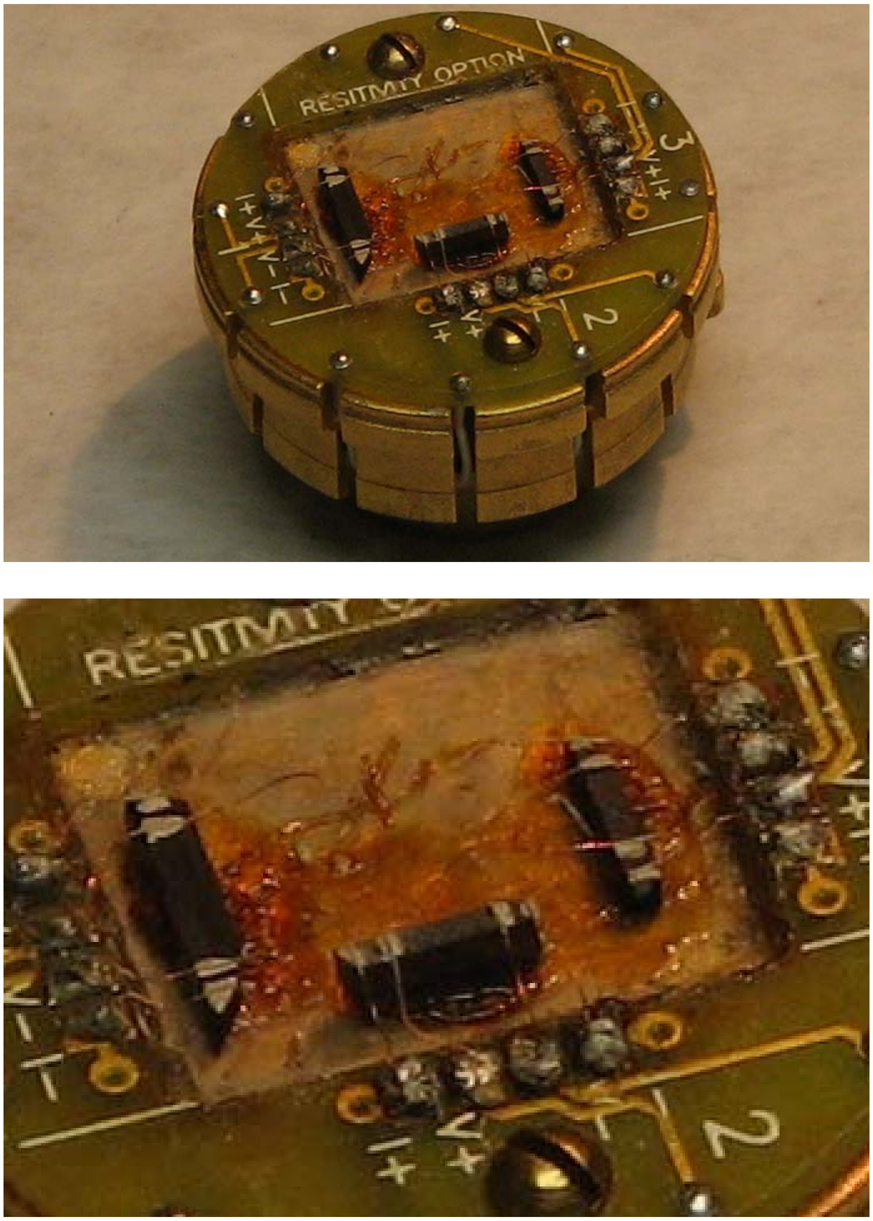

Figure 3.10 - Samples installed on a PPMS puck for resistivity measurement.

As shown in Figure 3.10, the 4-point configuration consists of four electrical leads attached to the sample in a line. The outer leads are for current supply. The inner leads are for voltage sensing. A known current (for this work, I = 5 mA) is passed through the sample, which (in the normal state) results in an electrical potential gradient between the current leads. The potential difference between the voltage taps is measured, and the resistance associated with the section of sample between the voltage taps can be calculated according to Ohm's Law ($R = V_{measured}/I_{sourced}$). By measuring the sample cross sectional area (A) and voltage tap separation (L), normal state resistivity (ρ) can be calculated according to:

$$(3.11) \qquad \rho = R\frac{A}{L}$$

In this work ρ is in μΩ-cm unless explicitly stated otherwise.

Uncertainty in 4-point bulk measurements is generally due to measurement of *A* and *L*. For example, in a sample with $A=1\ mm^2$ and L=2 mm, an error of 0.01 mm in each length measurement could result in > 2.5% error in ρ.

The theory and results of resistivity measurement in MgB_2 were described in Ch.1, along with application of the Rowell analysis. In addition to zero-field resistivity information, 4-point resistivity measurements can be used to determine $H_{c2}(T)$. In order to determine H_{c2} at a given T, a resistive transition is measured as a function of increasing applied field. A typical swept-field transition is shown in Figure 3.11. At low field, the entire sample can be considered to have zero resistance for the measuring current. As applied field increases resistance appears in the sample. Despite the existence of some resistive grains, the measured resistivity remains zero as long as one or more percolative superconducting paths exist that can carry the measurement current. The sample can then be thought of as many resistors in parallel with the superconductor. Since MgB_2 is anisotropic, the first grains to become resistive are those with the least favorable orientation with respect to the applied field, i.e. those with H//c-axis.

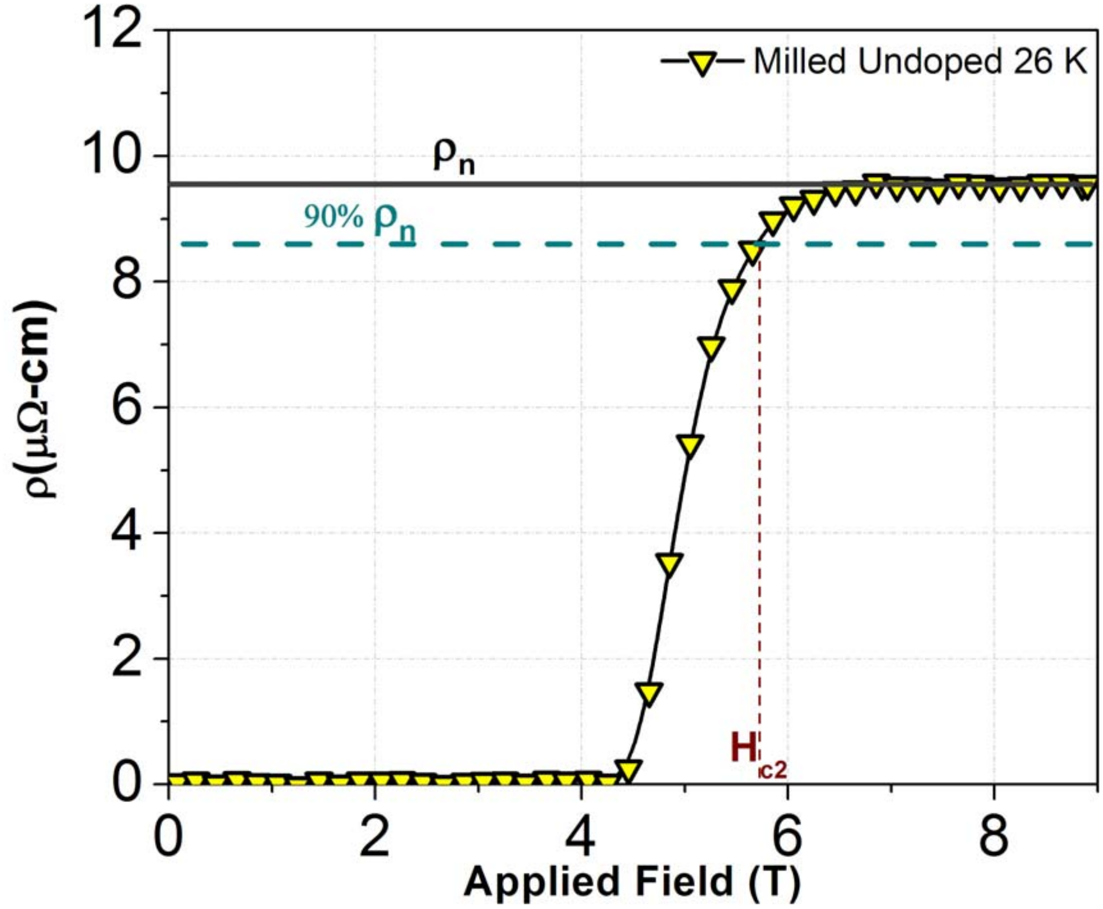

Figure 3.11 – Swept field resistive transition at 5 mA measurement current.

As grains in the zero-resistance percolative path become resistive, measured resistance begins to increase. This field is occasionally referred to as the irreversibility field H* in the literature, but not in this thesis because it lacks any real physical meaning to this work except as an indicator of homogeneity (in which case it can be useful to specify H(10%ρ_n)). H_{c2} occurs when the sample becomes entirely non-superconducting, as evidenced by the achievement of normal-state resistive behavior. H_{c2} by this measurement will therefore be characteristic of those grains with the highest H_{c2}, generally those with H//ab-plane. In Figure 3.11 the true $H_{c2} > 6.5$ T as defined by complete transition to the normal state, however that point is difficult to measure accurately. Typical bulk samples have a resistance of about 100 μΩ between the voltage taps. For a measurement current of 5 mA, the measured potential difference would be 500 nV, making application of a 99% ρ_n criterion for H_{c2} impractical due to noise. In some cases (particularly those samples with free Mg or very high RRR) significant magnetoresistivity is present that can further complicate determination of a true onset H_{c2}. In those cases ρ_n can be approximated by fitting a line to the normal state data just above H_{c2}, and then normalizing the superconducting data to the line, but some uncertainty is introduced. For those reasons we use a 90% ρ_n criterion in this work and report H_{c2}(26 K)//ab-plane = 5.71 T for the sample in the figure. This criterion is very widely applied in the literature.

By measuring multiple transitions at incrementally varying T, we can construct a plot of H_{c2}(T), such as the ones shown in later chapters. For a single band superconductor, [Gurevich04]

$$\text{(3.12)} \qquad \mu_0 H_{c2} = \frac{\phi_0}{2\pi\xi^2(T)}\left(1 - \frac{T}{T_c}\right)$$

Where $B_{c2} = \mu_0 H_{c2}$, ϕ_0 is the flux quantum, ξ is the superconducting coherence length, and T_c is the critical temperature. Upper critical field is also dependent on electron scattering. A sample with a negligibly small concentration of scattering centers is referred to as being in the "clean limit". Very high concentrations of scattering centers can drive the material to the "dirty limit", a condition in which the coherence length is actually limited by the presence of the scattering centers and dependent on the electron mean free path according to:

$$\xi_{dirty} = 0.85(\xi_o l)^{0.5} \tag{3.13}$$

Where l is the electron mean free path, ξ_{dirty} is the coherence length in the dirty limit, and ξ_0 is the coherence length in the clean limit. In dirty limit superconductivity, the zero temperature upper critical field (H_{c2}) then goes as:

$$H_{c2} \propto \rho \gamma T_c \tag{3.14}$$

where γ is the Sommerfeld coefficient and ρ is the residual resistivity. This is similar to the calculation of H_{c2} by mean free path in Ch.2. In MgB_2 the presence of two superconducting bands makes the relationship between resistivity and upper critical field more complicated, as described by Gurevich [Gurevich03] and briefly discussed in Ch.1.

The PPMS resistivity measurements are our primary tool for evaluation of connectivity, electron scattering, and H_{c2} – all of which are very important to this work.

3.2.2 – Magnetometry

Three magnetometers were used for this work, each measuring the magnetic moment *m* by slightly different methods. This allows us to obtain $\Delta M(T,H)$ from which the full critical state $J_c(H,T)$ can be derived to typical uncertainty < about 10%. This uncertainty is higher than the volume uncertainty given above because in calculating J_c, a geometrical multiplier is involved in addition to the volume, so any uncertainty in dimensions is counted twice, as well as the instrument reproducibility (~2% variation in the VSM). Extrapolation of $J_c(H,T)$ to zero defines an irreversibility field H* that is closely tied to both flux pinning and H_{c2}(H//c). $J_c(H,T)$ is our primary metric of sample quality, and so these measurements are critical to this work.

3.2.2.1 - PPMS DC magnetometer

The PPMS ACMS (Alternating Current Magnetic Susceptibility - and DC magnetization) unit can be used as a DC magnetometer when inserted into the VTI. It consists of a pair of pick-up coils with opposite winding directions connected in series. The coils are located one above the other with a small separation between them. The sample is fixed to the end of a sample rod that is connected to a linear actuator which moves the sample vertically from one coil to the other. Under applied field, the sample has some magnetic moment and the motion of the sample with respect to the coils generates an emf (*V*) according to Faraday's law of induction

(3.15) $$V = -N\frac{d\Phi_B}{dt}$$

Where N is the number of turns in the pickup coil and $d\Phi_B/dt$ is the time derivative of the magnetic flux through the coil. Since the coils are connected in series opposition, the measured voltages add, while any fluctuations in the applied magnetic field cancel. Given a reproducible sample motion, it is possible to calibrate the instrument and measure magnetic moment. In this work, we use m to denote magnetic moment (expressed in either emu or A-m^2) and M is used to denote the volumetric magnetization (m/V where V is the sample volume).

Typically magnetic moment is measured using isothermal m-H hysteresis loops, where H is increased from negative or zero field to high field at a constant rate (0.6 T/min for this work) and then decreased again. The magnetic moment of the superconductor is measured at numerous points during the field ramp. The result is a plot such as the one in Figure 3.12. Ramp rate does affect measured m values, because of the induced surface electric field (E) according to: $E = -a\mu_o \, {}^{dH}\!/_{dt}$ where a is the sample dimension. For dH/dt = 0.6 T/min and sample size (a) ~ 1 mm, E ~ 10 μV/m. This is an order of magnitude more sensitive than the typical transport measurement of 1 μV/cm. Hysteresis loops are the result of induced currents provided by vortex pinning in type II superconductors.

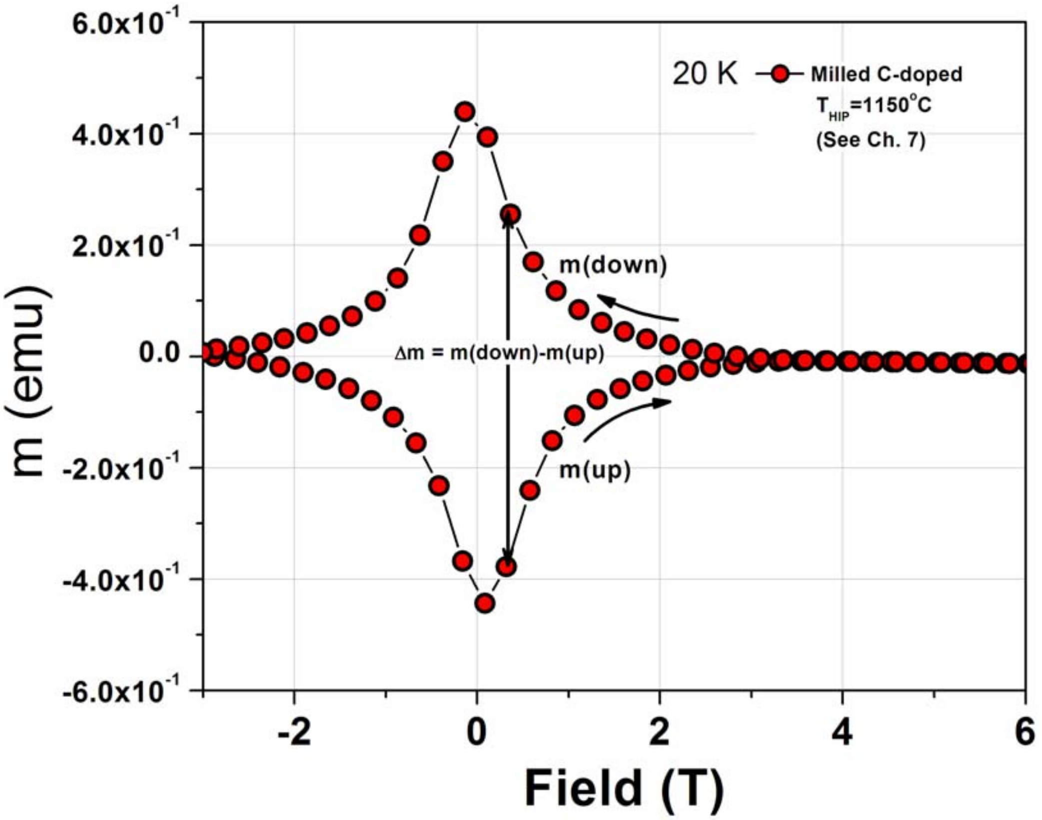

Figure 3.12 – Magnetic hysteresis (m-H) loop from the PPMS magnetometer

In type II superconductors, when $H > H_{c1}$ (the lower critical field), magnetic flux penetrates the superconductor in the form of flux vortices (or "normal cores"), each containing one flux quantum $\phi_o = h/2e = 2.07 \times 10^{-15}$ Wb and having radius ξ (the coherence length). Each flux vortex is surrounded by circulating currents that fall away on the length scale of the penetration depth λ. Flux vortices repel each other and therefore form a hexagonal lattice with spacing $a = (\phi_o/B)^{1/2}$. A free energy barrier exists for flux penetration through a superconductor compared with flux penetration through a normal material. Therefore a vortex can lower its free energy by finding some point where the superconductor is locally suppressed or destroyed, for example non-superconducting second phases, pores, or grain boundaries. Such a feature is known as a flux pinning center. The association of flux vortices with pinning centers gives rise to the pinning force density (F_p) which stabilizes the position of the flux lattice against the Lorentz force (F_L) associated with electrical conduction in a magnetic field, which is given by:

$$F_L = J_c \, x \, B \tag{3.16}$$

And at the critical current density (J_c), $F_p = -F_L$. J_c can be extracted from hysteresis loops by application of the critical state model, also known as the Bean model.[Bean01,Gurevich04,Evetts01]

The critical state model assumes that any electric field E induces current directed along E with a magnitude equal to the critical current density or zero. Flux penetration does not occur simultaneously within the sample as field is increased, but instead the current state is due to the gradient in the vortex density and

$$\frac{dH}{dX} = J_c(H) \tag{3.17}$$

Where X is the position within the sample and therefore the field of full flux penetration (H_P) is:

$$H_P = J_c a \tag{3.18}$$

where a is the sample dimension perpendicular to the field direction, $J_c = f(H_a)$, the applied field, and $H_a >> H_p$. The critical state model can be visualized using the sand pile analogy, where a pile of sand has a constant angle of repose (gradient) due to particle friction, density, etc. Changes in elevation applied to the edges of the sand pile will only propagate toward the center to a distance given by the product of the gradient and the elevation change. Figure 3.13 shows H and J as f(X).

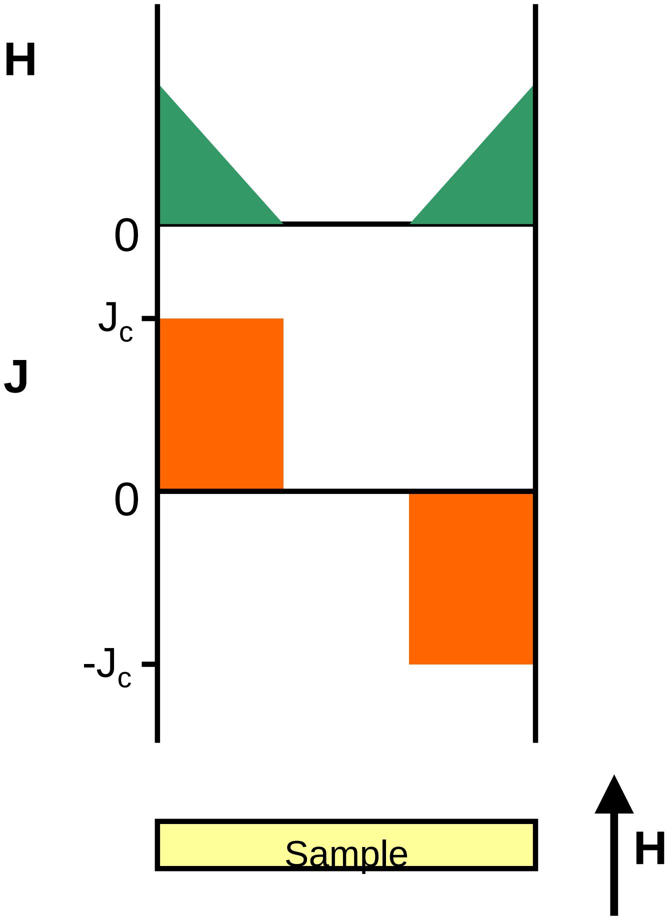

Figure 3.13 – Schematic showing H and J as changing as a function of position within sample.

After flux penetrates, it remains in the sample. Raising and then slightly lowering applied field (H_a) results in a situation where the net screening current must decrease, but since current density is constant ($J = J_c$) and since changes in H_a must affect the surface of the sample before the interior, the result is the induction of surface $J = J_c$ but moving in the opposite direction from J in the interior of the sample. Since the magnetic moment m is the sum of all current loops, this results in magnetic hysteresis, with the loop width (Δm) in the fully penetrated state given by

$$\Delta m = aVJ_c \tag{3.19}$$

where V is the sample volume and a is the sample size, which can be calculated from the sample geometry according to the formulas given in Table 3.II. For this work we used rectangular section bars.

Sample shape	**Orientation**	**M(A/m) =**
Cylinder (diameter 2a)	B // axis	$\frac{J_c a}{3}$
	B ⊥ axis	$\frac{4J_c a}{3\pi}$
Infinite slab (thickness d)	B // face	$\frac{J_c d}{2}$
Square section bar (d x d)	B // axis	$\frac{J_c d}{6}$
	B ⊥ face	$\frac{J_c d}{4}$
Sphere (radius a)		$\frac{3\pi J_c a}{32}$
Disk (2a, thickness d)	B ⊥ face	$\frac{J_c a}{3}$
Rectangular section bar (b x d with b > d)	B // axis	$\frac{3b-d}{12b} J_c d$

Table 3.II - Relationships between M and J_c for different sample geometries and orientations. M is in A/m, d and a are in m, and J_c is in A/m^2.[Evetts01]

Some points should be kept in mind. First, sample length parallel to the field does not appear in any of these equations because it is unimportant to the dimensions of the current loops, but length *is* important in calculating the volume of the sample so M=m/V can be obtained. Second, the magnetization of the whole sample is not equal to the sum of the magnetization of its subdivided parts – if the subdivision is in the plane of the field direction. For example, assume a rectangular section bar with dimensions b = 2 mm and d = 1 mm, and arbitrary length (with length // H) has volumetric magnetization M =0.000208 J_c. Without changing orientation, if the sample is cut into two similar bars with dimensions b = d = 1 mm, then each small bar will have M = 0.000166 J_c and the total magnetic moment will be less than before subdivision. However, if the sample is subdivided in the plane perpendicular to the field direction, then the calculated J_c will not be affected. This model should therefore be used with caution when samples are inhomogeneous, cracked, or subdivided. Use of this model to estimate J_c of a powder should only be attempted under special circumstances, such as when the powder can be approximated by a definite number of uniformly sized spheres that are electrically isolated from one another (such as a dispersion in epoxy). A typical J_c curve deduced from magnetization hysteresis is shown in Figure 3.14, plotted on both linear and log J_c axes.

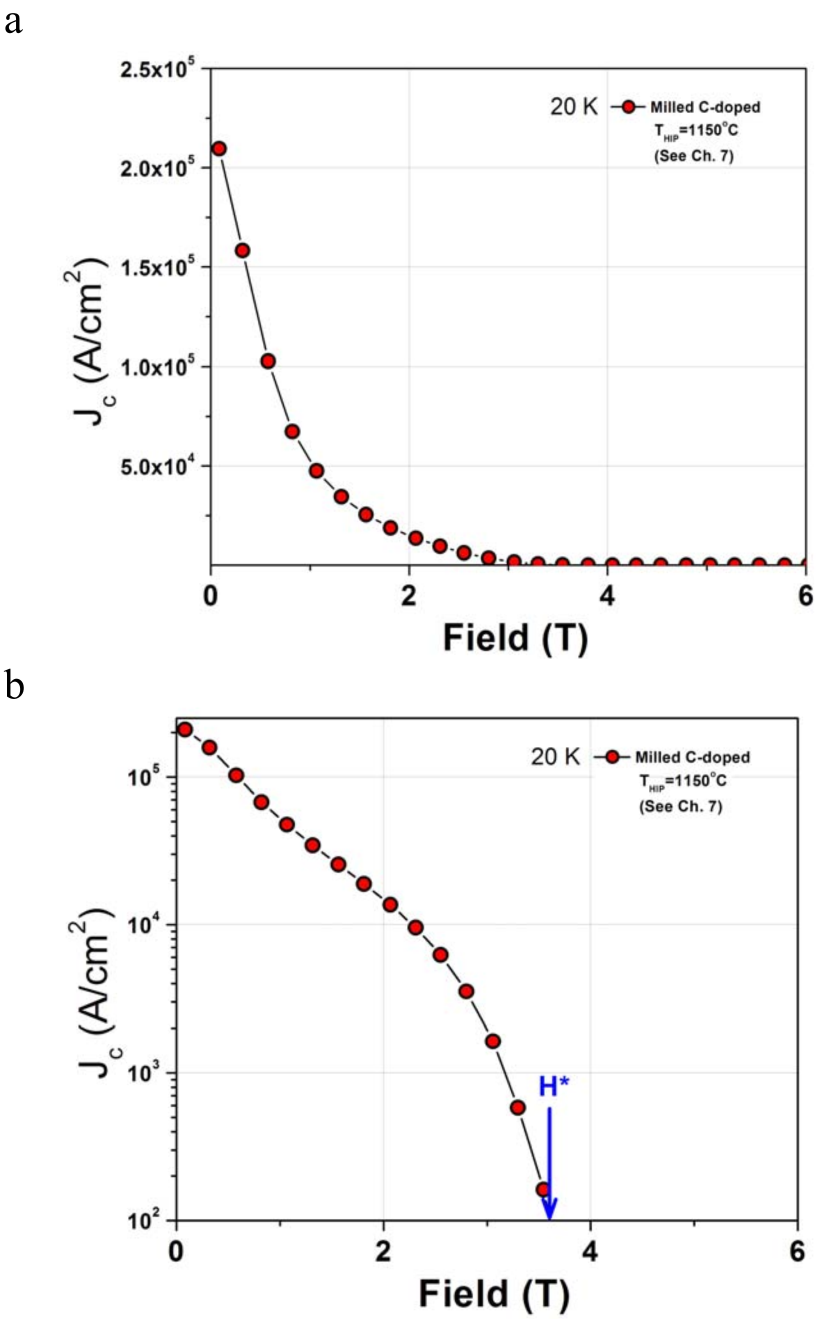

Figure 3.14 – J_c(H) calculated from m-H loops plotted on a) linear and b) log J_c axes.

The irreversibility field (H*) is the applied magnetic field at which the pinning force goes to zero and the sample cannot sustain any current without vortex motion.

Since vortex motion dissipates energy, this corresponds to the onset of resistance in transport. In terms of magnetic hysteresis-type measurements, H* is defined as the field (for a given temperature) at which the hysteresis loop closes, but a more practically applicable definition is the field at which J_c falls to some predetermined small value such as 100 A/cm^2, as shown above. The loop closure criterion and the fixed J_c criterion produce very similar results. In some cases, H* exceeds the capability of the measurement system. In those cases, H* must be determined by extrapolation. In this thesis, both the 100 A/cm^2 criterion and the extrapolation criterion are used.

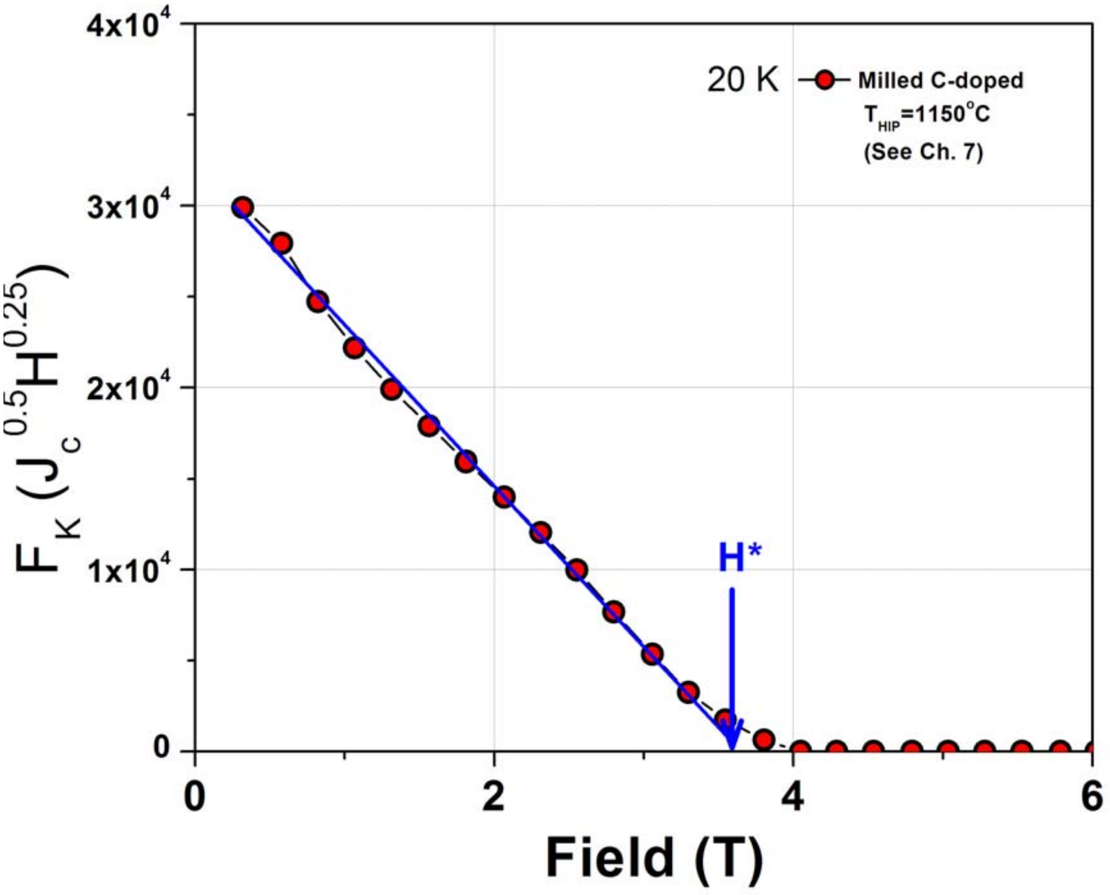

Figure 3.15 – Kramer plot. Intercept of the linear Kramer plot is taken as H*.

The Kramer extrapolation [Kramer01,Evetts01] is a power-law fit relating J_c and B with the goal of producing a straight line when $J_c^{\alpha}H^{\beta}$ is plotted against H. This line can then be extrapolated to the H-intercept, which approximates H*. For Nb_3Sn (a grain boundary pinner), typically $\alpha = 0.5$ and $\beta = 0.25$. For many MgB_2 samples (particularly homogeneous, milled samples) the Kramer function with $\alpha = 0.5$ and $\beta = 0.25$ is quite linear and H_K* is very close to H*(100 A/cm^2) as shown in Figure 3.15. Some samples deviate from the Kramer model in that J_c at high field falls off less rapidly than expected. This causes the Kramer plot to be curved near H*, and in these cases an extrapolation of the linear portion of the Kramer plot will underestimate H* compared to H*(100 A/cm^2). This frequently occurs for unmilled and in-situ MgB_2 samples – perhaps as a result of inhomogeneity or anisotropy.

In a randomly oriented anisotropic superconductor (such as the ones in this work), there exists a distribution of H_{c2} amongst the grains, even in a “homogeneous” sample. The resistive H_{c2} measurement is sensitive to the grains with the highest H_{c2} – those with H//ab-plane. The hysteresis measurement is sensitive to the grains with H//c-axis because J_c of a current loop is limited by the low J_c grains in the loop. For this reason we expect $H_{loop}^* < H_{c2}$(H//c-axis). This effect also causes H_{loop}* to always be less than $H^{10\%}$ associated with the resistive transition, which some refer to as H*.

In later chapters we will see that H* is the most important parameter defining the shape of J_c(H,T) at high fields (H > about 0.5 H*) and that improvement in H* is the main benefit of C-doping.

3.2.3 – Vibrating Sample Magnetometer (VSM)

The vibrating sample magnetometer (VSM) measures *m* as a function of T and H in much the same way as the PPMS DC magnetometer (above), but the VSM offers much greater density of data points and greater sensitivity (~10^{-6} emu). In the case of this work, the VSM also allowed measurement up to 14 T compared to 9 T in the PPMS. The VSM is similar to the DC magnetometer described above in that the sample is moved vertically, causing a signal to be induced in a pair of pick-up coils. The signal is then processed and a calibration factor applied to the measured voltage, resulting in *m* (emu). In contrast to the DC magnetometer, the VSM operates by continuously vibrating the sample at a frequency of 55 Hz and amplitude 1.5 mm. This results in an AC signal that can be measured by a lock-in device. The superiority of this system compared to the PPMS magnetometer is that the VSM can collect data continuously with very little measurement lag or point to point variation.

3.2.4 – Superconducting Quantum Interference Device (SQUID) magnetometer

The superconducting quantum interference device (SQUID) magnetometer is more sensitive than either the PPMS or the VSM (~5×10^{-8} emu), and can measure *m* in fields up to 5.5 T, but it is incapable of swept-field operation. The SQUID is a sensitive interferometer that exploits the Josephson effect. Two superconductors form halves of a ring and are separated by two weakly coupled Cooper-pair tunnel barriers. The phase difference between the Cooper-pair wave functions in the halves of the ring is determined by the magnetic flux penetrating the ring, allowing *m* to be measured as the sample is drawn through coils coupled to the ring.[Ibach01]

Given that the SQUID is best suited for sensitive measurements in persistent field, it is typically used to measure T_c traces. Such a measurement involves setting a fixed field (typically 50 Oe or less) and varying T stepwise while measuring *m*(T). This can be done in a zero-field cooled (ZFC) configuration. In the ZFC configuration the sample is cooled to some low T (such as 4.2 K) in the absence of applied magnetic field. Then the field is applied. The superconductor responds as a diamagnet, producing a negative moment due to induced screening currents which flow on the superconductor surface. T is then slowly increased. As T approaches T_c, the diamagnetic response weakens until superconductivity breaks down at T_c. Curves such as those shown in Figure 3.16 are produced. The T_c transitions are typically >1 K broad, so some criterion must be used to assign values to T_c. Common criteria are 1% or 10% of m(5K), or the transition midpoint. T_c measured by this method yields a more volumetric T_c distribution than the small-current resistive T_c measurement which tends to provide information pertinent only to the highest T_c percolative path. Often the resistive T_c equates to a very strict criterion in the magnetic T_c curve, typically $m/m(5\text{ K}) < 0.01$.

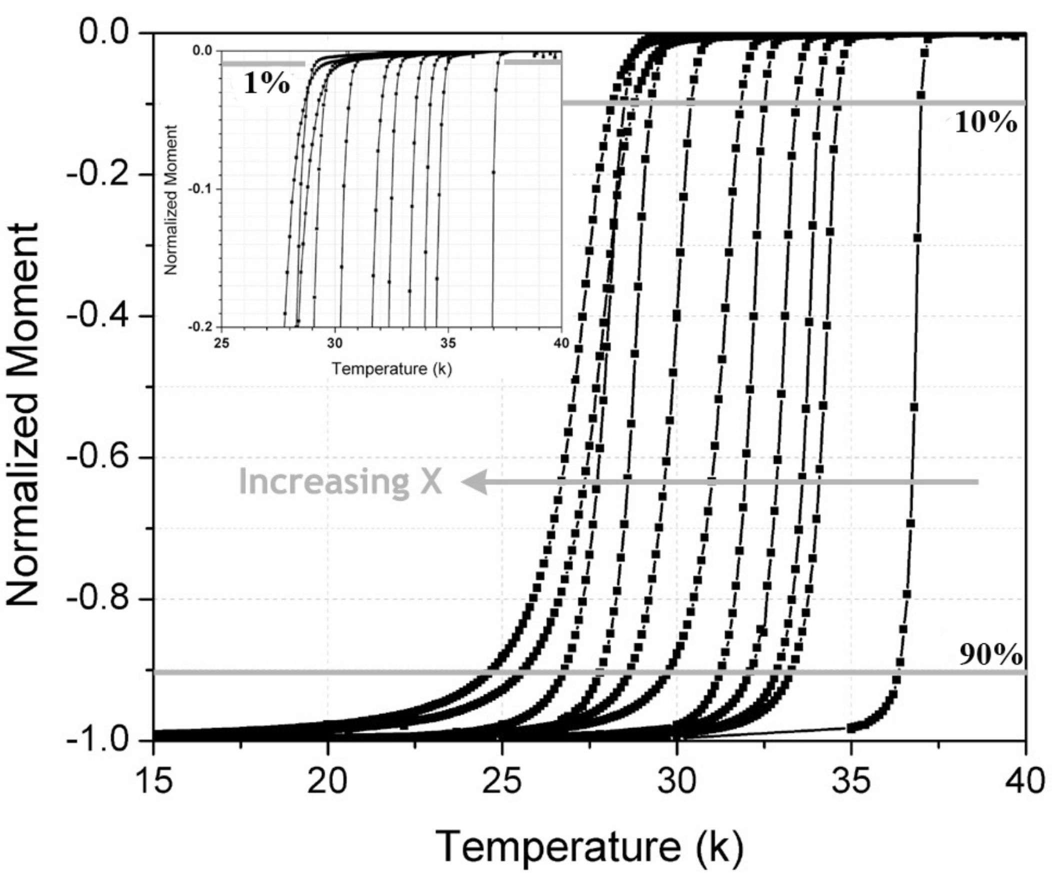

Figure 3.16 – Normalized moment (-m/m(5K)) From Ch.5. The line marked 1% corresponds to m/m(5K) = 0.01.

T_c depression to lower T than expected from the sample composition can indicate increased (usually interband) electron scattering, which can influence H_{c2}, anisotropy, H*, and J_c(H,T). The breadth of the transition carries additional information. Inhomogeneity broadens the transition, as well as the presence of pervasive non-superconducting phases (such as in Ch. 7).

3.2.4 – X-ray diffraction (XRD)

X-ray diffraction is used in this work for phase identification, lattice parameter measurements, and grain size estimation. Several XRD systems were used in this work, with slightly different modes of operation. All operate on the same basic principles. X-rays are generated by irradiation of Cu metal with high-energy electrons. Typical operating parameters for the source are 40 kV and 30 mA. High-energy electrons knock electrons out of their orbits around the Cu atoms. As higher-energy Cu electrons drop down in energy to fill the vacant orbitals, they emit x-ray photons. The x-rays then pass through a monochrometer that selects x-rays of the desired wavelength to irradiate the sample. For this work, Cu $K\alpha_1$ radiation was used with a wavelength of 0.15406 nm.

The sample is irradiated with x-rays, which can be considered to reflect from the planes of the crystal lattice. When the x-rays strike a set of parallel planes at some angle θ with respect to the plane normal, a path length difference proportional to $\sin \theta$ arises for x-rays reflected by each plane. When the path length difference between reflections from adjacent planes is an integer multiple n of the wavelength λ, then constructive interference occurs. This criterion is expressed by the Bragg equation:

$$n\lambda = 2d \sin\theta \tag{3.20}$$

Where d is the interplanar spacing. An XRD pattern such as that shown in Figure 3.1 is then generated by plotting diffracted intensity as a function of 2θ. Since peak position in 2θ is dependent on d, XRD can be used to determine interplanar spacing and therefore lattice parameter. In order to measure small shifts in lattice parameter, such as those associated with C-doping in MgB_2, care must be taken to minimize error.

Peak position error can arise from factors related to the sample (particularly sample displacement from the instrument center) or to the diffractometer. Sample displacement errors cause an error in *d* given by:

$$\frac{\Delta d}{d} = -\frac{D\cos^2\theta}{R\sin\theta} \tag{3.21}$$

where D is the height displacement from the instrument center and R is the diffractomer radius.[Cullity01]. This error (and diffractometer misalignment) can be corrected for by mixing a standard with the sample powder. Other errors include imperfect focusing, absorption within the sample, and beam divergence. These errors are mostly systematic in θ and can be accounted for by use of the Nelson-Riley method operating via the relation:

$$\frac{\Delta d}{d} = K\left(\frac{\cos^2\theta}{\sin\theta} + \frac{\cos^2\theta}{\theta}\right) \tag{3.22}$$

Lattice parameter can be calculated from each peak position and the results plotted against the Nelson-Riley function and a linear fit applied. The intercept of the linear fit yields a more accurate lattice parameter that those associated with the individual peaks. Error can be estimated from the goodness of the linear fit. In the case of hexagonal crystals (such as MgB_2) where a and c lattice parameters are not equivalent, the Nelson-Riley method can be used on the (00n) planes and then on the planes containing an a component. In practice, it is often impractical to apply the Nelson-Riley method to (00n) planes of MgB_2 due to the small number of reflections and the low diffracted intensity of all but (002). In this work, we took advantage of the observation that the c-axis lattice parameter in single crystals doesn't vary with C-doping, and typically used $c = 0.3521$ nm to calculate a for planes that had both and a and c component. The error associated with this measurement varied by instrument, but was ≤ about 0.005 Å for most data in this thesis.

Peak broadness is influenced by a variety of factors including slit width, degree of elimination of $K\alpha_2$, various other instrument factors, sample inhomogeneity, strain, disorder, and grain size. Grain size broadening is of particular interest. At small grain size it can be the dominant factor determining peak breadth, and under those conditions grain size can be estimated by the Scherrer formula:

$$t = \frac{K\lambda}{B\cos\theta_B} \tag{3.23}$$

where t is the calculated grain size, K is a constant between 0.9 and 1, B is the peak breadth in radians, and θ_B is the peak position. This relationship is highly useful for estimating the size of small grains, and is used extensively in this work for grain sizes too small for accurate measurement by scanning electron microscopy. For large grains, other broadening contributions dominate, and the effect of grain size can be difficult to discern.

The Scherrer formula thus gives a minimum estimate of grain size. The factors determining instrument broadening are difficult to quantify, and are best determined empirically by measuring the breadth of a peak from a large grained, perfect sample. With such a measurement in hand, it is possible (to some extent) to resolve the component of peak broadening due to grain size by using the Stokes and Wilson method (#Warren) involving Fourier transforms, but this analysis requires excellent patterns that are free from strain, inhomogeneity, and disorder, and even then is difficult to apply accurately.

Most of the XRD work presented in this thesis was performed on three instruments: a high-resolution Bragg-Brentano (standard) geometry instrument with point detector (operated by J. Giencke), a Philips Hi-Star 2D diffractometer equipped with an area detector, and a high-resolution Guinier camera instrument. None of these instruments was optimal. The high-resolution point detector instrument had a step size of 0.01° in 2θ and was capable of very accurate peak position measurements, but due to the low diffracted intensity associated with these samples, even scan times on the order of 10 hours produced very noisy data. The Hi-Star obtained good signal to noise ratios with ~5 min scans, and showed that the samples were randomly oriented, but step size was rather large (0.05° in 2θ) and peaks were quite broad, making it unsuited for accurate lattice parameter or grain size measurements. The Guinier camera instrument had a step size of 0.005° in 2θ and yielded the sharpest peaks of the three instruments. It was a transmission mode instrument and could not accommodate solid bulks (only powders). Due to sample holder effects, patterns collected by that instrument had a strong and complicated background signal that was difficult to eliminate by background subtraction, and was not fit well by programs such as FullProf or PowderCell. This instrument was used extensively in the work in Ch. 6-7.

One very important application of x-ray diffraction to this work is the calculation of a-axis lattice parameter, as described above. Calculated lattice parameter can then be compared with the single crystal and filament data shown in Ch. 2 to infer the C-content of the sample. The results produced by this method are self-consistent and also consistent with T_c, H_{c2}, and resistivity trends. However, these inferred carbon content values are not definitive composition measurements because other factors can influence lattice parameter – such as contamination by elements other than C. This may be a factor in Ch. 7, where lattice parameter contracted significantly for $T_{HIP} > 1000^oC$ in milled samples, and for $T_{HIP} = 1500^oC$ the inferred C-content was significantly larger than the available C thought to be in the system.

3.2.5 – Other Analytical Methods

Scanning electron microscopy (SEM) was used to identify second phases and observe microstructures, including grain and particle size estimations. Several microscopes were used for this purpose, all of which operated on the same basic principles. SEM is well understood and well known, and information about SEM is readily found.

A portion of this work (4 samples) involves transmission electron microscopy (TEM), and another portion of the work (2 samples) involves magneto-optical (MO) imaging. These analyses were carried out by Ye Zhu (TEM) and Anatolii Polyanskii

(MO) who are highly skilled in these measurements. TEM is a widely known but extremely complex microstructural analysis technique, and many books have been written on the subject. MO imaging is described in [Polyanskii02], and centers on the use of an indicator film which lightens under polarized light in the presence of a magnetic field. This can be observed with a light microscope. In this way the flux penetration can be visualized in different regions of a sample, and the flux gradient can be calculated, which can then be used to estimate J_c.

3.3 – Summary

Powder handling, milling, forming, sealing, and HIP treatment were described in detail. These processes produce hard, dense pellets with finer grain size in milled compared to unmilled material. These pellets were suitable for shaping into rectangular bars for further measurement. The principle sources of variation in sample properties are thought to result from contamination – primarily by C, O, W, and possible Co. The most important (and most difficult to control) source of contamination is thought to be the air (see also Ch. 4). Some such contamination was present in the starting powders, and the possible sources of further contamination (and therefore random variation in sample properties) were described.

A broad suite of measurement techniques were used to critically assess sample quality by a variety of metrics. This permitted refinement of the sample processing based on results from each set of samples. This innovation of preparation will be clear from the multiple experiments in this thesis. A final summation of how J_c(H) is influenced by these various sample properties (and thus processing) can be found in Chapter 8.

Chapter 4 – Atmospheric contamination effects

(Contains material published in SuST **19** (2006) 1173[Senkowicz03])

In order for C-doped MgB_2 to emerge as a competitive conductor, it must be able to be made with known and controlled composition at different facilities around the world. At present, that is not the case. Despite careful preparation from high purity starting powders, "undoped" samples in the literature have widely varying properties. For example, in nominally "pure" polycrystalline bulk samples, Bud'ko et al [Budko01,Budko02] reported H_{c2}(0 K) ~ 16 T, Bhatia et al.[Bhatio02] H_{c2}(0 K) ~ 20.5 T, and Matsumoto et al[Matsumoto03] H_{c2}(0 K) ranging from 17 to 24 T.

In the rush to understand carbon and SiC doping, not enough attention has been devoted to understanding the wide variation in intragrain properties between nominally undoped samples. Some seemingly uncontrolled mechanism has a substantial effect on these properties. This chapter examines the effect of atmospheric contact before and after ball milling commercially available (Alfa-Aesar) pre-reacted MgB_2 precursor powder by examining the properties of sintered bulk samples subsequently made from the milled powder. Changes in superconducting and normal state properties as a result of exposure to air were wholly consistent with the hypothesis of carbon doping from the air. This work suggests that carbon contamination can arise from exposure to air, and that reproducibility and control of superconducting properties can only be achieved if exposure of powders to air is acknowledged to be a processing variable.

4.1 - Experimental Procedures

All four samples in this set were made from Alfa-Aesar pre-reacted MgB_2. We milled for 10 hours in a Fritsch Pulverisette 4 ball mill (not a SPEX mill) both to promote compositional homogeneity and in order to facilitate interaction with gas in the milling jar. For all samples, the WC milling jar was housed inside a specially made brass can with a compressed O-ring seal and a port for an optional valve used only for sample D. Milling was carried out with hardened steel balls. Although there is a possibility of contamination by the milling apparatus, the jar and balls did not show any visible wear, and there was no evidence for iron or WC contamination based on x-ray diffraction patterns. Moreover the milling procedure was identical for each sample.

The four samples were handled and milled under slightly different atmospheric conditions. For sample A, the milling jar was loaded and sealed into the brass can in a glove box filled with dry nitrogen and equipped with active oxygen and water scavenging. After milling, the jar was opened and the powder was handled in the same glove box. For sample B, a similar milling jar was loaded and sealed in the brass can in a nitrogen filled glove bag filled with flowing N_2 gas from which residual oxygen and water were not removed. Unsealing and post-milling handling were done in the glove box, as for A. For samples C and D, the milling jars were loaded and sealed in the brass can in the typically humid atmosphere of Mayaguez, Puerto Rico and, after milling, were unsealed and handled in the dry winter air in Madison, Wisconsin. The brass can was hermetically sealed for sample C, whereas for sample D the brass can was fitted with a one-way check valve that could open to vent excess pressure from the milling can. The handling atmospheres and property summary are listed in Table 4.I.

The milled powders were pressed into pellets and sealed in evacuated stainless steel tubes, then hot isostatic pressed at 1000°C and ~200 MPa for 5 hours. The pellets were sufficiently dense after sintering that they had hardness $H_V > 10$ GPa and needed to be sectioned with a diamond saw before measurement.

4.2 - Results

X-ray diffraction patterns are shown in Fig. 4.1 using a linear intensity scale. All four samples had similar XRD patterns, and all contained small amounts of MgO and MgB_4. The peak at ~63° is a composite of an MgB_2 peak at 63.27° and an MgO peak at 62.22°. For samples A, B, C, and D the peak positions are 62.85°, 62.8°, 62.2°, and 62.3° respectively. The shift to lower 2θ for samples C and D indicated that those samples milled in air contained more MgO than samples A and B, which were milled in an inert atmosphere.

Table 4.I – Processing parameters, sample designations, and properties

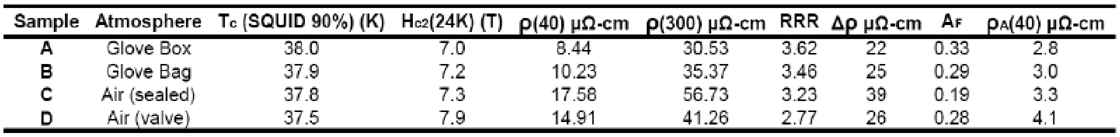

Sample	Atmosphere	T_c (SQUID 90%) (K)	H_{c2}(24K) (T)	ρ(40) μΩ-cm	ρ(300) μΩ-cm	RRR	$\Delta\rho$ μΩ-cm	A_F	ρ_A(40) μΩ-cm
A	Glove Box	38.0	7.0	8.44	30.53	3.62	22	0.33	2.8
B	Glove Bag	37.9	7.2	10.23	35.37	3.46	25	0.29	3.0
C	Air (sealed)	37.8	7.3	17.58	56.73	3.23	39	0.19	3.3
D	Air (valve)	37.5	7.9	14.91	41.26	2.77	26	0.28	4.1

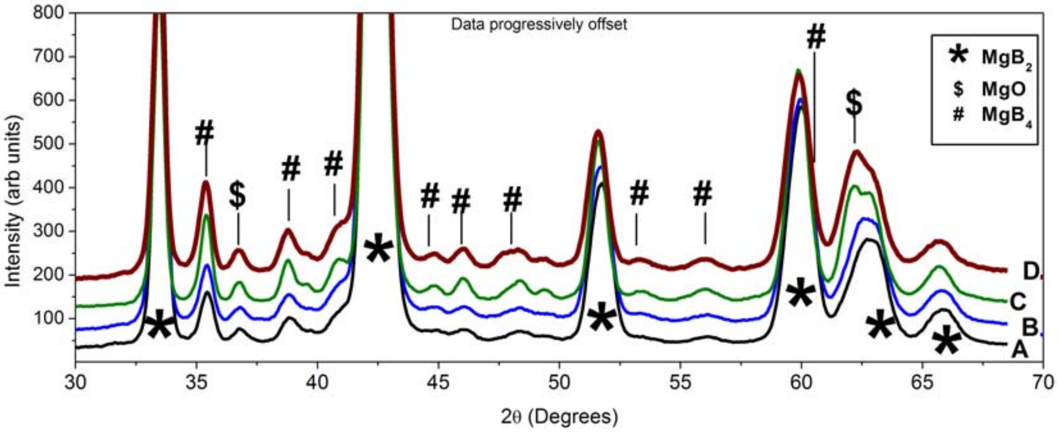

Figure 4.1 – Progressively offset x-ray diffraction patterns of heat treated samples.

The superconducting moment was measured in a SQUID magnetometer as a function of increasing T after zero-field-cooling to 5 K. Figure 4.2 shows the magnetic moment **m** as a function of temperature between 36 K and 39 K, normalized to the moment at 5 K. Sample A had the highest T_c and the sharpest transition. Sample B had an onset T_c nearly as high as sample A, but its transition was not as sharp. Sample C had a sharp transition, beginning ~0.1 K below that of sample A. Sample D also had a fairly sharp transition, beginning ~0.5 K below that of sample A. Thus there was a small monotonic depression of T_c with increasing presumed exposure to air.

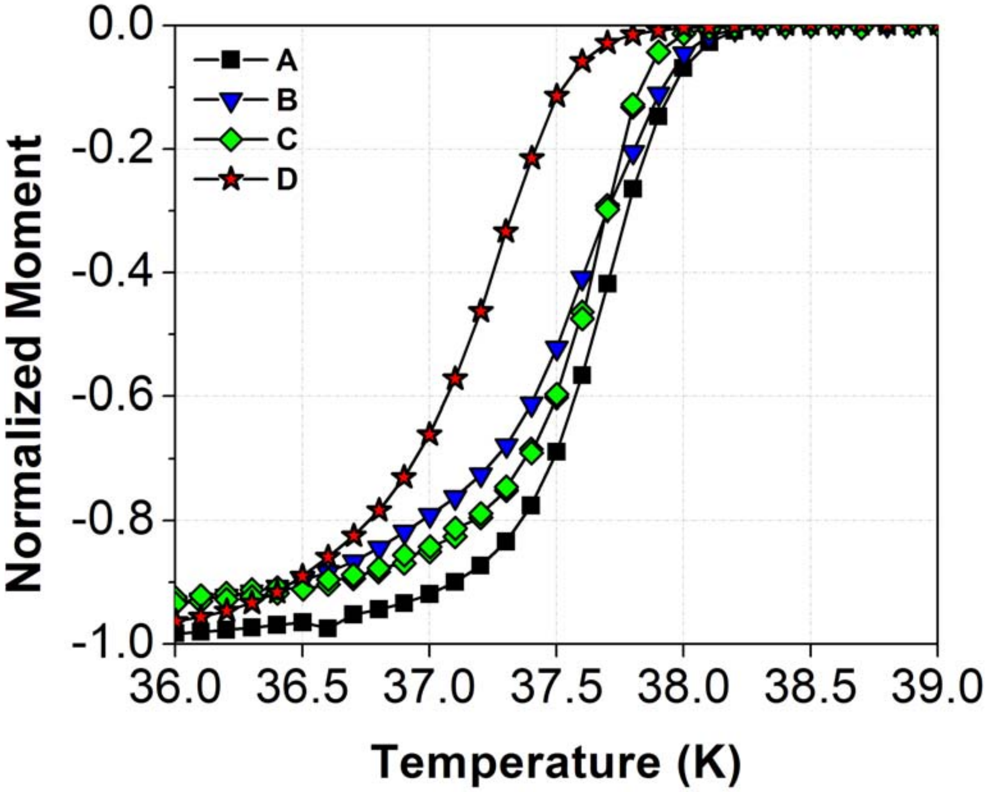

Figure 4.2 – Magnetic ZFC (see Ch. 3) T_c traces normalized to m(5 K).

Using a Quantum Design Physical Property Measurement System (PPMS) we measured the normal state resistivity as a function of temperature and field in the normal and in the superconducting state. Figure 4.3 shows the dependence of the upper critical field H_{c2} on temperature, defined using 90% of the normal state resistivity as our criterion for H_{c2}. The trend in H_{c2} was similar to that seen in T_c but of opposite sign – as atmospheric exposure increased, H_{c2} increased. The H_{c2} values at 24K increased from 7.0 T for sample A to 7.9 T for sample D. Our data fall between H_{c2} values from the literature taken on pure and 3.8% carbon-doped filaments.[Wilke03]

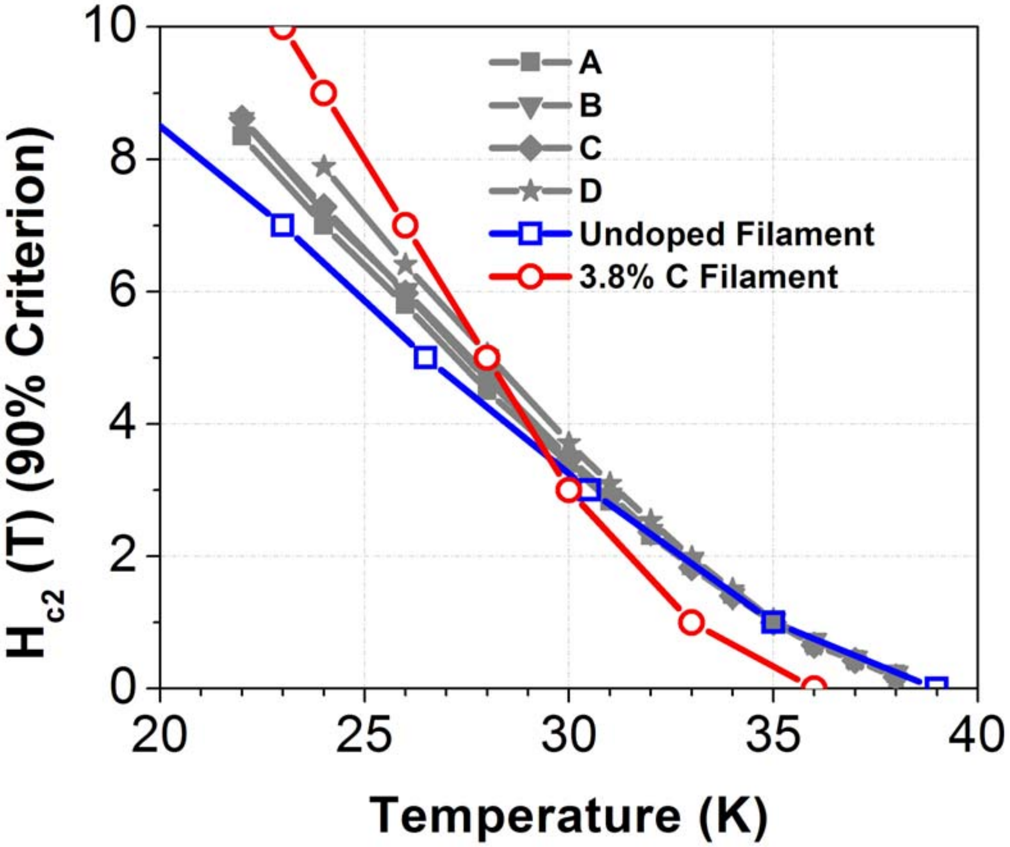

Figure 4.3 – H_{c2}(T) using 90% ρ_n criterion. Included for comparison are data taken from Wilke *et al* [Wilke03] using the same criterion.

The temperature dependence of ρ is shown in Fig. 4.4. We observed an increase in normal state resistivity at all temperatures, as well as an increase in $\Delta\rho = \rho(300\ \mathrm{K}) - \rho(40\ \mathrm{K})$ and a decrease in RRR from samples A through C corresponding to the MgB_2 having had increasing exposure to air. Sample D falls between samples B and C in measured ρ and in $\Delta\rho$, but has the lowest RRR of the set.

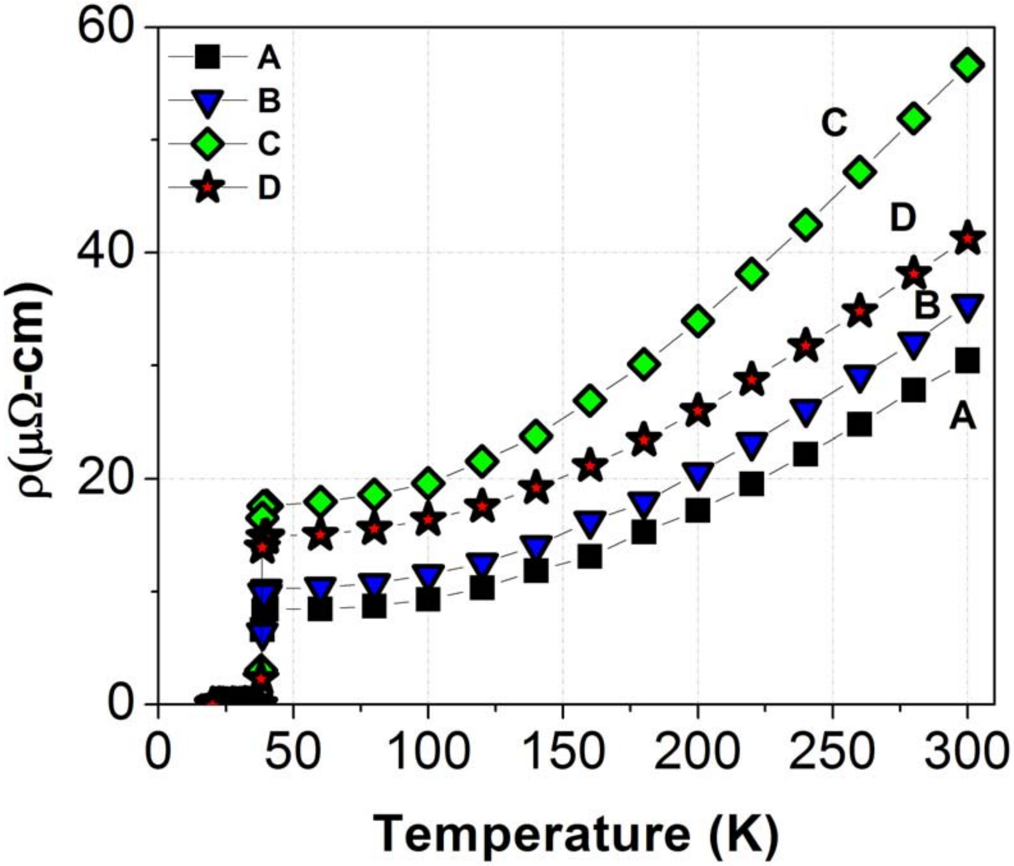

Figure 4.4 – *ρ(T)* from 5 mA, four-point measurement.

Fig. 4.5 shows J_c(H) at 4.2 K for each sample, as calculated from M-H hysteresis loops using the equation $J_c(H,T) = 0.5*\Delta M*12b/(3bd-d^2)$, (see Ch. 3) where *b* and *d* are the width and thickness of the rectangular section bar and ΔM is the difference in volumetric magnetization between the arms of the MH loop.[Evetts01] Low field J_c was very similar for all samples, but high field J_c increased progressively from A to D, and 4.2 K H*(J_c = 100A/cm^2) ranged from less than 8 T for sample A to more than 9 T for sample D.

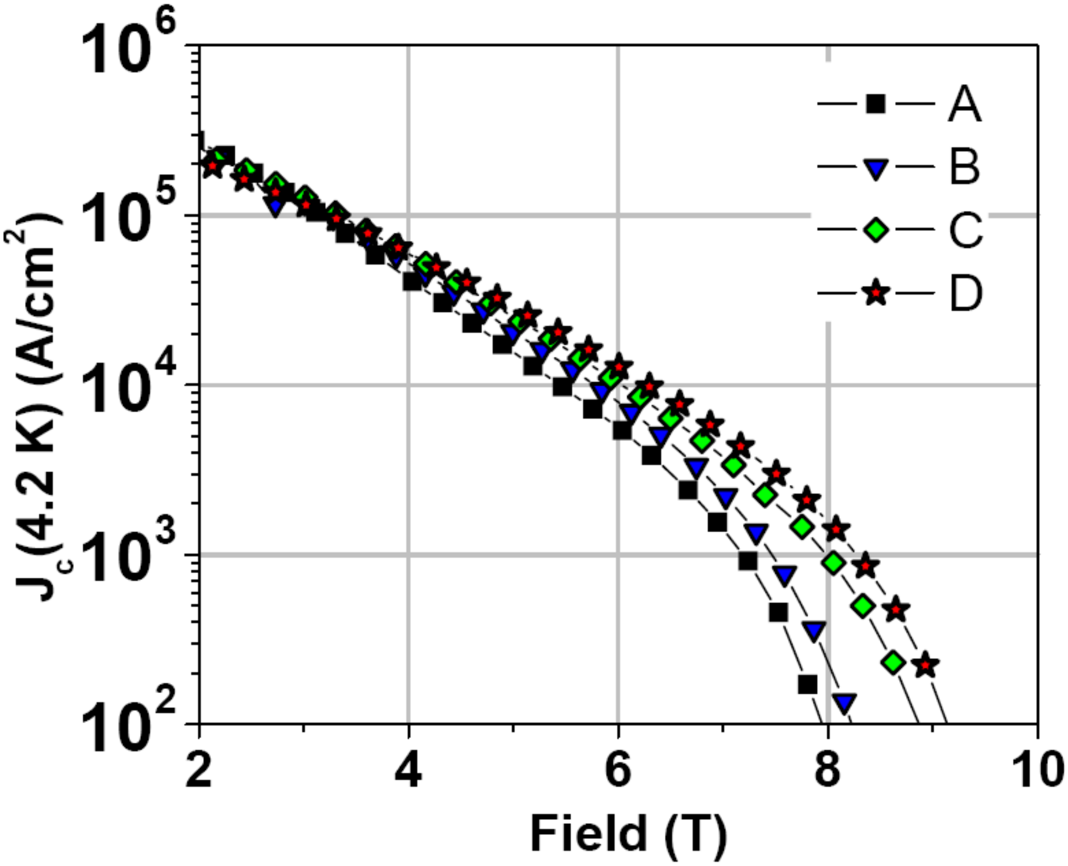

Figure 4.5 – J_c(H) at 4.2 K determined from M-H loops.

4.3 - Discussion

The Alfa Aesar MgB_2 used for this experiment is one of the most widely used starting materials for experiments on pre-reacted MgB_2 yet our post-processing resulted in clear property change trends in every quantity studied, as shown in Table 4.I. T_c decreased and H_{c2} increased as supposed atmospheric exposure increased. Rowell analysis resistivity of the connected portion (which we call adjusted resistivity, ρ_A) increased. A less clear trend linking increased atmospheric exposure with a decrease in the calculated current-carrying cross sectional area was also observed. Given that the starting powder was probably exposed to air before it came into our hands and considering that in all cases additional exposure to air during and after milling was rather limited (for example, none of the samples was milled in an unsealed jar) the observed differences are very significant. The remainder of this paper is devoted to explaining the nature of the observed effects.

Key facets of the data that require explanation are as follows: T_c and H_{c2} show a monotonic trend that is consistent with trace alloying exerting intragrain scattering effects. The T_c and H_{c2} trends are generally supported by the measured RRR and normal state resistivity, the latter of which can be controlled by both scattering and by variable sample connectivity. Greater amounts of MgO and MgB_4 were found as atmospheric exposure increased.

The x-ray diffraction result indicates larger concentrations of MgO and MgB_4 in samples C and D than in samples A and B. This observation is wholly consistent with the milling atmospheres. Exposure to O_2 and H_2O appears to have resulted in the reactions

$$2MgB_2 + \tfrac{1}{2}O_2 \rightarrow MgO + MgB_4 \tag{4.1}$$

$$2MgB_2 + H_2O \rightarrow MgO + MgB_4 + H_2 \tag{4.2}$$

There has been some debate about the line-compound nature of pure MgB_2. Although no material is a perfect line compound, the simultaneous increase in MgB_4 and MgO content indicate that any formation of Mg vacancies in the MgB_2 lattice to compensate for the loss of Mg to MgO must be small. Similarly, these observations imply that oxygen solubility in MgB_2 must also be small.

Comparing samples A and D, the ~0.5 K T_c reduction in sample D (the sample with the most presumed exposure to air) can be explained by either a small amount of oxygen doping having a profound effect on T_c or the more likely explanation that the scattering behavior of these samples is changing because carbon present in air as CO_2 is being milled into the samples.

Kazakov et al.[Kazakov01] published a detailed study relating carbon content to T_c in C-alloyed MgB_2 single crystals. From their data, one can extract the following relationship for carbon content X < about 0.05:

(4.3) $$T_c\,(\mathrm{K}) = 38.58 - 79.2\,X$$

Where X is the carbon content expressed by $Mg(B_{1-X}C_X)_2$. Applying eqn. (4.3) to this sample set and using the T_c values given in Table 4.I (90% normal criterion) we find $T_c(A) - T_c(D) = 0.5$ K. This change in T_c corresponds to $\Delta X \sim 0.006$, or about 0.6% additional substitution of C for B. Applying a modified formalism of the Rowell analysis[Jiang01,Rowell01,Rowell02] with $\Delta\rho_{ideal} = 7.3$ μΩ-cm we calculated the active area fraction A_F (the fraction of the cross section carrying the measurement current), and the adjusted resistivity $\rho_{A(}40$ K) (the normal state resistivity of this active fraction), finding that A_F ranged between 0.19 and 0.33, which is higher than for the MgH_2 -precursor tapes of Matsumoto et al.[Matsumoto02] but less than most of the HIP processed samples in our other work (see Ch. 5-7).[Senkowicz01,Senkowicz02] As expected, the largest A_F was found for sample A, milled under the cleanest conditions and possessing the least MgO and MgB_4, which is consistent with our recent observation that MgO and MgB_4 obstruct current flow.[Jiang01] Sample A also had the lowest ρ_A(40 K), indicating the smallest amount of electron scattering by defects and dopants. Even though it was the lowest in the set, $\rho_{A(}$40 K) = 2.79 μΩ-cm is quite high compared to pure samples,[Canfield03,Budko01] but if we conclude that these samples are C-doped and calculate X from equation (4.3), then ρ_A(40 K) for these samples agrees rather well with ρ(40 K) measured in fully connected C-doped samples in the literature[Kazakov01,Wilke03] as shown in Fig. 4.6. The ρ_A(40 K) trend shows an entirely monotonic increase with presumed exposure to air, agreeing well with other indicators of intragranular electron scattering such as T_c, H_{c2}, and RRR summarized in Table 4.I.

The A_F of Sample B was 12% smaller than sample A, while samples C and D had A_F even lower, linking current obstruction with exposure to air. Curiously, sample D had greater A_F than sample C. We do not have a clear understanding of this facet of the data, but we do stress that both samples C or D have lower A_F than sample A or sample B. Despite recent advances in analysis, an accurate quantitative measure of connectivity is still unavailable.

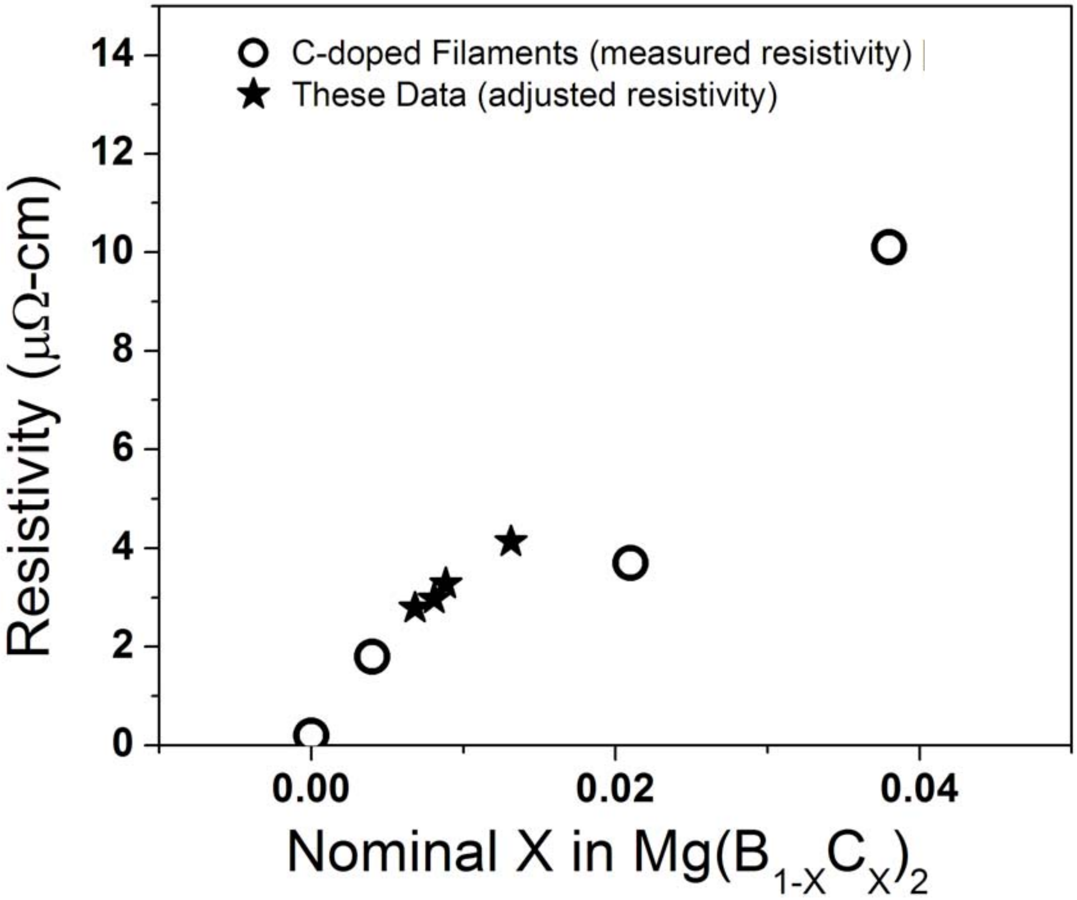

Figure 4.6 – Comparison of Rowell adjusted resistivity for these samples to measured resistivity of well connected C-doped filaments from [Wilke03,Wilke04]

Further evidence for carbon doping resulting form atmospheric exposure is that for these samples $H_{c2}(T)$ was rather higher than that of the pure filament from Wilke et al.[Wilke03] for which H_{c2}(24 K, 90% criterion) is only about 6.5 T, but less than the ~ 9 T H_{c2}(24 K, 90% criterion) of their X = 0.038 C-doped filament.[Wilke03] We found that, as expected, our samples rank in the same order by dH_{c2}/dT as by ρ_A(40 K) because dH_{c2}/dT is generally increased by electron scattering. These results are also consistent with our proposal that C is accumulating in the samples as a result of exposure to air.

Low field J_c(H) was found to be similar across our sample set, (samples A, B, C, and D had J_c(2 T, 4.2 K) of 212, 244, 220, and 208 kA/cm^2 respectively) indicating no strong effect from varied connectivity. More significantly, J_c(H) decreased more slowly with increased magnetic field as the atmospheric exposure increased, with a difference in H*(4.2K) of more than 1 T which means that H*(4.2K) for sample D is about 12% greater than for sample A. This result is consistent with increased carbon doping.

4.4 - Conclusions

This experiment studied the effect of variable air exposure during processing on nominally undoped pre-reacted MgB_2 subjected to ball milling. Both intergrain and intragrain effects were observed. Small amounts of MgO and MgB_4 were observed by x-ray diffraction, indicating reaction with oxygen. The amount of MgO and MgB_4 increased with presumed increased exposure to air. The connectivity related parameter A_F was observed to generally decrease as presumed exposure to air increased. All four samples showed greater electron scattering than the purest single crystals and CVD filaments[Canfield02,Kazakov01,Wilke03] as indicated by RRR, T_c, H_{c2}, and ρ_A(40 K). Strong circumstantial evidence indicates carbon doping, most notably the similarity between these samples and published data on C-doped CVD filaments.[Wilke03] The most likely source of this C is from CO_2 in air.

We conclude that MgB_2 is highly sensitive to atmospheric O_2 and CO_2. Reaction with oxygen results in the formation of MgO and MgB_4 that could block current flow. Reaction with CO_2 dopes MgB_2 with carbon, increasing electron scattering and having a strong effect on T_c, H_{c2}, H*, and resistive properties. We believe these mechanisms are largely responsible for the wide variations in connectivity and differences in T_c, resistivity, and H_{c2} reported in the literature for "pure" MgB_2.

This work highlights our previous assertion that the air is a major (perhaps *the* major) source of contamination with C and O. This result justifies the considerable effort invested in preventing air exposure (Ch. 5-7), and also suggests that unpredictable sample to sample variation in later chapters is a result of incomplete control over air exposure.

Chapter 5 – Effects of variable C-content

(Contains material from SuST **20** 650 [Senkowicz02])

Our very first result on C-doping ex-situ powder appeared in Applied Physics Letters [Senkowicz01]. It is not included in this thesis because the pertinent information it contains is reproduced with more control and detail in the experiments described in Ch. 5-7. Briefly, we found that high energy ball milling was an effective method for C-incorporation into ex-situ MgB_2 powder. The result was one sample with X~0.05 (in $Mg(B_{1-X}C_X)_2$) which had H_{c2}(0 K) ~ 35 T and then-record J_c(8 T, 4.2 K) ~ $5x10^4$ A/cm^2. At the time we did not fully understand the mechanisms behind this provocative result, or how to further improve J_c. Understanding the development of J_c(H) in milled ex-situ samples (with and without C-doping) required additional experimentation which forms the core of this thesis.

This chapter describes an experiment intended to determine the optimum C-content in milled ex-situ MgB_2 by exploring the effects of systematic doping with C by high-energy ball milling. In this way peak J_c(8 T, 4.2 K) > $5x10^4$ A/cm^2 was obtained in a form compatible with powder-in-tube wire manufacture. Effects of carbon doping by this method were qualitatively similar to single crystals and CVD filaments, but T_c, H_{c2}, and resistivity measurements indicated more electron scattering than in single crystals and CVD filaments of similar composition. Both the high J_c(H) and the large degree of electron scattering were largely attributable to the high grain boundary density associated with the very fine ~50 nm grain size. At high C concentrations (C / (B+C) > 0.07) J_c fell sharply due to a decline in connectivity. This work demonstrates how J_c(H) of pre-reacted MgB_2 can be improved by simultaneously alloying with C and refining grains through cold work. We found that the beneficial effects of carbon doping by this method on J_c(8 T, 4.2 K) peaked at a few percent C, and then J_c(8 T, 4.2 K) declined due to breakdown of connectivity.

5.1 - Experimental Details

Pre-reacted MgB_2 powder from Alfa-Aesar was milled in a Spex 8000M mill for 600 minutes with powdered graphite and a stoichiometric amount of Mg powder to achieve nominal composition $Mg(B_{1-X}C_X)_2$. Tungsten Carbide (WC) milling vials and media were used. Milling and pre-heat treatment sample processing were carried out in a nitrogen-filled glove box equipped with oxygen and water scavenging. Pellets were cold pressed and sealed in evacuated stainless steel tubes and then hot isostatic pressed (HIP) for 200 minutes at maximum temperature of 1000^oC pressure of 0.2 GPa. HIP processing was used in order to achieve maximum densification and homogeneity. HIP also minimizes void space around the pellets and thus prevents Mg loss by decomposition during heat treatment (See Ch. 3). X-ray diffraction patterns, magnetization loops, magnetic T_c and $\rho(T,H)$ were measured on the reacted samples. Resistive transitions were also measured for selected samples in fields up to 33T at the National High Magnetic Field Laboratory (NHMFL) in Tallahassee, Florida. J_c values were established with a vibrating sample magnetometer (VSM). J_c was calculated from M-H hysteresis loops using the equation $J_c(H,T) = 0.5*\Delta M*12b/(3bd-d^2)$, where b and d are the width and thickness of the rectangular section bar and ΔM is the difference in volumetric magnetization between the arms of the M-H loop.[Evetts01]

5.2 Results

X-ray diffraction patterns revealed primarily single phase MgB_2 with some WC and a small amount of MgO. Peak positions were measured for the samples up to nominal X = 0.08. The Nelson - Riley method[Cullity01] was then used to calculate lattice parameters. C-axis lattice parameters did not vary significantly within the set, but a-axis lattice parameters decreased as nominal carbon content (X) increased, as shown in Figure 5.1a.

The data in figure 1(b) were generated by comparison of our a-axis lattice parameters to those of single crystals from the literature (see Ch. 2).[Kazakov01] These data indicate that our "undoped" sample actually contained a small amount of carbon, and that measured carbon content roughly matched nominal carbon content for $X \leq 0.04$. At higher carbon content, uncertainty in peak positions made it difficult to judge doping efficiency, but it does appear that carbon was not fully incorporated into the lattice for $X > 0.04$.

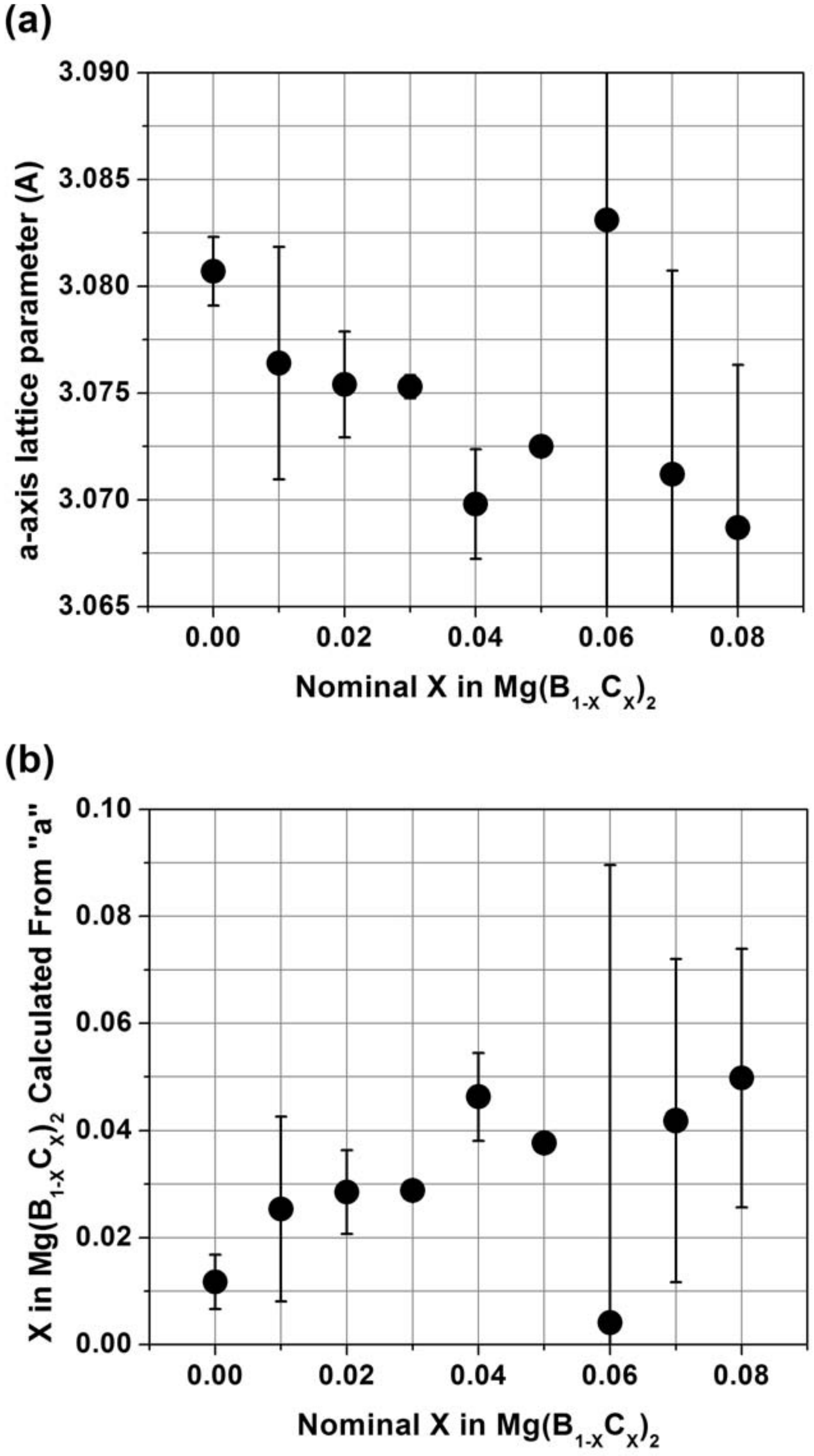

Figure 5.1 – (a) a-axis lattice parameter as a function of nominal X calculated from x-ray diffraction pattern peak positions. (b) Lattice X calculated from a-axis lattice parameter using C-doped single crystals as reference.[Kazakov01] In some cases error bars are not visible because they were smaller than the data circles.

Figure 5.2 shows magnetization T_c curves measured in a superconducting quantum interference device (SQUID) magnetometer. T_c (m/m(5K)=0.1) of the X = 0 sample was 37.0 K, slightly lower than the accepted value for pure MgB_2.[Budko01] T_c declined with increasing X as shown. It can also be seen that the transition broadens at the highest C contents.

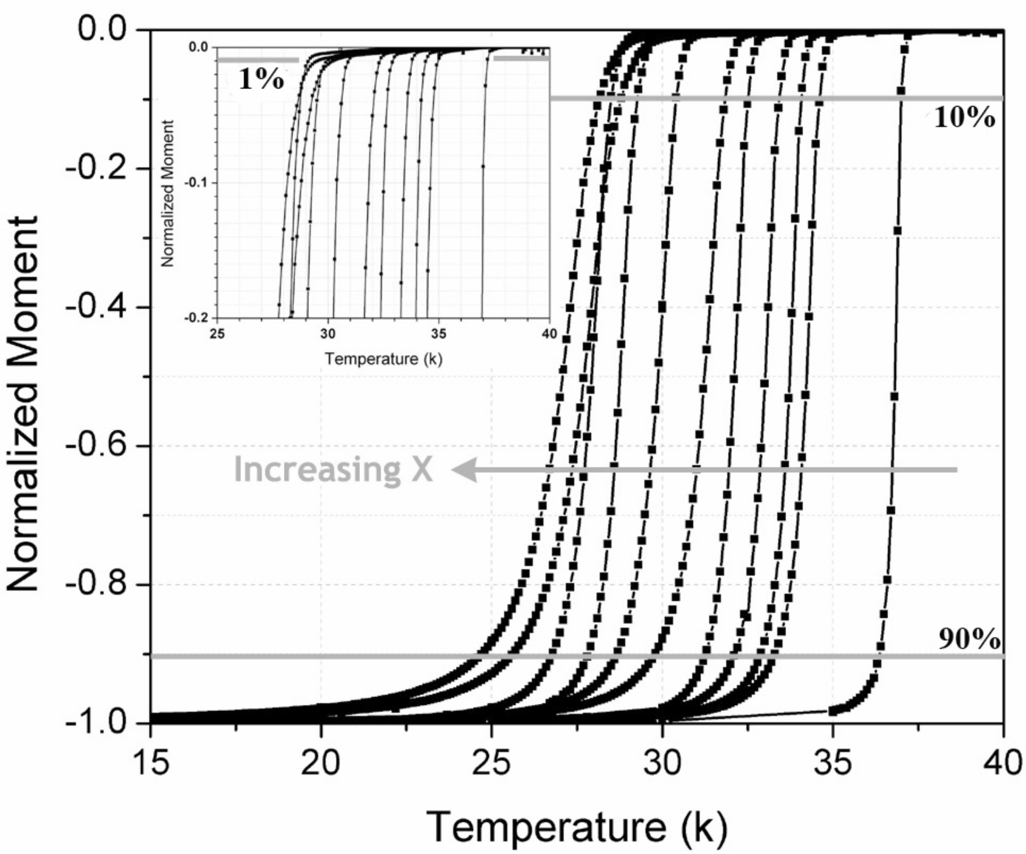

Figure 5.2 – Zero-field-cooled (ZFC) warming transitions from SQUID magnetometry.

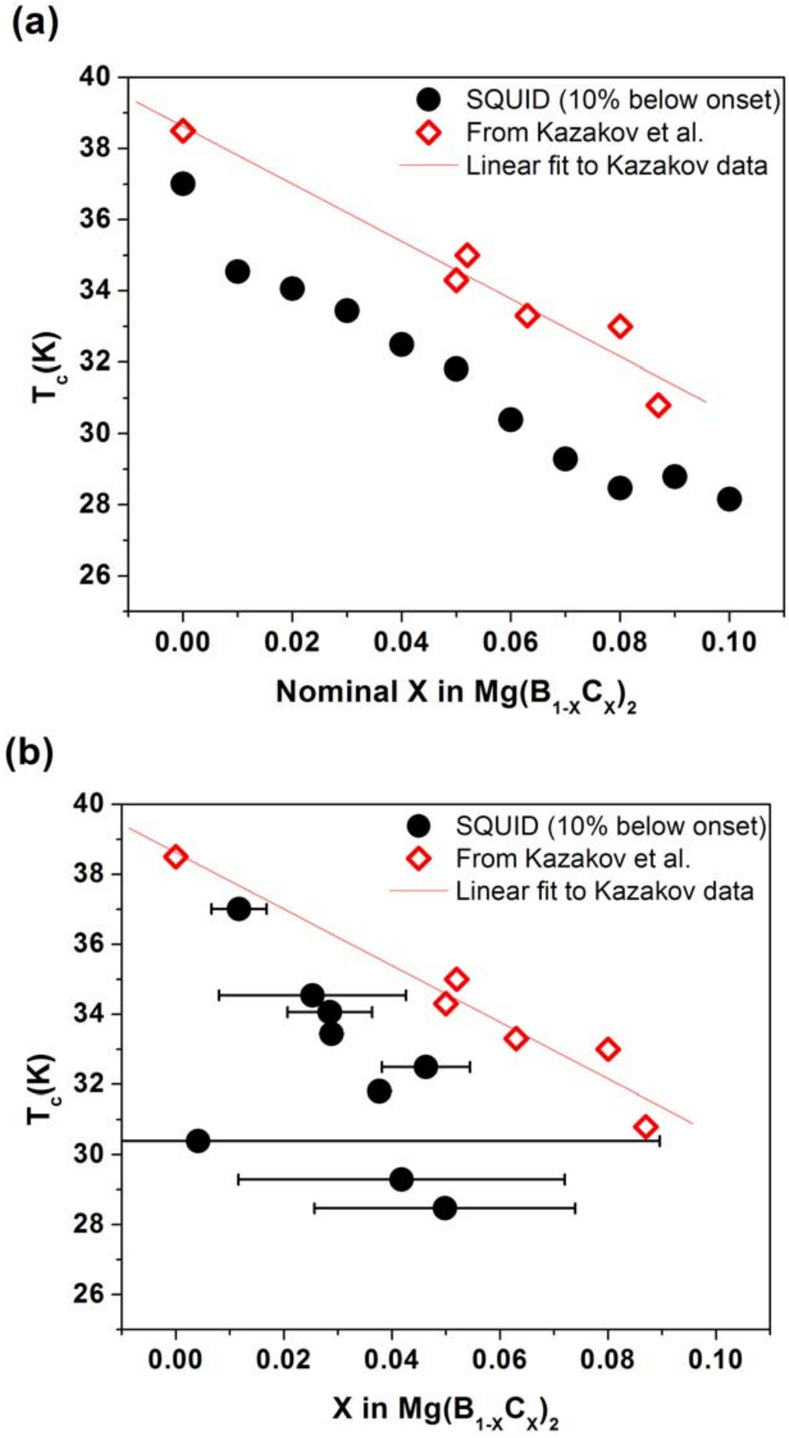

Figure 5.3 – Measured T_c as a function of (a) nominal X and (b) X derived from x-ray diffraction pattern peak positions (see Fig 1). Single crystal data from Kazakov et al. [Kazakov01] (bottom of resistive transition) included for comparison.

Figure 5.3 relates measured T_c (m/m(5 K) = 0.1) with nominal carbon content (5.3a) and calculated carbon content (5.3b) from Figure 5.1. Also included for comparison is single crystal T_c data from Kazakov et al.[Kazakov01] where the T_c criterion was the bottom of the (sharp) resistive transition. Even taking into account the fact that our measurements were magnetic, while the single crystal measurements were resistive (with very sharp transitions) our measured T_c values were consistently 2-3 K lower than those of the single crystals.

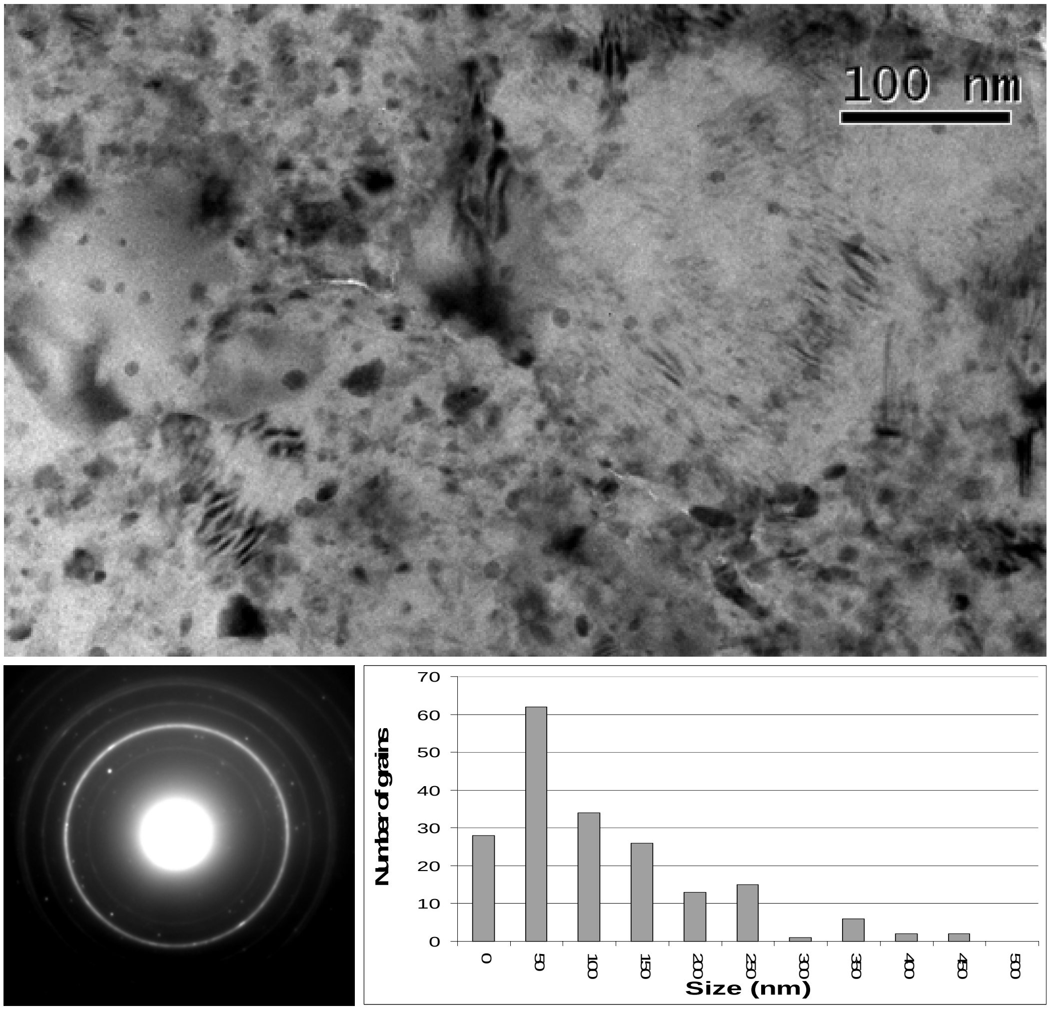

Figure 5.4 – Transmission electron micrograph, selected area diffraction pattern and associated grain size chart for previously synthesized X=0.05 sample.[Senkowicz01] TEM by Ye Zhu.

Transmission election microscopy (TEM) investigation was not carried out on these specific samples, but previously unpublished TEM on a similar sample[Senkowicz01] with X = 0.05 indicated a typical grain size slightly larger than 50 nm. We have observed typical grain size ~10-15 nm in our milled powders before heat treatment, so the grain size shown in Fig 5.4 represents grain growth from the as-milled state. The selected-area diffraction pattern shown in Fig 5.4 indicates that the sample mainly consists of well crystallized MgB_2 grains, with a small fraction of MgO. Numerous defects such as dislocations and nano-pores were observed. Even with HIP processing, pores of size 20 ~ 250 nm were still present. A small population of intact WC particles, entrained during milling, were found dispersed inside the sample with the size ~ 100 nm up to a few microns.

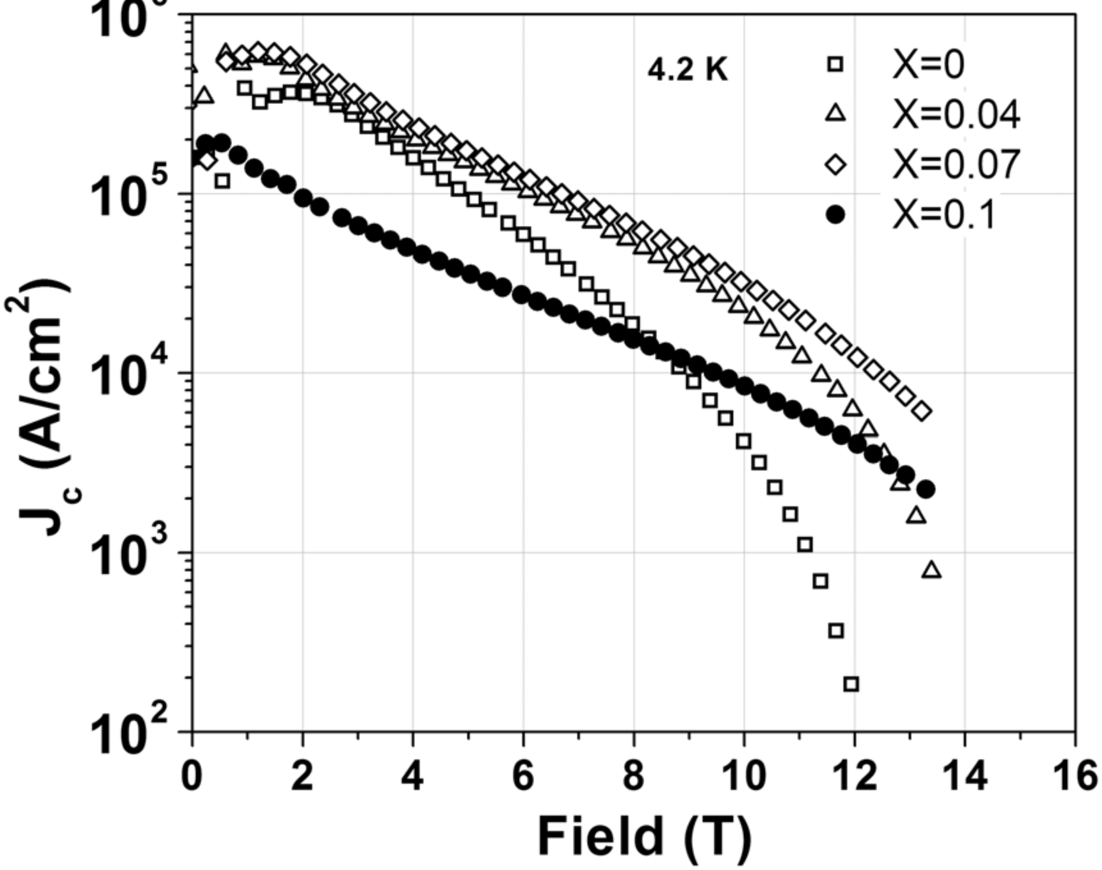

Figure 5.5 – J_c(H) at 4.2 K for selected samples, calculated from magnetic hysteresis loops.

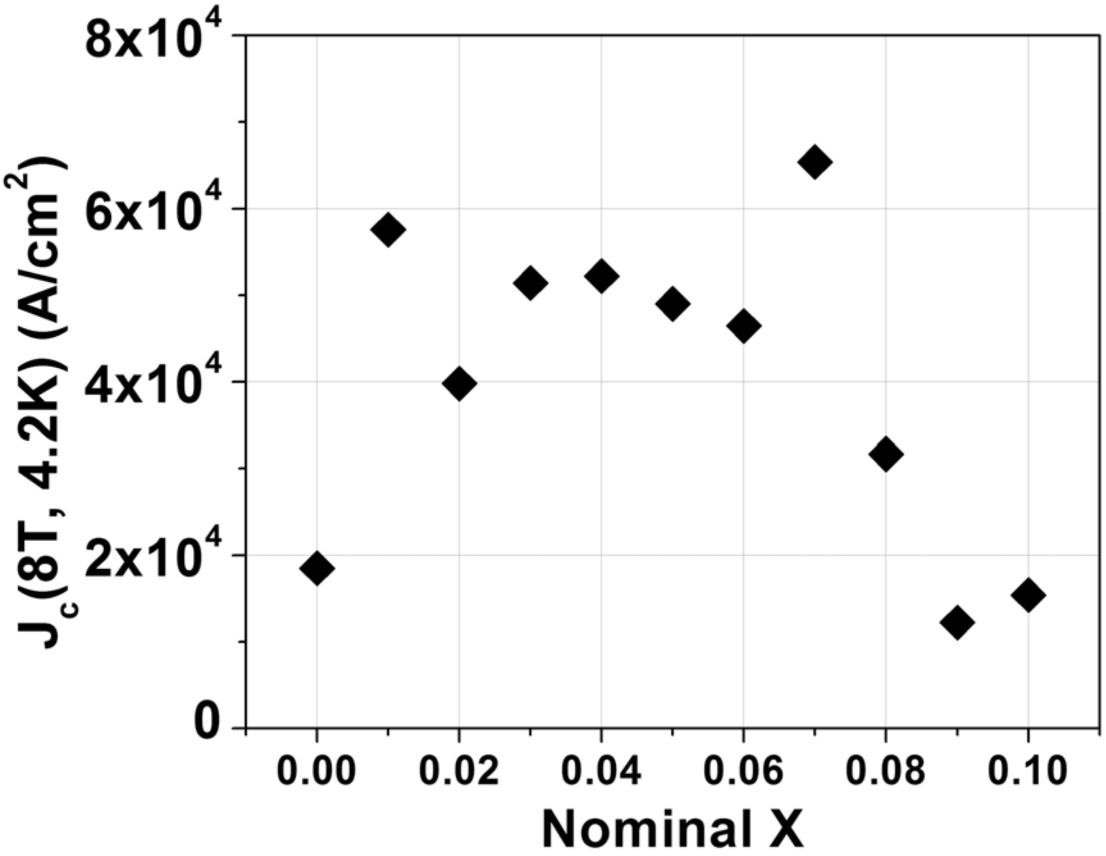

Figure 5.6 – J_c(8 T, 4.2 K) for all samples, calculated from magnetic hysteresis loops.

Figure 5.5 shows J_c(4.2 K) for selected samples, and Fig 5.6 shows J_c(8 T, 4.2 K) for the entire sample set. Some scatter (X = 0.01, X = 0.07) was observed due; we presume, to macroscopic inhomogeneity observed by MO discussed below. J_c(8 T, 4.2 K) increased rapidly with increasing X as a result of the irreversibility field increase with increasing C content which is evident in figure 5.5. However, the J_c(8 T, 4.2 K) values declined for X > 0.07, falling to less than 25% of the maximum value by X = 0.1. J_c(8 T, 4.2 K) (Figure 5.5). H* was taken from the M-H loops and is shown in Figure 5.7. Our criterion was $J_c = 100$ A/cm^2 or the extrapolated intercept of the Kramer function.[Evetts01] At low X, Kramer plots exhibited slight "inhomogeneity tails" so H* from the linear extrapolation was slightly less than H* obtained using the J_c criterion. At high X, Kramer lines bulged upwards for fields less than H* and thus the linear extrapolation slightly overestimated H*. For these samples, H* ~ 0.5 H_{c2}(H//a-b).

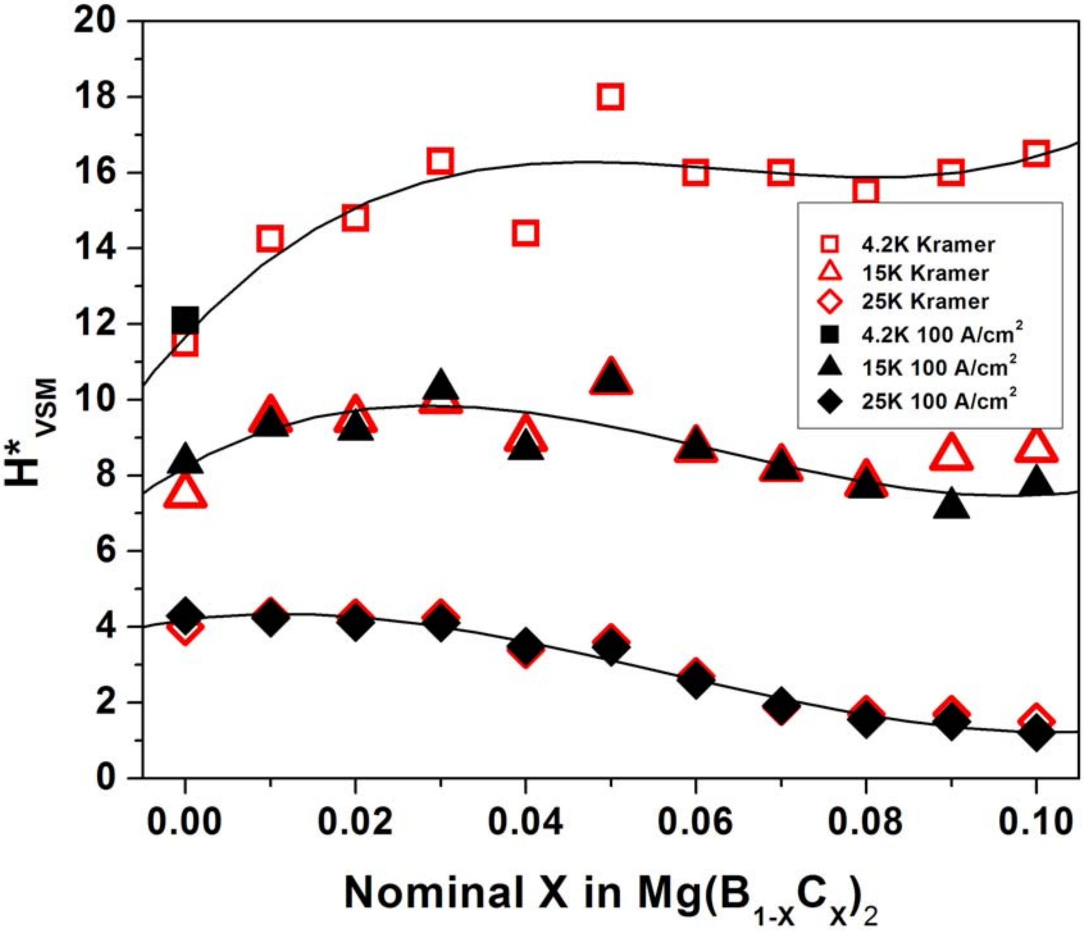

Figure 5.7 – Irreversibility field from magnetic hysteresis loops. Criterion was J_c =100 A/cm^2 (solid symbols) or Kramer extrapolation (hollow symbols).

Since hysteretic M-H loops are dominated by current loops through the whole sample, J_c is limited by the properties of the least favorably oriented (H $\perp$ ab-plane) crystals, and therefore this measurement yields H*($\perp$). Two competing J_c trends were observed. Low X samples had good low-field J_c but low H* and thus poor high field J_c. High X (over-doped) samples had poor low field J_c but higher H*. A peak in J_c(8 T, 4.2 K) was therefore observed near the middle of the sample set.

Table 5.I – Resistive property data. RRR is ρ(300 K / ρ(40 K)

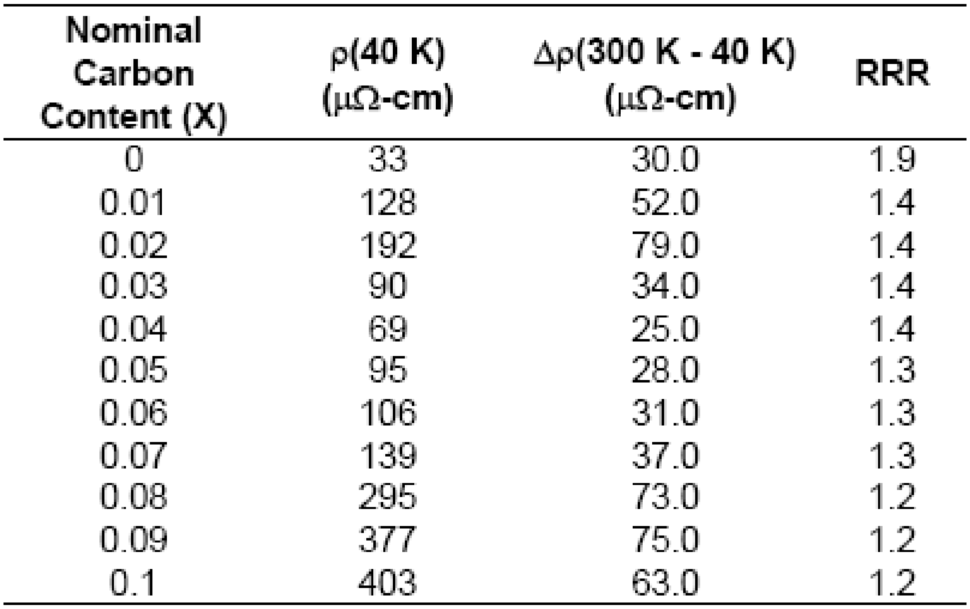

Nominal Carbon Content (X)	ρ(40 K) (μΩ-cm)	Δρ(300 K - 40 K) (μΩ-cm)	RRR
0	33	30.0	1.9
0.01	128	52.0	1.4
0.02	192	79.0	1.4
0.03	90	34.0	1.4
0.04	69	25.0	1.4
0.05	95	28.0	1.3
0.06	106	31.0	1.3
0.07	139	37.0	1.3
0.08	295	73.0	1.2
0.09	377	75.0	1.2
0.1	403	63.0	1.2

Table 5.I shows measured resistivity values and residual resistivity ratio (RRR = ρ(300 K) / ρ(T_c)). The measured ρ(40K) values ranged from 33 μΩ-cm for the undoped sample to 403 μΩ-cm for X = 0.1 and varied widely from sample to sample. These values are all too high to be consistent with full connectivity, as we discuss later.

The ρ(H,T) measurements were used to determine $H_{c2}(T)$, as defined at 90% of the normal state resistivity during fixed T measurements where H was swept at a rate of 0.6 T/min. These data therefore represent the most favorably oriented crystals, which yield H_{c2}(H // ab-plane). All measurements above 15 T were performed at the NHMFL in the 33 T Bitter magnet. Figure 8 shows H_{c2} as a function of temperature and composition.

At high T, little or no H_{c2} benefit was achieved from carbon addition, as the T_c reduction associated with doping was more significant near T_c than the observed dH_{c2}/dT increase. Around 24 K, H_{c2} of the carbon doped samples surpassed that of the nominally undoped sample. At 4.2K, H_{c2} peaked around $X \sim 0.05$, as also seen in single crystals.[Lee02,Masui01] When measured carbon content is taken into account, our H_{c2} values were slightly higher than, but not qualitatively different from, the established single crystal values shown in Ch. 2.

Both optical and scanning electron microscopy showed inhomogeneous sample density. An inhomogeneous “island-in-matrix” morphology was observed in all but the X = 0 sample. Figure 5.9 presents secondary electron images of the X = 0.1 sample. The “matrix” appears bright due to the large concentration of edges resulting from the porosity (inset a). The “islands” appear dark due to the absence of porosity (inset b). The contrast between the islands and matrix generally increased with increasing X. At low X, differences between the regions could only be distinguished in fractured or roughly polished sections, while at high X the island - matrix morphology was apparent even in highly polished sections.

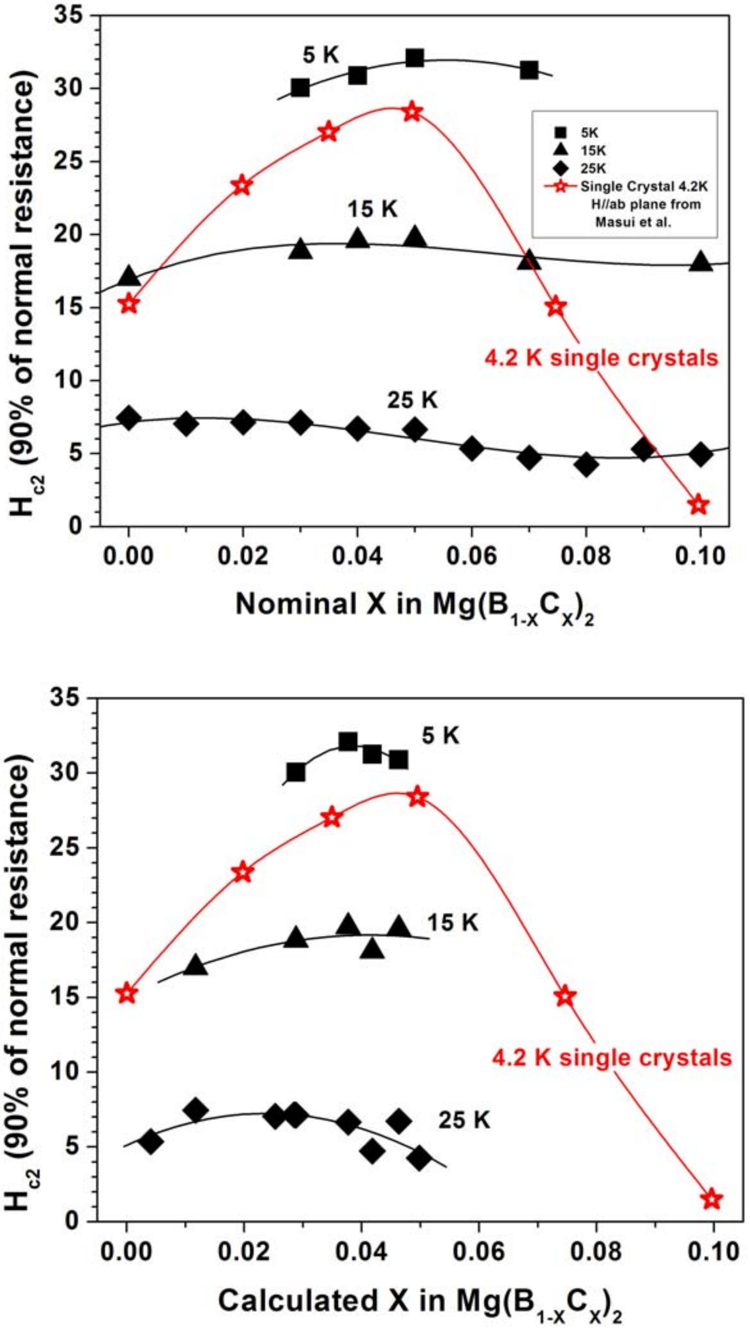

\

Figure 5.8 – $H_{c2}^{//ab}$ at 5 K, 15 K, and 25 K as a function of a) nominal X and b) X calculated from x-ray diffraction results. Open stars represent 5 K data from Masui et al.[Masui01] representing single crystals with H//ab plane. Lines are a guide to the eye. X error bars are omitted from (b) for clarity, but are the same as those in Fig 5.3b.

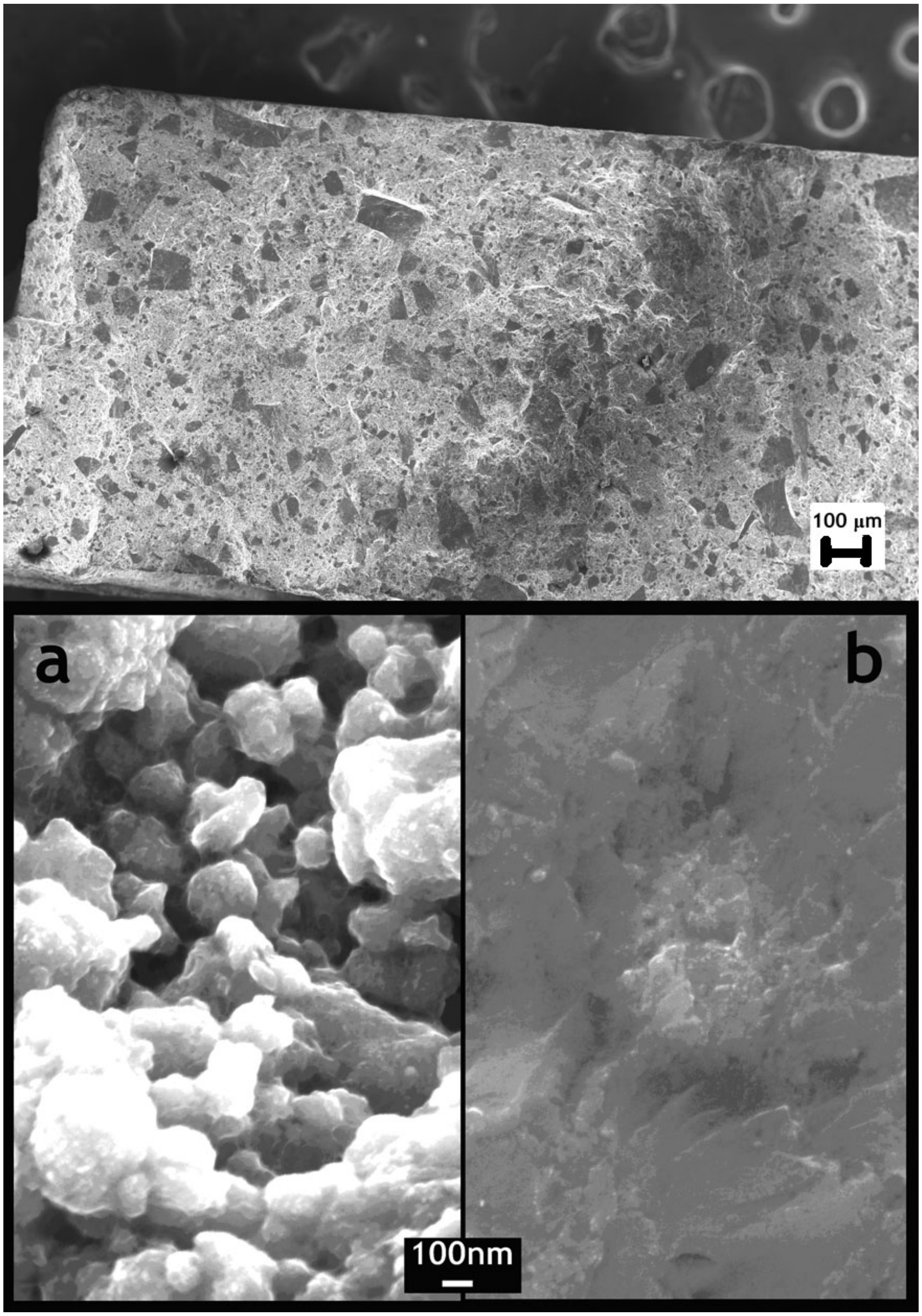

Figure 5.9 – Secondary electron micrographs of the X = 0.1 sample fracture surface. a) Representative porous matrix. The brightness is due to the high density of edges within the microstructure. b) Representative dense island.

We used magneto-optical (MO) imaging[Polyanskii01,Polyanskii02] (All MO by A. Polyanskii) to determine the effect of this physically inhomogeneous morphology on local J_c for two samples with compositions X = 0.1 and X = 0.04. Figure 5.10a-c shows images of a polished ~110 μm thick section of the X = 0.1 sample, first by conventional light microscopy and then by magneto-optical (MO) imaging in the superconducting state. Fig. 5.10a shows bright, highly reflective "islands" ranging in size from a few microns to more than 100 μm embedded in the less lustrous, more porous matrix. The MO images of this same section (Fig. 5.10b) show that polishing to thin sections did produce some large cracks, but more significantly that many of the bright islands in Fig. 5.10a correlate directly to important features in the MO image, as particularly noted by the three islands marked by arrows. Fig 5.10b shows the sample after zero-field cooling to 10 K and then after applying 80 mT, which is not high enough to penetrate the whole sample. The small dark spots visible in that image correspond to dense islands. The dark MO contrast of the islands indicates that they preferentially exclude flux compared to the matrix around them. The higher field (120 mT) inset MO image (Fig 5.10c) shows field penetrating the whole sample. The flux gradient was measured along line C-D and found to be at least 3 times steeper in the island compared to the matrix. Other islands (including those marked by the arrows) had 2-6 times larger gradients than that of the matrix, indicating a proportional variation of J_c.

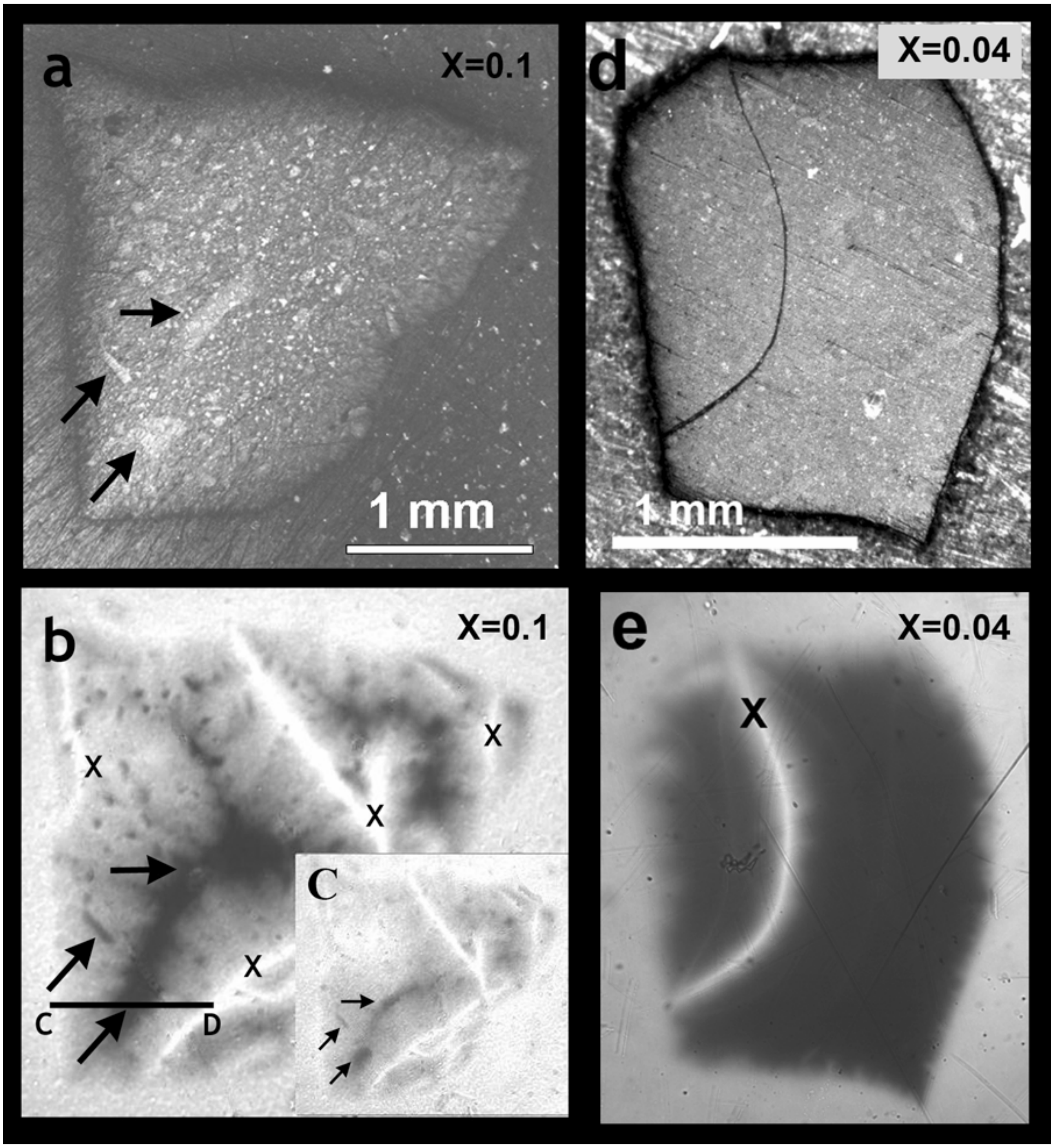

Figure 5.10 – a) Optical image of a polished thin section with nominal X = 0.1. b) and c) Magneto – optical (MO) images of the same sample. b) Zero-field cooled (ZFC) to 10 K , then 80 mT was applied. c) ZFC to 10 K before 120 mT was applied. d) Optical image of polished thin section with nominal X = 0.04. e) MO image of the same sample, ZFC to 10 K then 120 mT applied. Cracks are marked with "X"

In contrast to the X=0.1 sample, MO imaging of the X = 0.04 sample (Fig. 5.10d-e) did not show any such local J_c variation. It appeared to be a well-connected, homogeneous sample, as shown in Figure 5.10e. Flux penetration gradients were much steeper for the X = 0.04 sample than for the X = 0.1 sample, in accordance with the observation of higher whole-sample J_c.

5.3 - Discussion

These samples had excellent J_c(H), particularly at high fields (between 5 and 10 T) and low temperatures, when compared to other samples from the literature.[Dou01,Matsumoto02,Sumption01] Resistivity analysis (described later) indicates that at best only about half of the sample cross section contributes to current transport. Therefore J_c values within the connected region are even higher than whole sample values. At high carbon concentrations, J_c declined, and MO imaging provided direct evidence that the decline in J_c was due to breakdown of connectivity. The rest of the paper will be devoted to explaining these observations.

The relationship between a-axis lattice parameter and X has been established in single crystals.[Lee02,Kazakov01] Accordingly, we used data from Kazakov et al.[Kazakov01] to calculate the carbon content of the lattice. The data up to nominal X = 0.04 indicate that essentially all of the added graphite was incorporated into the lattice. At nominal X > 0.05 the error bar in the lattice parameter measurement became too large to draw true conclusions, but at X > 0.08, T_c became fairly insensitive to nominal X – probably indicating a limit to carbon incorporation into the lattice. Therefore, we conclude that our samples heat treated at 1000°C at $X > 0.8$, and possibly at $X > 0.05$, contain excess carbon that was not incorporated into the MgB_2 crystal lattice. We note that a recent comparison of electron energy loss and x-ray diffraction determination of C incorporation into SiC-doped bulk MgB_2 gave $X = 0.014$ for reactions at 600°C and $X= 0.022$ for reactions at 900°C.[Zhu02]

H_{c2} was not observed to be a strong function of normal state resistivity, despite measured resistivity values which if fully connected would place these samples in the dirty-limit regime. This paradox has been observed before in MgB_2 and was explained[Rowell01,Rowell02] to be a result of the resistivity being influenced by incomplete connectivity. The Rowell analysis can be adapted to provide insight into the connectivity of these samples.[Jiang01,Senkowicz03]

The Rowell analysis assumes that the true value of $\Delta\rho = \rho(300K) - \rho(\text{just above } T_c)$ is independent of sample processing, and that an ideal value that we call $\Delta\rho_{ideal}$ can be obtained from fully-connected reference samples. Measured $\Delta\rho > \Delta\rho_{ideal}$ therefore indicates that only a fraction of the cross sectional area (which we call $A_F = \Delta\rho_{ideal} / \Delta\rho$) is electrically connected. Using A_F as a scaling factor, the normal state resistivity of the connected portion of the sample (that we call ρ_A) can be obtained.

Since the Rowell analysis was originally intended only for undoped MgB_2 it requires adaptation to the carbon doped case. Instead of using a constant $\Delta\rho_{ideal} = 7.3\ \mu\Omega$-cm as in Ch. 4, $\Delta\rho_{ideal}$ was taken to be a function of carbon concentration. “Trusted” samples with near-perfect connectivity are required to obtain $\Delta\rho_{ideal}$. The most appropriate samples appear to be the filaments of Wilke et al.[Wilke03] because they have randomly oriented grains and are non-porous with well defined, homogeneous composition. Despite some scatter in their data we applied the linear fit $\Delta\rho_{ideal} = 109.59\ X + 8.8794$ (μΩ-cm) to our samples. We note that Masui et al.[Masui01] measured a-b plane resistivity on C-doped single crystals and found $\Delta\rho_{a\text{-}b}$ varied unpredictably with C-content, so this adaptation of the Rowell analysis should only be taken as semi-quantitative.

The adapted Rowell analysis results (shown in figure 11) indicate that A_F varied substantially, but was never much more than 0.5. Therefore, local J_c values within the connected portion of the sample may greatly exceed the whole-sample values given above. The TEM images indicated the primary impediments to connectivity were nano-porosity and amorphous regions, rather than insulating oxide phases observed elsewhere.[Jiang01] Variation in A_F at low X may be related to microstructural inhomogeneity (such as island / matrix morphology) and is probably not related to intrinsic properties of the grains.

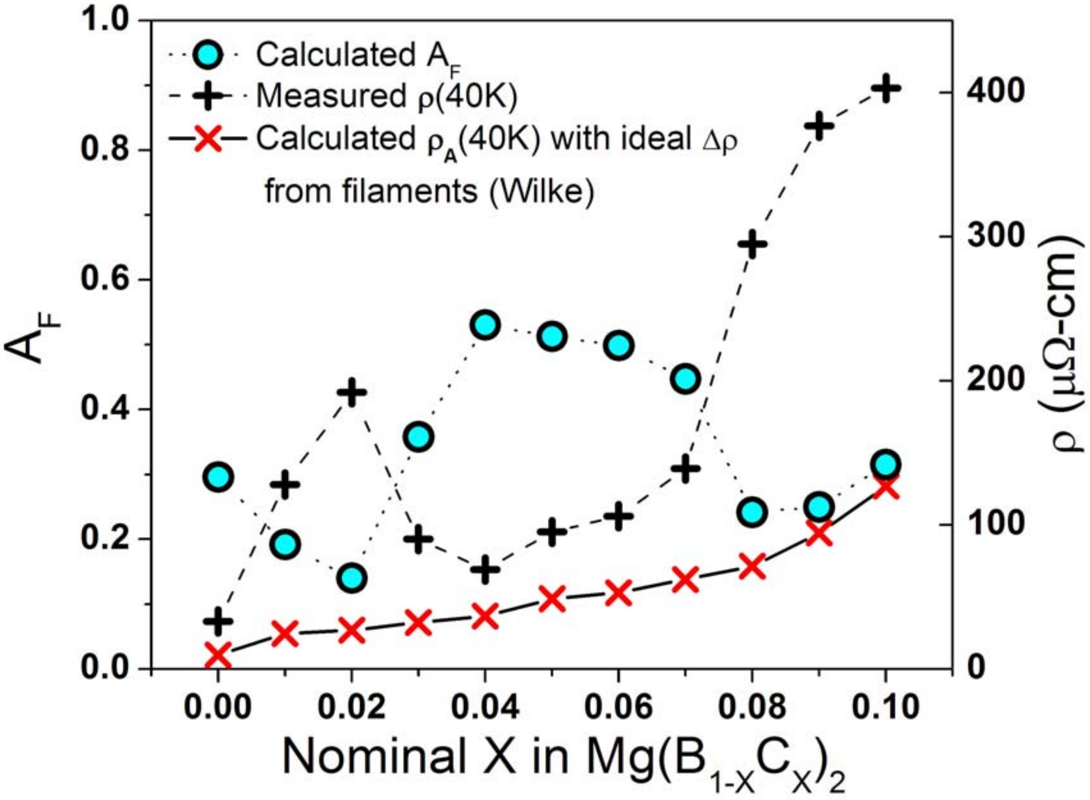

Figure 5.11 – Measured ρ(40 K), calculated ρ_A(40 K) and calculated A_F as a function of nominal composition using Δρ data taken from dense, low-resistivity, carbon doped filaments.[Wilke03,Wilke04]

Although ρ_A(40 K) was a smooth function of nominal X, its magnitude was much higher than normal state resistivity values from C-doped filaments and single crystals. This could indicate non-carbon-doping electron scattering exists in these samples. Alternately it may also indicate systematic errors in the magnitude of A_F deduced from this modified Rowell analysis.

The high ρ_A(40 K) values are not the only indicator of non-C-doping scattering. We also observed lower T_c values than single crystals (or CVD produced filaments). Increased normal state resistivity and decreased T_c have been observed by Lorenz et al.[Lorentz01] and attributed to very fine grain size. One conclusion of the depressed T_c is that fine scale scattering on scales less than the pure MgB_2 mean free path (~60 nm)[Canfield02] produces a small degree of interband scattering.

TEM and scanning electron microscopy (SEM) showed a typical grain size of ~50 nm or less. We suggest that the high grain boundary density is responsible for both the excess electron scattering lowering T_c as well as the large flux pinning force enabling high J_c. The high J_c(8 T, 4.2 K) values reported here are thus a result of the combined effects of carbon doping and grain refinement as a result of the milling process.

At high X, T_c transition broadening, resistivity data and resistivity results discussed above lead to the conclusion that as X exceeds 0.05 – 0.07, J_c degraded by the breakdown of connectivity. Magneto-optical imaging on the X = 0.1 sample provided direct evidence that J_c was disrupted by connectivity breakdown, and that the breakdown was inhomogeneous on a macroscopic scale.

Magneto-optical imaging allowed us to estimate local J_c in the X = 0.1 sample from the flux gradients observed along line C-D in Fig. 5.10 from which we calculated the local J_c of the matrix and an island.[Polyanskii02] Fig. 5.12 compares J_c(T) of the matrix as estimated from the MO images with the data calculated from the vibrating sample magnetometer (VSM) measurements. Their close agreement indicates that the VSM - derived J_c values are determined by the whole-sample matrix currents, where the islands did not contribute significantly to overall J_c because they are disconnected from each other. We found J_c of the islands to be 2 to 6 times higher than that of the matrix.

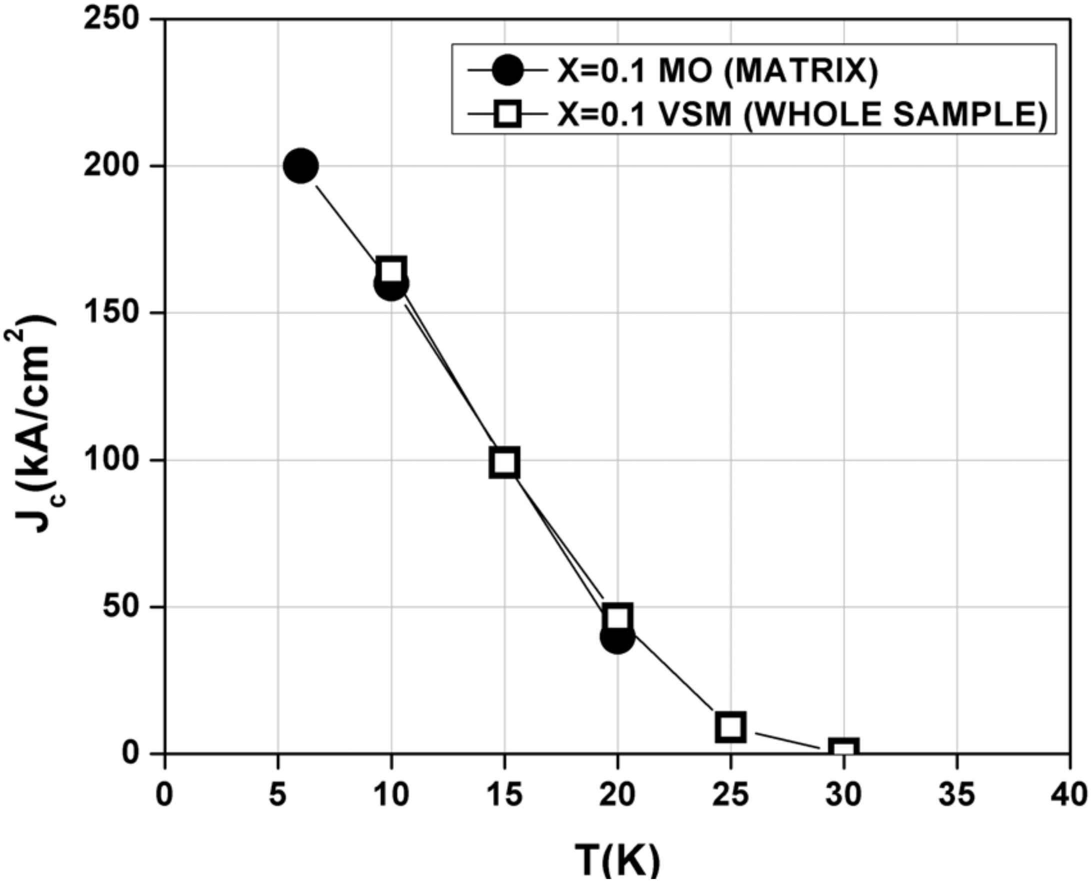

Figure 5.12 – J_c as a function of temperature for X = 0.1 at low field as measured by vibrating sample magnetometer (open squares) and as reconstructed from flux penetration gradients across the *matrix area* along line C-D in Fig. 5.10 measured by magneto-optical imaging with H < 200 mT.

The X = 0.04 sample was at or near the peak J_c in the set, and for that sample MO imaging showed no J_c variation between the islands and the matrix. The whole X = 0.04 sample had similar J_c to the islands in the sample with X = 0.1. Although the dense, well connected island regions retain their high J_c despite failure to fully incorporate the C, the high J_c regions become isolated from each other so that whole sample J_c is gated by the poorer properties of the matrix region.

Magneto-optical imaging linked J_c degradation at high X with connectivity degradation in agreement with the decreasing A_F values presented in figure 5.11. However low A_F values were obtained in the absence of J_c degradation at X~0.02. The reason for the low A_F values around X~0.02 are not fully understood but may be evidence of some shortcoming in our adaptation of the Rowell analysis.

5.4 – Conclusions

High energy ball milling enabled C-doping of pre-reacted MgB_2 powder while simultaneously refining grains by cold work. The high grain boundary density resulted in enhanced J_c and increased electron scattering. The combined effects of grain refinement and carbon doping resulted in J_c(8 T, 4.2 K) values among the best reported for bulk MgB_2. However an adapted Rowell analysis on resistivity data indicated that even in the best samples, only ~1/2 of the cross section actively carries current. Therefore the local J_c of the connected region is much higher than whole-sample J_c, indicating high potential for further J_c improvement. At high carbon concentrations ($X > 0.07$) J_c breakdown occurs due to connectivity breakdown, leaving well-connected "islands" in a poorly connected "matrix" suggesting that excess carbon presents a barrier to sintering.

This work accomplished its goal – finding optimal X for J_c(8 T, 4.2 K). This was X~0.04, where H* was high enough for good high-field performance, but connectivity was not significantly degraded by unreacted C. This composition was adopted for all further C-doping work in this thesis.

Chapter 6 – Effects of milling time C-doped MgB_2

In Chapter 5 we studied variable carbon addition to pre-reacted MgB_2 by high energy milling for 10 hours. Carbon successfully entered the MgB_2 lattice and enhanced H_{c2}, H*, and J_c(H). With our 1000°C heat treatment, the maximum carbon incorporation was X ~ 0.06. At higher nominal C-content, not all of the available carbon was incorporated into the lattice. As a result, at X>0.07, reduced connectivity resulted in decreased whole-sample J_c. We found J_c(8 T, 4.2 K) peaked around nominal X=0.04 or X=0.05. We also found that our high J_c was partly due to non-compositional factors associated with milling – the most relevant being the small (~50 nm) grain size that produces strong flux pinning. The motivation for the experiment in this chapter was to 1) determine the milling time required for C-incorporation and 2) further optimize J_c(H) by investigating such non-compositional effects of high energy milling on sintered sample properties as a function of milling time.

In this experiment, pre-reacted magnesium diboride powder was mechanically alloyed with C by high-energy ball milling to a fixed nominal composition of $Mg(B_{0.96}C_{0.04})_2$ and then sintered at 1000°C in a hot isostatic press. Milling times varied from 1 to 3000 min.

Lattice parameter measurements indicated full alloying resulted from milling times (t_{mill}) < 60 min, but properties continued to evolve for non-compositional reasons. As milling time increased, grain size of the sintered samples decreased. Long milling times (600 min or more) resulted in 20-30 nm grains after heat treatment, which were probably prevented from growing further during heat treatment by a fine dispersion of second phases. Grain refinement resulted in increased H*, which boosted mid to high-field J_c. J_c(8 T, 4.2 K) peaked at ~ 850 A/mm^2 for 1200 min of milling, and then declined probably due to loss of connectivity.

This work shows substantial J_c(8 T, 4.2 K) improvement from high energy milling on a time scale far exceeding the ~1 hr necessary for C-incorporation. This improvement was due mostly to increased H*. There was no clear effect of milling on low-field J_c. The effect of grain refinement by milling on H*(4.2 K) was nearly as large as that of C-doping. Full C-alloying (60 min milling) resulted in H*(4.2 K) ~ 13.5 T, but additional milling of the alloyed powder raised H*(4.2 K) to 17.2 T. As a result, J_c(8 T, 4.2 K) more than doubled for t_{mill}=1200 min compared to less heavily milled samples with similar C-content and connectivity.

6.1- Experimental Procedure

We used high energy ball milling in a SPEX 8000M mill with WC jar and media to mix pre-reacted MgB_2 from Alfa-Aesar with powdered graphite and a stoichiometric amount of Mg to make the nominal bulk composition $Mg(B_{0.96}C_{0.04})_2$. We produced samples from powders milled 1, 15, 60, 300, 600, 1200, and 3000 min.

After milling, powders were pressed into pellets, sealed in evacuated stainless steel tubes, and hot isostatic pressed (HIP) at a maximum T and P of 1000^{o}C / ~30kpsi / 200 min. All pre-heat treatment work was carried out in a nitrogen-filled glove box equipped with active oxygen and water scavenging. After heat treatment, hard > 1000

H_V and ~90% dense samples were sectioned with a diamond saw and their properties measured.

6.2 - Results

X-Ray diffraction (Fig 6.1) after heat treatment shows untextured MgB_2. As milling time increased, the MgB_2 peaks became weaker and broader. Small amounts of MgO were identified in the samples milled for short times. In samples milled for longer times WC, WB, and MgB_2C_2 were present. The WC signature increased in prominence with increased milling time. High resolution XRD was carried to determine precise peak positions and widths. The Nelson-Riley method [Cullity01] was applied to the peak positions to calculate a-axis lattice parameter values (Figure 6.2a) that were then used in conjunction with the single crystal data in Chapter 2 to estimate the actual (rather than nominal) C-content of the lattice, as described in the discussion section. For $t_{mill} \geq 60$ min, a-axis lattice parameter was nearly constant which tends to suggest that C is not being introduced by breakdown of the greater amount of WC at this $T_{HIP} = 1000^oC$. Table 6.I gives FWHM values for the (100) and (002) reflections, and calculated lattice parameters from the high-resolution patterns (not those shown in Fig 6.1). Rapid a-parameter decrease with t_{mill} was observed for the first hour of milling, with a going from ~3.076 Å to ~3.0695 Å. Further milling did not significantly affect a. Peak broadening mostly occurred within the first 300 – 600 minutes of milling, with peak breadth increasing from ~0.25^o to ~0.4^o in 2θ.

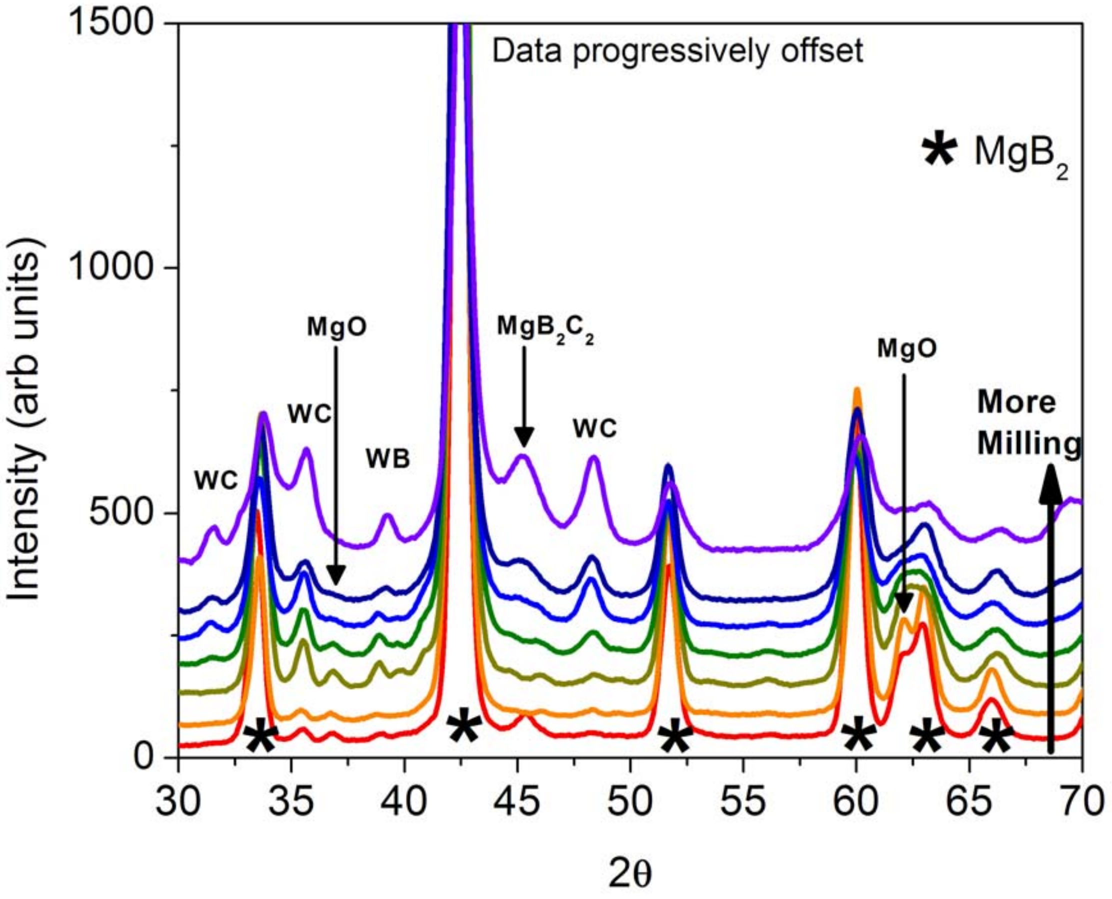

Figure 6.1 – X-ray diffraction patterns (from the Hi-Star 2D area detector) for each sample, progressively offset with low t_{mill} at bottom.

Table 6.I – High resolution x-ray diffraction results from sintered samples.

Milling Time (min)	a-parameter (A)	Estimated Uncertainty (+-) (A)	FWHM (100) (Degrees 2θ)	FWHM (002) (Degrees 2θ)
1	3.0758	0.0040	0.25	0.26
15	3.0746	0.0031	0.27	0.31
60	3.0695	0.0036	0.31	0.33
300	3.0698	0.0061	0.38	0.44
600	3.0683	0.0032	0.45	0.52
1200	3.0685	0.0060	0.37	0.42
3000	3.0685	0.0112	0.48	0.52

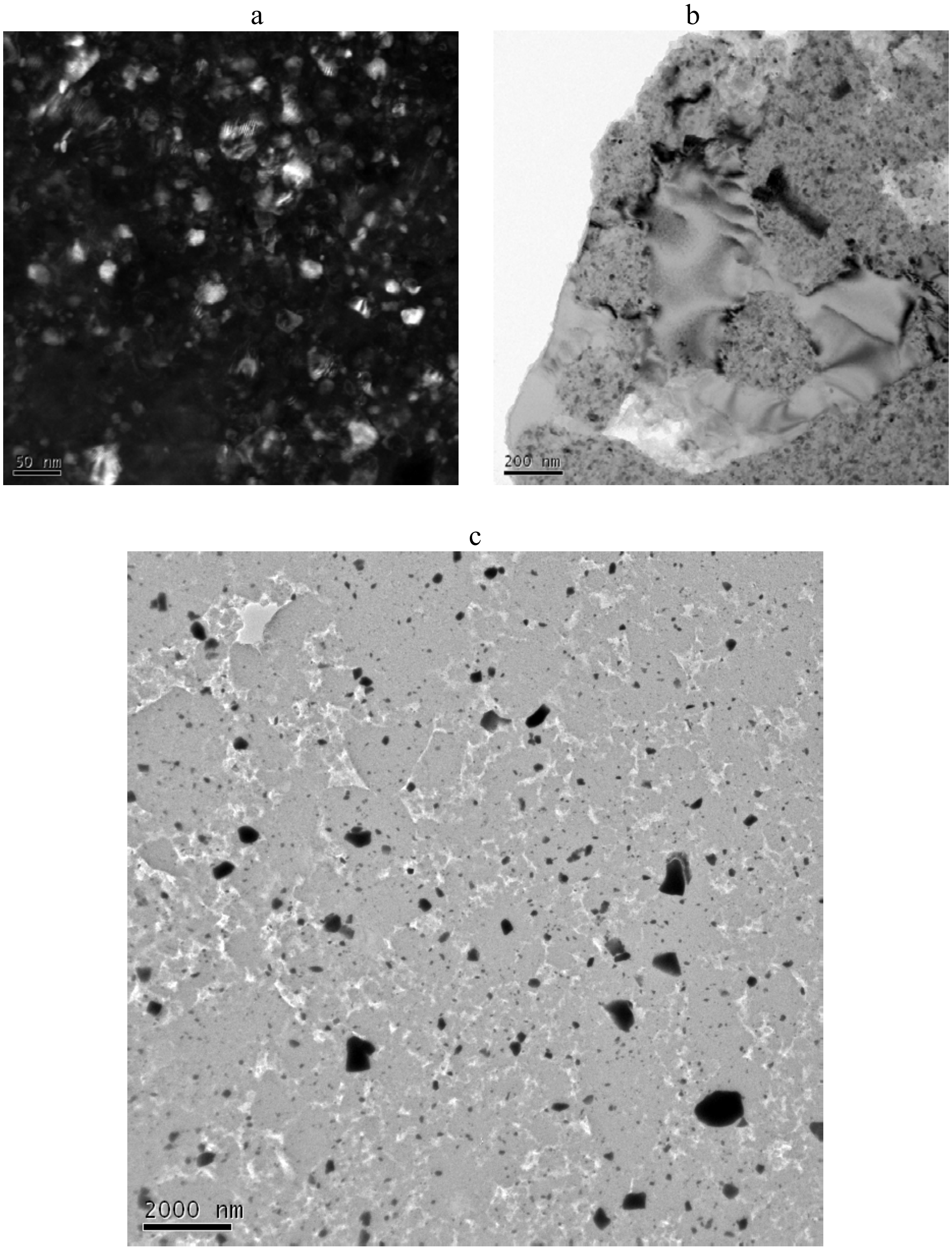

Figure 6.2 – (a) dark-field and (b,c) bright-field TEM images by Ye Zhu showing grain related diffraction contrast in sintered samples made from powder milled for a) 1200 min and b and c) 3000 min. Scale bar size is (a) 50 nm (b) 200 nm and (c) 2000 nm. Average grain size for 1200 min sample <30 nm. Typical grain size for 3000 min sample may be smaller, but large grains also exist. Dark areas in (c) are WC and constitute 6.1% by area. Bright regions in (c) occupy 14% by area and are a combination of porosity, amorphous / very fine grained regions, and second phases.

Transmission electron microscopy (Fig 6.2) was done by Ye Zhu on the 1200 and 3000 min samples. It revealed an average grain size about 20 to 30 nm in the 1200 min sample. The 3000 min sample appeared to have even smaller grains, but a number of much larger (0.5 – 1 μm), comparatively strain-free grains were also observed. Larger amounts of WC rubble were observed in the 3000 min sample (6.1 vol%, Fig 6.4c) than the 1200 min sample. Trace amounts of cobalt from the milling media were detected in regions of both samples with fine grains but no Co was found within single large grains by energy dispersive spectroscopy (EDS).

Numerous potential obstacles to current flow were observed in the 3000 min sample, (Figure 6.2c) including WC (dark regions) and porosity, amorphous regions, and perhaps other second phases (bright regions) but pervasive grain boundary oxides were not observed.

Zero-field-cooled warming T_c traces (5 mT field) showed decreased T_c with increased milling time, but the relationship was not simple, as shown in figure *6.3*. A rapid T_c decrease from 37.1 to 32.6 K was observed up through the 300 min sample but then T_c decreased only from 33 K to 31 K between the 300 min sample and the 1200 min sample. The 3000 min sample exhibited a double transition (Fig 6.3b). The upper transition had onset T_c ~31 K, and consisted of about 1.5% of the whole sample signal. The lower transition had onset T_c ~ 25 K and represented about 98.5% of the whole sample signal.

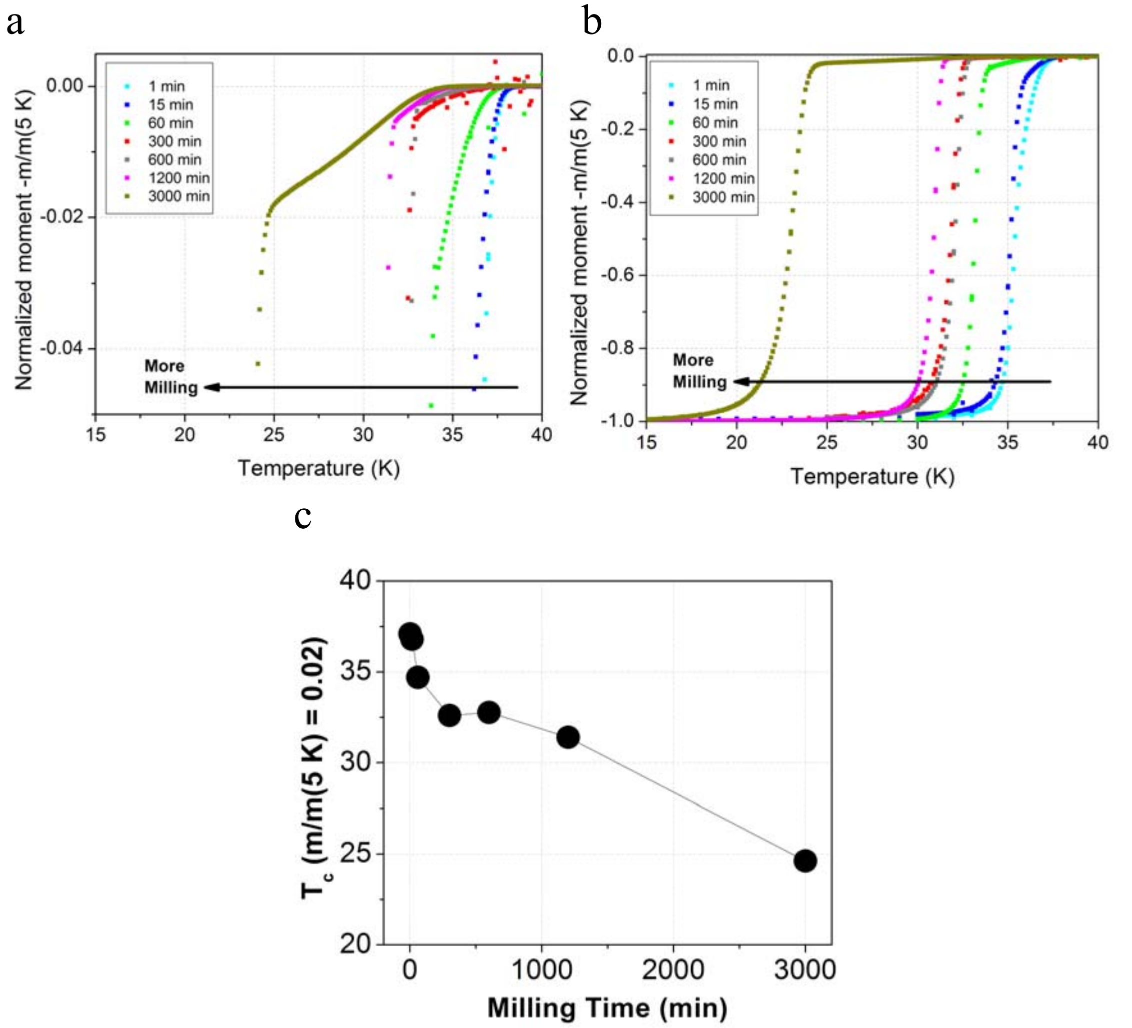

Figure 6.3 – a) and b) T_c traces at 50 Oe applied field. C) T_c at 2% below onset (98% normal) as a function of milling time.

All samples exhibited metallic-type resistivity behavior. Resistive properties are shown in Table 6.II along with SQUID-derived T_c. Measured ρ(40 K) and ρ(300 K) both increased with longer increasing milling time from ρ(40 K) = 14 μΩ-cm for t_{mill} = 1 min to ρ(40 K) = 281 μΩ-cm for t_{mill} = 3000 min. RRR decreased as milling time increased from 2.36 to 1.15 over the same range. Δρ=ρ(300 K) – ρ(40 K) increased with longer milling time, but only by a factor of ~2 over the entire sample set. For low t_{mill} samples (say 15 min) the values of $\rho(40\ K) = 16\ \mu\Omega\text{-cm}$, RRR = 2.13, and $T_c = 36.8$ K are quite reasonable for C-doped bulks. However, the trends toward increasing ρ and decreasing T_c continue through the sample set – long after lattice parameter ceases to change. We will show that as long as $\Delta\rho$ remained fairly constant (up to $t_{mill} = 1200$ min) the resistivity trends correlated with *increased* J_c(8 T, 4.2 K).

Table 6.II – Resistive properties and T_c as a function of milling time.

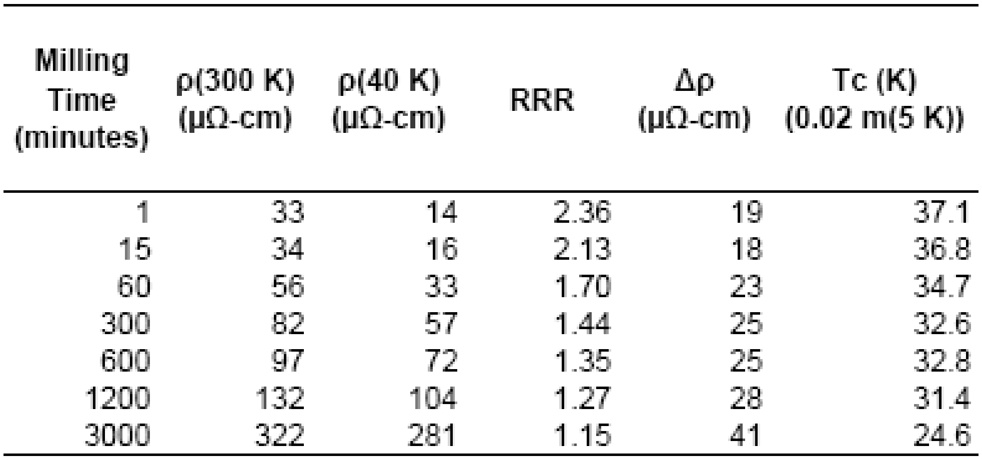

Milling Time (minutes)	ρ(300 K) (μΩ-cm)	ρ(40 K) (μΩ-cm)	RRR	Δρ (μΩ-cm)	Tc (K) (0.02 m(5 K))
1	33	14	2.36	19	37.1
15	34	16	2.13	18	36.8
60	56	33	1.70	23	34.7
300	82	57	1.44	25	32.6
600	97	72	1.35	25	32.8
1200	132	104	1.27	28	31.4
3000	322	281	1.15	41	24.6

H_{c2} was extracted from swept field (0.6 T/min) 4-point resistive transitions using a measurement current of 5 mA. H_{c2} was taken at 90% of $\rho(40\ K)$, and appears in Figure 6.4. Progressive T_c suppression by milling (see Table 6.II) is evident. In all but the 3000 min sample T_c suppression is associated with steeper $H_{c2}(T)$ curves, so that at 24 K, $H_{c2}(H//ab)$ was between about 7.5 and 8.5 T and extrapolated $H_{c2}(0\ K)$ was about 30 – 35 T. The 3000 min sample had extrapolated $H_{c2} \sim 18$ T.

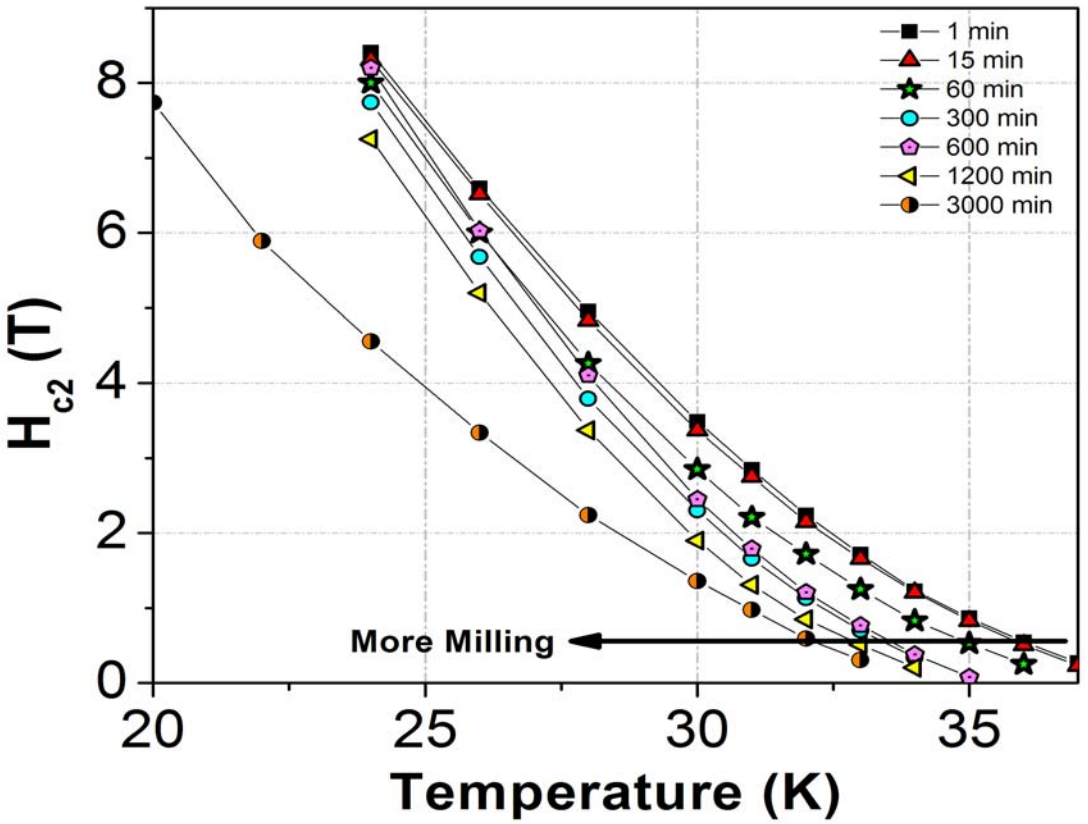

Figure 6.4 – H_{c2}(T) from resistivity curves.

M-H loops were measured in a vibrating sample magnetometer (VSM) and J_c calculated using the Bean model according to the expression

(6.1) $$M = \frac{3b - d}{12b} J_c d$$

Where M is the volumetric magnetization, and b and d are the sample dimensions perpendicular to the field direction, with $b > d$.[Evetts01,Bean01] J_c (15 K) and J_c(4.2 K) are shown in Figure 6.5.

The 15 K J_c(H) curves (Fig 6.5a) show that the sample milled 60 min had the highest low-field J_c, exptrapolating to ~1 MA/cm^2 at self field, while further improvement at longer milling times in medium to high field J_c is mostly due to reduced dependence of J_c on field produced by steadily increasing H*. Maximum (zero field) J_c(15K) of each sample (in order of ascending milling time) was: 392, 472, 548, 290, 335, 483, and 76 kA/cm^2. At 4.2 K, the 1200 min sample had only slightly higher low-field (3-4 T) J_c than the 60 min sample. Figure 6.6 plots H*(4.2 K) as a function of milling time using J_c = 100 A/cm^2 criterion where available or calculated by Kramer extrapolation[Evetts01] where J_c criterion was not available. H*(4.2 K) increased from 12 up to ~17 T after 600 min of milling. Further milling resulted in no further increase in H*(4.2 K).

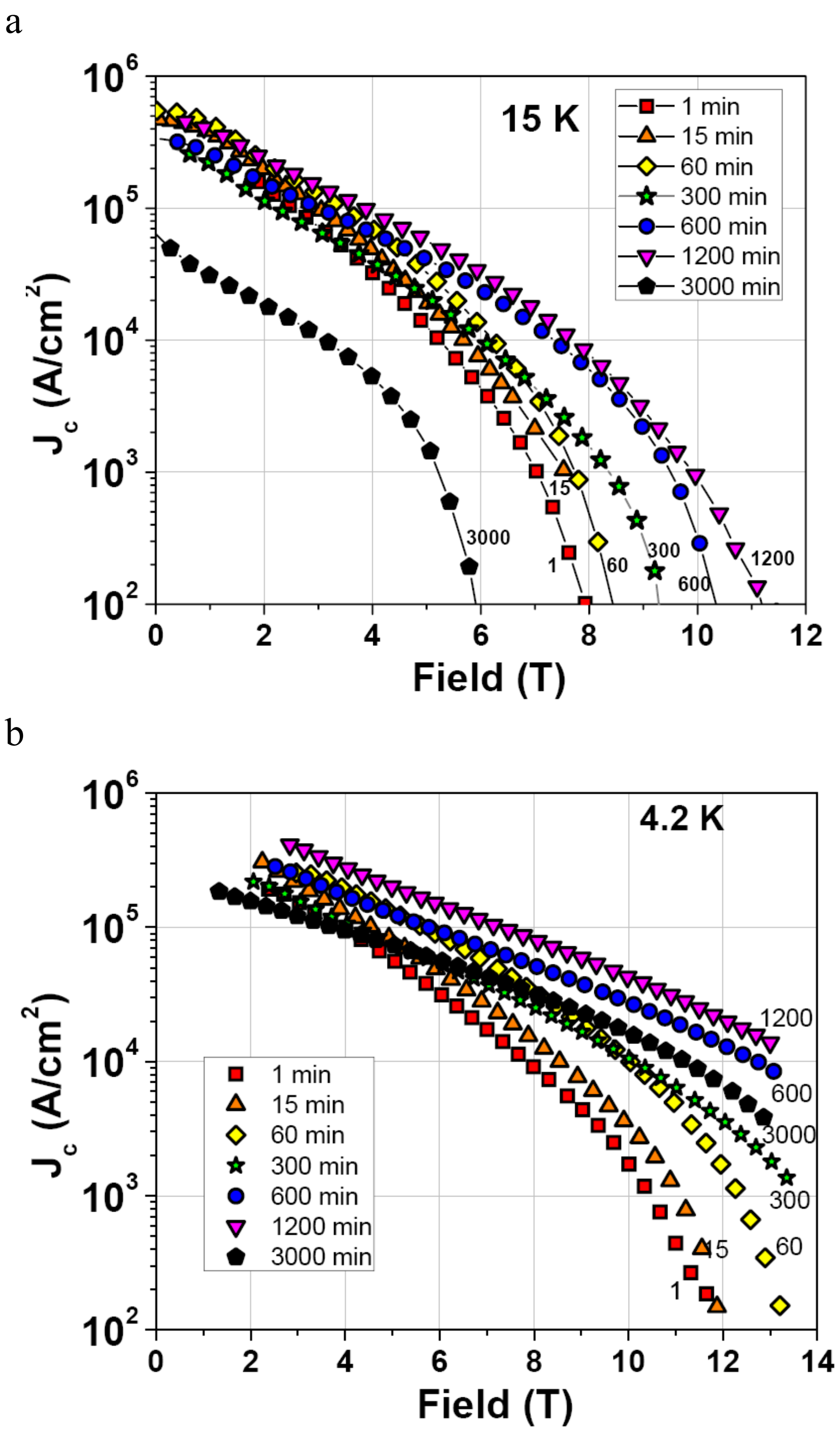

Figure 6.5 – J_c(H) at a) 15 K and b) 4.2 K.

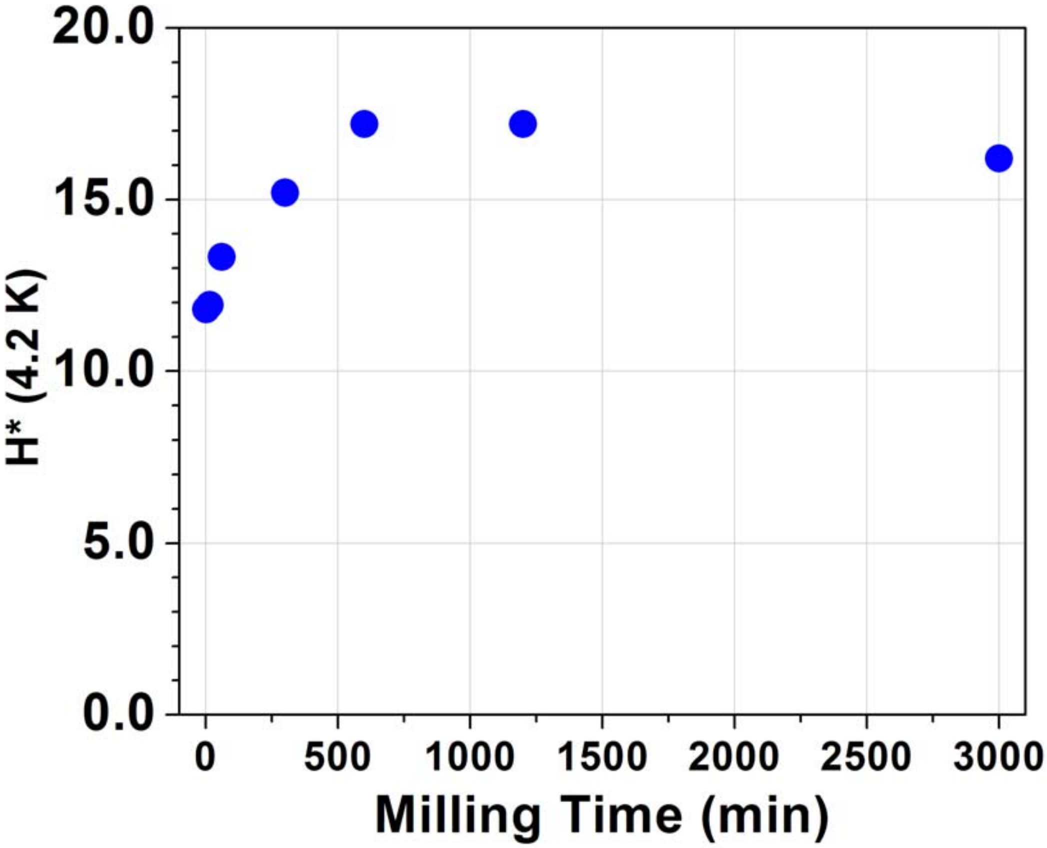

Figure 6.6 – H*(4.2 K) as a function of milling time using 100 A/cm^2 criterion (where available) or Kramer extrapolation.

Scanning electron micrographs (Fig 6.7) show the microstructural evolution as milling time increased. In the sample milled for 1 min, pebbly features ≤ 43 microns in size are remnants of the original 325 mesh powder particles. The 1 min sample was mostly composed of original powder particles welded together by smaller MgB_2 fragments. Carbon incorporation had not progressed to completion, as evidenced by pieces of elemental carbon (black in the figure), as well as bits of what are probably elemental Mg. As milling time increased, the quantity and size of the original powder particles visible by SEM decreased. After 60 min of milling, little or no evidence of intact original powder particles was seen (bright bits are now mostly WC). This was the most physically homogeneous sample in the set. Unmixed C and Mg were not detected. As milling increased to 300 min, we saw the emergence of the extremely dense, angular "islands" described in Ch. 5. It has been previously shown [Senkowicz02] that this morphology is the result of inhomogeneous sintering and whole sample J_c can be limited by the poorly sintered matrix.

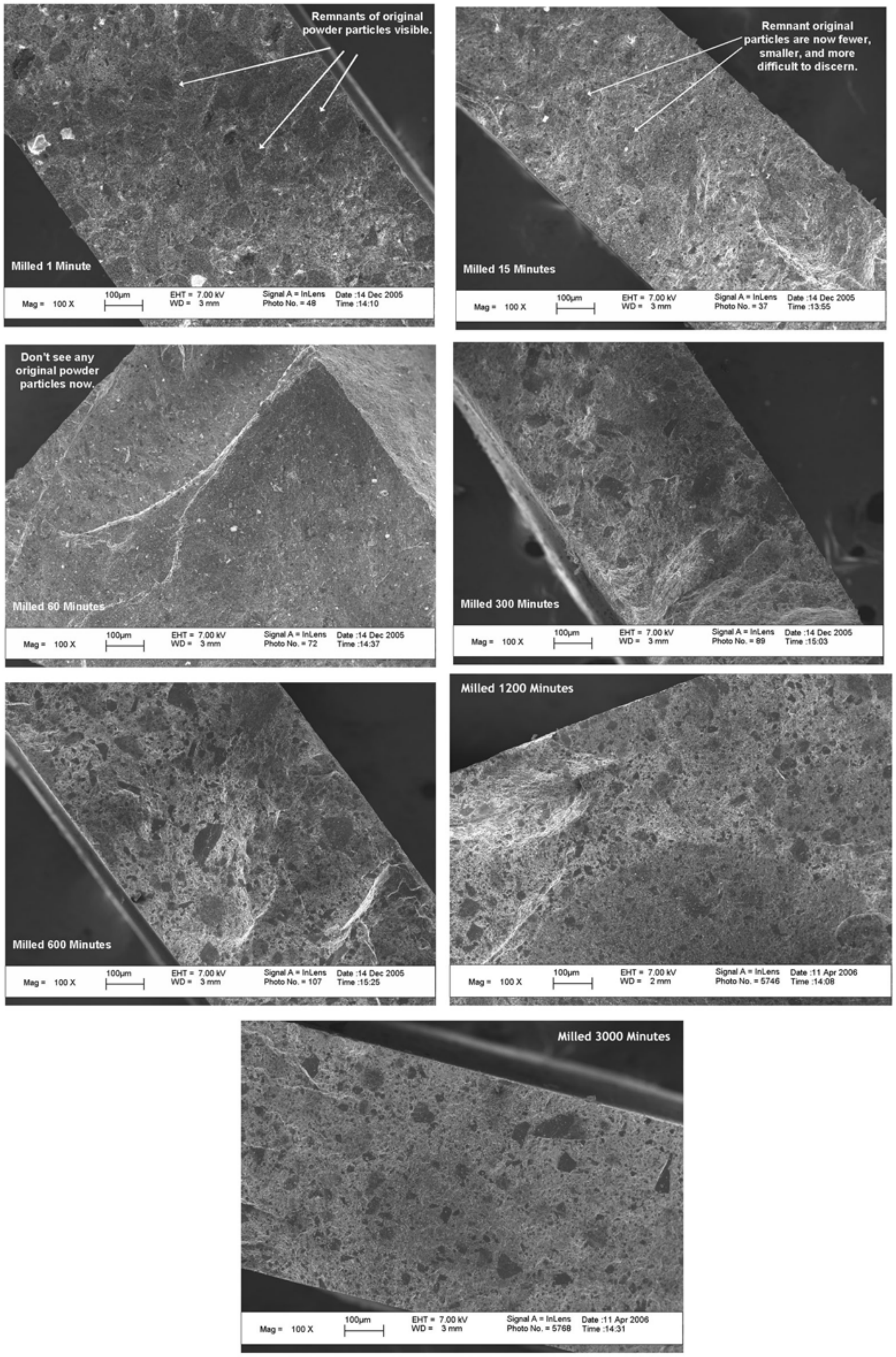

Figure 6.7 – Secondary electron micrographs showing heterogeneous microstructures of fracture surfaces for heat treated samples milled for times ranging form 1 min to 3000 min. Scale bar is 100 µm in all cases.

6.3 – Discussion

This study was motivated by the conclusion that the high H* and J_c(8 T, 4.2 K) values observed in our previous work was only partly a consequence of H_{c2} enhancement by C-doping, and partly a result of milling itself. Thus this experiment investigated the effects of variable milling time on properties of C-doped MgB_2. The motivation for the work was 1) to determine the duration of milling necessary to alloy the material with C, and 2) to investigate the nature of non-compositional J_c enhancement due to milling. In order to isolate the effect of progressive milling from the effect of C-doping, nominal composition was fixed at $Mg(B_{0.96}C_{0.04})_2$, with fixed heat treatment (T_{HIP}=1000°C, t_{HIP} = 200 min). A-axis lattice parameter was 3.068-3.069 Å for all t_{mill}=60 min and above. In this section, we show that corresponds to a nearly constant lattice C-content of X~0.05. Therefore, the continued improvement of H* and J_c with further milling had non-compositional causes. We find that low-field J_c did not change systematically with t_{mill}, but high-field J_c enhancement was strongly determined by H*. Finally, we estimate grain size from XRD peak breadth and correlate H* to inverse grain size, concluding that the ~50% H* enhancement is largely due to grain refinement resulting from milling.

Lattice carbon content (X) has been shown[Avdeev01,Lee02,Kazakov01] to produce a linearly varying a-axis lattice parameter. By comparison to single crystals[Kazakov01] we can estimate X for our heat treated samples. Those data are shown in Figure 6.8. Even 1 min of milling provided enough mixing to achieve a lattice parameter shift corresponding to X ~ 0.03, and after 60 min of milling, X ~ 0.05 was calculated. Longer milling times did not result in further lattice parameter shifts suggesting constant C-content of the lattice.

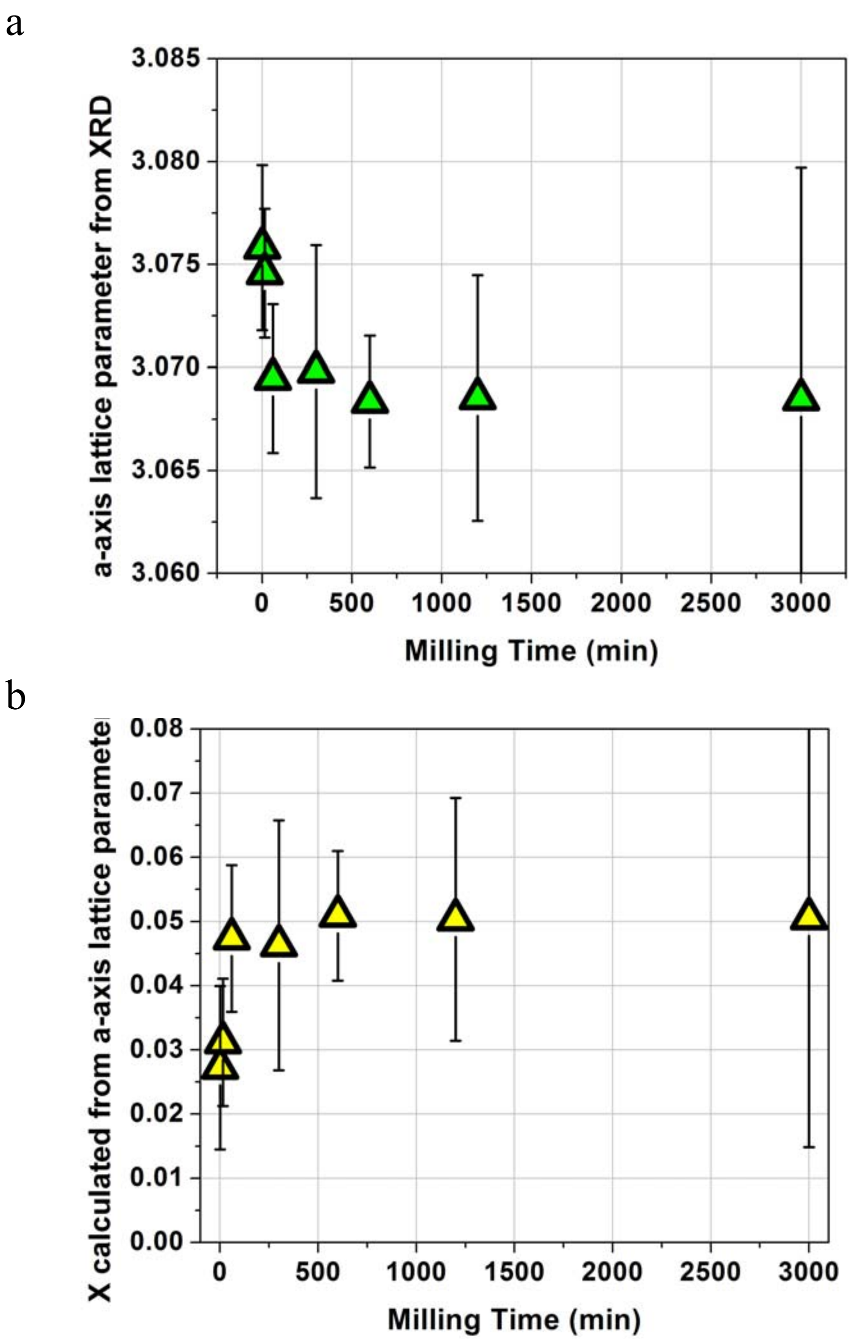

Figure 6.8 – a) a-axis lattice parameter (in Å) calculated from XRD peak positions and b) lattice C-content X in $Mg(B_{1-X}C_X)_2$ calculated from the data in 6.2a.

No published reports exist of W or Co detected within the MgB_2 lattice, nor did our TEM analysis detect W or Co within MgB_2 grains, so those species do not appear to have doped the MgB_2 lattice to any significant level. We conclude that changes in properties for samples milled 60 min and longer were therefore due to microstructural factors such as connectivity and grain size.

Connectivity can be assessed by the Rowell analysis if one assumes a universal $\Delta\rho_{ideal} = \rho(300)-\rho(residual)$ and then scales the measured resistivity curves assuming only the connected fraction of the cross sectional area (A_F) carries electrical current. $\Delta\rho_{ideal}$ as a function of carbon content can be taken from the well connected, randomly oriented polycrystalline CVD filaments of Wilke et al.[Wilke03], as discussed in Ch. 2 and Ch. 5. When we match our calculated lattice C-content to the CVD filaments, and apply that $\Delta\rho_{ideal}$ to the data in Table 6.II (using C-contents from Figure 6.8b), we obtain the data in Table 6.III.

Table 6.III – Modified Rowell analysis results.

Milling Time (minutes)	X From XRD	$\Delta\rho_{ideal}$ from CVD filaments (μΩ-cm)	A_F	ρ_A (40 K) (μΩ-cm)
1	0.027	11.86	0.62	9
15	0.031	12.29	0.68	11
60	0.047	14.07	0.61	20
300	0.046	13.95	0.56	32
600	0.051	14.46	0.58	42
1200	0.050	14.40	0.52	54
3000	0.050	14.41	0.35	99

Here we see that the A_F started at ~0.65 for short t_{mill}, then decreased slowly with increased t_{mill}, falling severely between t_{mill}=1200 min and 3000 min to only ~0.35. This probably accounts for the 3000 min sample having the worst low-field J_c of the set. However, in the region of non-compositional J_c(8 T, 4.2 K) increase (60 min ≤ t_{mill} ≤ 1200 min) A_F changed by only 0.09, and was not the main factor determining J_c, even at low field. In fact, zero-field J_c(15 K) bore no apparent relation to A_F, except that the 3000 min sample had both low A_F and low J_c. J_c(8 T, 4.2 K) also had no clear connection to A_F but was closely linked to H*(4.2 K).

The J_c(H,T) behavior of these samples was close to Kramer-like. $J_c \approx nb^{-1/2}(1-b)^2$, where n is a constant, $b = B / B^*$, and $B^*=\mu_o H^*$. Connectivity effects are assumed to be field-independent and therefore a part of n. As B approaches B*, J_c is heavily dependent on B*. For example, assume Sample A with B*=13.5 T and Sample B with B*=17.2 T. At 8 T, J_c(A) ~ 0.22n, and J_c(B) ~ 0.42n – almost twice as high. At 10 T, the difference would be a factor of about 3. Under those conditions, Sample A would have to have far better connectivity in order to have the same J_c as Sample B. If we presume that $J_c(0\ \mathrm{T})$ should be directly proportional to A_F then only the 3000 min sample has sufficiently different A_F to significantly affect J_c. In all other cases, it appears that $J_c(8\ \mathrm{T}, 4.2\ \mathrm{K})$ is primarily controlled by H*.

We will now argue that H* depends on grain size. XRD peak widths from the high-resolution instrument (Table 6.I) (not the area detector data shown in Fig 6.1) were used to estimate grain size according to the Scherrer formula[Cullity01]:

$$t = \frac{0.9\lambda}{B\cos\theta_B} \tag{6.2}$$

Where t is the grain thickness, λ is the x-ray wavelength, B is the peak full width at half maximum (FWHM) in radians, and θ_B is the peak position. In these measurements peak position was determined by least squares data fit using FullProf software. It should be remembered that factors other than small grain size can cause peak broadening, for example inhomogeneity within the sample or properties of the diffractometer. Therefore grain thickness from the Scherrer-formula should be viewed as a *minimum* estimate of actual grain size. The grain sizes calculated from data in Table 6.I are given in Figure 6.9 as a function of t_{mill}. Scherrer-derived grain size decreased rapidly to 20 nm for $t_{\mathrm{mill}} < 600$ min and then more slowly (if at all) thereafter.

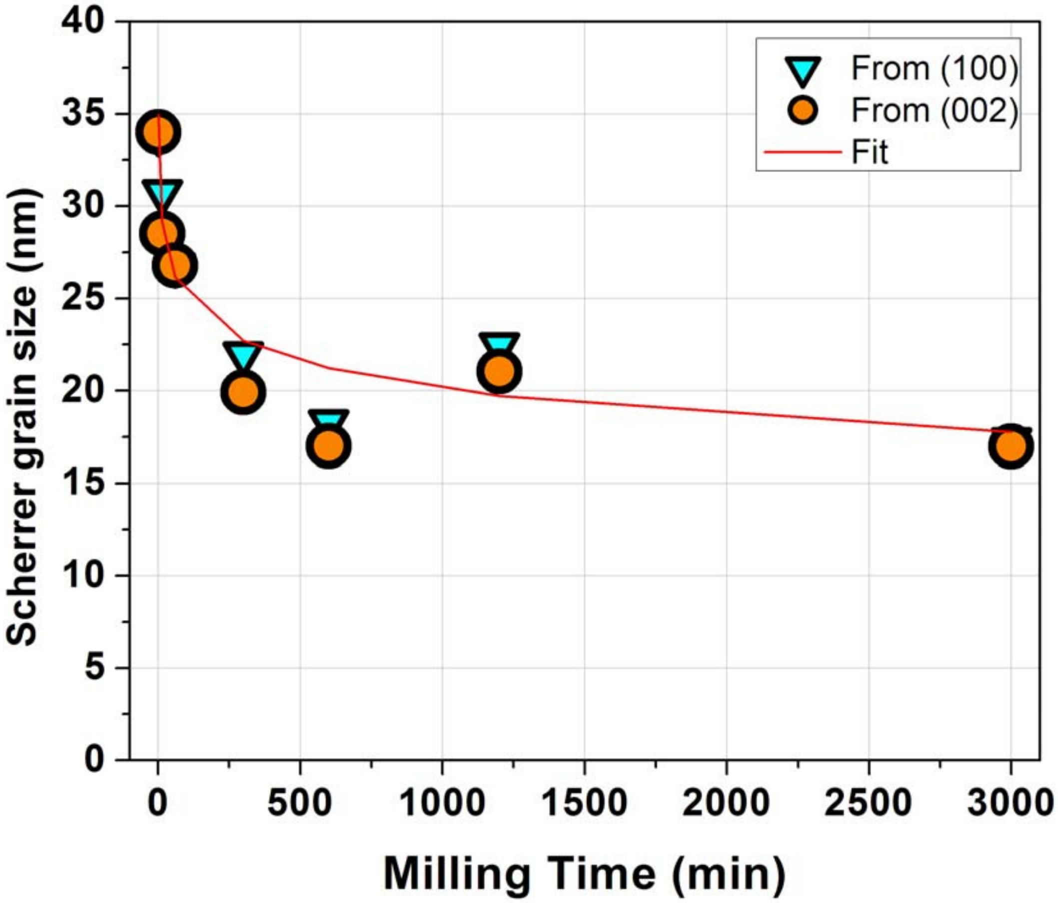

Figure 6.9 – Grain size estimated using the Scherrer formula as a function of milling time in min. Triangles are derived from (100) reflections. Circles are derived from (002) reflections. Red line is a guide to the eye.

These data agreed fairly well with the TEM results (Figure 6.2) on samples with t_{mill}=1200 and 3000 min. Grain boundaries are important for the superconducting properties because vortex pinning can occur at MgB_2 grain boundaries, as can electron scattering. Grain boundary density (boundary area per unit volume) goes as the inverse of grain size (1/d). Figure 6.10 shows that hour measured H*(4.2 K), which may (or may not) track the not measurable H_{c2}(H//c) scales linearly with 1/d. While this correlation does not indicate a mechanism by which grain size might have affected H*, it does indicate that H*(4.2 K) was closely linked to grain size. We suggest that either grain boundary flux pinning increased H* or grain boundary electron scattering effects boosted H_{c2}(H//c-axis) which in turn increased H*.

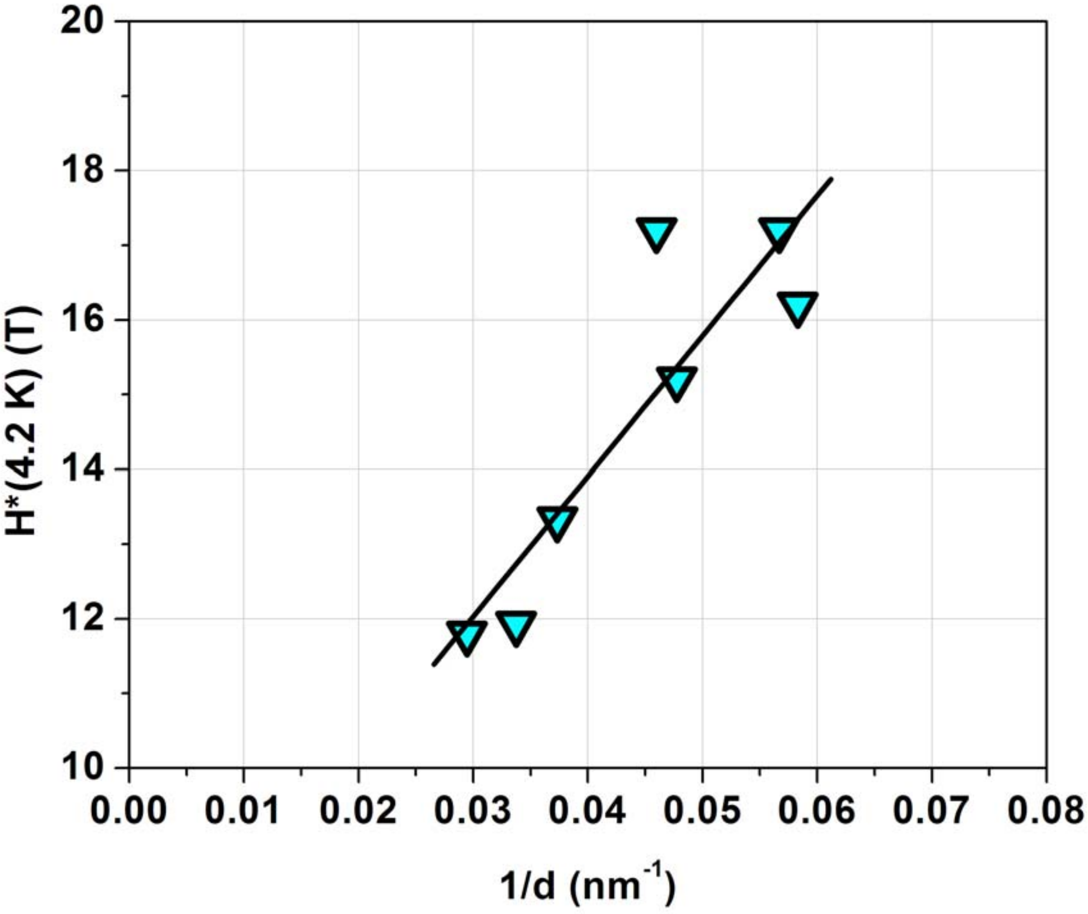

Figure 6.10 – Linear relationship between H* (4.2 K) from Figure 6.8 and inverse grain size.

However, the observation that long t_{mill} can be responsible for very fine ~30 nm grains even after sintering at 1000°C requires explanation. In principle, one expects that the driving force for grain growth (see Ch. 3) is increased by both grain refinement and cold work, leading to an expectation that grain growth should be rapid in fine grained crystals. We might therefore expect much larger grain size in heavily milled samples. However, there are two possibilities why the grains remained fine: grain boundary mobility was either limited by slow diffusion kinetics or boundaries were pinned by second phases. Concerning the possibility that 200 min at 1000°C was insufficient for diffusional grain growth, we note that $1000^{\circ}\text{C} < 0.5\ T_m$ but also that Wilke et al[Wilke01,Wilke02] showed clear evidence of point defect annealing at $T < 700^{\circ}\text{C}$ which would lead to the expectation of reasonable diffusion rates at 1000°C. We thus believe that pinning of the grain boundaries seems more likely.

Observation by TEM of some extremely large grains (1 μm) in the most heavily milled sample (Fig 6.2b) appears to constitute an example of abnormal (discontinuous) grain growth – a phenomena known to occur when normal grain growth is partly constrained by an inhomogeneous distribution of fine precipitates. In extreme cases, this can result in stagnation of grain growth with the maximum average grain size defined by:

$$D_{\max} = \frac{4r}{3f} \tag{6.3}$$

Where f is the volume fraction of precipitate particles with radius r.[Porter01] Assuming $D_{\max} \sim 20$ nm, the equation could be satisfied by 10 vol % of 3 nm diameter particles. Nano-porosity, WC rubble, and (as-yet unidentified) second phases suitable for inhibiting grain growth were all observed by TEM. The unidentified second phases visible in TEM may have resulted from atmospheric reaction layers originally present on powder particle surfaces, thus likely being B or Mg oxides. The anomalously large grains occasionally seen in the TEM then occur at regions where such particles are not present and grain growth becomes possible.

6.4. Conclusions

In this work we determined the effect of milling time on alloying, connectivity, and grain size in order to optimize J_c(H,T). We found that only 60 min of milling was necessary to incorporate X=0.05 of carbon dopant, but grain size continued to decrease to the very small value of 20-30 nm with additional milling time. As a result of this grain refinement H*(4.2 K) increased strongly from about 12 to 17 T, probably due to either improved pinning or improved H_{c2}(H//c-axis). By assessing the connectivity using the Rowell analysis, we found that J_c(8 T, 4.2 K) was more strongly influenced by H* than by A_F, which was only a weak function of milling time. Therefore we conclude that grain refinement was the primary mechanism by which high energy milling increased J_c(8 T, 4.2 K) to a peak value of ~ $8.5\text{x}10^4$ A/cm^2 for t_{mill}=1200 min. The perhaps surprising result that the grain size could be maintained at 20-30 nm is explained by the inhibition of grain growth by finely dispersed second phases produced as a side-effect of the milling process.

This work has identified the irreversibility field H* increase as the primary non-compositional benefit of milling. At 4.2 K, H* increased from ~13.5 to 17 T in samples with similar composition, more than doubling J_c(8 T, 4.2 K).

Chapter 7 – Influence of heat treatments up to 1500°C on the properties of milled and unmilled, pure and C-doped MgB_2.

The relevance of MgB_2 technology for applications is driven by developing a high J_c(H), which is thought to be controlled by both connectivity and vortex pinning, principally at grain boundaries. In our previous work, we obtained high J_c(8 T, 4.2 K) > $5\text{x}10^4$ A/cm^2 by refining grain size by high-energy ball milling. Rowell analysis results combined with TEM indicated that those samples were far from fully connected – largely due to incomplete sintering. However, the temperature dependence of sintering and grain growth is not well known yet, nor are the relative importance of connectivity and grain size to J_c(H). The primary purpose of this experiment was to explore these unknowns by varying T_{HIP} in the probable region of interest (900°C – 1150°C) for unmilled, milled, and C-doped milled samples. We found that optimal processing parameters depended on applied field at which we sought to maximize J_c. Low-field J_c was heavily dependent on connectivity, while high-field J_c was largely determined by H*, which scaled with inverse grain size. Grain growth was roughly exponential in HIP temperature (T_{HIP}), and sintering improved rapidly as T was increased from 900°C to 1000°C. Milling the powder reduced T_{HIP} required for sintering. Adding C increased T_{HIP} required for sintering. The secondary goal of this work was to determine the importance of non-compositional effects on fundamental properties (such as T_c, H_{c2}(T), resistivity) of our samples. To achieve this we heat treated at 1500°C to achieve fully dense, large grained, well annealed, homogeneous samples for comparison to the rest of our sample set. In this secondary goal, we were less successful. For the unmilled sample, we found a suite of properties consistent with established values for X~0.01 as expected, but some free Mg was detected by XRD. The milled undoped and milled C-doped samples contained large amounts of free Mg, visibly separating MgB_2 grains in SEM micrographs. In milled samples, 1500°C heat treatment resulted in significantly reduced lattice parameter, combined with effects on T_c and H_{c2}. These observations are thought to be the result of high-temperature reaction with entrained WC-Co milling media.

7.1 - Introduction

The work presented in this chapter includes sintering, grain growth, and densification of pre-reacted MgB_2 as a function of hot isostatic pressing temperature T_{HIP}. The J_c dependence on those parameters is important to this work, as is bulk C-solubility as a function of T. None of these relationships is well known.

Zhu et al.[Zhu02] used TEM analysis of SiC-doped tapes to estimate the C-solubility (X in $Mg(B_{1-X}C_X)_2$) at 600°C and 900°C as X= 0.014 and 0.021, respectively. Wilke et al.[Wilke05] reported maximum X ~ 0.07 at 1200°C co-existing with MgB_2C_2, and Avdeev et al.[Avdeev01] achieved X=0.1 at 1200°C. The primary region of interest for this work was 900°C-1150°C, and from these reports we would expect C-solubility to vary considerably within that range. These values agree reasonably well with our results in Ch. 5 and 6 which showed maximum X about 0.05 – 0.07 achieved at 1000°C.

As part of a recent review article Braccini et al. [Braccini02] reported on the effect of high-energy ball milling on J_c of undoped powder. In an experiment somewhat similar to Ch. 6 of this thesis, they found that increased milling time had only a small effect on low-field J_c of the heat treated samples, but H* was increased from 5.7 T to 11 T with H⊥tape surface and 8.8 to 12 T with H//tape surface. This was due to "lowered… average grain size". They suggest that grain refinement due to milling may result in less texturing. One possibility they do not suggest is that grain boundary electron scattering effects may decrease the H_{c2} anisotropy within the grains.

Kiuchi et al.[Kiuchi01] observed H* increase in undoped, in-situ samples as a result of low reaction temperature, which they attributed to "small grains" but did not attempt to estimate grain size. Yamamoto et al [Yamamoto01] also observed decreased H* with increased heat-treatment temperature.

Kim et al.[Kim02] explored heat treatment temperature on in-situ MgB_2 and found that T_c increased from ~36.7 K to ~38.1 K as heat-treatment temperature increased from 650 to 900°C. In the same T span, FWHM of the (100) peak in the XRD pattern decreased from ~0.57 to ~0.43 degree, which they attributed mostly to strain, but which may also have been influenced by grain size.

In another experiment, Braccini et al.[Braccini04] investigated the effect of sintering temperature on ex-situ tapes between 200°C and 950°C. They found T_c(10% below onset) was decreased to as low as 35 K for samples which were sintered at very low temperature, and increases linearly with T up to ~38 K for 950°C. However, dH_{c2}/dT was not significantly affected by heat-treatment temperature, indicating that some of the apparent T_c suppression could result from poor connectivity broadening the transition. J_c was negligible for samples annealed below 800°C, but between 800 and 900°C Jc increased strongly with increased heat treatment temperature, probably due to increased connectivity. Above 900°C, J_c again decreased due to reaction of tape cores with the Ni sheath that effectively limited their experiment. These results seem to indicate that sintering does not occur below 800°C, and that 900°C connectivity is still evolving rapidly. This agrees with our unpublished preliminary data.

Yamamoto et al. [Yamamoto02] used mean-field theory to model percolation in incompletely connected MgB_2, and established some link between packing factor, connectivity, and $J_c(0\ T)$ of one sample set. They showed that for their sample set, Jc scaled about linearly with connectivity (κ) which is known as A_F in this thesis. This scaling relationship has not been demonstrated to be general. After accounting for their estimated 13% of grains isolated by insulating oxides, they established a roughly linear dependence of κ on packing factor (P) (which is the volume fraction occupied by MgB_2 after reaction) with $\kappa = 0$ at $P \sim 0.35$ and $\kappa \sim 0.5$ at $P \sim 0.88$.

The results of the present work agree fairly well with the studies described above, but the present work goes farther. We explore the evolution of both connectivity and grain size as a function of T_{HIP} in the unmilled, milled, and C-doped state. We more clearly relate H* to grain size, and we separate the effects of C-doping and milling.

7.2 - Experimental Procedure

This work involved 3 sample sets. The first set was made from nominally undoped MgB_2 powder as-received from Alfa-Aesar. The second set was made from the same Alfa-Aesar powder, milled for 20 hours in a SPEX 8000M mixer/mill with WC media in Ar atmosphere. The third sample set was made from the same Alfa-Aesar powder, mixed with graphite and Mg powders in the mol ratio 0.96 MgB_2 + 0.04 Mg + 0.08 C to produce a nominal composition $Mg(B_{0.96}C_{0.04})_2$ and milled under the same conditions as the second set. Powders were cold isostatic pressed into pellets and welded into evacuated tubes. Tubes were either stainless steel with Nb foil lining (for T_{HIP} up to 1150°C) or pure Nb (for T_{HIP} = 1500°C). Samples were hot isostatic pressed (HIP) for 300 minutes at peak T_{HIP}, with maximum pressure of 29,000 psi. After heat treatment, samples were typically ~90% dense and very hard. Pellets were sectioned with a diamond saw and their properties measured.

During heat treatment, MgB_2 reacts with Nb resulting in free Mg and Nb-B compounds. This reaction is negligible for most T_{HIP} studied here, but for T_{HIP} = 1500°C the reaction layer became ~0.5 mm thick. As a result, the samples (particularly the milled undoped sample) with T_{HIP} = 1500°C contained a phase believed to be free Mg, concentrated at grain boundaries. This phase may affect sample properties, particularly connectivity. T_{HIP} = 1700°C was attempted, but resulted in complete MgB_2 breakdown.

In the previous chapters, the experiment required each sample to be made from a unique batch of milled powder. This may have been the source of some sample-to-sample variation. The present experiment required only 3 unique powders, so it was possible to use identical powder for all samples within each of the 3 sets. This was accomplished by milling several 10 g batches and then mixing them all together to form a single homogeneous powder source for each set. As a result, the data within each set shows less random variation (particularly in J_c) than the samples in Ch. 6 or especially Ch. 5.

As discussed in Ch. 3, the milled powders contained ~5 wt% WC, which could introduce enough C into the system to increase X by ~0.006.

7.3 Results

Green density (geometric density) of a CIPed pellet made from milled, C-doped powder was 1.73 g/cm^3. Neglecting the effects of entrained WC, that corresponds to 66% of the theoretical density (2.625 g/cm^3). After HIP treatment, small rectangular bars were ground for VSM measurement. Their volume and mass were measured and used to calculate post-HIP geometric density. Those values are presented in Table 7.I, expressed as the fraction of theoretical density. The primary sources of uncertainty were in both forming and measuring the dimensions of the bars. In these calculations we assumed 0.01 mm uncertainty in each dimension, and the resulting volume uncertainty was generally 6-10%, depending on sample size. Some values in the table are > 1, which in some cases may represent a correct value since WC was entrained during milling (see Ch. 3).

Table 7.I – Geometric density expressed as fraction of theoretical density. Uncertainty typically 6-10%.

T_{HIP} (°C)	Unmilled	Milled	C-doped
900	0.84	1.04	0.91
950	0.89	1.05	0.98
1000	1.06	0.97	1.03
1150	0.98	1.09	1.03
1500	0.95	1.02	1.04

Density was only ~84% for the unmilled 900°C sample, and ~90% for the C-doped and unmilled samples with T_{HIP} = 950°C. The rest of the set, including all milled undoped samples, had geometric density similar to the theoretical value.

X-ray diffraction patterns were collected for each sample using a Gunier camera detector manufactured by Huber. This permitted high resolution (0.005° step in 2θ) measurement in a short time. Despite careful handling intended to prevent oxidation, XRD typically showed the presence of a small amount (a few %) of MgO. Free Mg was detected in samples with $T_{HIP} \geq 1150$°C. At 1500°C, Mg was by far the predominant phase impurity. At T_{HIP} = 900°C, WC was detected in milled samples. At T_{HIP} = 950-1150°C WC and WB were both detected. At T_{HIP} = 1500°C neither WC nor WB were found.

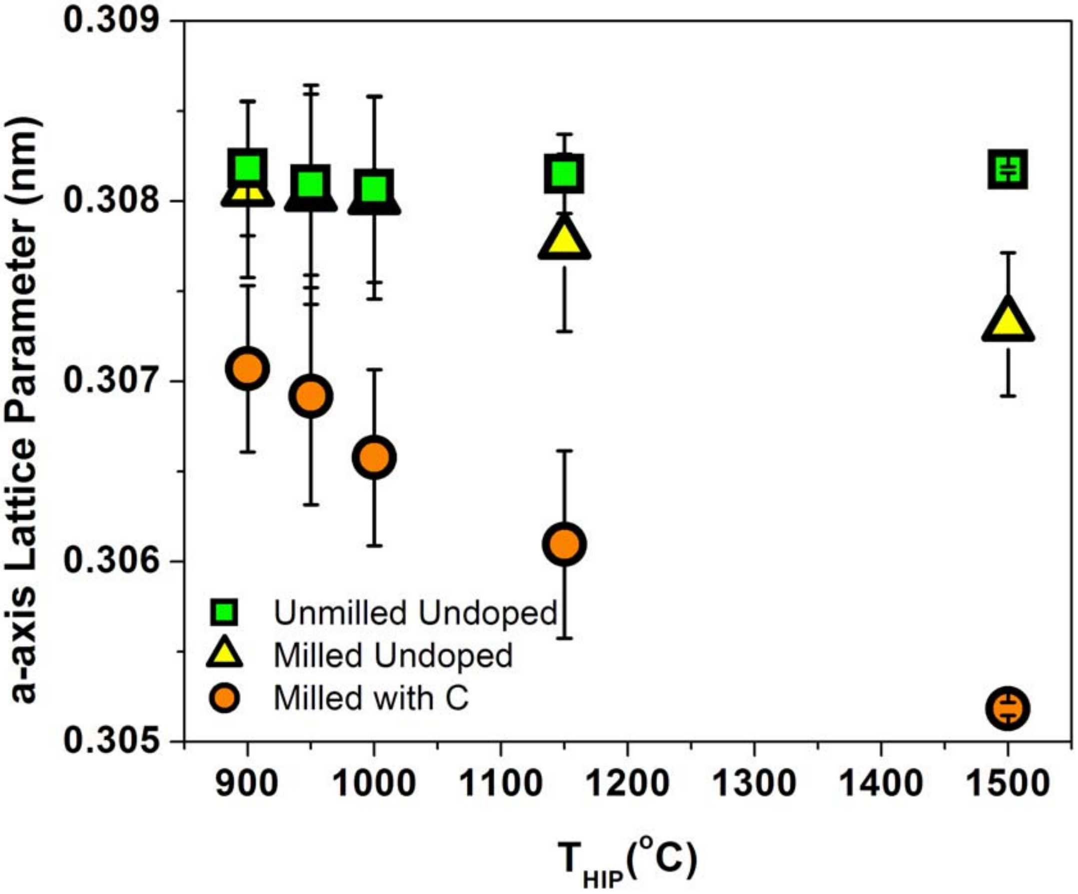

Figure 7.1 – a) a-axis lattice parameter from x-ray diffraction.

The Nelson-Riley method was used to determine lattice parameters. No significant shifts in the c-axis parameter were observed. The *a* lattice parameter values are shown in Figure 7.1. The *a* lattice parameter was nearly constant at all T_{HIP} for unmilled samples, and for milled undoped samples at ≤ 1000°C. Lattice parameter contracted with increased T_{HIP} for all C-doped samples, as well as for the milled undoped samples with $T_{HIP} \geq 1150^{o}C$.

Table 7.II – XRD peak widths for each sample.

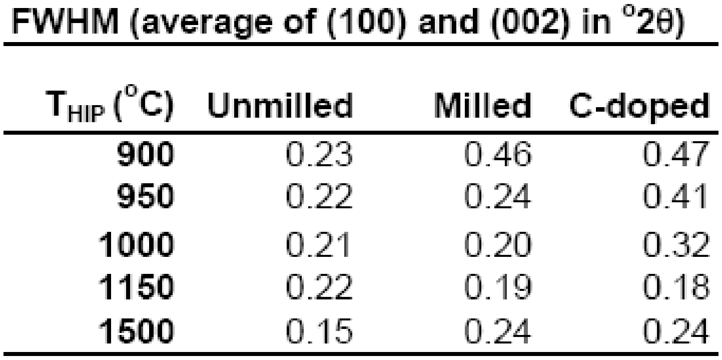

FWHM (average of (100) and (002) in $^{o}2\theta$)

T_{HIP} (^{o}C)	Unmilled	Milled	C-doped
900	0.23	0.46	0.47
950	0.22	0.24	0.41
1000	0.21	0.20	0.32
1150	0.22	0.19	0.18
1500	0.15	0.24	0.24

Full-width half-maximum (FWHM) peak widths were measured for the (100) and (002) reflection of each peak. Those data are given in Table 7.II. Peak widths were broadest for low T_{HIP}, especially in milled samples. The milled and C-doped 1500^{o}C samples were measured last after some adjustments (not intended to improve broadening) were made to the diffractometer, and may have suffered from a greater degree of instrument broadening than the other samples.

Scanning electron microscopy was used to image the progression of sintering and grain growth as T_{HIP} was increased. Figure 7.2a-e show each sample in the unmilled set, in order of increasing T_{HIP}. Scale bars are all 1 μm.

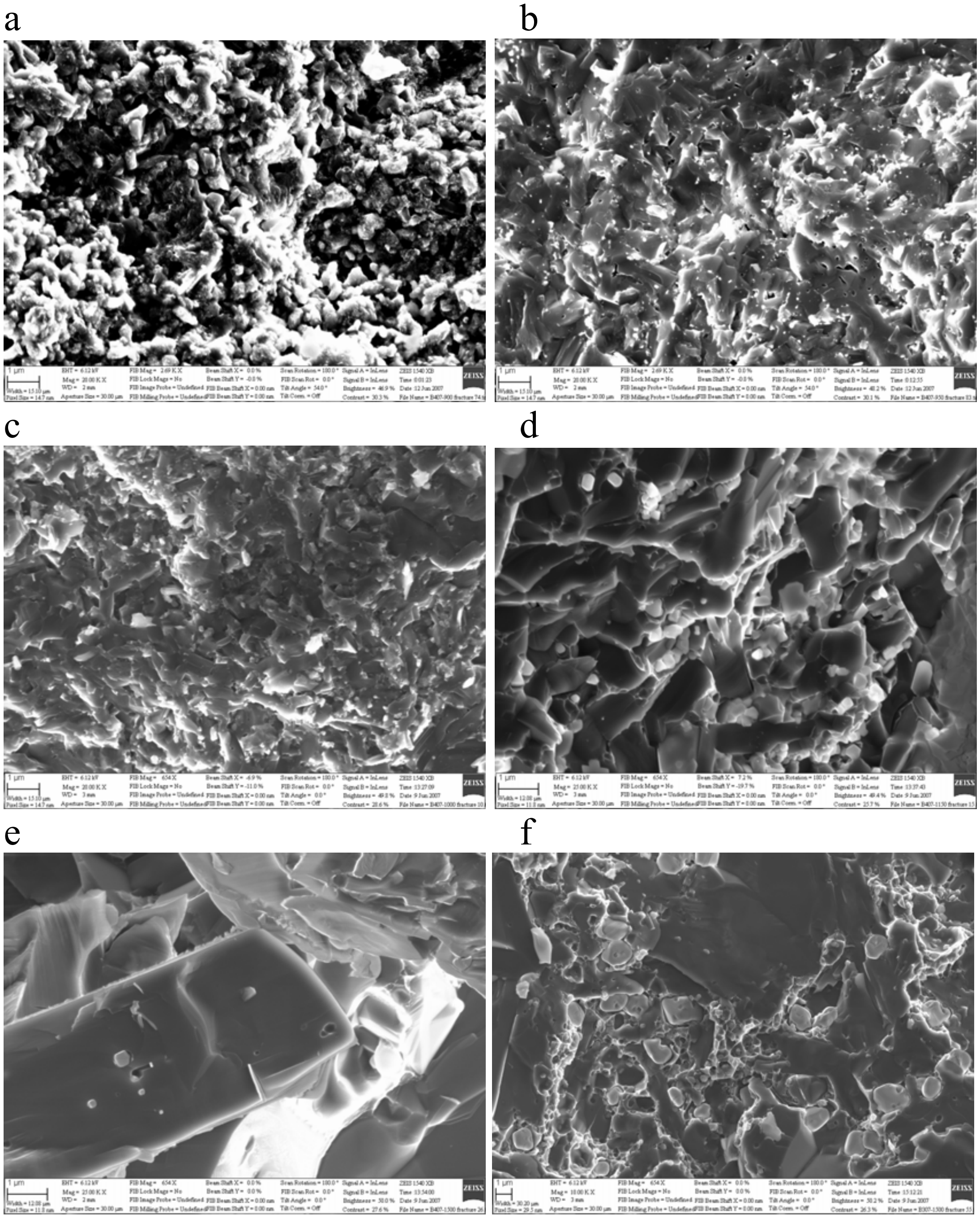

Figure 7.2 – Secondary electron micrographs of fracture surfaces for unmilled samples with T_{HIP} = a) 900°C, b) 950°C, c) 1000°C, d) 1150°C, and e) 1500°C. F) is milled undoped with T_{HIP}=1500°C. All scale bars are 1 μm. Particles visible in a) are polycrystalline aggregates. Black regions in a) are pores. Small white spots visible in b) and c) may be MgO (see Jiang et al.[Jiang01] for similar features). Colonies of ~0.25 μm white grains visible in d) are probably Mg. F) shows large (dark) MgB_2 grains separated by colonies of small (light) grains that are probably Mg.

The images (a-e) show grain growth and sintering in unmilled samples. In a) the rounded particles are polycrystalline and interparticle fracture is the dominant mode, indicating that particles are not well sintered. Open porosity is abundant. This sample appears to be in the neck-growth stage of sintering (stage I), and was only ~84% dense (Table 7.I). In b) porosity is still visible but sintering has progressed significantly, consistent with density increase to ~90%. Transgranular fracture indicated good mechanical strength at grain boundaries. Transgranular fracture renders grain boundaries visible within the fractured particles. Some closed pores exist. This sample appears to be undergoing intermediate sintering. In c) the sample is well connected and was very dense. Most of the remaining porosity is closed. Grain size is on the order of 1 micron. The samples shown in a), b), and c) had J_c(20 K, 0 T) = $1.5\text{x}10^5$, $5.5\text{x}10^5$, and $6.8\text{x}10^5$ A/cm^2 respectively. Samples shown in d) - f) contain virtually no porosity, but did contain free Mg, which is particularly visible in the milled sample in f). Visual inspection showed less free Mg in the center of the sintered pellets than near the Nb-MgB_2 reaction layer.

Table 7.III – Grain size by SEM.

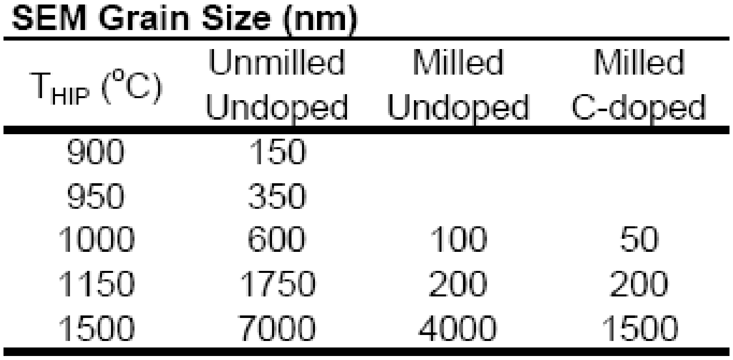

SEM Grain Size (nm)

T_{HIP} (°C)	Unmilled Undoped	Milled Undoped	Milled C-doped
900	150		
950	350		
1000	600	100	50
1150	1750	200	200
1500	7000	4000	1500

Micrographs such as these were used to estimate grain size. Those data are given in Table 7.III. The best way to estimate grain size would be TEM, but we have not yet applied that method to these samples. Grain size estimates by SEM involve some uncertainty, especially for fine grain sizes where 1) small grains are not always observed and 2) grain boundaries are not always visible. Therefore, as grains become finer, SEM is likely to overestimate grain size. However, it should be kept in mind that even though there may be some inaccuracy in these data, grain size observed by SEM spanned nearly 2 orders of magnitude, so uncertainty is generally not large compared to the range of the data. At low T_{HIP} the milled samples had much smaller (<100 nm) grain size, but after 1500^{o}C heat treatment all samples had grains > 1μm.

T_c traces were measured at 5 mT applied field in ZFC configuration (see Ch. 3). Results are shown in Figure 7.3. In the unmilled undoped set (7.3a) all transitions were fairly sharp, with the broadest (T_{HIP} = 900^{o}C) having width (10% to 90% m(5 K)) only ~2 K. Onset T_c values did not change significantly with T_{HIP}. The milled undoped set has slightly reduced T_c at both T_{HIP} = 900^{o}C and T_{HIP} = 1150^{o}C, but all transitions for $T_{HIP} \leq$ 1150^{o}C were sharp. Suppression of T_c in the 900^{o}C sample was not accompanied by *a* lattice parameter contraction as shown in Fig 7.1. This observation seems consistent with Kim et al.[Kim02] and Braccini et al.[Braccini04] For T_{HIP} = 1500^{o}C (in which free Mg was found) onset T_c was depressed to ~34 K, and the transition was almost 20 K broad. The milled C-doped samples all had reasonably sharp transitions typically spanning a few K or less. T_c for both milled sets decreased as T_{HIP} increased above 1150^{o}C.

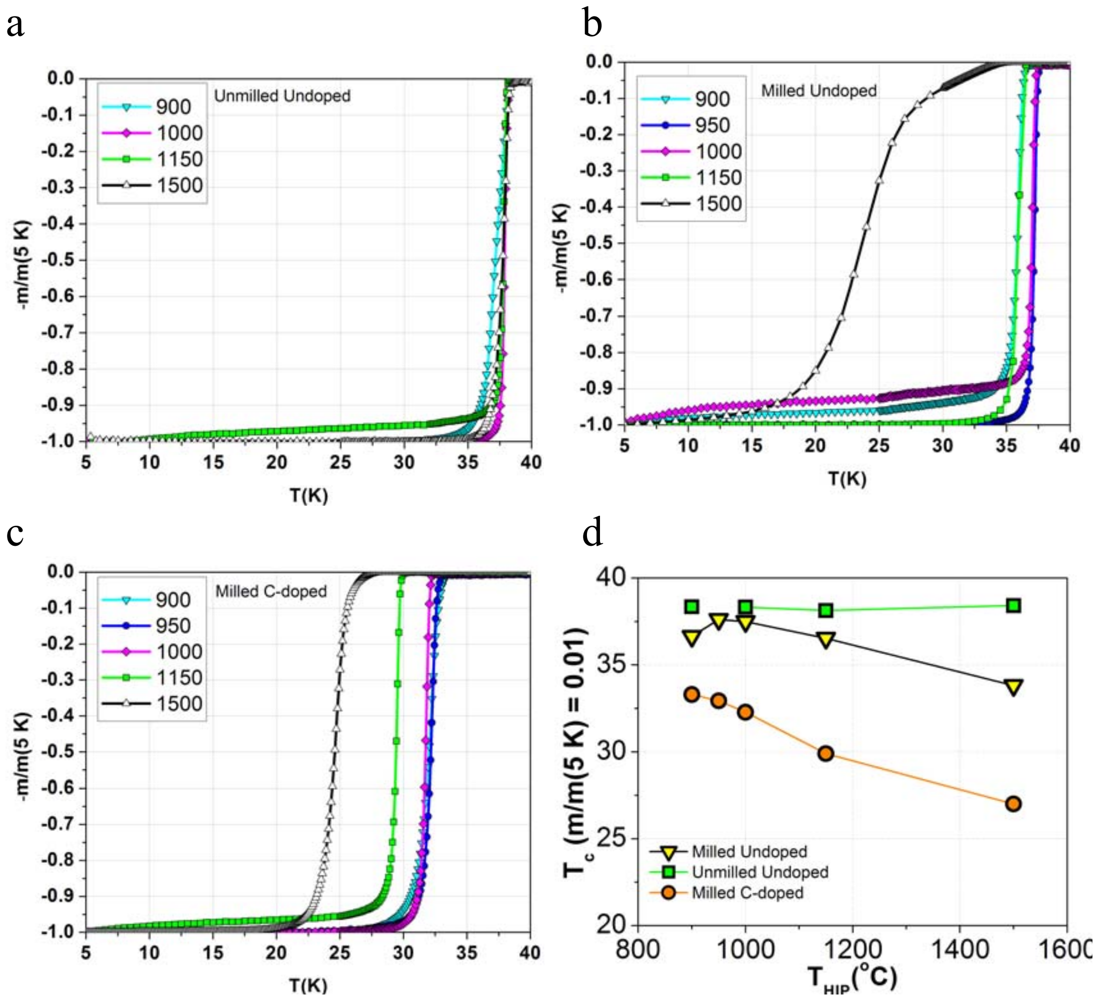

Figure 7.3 – Magnetic ZFC (see Ch. 3) T_c results at 5 mT applied field. Curves shown for a) unmilled undoped set, b) milled undoped set, and c) milled C-doped set. Compiled T_c values with m/m(5 K) = 0.01 criterion shown in d).

Figure 7.4 reproduces the T_c against lattice parameter plot from Ch. 2, with the addition of these data, showing reasonable agreement between these data and the C-doped single crystal work of Lee et al.[Lee02] and Kazakov et al.[Kazakov01]

Differences between these data and the Kazakov results may be related to the type of T_c measurement (see Ch. 2).

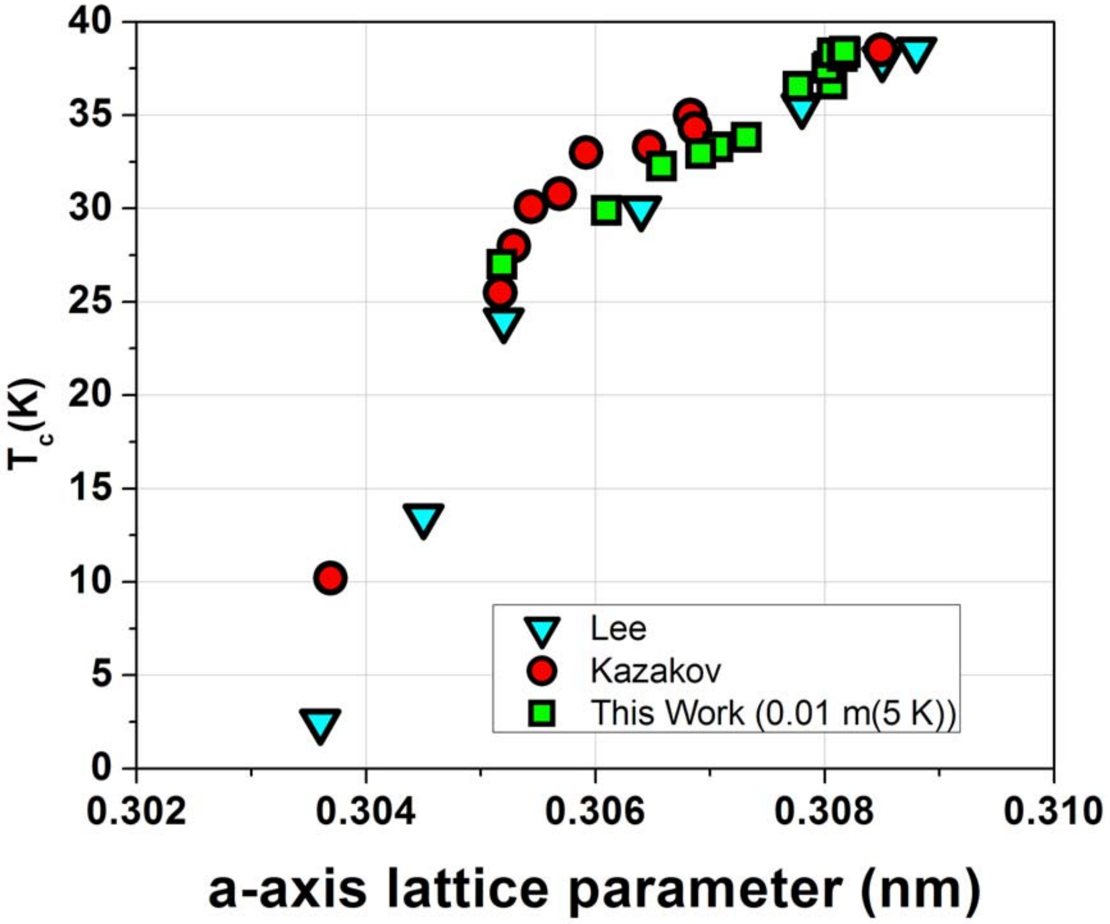

Figure 7.4 – Plot of T_c against lattice parameter (from Ch. 2) with these data included.

$H_{c2}(T)$ was taken as the field where $\rho = 0.9\rho_n$ in swept-field resistive transitions. In the unmilled samples, we found only slight changes in $H_{c2}(T)$ with changing T_{HIP} for all T_{HIP}. In milled undoped samples, $H_{c2}(T)$ was suppressed at high T_{HIP}. $H_{c2}(T)$ for the

1500°C sample was 1-2 T lower than for the other samples in the set, and H_{c2}(0 K) extrapolated to only 15 T compared to ~22 T for the rest of the milled undoped samples. The milled C-doped samples followed a trend of decreased $H_{c2}(T)$ with increased T_{HIP}. Decreased $H_{c2}(T)$ is generally associated with a-axis lattice parameter contraction in C-doped samples.[Avdeev01,Wilke03,Kazakov01,Lee02] For those samples with lattice parameter ~0.3081 nm, $H_{c2}(T)$ was essentially identical regardless of milling status, as illustrated in Figure 7.5d.

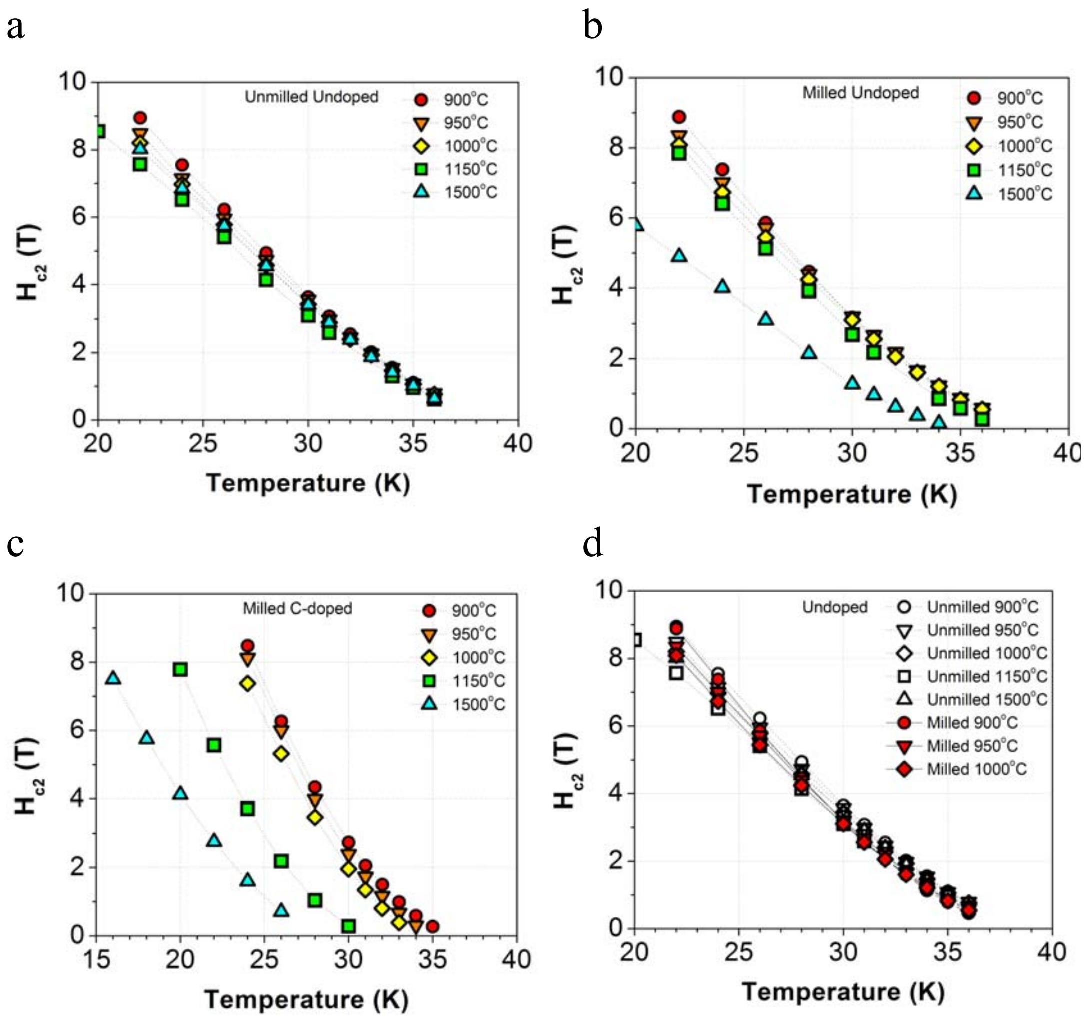

Figure 7.5 - $H_{c2}(T)$ from resistivity measurements using 90% (ρ_n) criterion for a) milled undoped, b) unmilled undoped, c) milled C-doped, and d) all samples with a~0.3081 nm. These data represent H_{c2}//ab-plane.

4-point resistivity measurement (I = 5 mA) results are given in Table 7.IV. All samples showed metallic-type ρ(T) behavior. ρ(40 K) resistivity decreased monotonically with increased T_{HIP} for all sample sets. The lowest value obtained was ρ(40 K) = 1.6 μΩ-cm for the unmilled 1500°C sample. That sample also had the highest RRR at 6.8. In all samples but one, RRR increased with T_{HIP}. Increase in RRR is generally taken to signify less electron scattering from compositional and microstructural sources, independent of connectivity. For milled material, 1500^{o}C samples with reduced T_c, actually had the lowest 40 K resistivity and highest RRR of their sets. $\Delta\rho$ varied from a minimum of 9.2 to a maximum of 32.5 μΩ-cm and followed a trend of decreasing $\Delta\rho$ with increasing T_{HIP}, for $T_{HIP} < 1150^o$C.

Table 7.IV – summarized resistivity data for each sample set. RRR is dimensionless.

Unmilled Undoped (All ρ values in μΩ-cm)

T_{HIP} (^{o}C)	ρ(40 K)	ρ(300 K)	Δρ (300 K - 40 K)	RRR (ρ(300 K) / ρ(40 K))
900	18.6	51.0	32.5	2.7
950	4.9	18.7	13.8	3.8
1000	3.5	14.1	10.7	4.1
1150	2.6	13.8	11.2	5.3
1500	1.6	10.8	9.2	6.8

Milled Undoped (All ρ values in μΩ-cm)

T_{HIP} (^{o}C)	ρ(40 K)	ρ(300 K)	Δρ (300 K - 40 K)	RRR (ρ(300 K) / ρ(40 K))
900	22.2	39.4	17.2	1.8
950	9.5	22.4	12.9	2.4
1000	5.4	15.5	10.1	2.9
1150	9.5	24.5	15.0	2.6
1500	7.6	28.7	21.1	3.8

Milled C-doped (All ρ values in μΩ-cm)

T_{HIP} (^{o}C)	ρ(40 K)	ρ(300 K)	Δρ (300 K - 40 K)	RRR (ρ(300 K) / ρ(40 K))
900	79.0	106.6	27.6	1.3
950	52.0	72.1	20.1	1.4
1000	33.7	48.6	14.9	1.4
1150	19.3	32.5	13.2	1.7
1500	15.9	38.3	22.4	2.4

M-H loops were measured in a vibrating sample magnetometer (VSM) and J_c calculated using the Bean model according to the expression $M = \frac{3b-d}{12b} J_c d$ where M is the volumetric magnetization, and b and d are the sample dimensions perpendicular to the field direction, with $b > d$.[Evetts01,Bean01] J_c (4.2 K) and J_c(20 K) for each sample set are shown in Figure 7.6.

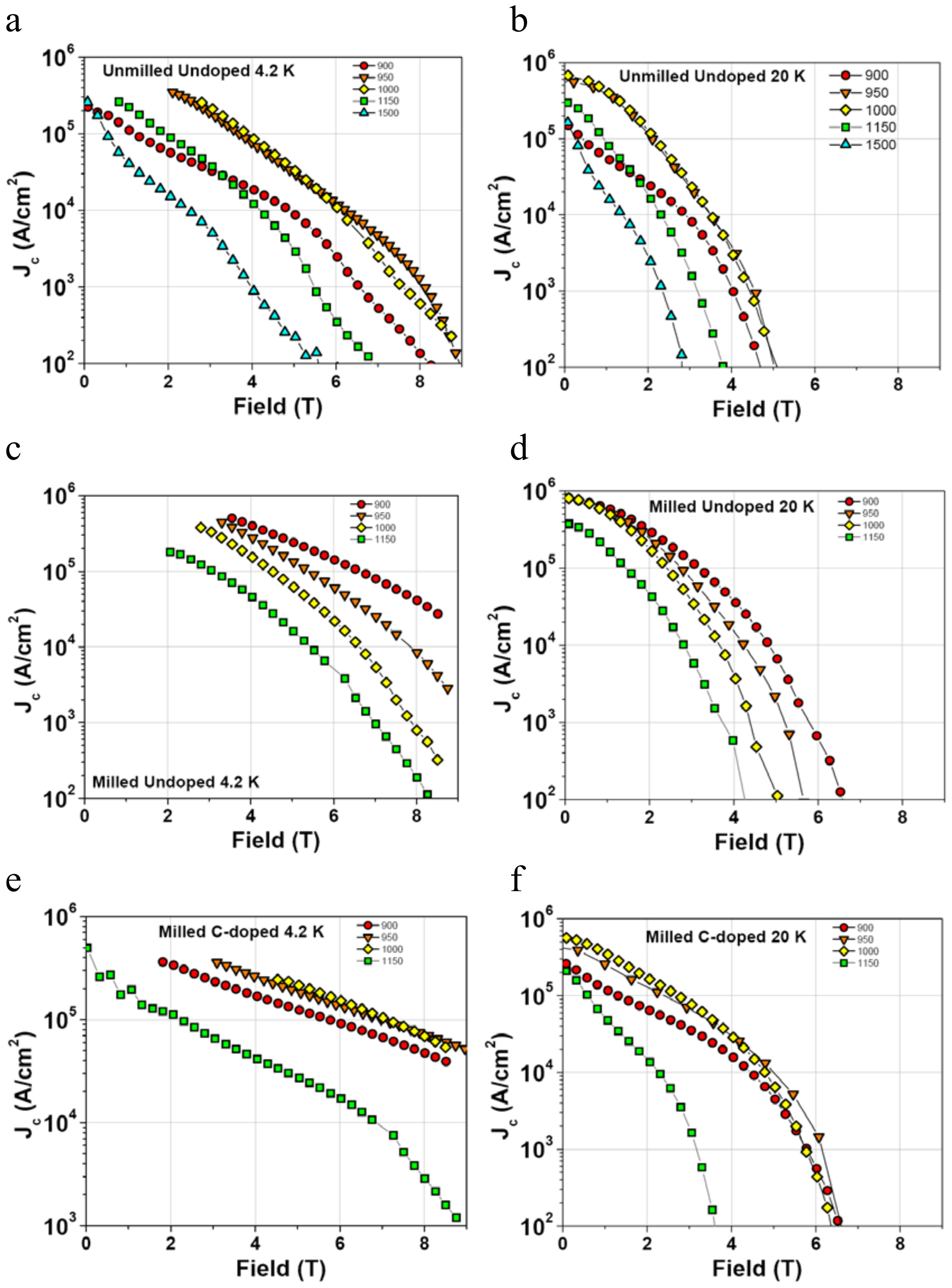

Figure 7.6 – J_c(H) calculated from magnetic hysteresis loops for a,b) unmilled, c,d) milled undoped, e) and f) C-doped sample sets with measurement temperature a,c,e) 4.2 K and b,d,f) 20 K.

Most samples had close to Kramer-like J_c dependence on field, where $J_c \sim b^{-0.5}(1-b)^2$. Where $b \sim B/B^*$ and $B = \mu_o H$. This is a similar dependence to that seen in Nb_3Sn and Chevrel phase superconductors, which are grain boundary pinners.[Evetts01,Rodrigues01,Bonney01] In all sets, low-field J_c decreased for increasing T_{HIP} above 1000°C. In unmilled and C-doped, low-field J_c peaked at 1000°C.

It is important to note that the curves are not parallel in any of the sample sets, i.e. both J_c(0 T) and H* do not scale with only one parameter in any of the sets. In both undoped sets at 4.2 K, the sample with T_{HIP} = 900°C had the smallest dependence of J_c on H. In the C-doped set, T_{HIP} = 950°C resulted in slightly more field-invariant J_c. Low J_c variation with applied field was a strong determinant of relative J_c at high field (~8 T and above). These results are qualitatively similar to those of Braccini et al.[Braccini04] and Kim et al.[Kim02], which were attributed to grain size effects.

H* (4.2 K) was obtained by extrapolating the Kramer line (not shown, see Ch. 3) ($J_c^{0.5}H^{0.25}$ as a function of H) to the H-axis intercept.[Evetts01] For samples that exhibit good Kramer-like behavior (such as the C-doped set), this result is close to H*(J_c=100 A/cm^2), as shown in Ch. 5. In undoped samples, Kramer lines tailed toward high H at low J_c, possibly due anisotropy effects. This resulted in slightly underestimated H* by Kramer extrapolation compared to J_c = 100 A/cm^2 criterion. H*(4.2 K) by Kramer extrapolation is given in Figure 7.7. In all cases but one (milled C-doped, T_{HIP}=900°C) increasing T_{HIP} resulted in lower H*. The milled undoped samples had higher H* than the unmilled samples, particularly at T_{HIP} < 1000°C. At T_{HIP} = 900°C, H*(4.2) was 10.5 T for the milled undoped sample and about 7.5 T for the unmilled sample. The C-doped samples had H* 3-8 T higher than the milled undoped samples. In the C-doped samples, H*(4.2 K) decreased 40% from ~16 T at T_{HIP} = 950°C to ~10 T at T_{HIP} = 1150°C.

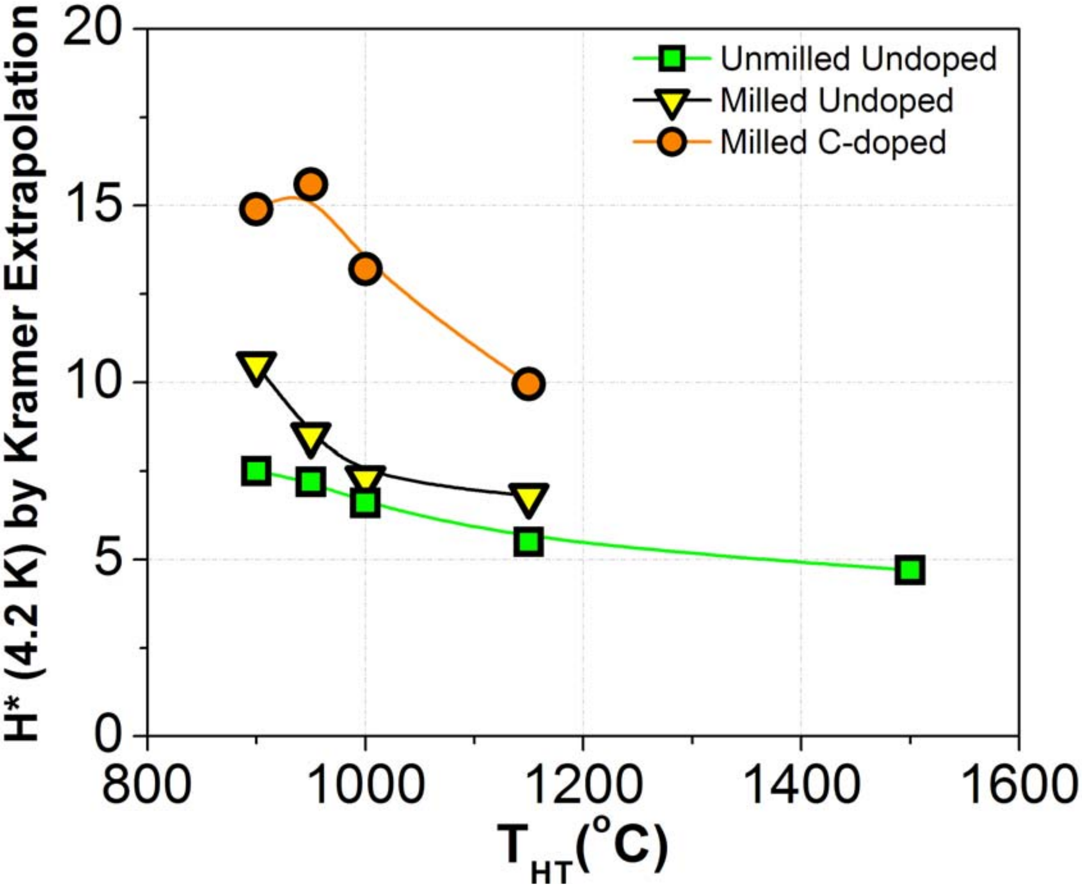

Figure 7.7 – H* (4.2 K) by Kramer line extrapolation generally decreased with increased T_{HIP}.

7.4 Discussion

The key numerics in this work are J_c(H), composition, grain size, and connectivity. We measured J_c(H) by hysteresis loops and presented the result above, but understanding that result requires knowledge of composition, grain size and connectivity. Composition can be estimated from a-axis lattice parameter. Grain size was directly measured by SEM down to 50-100 nm but SEM becomes less reliable the smaller grain size gets, and can be expected to overestimate small grain sizes. Below we will generate more reliable grain size data over a broader range by combining SEM results with XRD peak broadening results. Connectivity will be estimated following the Rowell analysis, and the results compared to the packing factor calculations of Yamamoto et al.[Yamamoto02]

Single crystal work [Kazakov01,Lee02] has shown a linear dependence of a-axis lattice parameter on X (in $Mg(B_{1-X}C_X)_2$). As described in Ch. 2, 4, 5, and 6, this relationship is widely used to estimate X based on x-ray diffraction results in polycrystalline bulks. Application of this method results in the data shown in Figure 7.8.

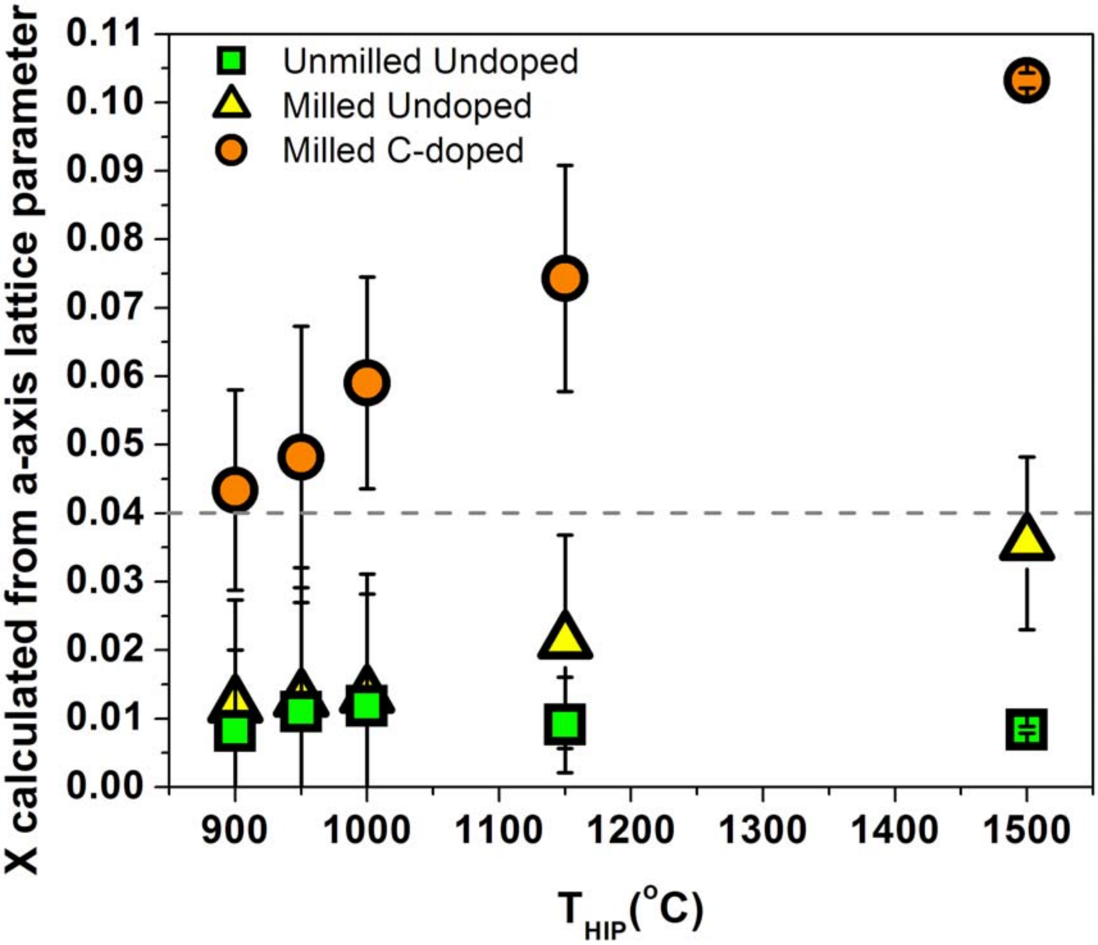

Figure 7.8 – Composition (X in $Mg(B_{1-X}C_X)_2$ from a-axis lattice parameter by comparison to single crystals.[Kazakov01] Horizontal dotted line is nominal doping level for C-doped set.

Unmilled samples had X~0.008, which is typical of samples made from this Alfa-Aesar powder, and X was independent of T_{HIP}. For the milled C-doped samples, calculated C-content increased with T_{HIP}, at all T_{HIP}. Our calculated X for T_{HIP} = 900°C was 0.043, which was higher than the solubility limit suggested by Zhu et al.[Zhu02] At T_{HIP} = 1150°C, our calculated X = 0.074 was between the 1200°C solubility limit given by Wilke et al.[Wilke05] and that given by Avdeev et al.[Avdeev01] For the C-doped at

1500^{o}C, we calculated X = 0.1. Milled undoped samples showed X similar to the unmilled samples for T_{HIP} < 1150^{o}C but for T_{HIP} = 1150 and 1500^{o}C, calculated X increased.

This high T_{HIP} decrease in lattice parameter (which we are here associating with increased C-content) requires explanation. For milled samples, additional C is known to be present in the system in the form of WC milling media debris, which is known (See XRD results above) to react with MgB_2 at high temperature, liberating C. Total reaction of 5wt% WC at high temperature could yield enough C to increase lattice C-content by up to X~0.006. Combining the C present in the MgB_2 starting powder (enough for X = 0.008) with that present as WC (enough for X = 0.006), we would expect milled undoped samples to have enough C in the system to achieve X ~ 0.014, and milled C-doped samples could reach X ~ 0.054. At T_{HIP} = 1150^{o}C and above, the lattice parameter shift in the milled samples is too large to be accounted for only from those known C sources. Since this effect was only observed in the milled samples and since T_{HIP}=1500^{o}C was high enough to anneal out any milling-induced strain, disorder, and fine grain size effects, we conclude that *either* much more C was available as WC than we supposed, *or* reaction of WC provided some new dopant such as W or Co that reduced a-axis lattice parameter. Broad T_c transitions in 1500^{o}C samples may be attributable to the effects of intergranular Mg since onset T_c values were fairly reasonable for the whole set, as shown in Figure 7.4.

The most accurate measure of grain size is by TEM; however we do not yet have TEM data for these samples. Grain size can be estimated from XRD peak breadth using the Scherrer formula (see Ch. 3), if grain size is sufficiently small to be the only significant source of XRD peak broadening. We found previously (Ch. 6) that Scherrer formula results agreed fairly well with TEM results on 20-30 nm grains. The Scherrer analysis can not be used when instrument broadening dominates, because increasing grain size no longer sharpens peaks. Instrument broadening can be determined by measuring peak width in large grained, unstrained, homogeneous samples. Results of the Scherrer analysis are given in Table 7.V.

Table 7.V – Grain size from Scherrer analysis.

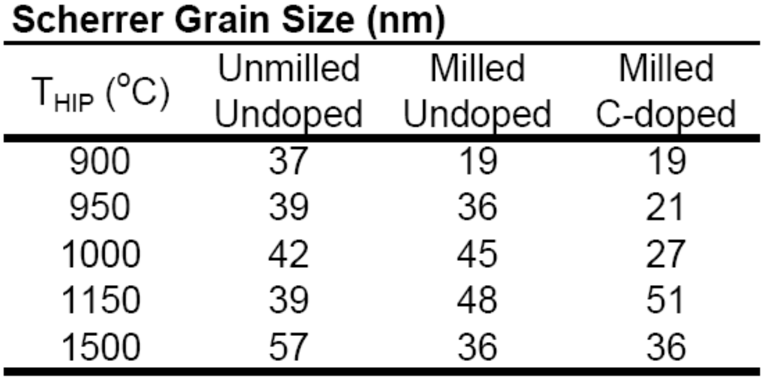

Scherrer Grain Size (nm)

T_{HIP} (°C)	Unmilled Undoped	Milled Undoped	Milled C-doped
900	37	19	19
950	39	36	21
1000	42	45	27
1150	39	48	51
1500	57	36	36

As grain size became large, Scherrer-calculated grain size leveled off at 40-50 nm, (except for the milled undoped and C-doped 1500°Csamples, discussed above) indicating the limit of the analysis. We can therefore use the Scherrer formula result with reasonable accuracy for fine (< 40 nm) grains, whereas the SEM is reliable for large (a few hundred nm) grains. In the region where neither method was entirely applicable, we averaged the two results. The averaging method involves some uncertainty, but is sufficiently reliable to establish data trends because 1) the grain size estimation is most accurate for very large or very small grains and 2) measured grain size ranged over almost 3 orders of magnitude, so a factor of (for instance) 2 uncertainty in a (for instance) 300 nm grain size is not so large as to preclude thoughtful interpretation. The combined SEM and Scherrer formula result is given in Table 7.VI.

Table 7.VI – Grain size estimate by combining SEM and Scherrer formula results.

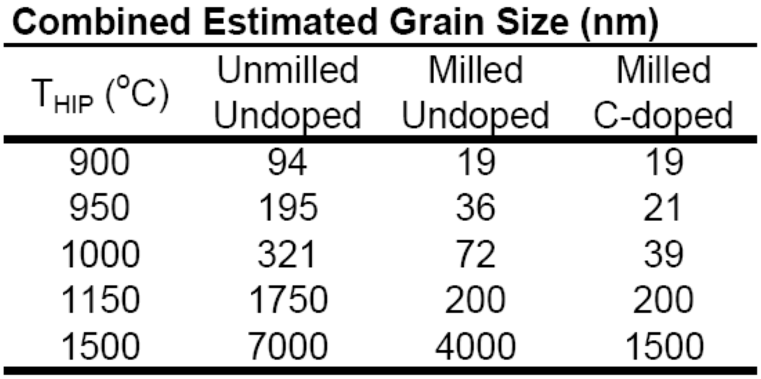

Combined Estimated Grain Size (nm)

T_{HIP} (°C)	Unmilled Undoped	Milled Undoped	Milled C-doped
900	94	19	19
950	195	36	21
1000	321	72	39
1150	1750	200	200
1500	7000	4000	1500

During sintering grain size for porous solids generally goes as: [German01]

(7.1) $$d^n = d_0^n + Kte^{\frac{-Q_s}{kT}}$$

Where d is the grain size, d_0 is initial grain size, t is time, T is temperature, K and k are constants, Q_s is an activation energy for grain growth, and the kinetic grain growth exponent (n) is between 3 and 5 depending on diffusion mechanism, and $n = 3$ for coarsening in a dense material with liquid present (such as MgB_2 + Mg). For a set of isochronal heat treatments at different T_{HIP}, final grain size would be expected to follow an Arrhenius relationship. The Arrhenius plot in Figure 7.9 shows that the 1/T dependence of grain size seems to follow the Arrhenius relationship in MgB_2. Here we used $n = 3$. Variation of n between 3 and 5 had no effect at all on R^2 values for the lines, or their relative positions, but did change the slope by a factor of ~2.

Figure 7.9 - Arrhenius plot with $n = 3$.

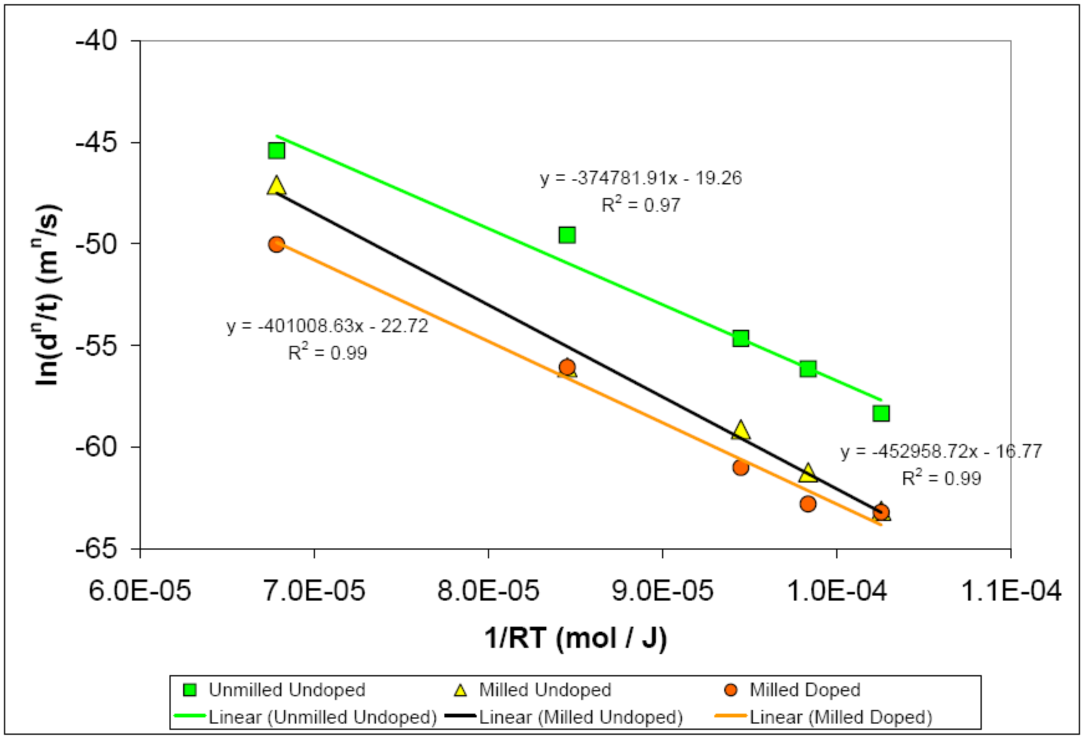

Without a calculated n value, we cannot quote an accurate value for Q_s, but we can say that the activation energy Q_s is on the order of 500 kJ/mol. We can also see that the activation energy for grain growth in the milled samples is only slightly different from that in unmilled samples.

Connectivity is difficult to measure directly, but is thought to be indexed by the Rowell analysis, which can be adapted to the C-doped case by choosing standards for $\Delta\rho_{ideal}$ that have similar a-axis lattice parameter to the current samples. Yamamoto et al.[Yamamoto02] went as far as taking the ratio $\Delta\rho_{measured}/\Delta\rho_{ideal}$ as a definition of connectivity. The Rowell analysis produces the parameter A_F, which is the connected area fraction. Some correlation exists between A_F and J_c. Theoretically, we would expect J_c to be directly proportional to A_F, but in bulk samples this has never been reliably found. Because this is a normal state measurement, the presence of conductive phases at grain boundaries (such as Mg) might confuse the analysis because the analysis assumes a homogeneous material where grain boundaries are either superconducting or insulating. For this reason, the A_F values reported for $T_{HIP} = 1150^oC$ and above should be viewed skeptically. As described in Ch. 5 and 6, we can obtain $\Delta\rho_{ideal}$ from well-connected C-doped samples such as CVD filaments.[Wilke03,Wilke04] Application of the Rowell analysis to these data (using X values from Figure 7.1) gives the result in Figure 7.10. We see that A_F evolves rapidly over T_{HIP} between 900 and 1000.

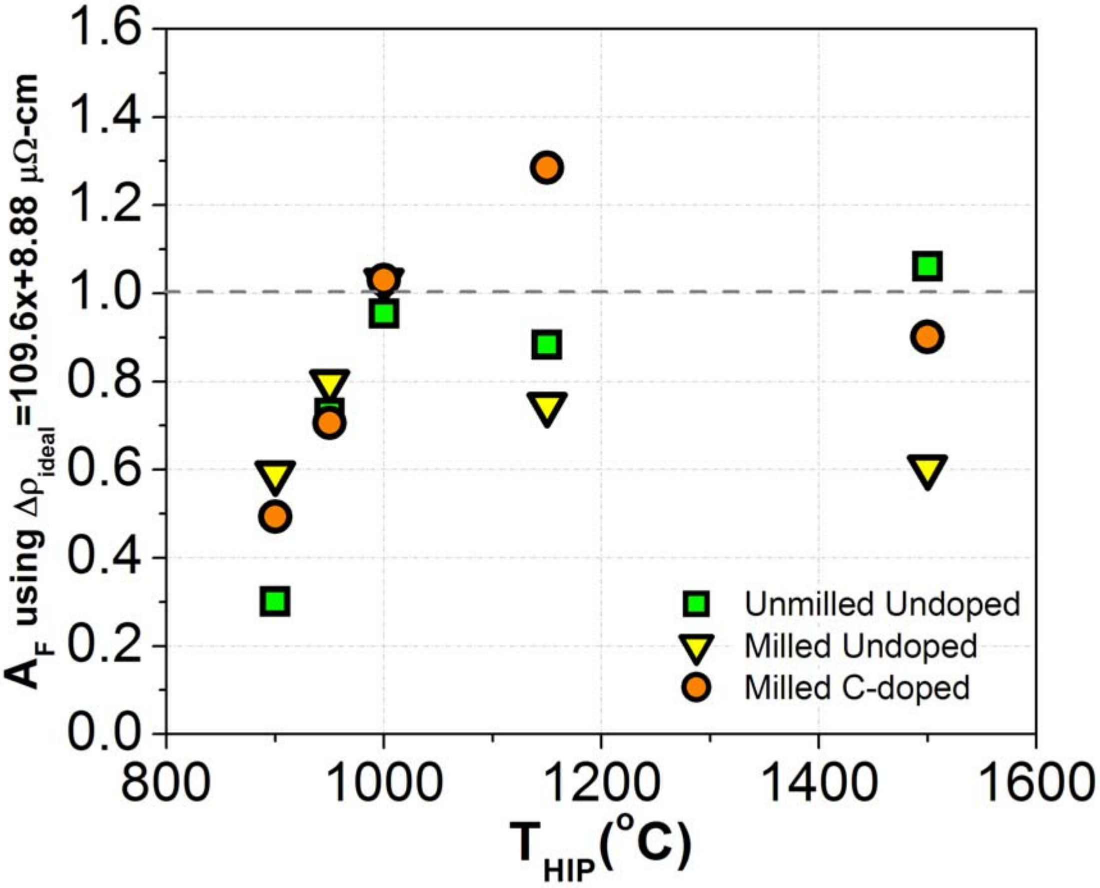

Figure 7.10 – Connected area fraction (A_F) derived from adapted Rowell analysis using $\Delta\rho_{ideal}$ selected based on compositions given in Figure 7.8. X from lattice parameter.

At T_{HIP}=900°C A_F was highest for the milled undoped sample (0.59), followed by the C-doped sample (0.49). The unmilled sample was poorly connected (A_F = 0.30). A_F increased rapidly with T_{HIP} up to 1000°C at which point the samples contained only small amounts of residual porosity. Yamoto et al.[Yamamoto02] predicted (for their samples) A_F ~ 0.4 for packing factor 0.8 and A_F~0.55 for packing factor 0.9. Comparing our densities from Table 7.I to A_F, we do find that samples with particularly low packing factor (such as unmilled 900^{o}C with P = 0.84) also have low A_F, but there does not seem to be a quantitative link. These A_F values are generally higher than those in Ch. 4-6 for similar processing and heat treatment. The reason for this difference is not clear, but there were several differences in processing. These samples were heat treated for 300 min at T_{HIP} compared to 200 min in Ch. 5 and 6, but the work in Ch. 4 also used 300 min. Another possibility is that this work was conducted with a new batch of powder in a recently refurbished glove box and so there was less powder oxidation. These samples also were heat treated in Nb lined tubes, while the previous work did not use the Nb liner.

The Rowell analysis also yields adjusted resistivity (shown in Figure 7.11) that is taken to be the true resistivity of the connected portion of the sample. Except for one sample, adjusted resistivity decreased monotonically with increasing T_{HIP} for each sample set. This indicates less electron scattering as T_{HIP} increased, which is particularly significant because in milled samples, this behavior was accompanied by a simultaneous decrease of T_c, which would be expected from *increased* electron scattering. Furthermore, as T_{HIP} increased, we saw either constant or increasing X (as measured by *a*-lattice parameter) which should result in the same or greater electron scattering from the dopant atoms. The observed decrease in ρ_A (in Fig. 7.11) runs counter to the compositional trend, and leads us to suggest that electron scattering results here from the superposition of a compositional and a non-compositional effect, and that the non-compositional effect anneals away with increasing T_{HIP}.

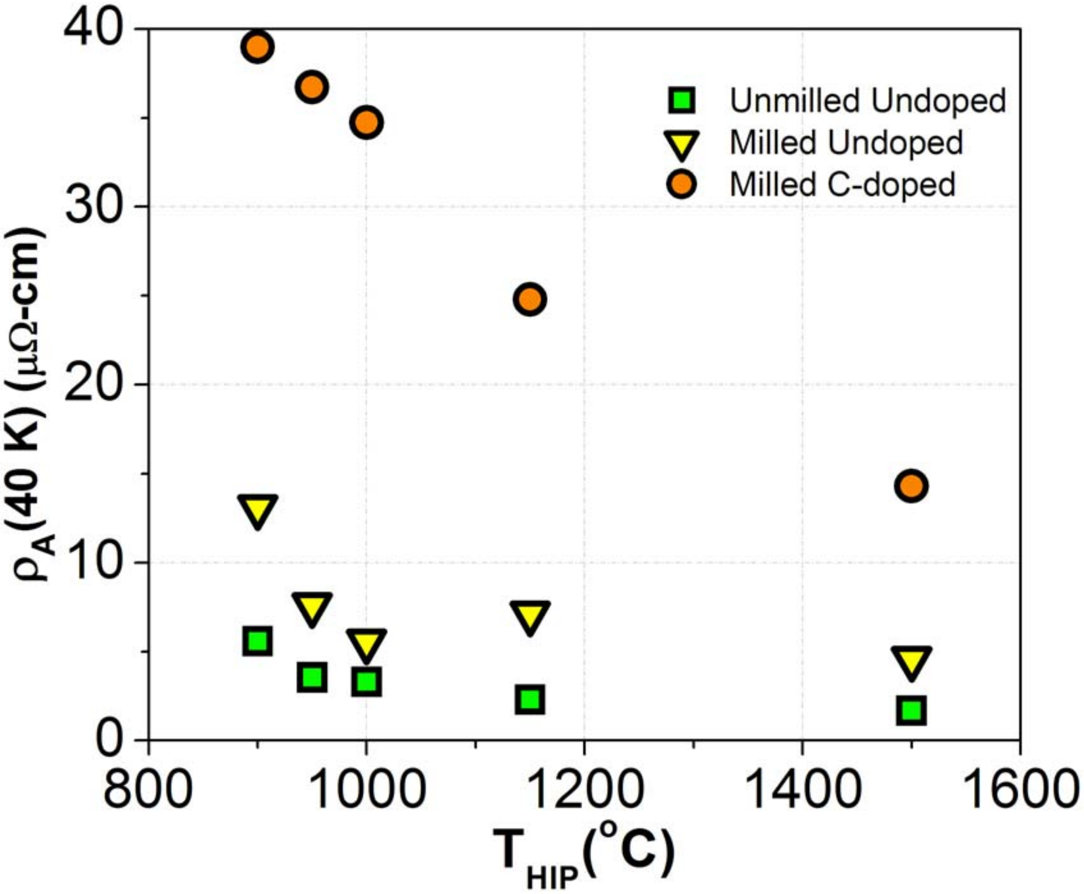

Figure 7.11 – Adjusted resistivity ρ_A derived from Rowell analysis using $\Delta\rho_{ideal}$ selected based on compositions given in Figure 7.8.

In fact, ρ_A scales with grain boundary area per unit volume (which goes as 1/d). Figure 7.12 shows ρ_A(40 K) plotted against 1/d where *d* is the estimated grain size given in Table 7.VI. ρ_A(40 K) increases linearly with 1/d for samples with similar composition, indicating that normal-state electron scattering is proportional to grain boundary density. This implies that non-compositional electron scattering effects are primarily the result of electron interaction with grain boundaries rather than intragranular defects. Normal state residual resistivity can be considered as the combined effects of C alloying and grain boundary scattering: $\rho_A(40\ K) = \rho_{alloying} + \rho_{GB}$. Adjusted resistivity is larger for the C-doped samples than for the nominally undoped samples because of greater electron scattering from dissolved C. This would seem to support (but not prove) the suggestion put forth in Ch. 6 that H_{c2}(H//c-axis) could be affected by grain size. Interband scattering would be expected from grain boundaries which would tend to decouple the bands and perhaps explain the lower T_c observed in the fine-grained milled undoped 900°C sample, and the depressed T_c observed by Braccini et al.[Braccini04]

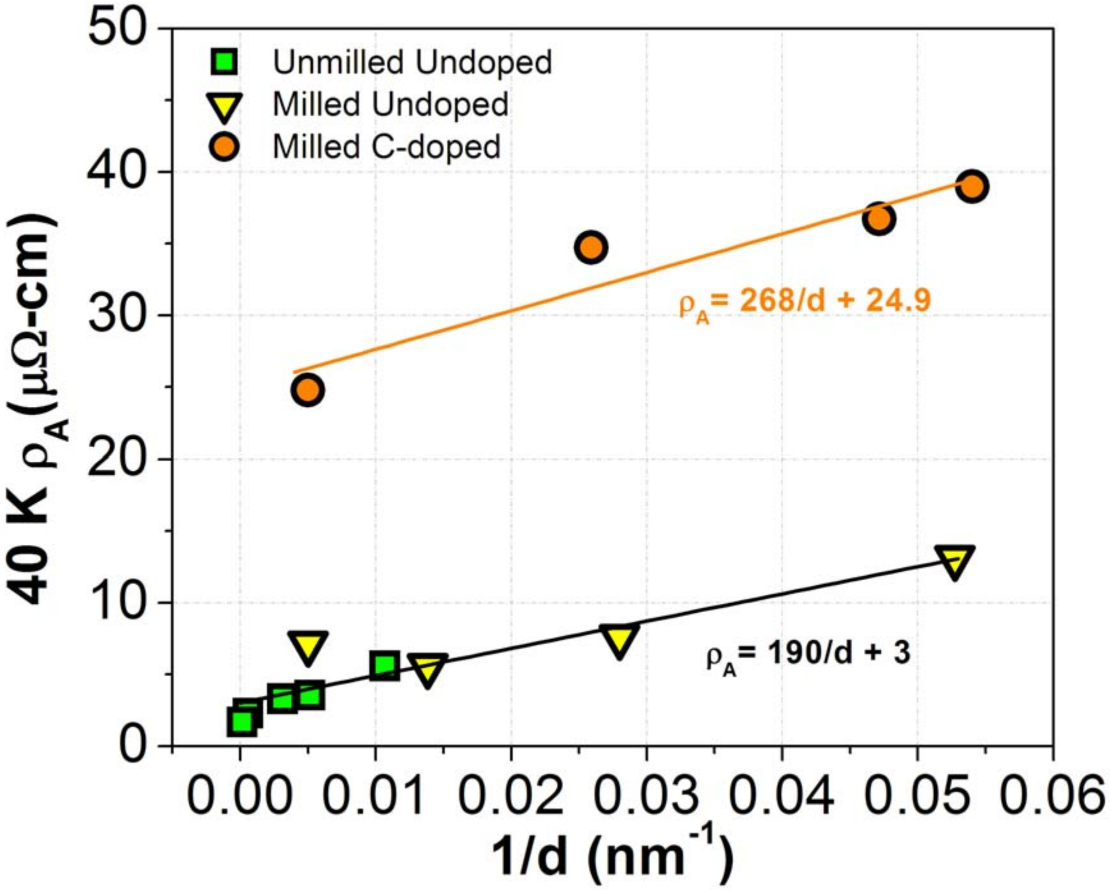

Figure 7.12 – Residual resistivity of hypothetical fully connected samples scales linearly with inverse grain size (1/d), indicating grain boundary electron scattering. Linear fits are for C-doped set and combined undoped set.

C-content was the largest determinant of H*, but non-compositional (and therefore microstructural) factors had a strong effect. In figure 7.13 we see that for samples with similar a-axis lattice parameter (and therefore similar inferred composition) H* scales linearly with 1/d and therefore grain boundary density. This scaling could be due to enhanced grain boundary flux pinning, or it could be due to enhanced H_{c2}(H//c-axis) resultant from grain boundary electron scattering effects. The H* increase with decreasing grain size was independent of H_{c2}(//ab), which did not show strong non-compositional effects. This could indicate the connection between H* and grain size might be through improved grain boundary flux pinning rather than H_{c2}(H//c). In order to resolve this issue, measurement of H_{c2}(H//c) may be necessary.

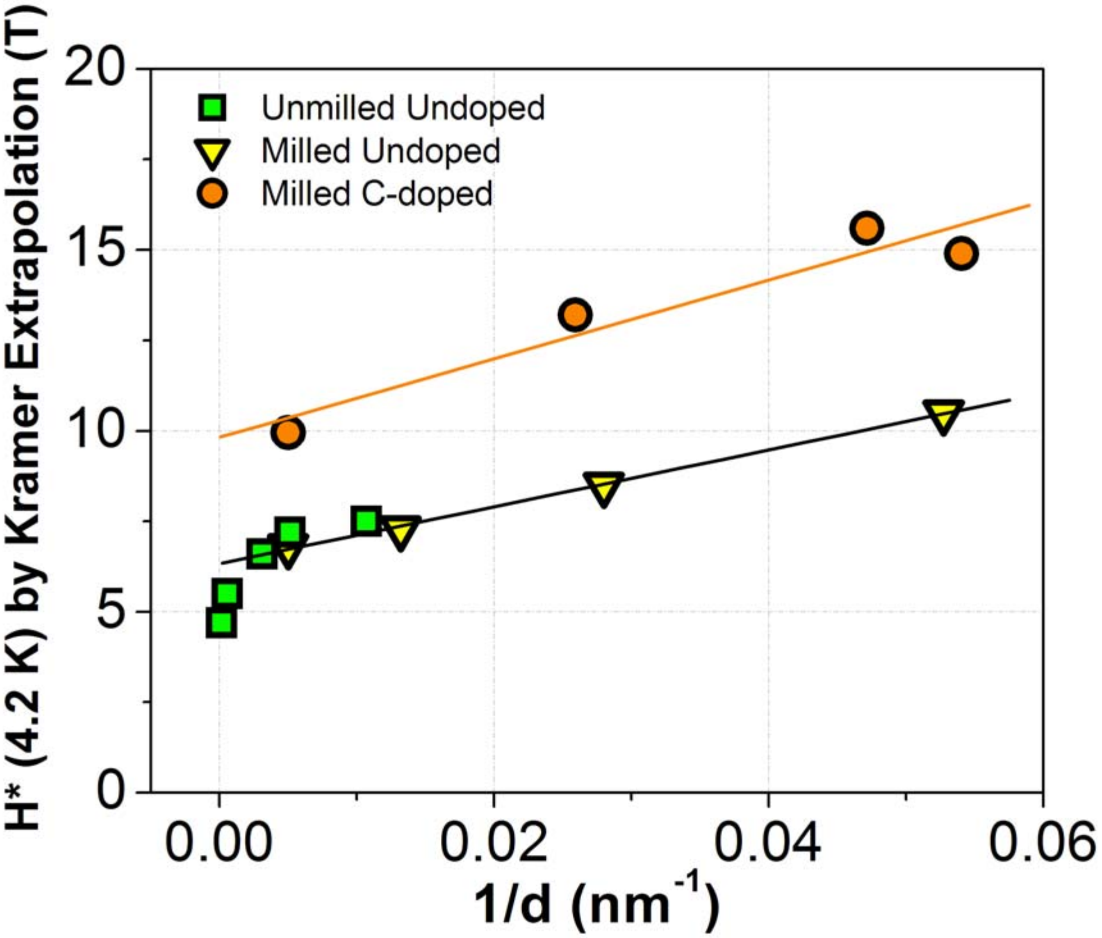

Figure 7.13 – Kramer extrapolated H* depends linearly on inverse grain size (1/d) in milled samples. Linear fits are for milled sets.

At low field J_c(H) is dominated by connectivity, while at high field it is mostly determined by H*. J_c dependence (especially for C-doped samples) on H is close to Kramer-like behavior over a range of fields where $J_c \sim h^{-0.5}(1-h)^2$. Where h ~ H/H*. Therefore comparing hypothetical samples A and B,

$$\frac{J_c(SampleA)}{J_c(SampleB)} \propto n \frac{H_A^{*\,-1/2}\left(1-\frac{H}{H_A^*}\right)^2}{H_B^{*\,-1/2}\left(1-\frac{H}{H_B^*}\right)^2} \tag{7.2}$$

Where *n* includes the field independent effect of A_F on J_c. A reasonable value for *n* would be somewhere between 0.1 and 10, based mainly on connectivity differences. According to this relationship, as H approaches H* of one of the samples, the other sample (with higher H*) will have the higher J_c. The constant *n* can determine whether the J_c(H) curves will cross, but the effect of *n* is minor if H_A* is significantly les than H_B*. On the other hand, at low field *b* is small and $J_c \sim nH^{*1/2}$ in which condition changes to connectivity (and therefore *n*) are more important than similar fractional changes to H*. When one considers that A_F can vary by a factor of 5 or more between samples, while H* rarely varies by more than a factor of 2 it becomes apparent that connectivity is the dominant factor controlling low-field J_c. This is close to what we see.

Since H* scales linearly with inverse grain size(1/*d*), it would be possible to replace the H* terms in the equation with $(m/d)+c$ where *m* and *c* are constants and the J_c ratio would then break down to connectivity, grain size, and some constants. It is tempting to attempt to quantify this model for low-field J_c as a function of A_F and grain size, but due to the lack of a quantitative relationship between J_c and A_F (we would have to invent one, such as a power law), and the limited size of our data set, the physical significance of any such relationship might be questionable.

7.5 Conclusions

J_c was primarily determined at low field by connectivity and at high field by H*. Connectivity increased rapidly in the T_{HIP} range 900-1000°C, probably because this region covers the transition from stage 1 to stage 3 sintering (probably stage 2 to stage 3 for milled undoped samples) This helps establish the range for optimum J_c when J_c is determined by connectivity. For fixed composition, H* scales with inverse grain size, therefore fine grains result in good high-field J_c. We determined that grain growth in MgB_2 (even when it contains abundant second phases) follows the expected Arrhenius relationship, with grain size significantly finer for milled compared to unmilled samples in the critical 900°C-1000°C T_{HIP} range. From this data we conclude the following: 1) because milling refines grains, raises H*, and facilitates sintering, milling is *always* beneficial to J_c at all fields. All *ex-situ* samples should be made with milled powder. 2) Since H* is controlled by grain size, and high-field J_c is dominated by H*, the best high-field samples actually had incomplete connectivity. The cost of full connectivity is grain growth, and for J_c at >8 T, 4.2 K, grain size is more important. 3) C-doping improves H* but does not improve low-field J_c. In fact, C-doping hindered A_F compared to undoped milled samples. At the same time, C-doping lowered T_c so that at 20 K, there is virtually no H* benefit to adding C. Therefore, C-doping is beneficial for operation at 4.2 K and 8 T or greater, but is not beneficial at 20 K.

A great deal of effort is currently devoted to discovery of new and better methods of C-doping. This work suggests that for operating conditions above ~15 K, or for H below 8 T at 4.2 K, undoped or very lightly doped MgB_2 is actually optimal. For those conditions, the most direct route to high J_c (and thus applications) is to work toward achievement of a combination of good connectivity while retaining the smallest possible grain size.

Chapter 8 – Bringing the Results Together

The goal of this thesis has been to optimize J_c(H) in ex-situ MgB_2. This work investigated the effects on J_c(H) of varying four processing parameters: variable air exposure, C-content, variable milling time, and heat treatment temperature. Interpretation was often difficult because 1) J_c is often determined by several simultaneously changing properties (i.e. low T_{HIP} gives increased H* but decreased A_F). And 2) many effects on J_c are temperature and field dependent. Thus our understanding is still somewhat phenomenological. In order to improve the material, we want to *predict* J_c(H) trends under hypothetical processing conditions. That requires knowledge of how J_c(H) is controlled by changing *properties* such as A_F and H* rather than *processing conditions* like T_{HIP}.

This chapter will first summarize what we know, enumerate the main variables influencing J_c(H,T) and explain how they relate to processing – as determined in the previous chapters. Then we will evaluate the comparability of samples between experiments and reach the following conclusions: 1) reproducible properties are not always obtained from the same synthesis parameters. 2) The effects of connectivity (A_F), grain size (d), and lattice composition (X) on J_c(H) are mostly consistent 3) Inconsistencies may be explained by an uncontrolled processing variable.

Then we will compare J_c(H) in samples from different experiments which differ in only one significant property, thus isolating the effects of that property. In practice, this is somewhat difficult due to the finite size of the sample set, and the need to fix numerous parameters. The results obtained should be regarded as somewhat speculative as the purpose of this exercise is understanding rather than proof. We will discover several correlations: 1) C-doping reduces low-field J_c. 2) J_c is almost directly proportional to A_F. 3) An additional variable exists – which we will suggest is intragrain pinning from dispersed second phases (such as MgO). We will relate this new information back to the main goal of J_c optimization. Finally, we will list a set of recommendations to obtain the best J_c for given H and T with this process, which should permit best-in-class samples to be tailored for H and T of application.

In all of this work, J_c(H) was mostly determined by two main factors, H* and connectivity. H* primarily determined high-field J_c(H) while connectivity was the most important influence low-field J_c(H). H* was controlled by both C-content and grain size. Therefore, the three most important properties controlling J_c were composition, grain size, and connectivity. This is expressed in Figure 8.1. The work in Ch. 4 – 7 established the relationships between processing and properties shown in the diagram, and the strong relationship between grain size and H*. The specific contributions of each chapter will now be summarized.

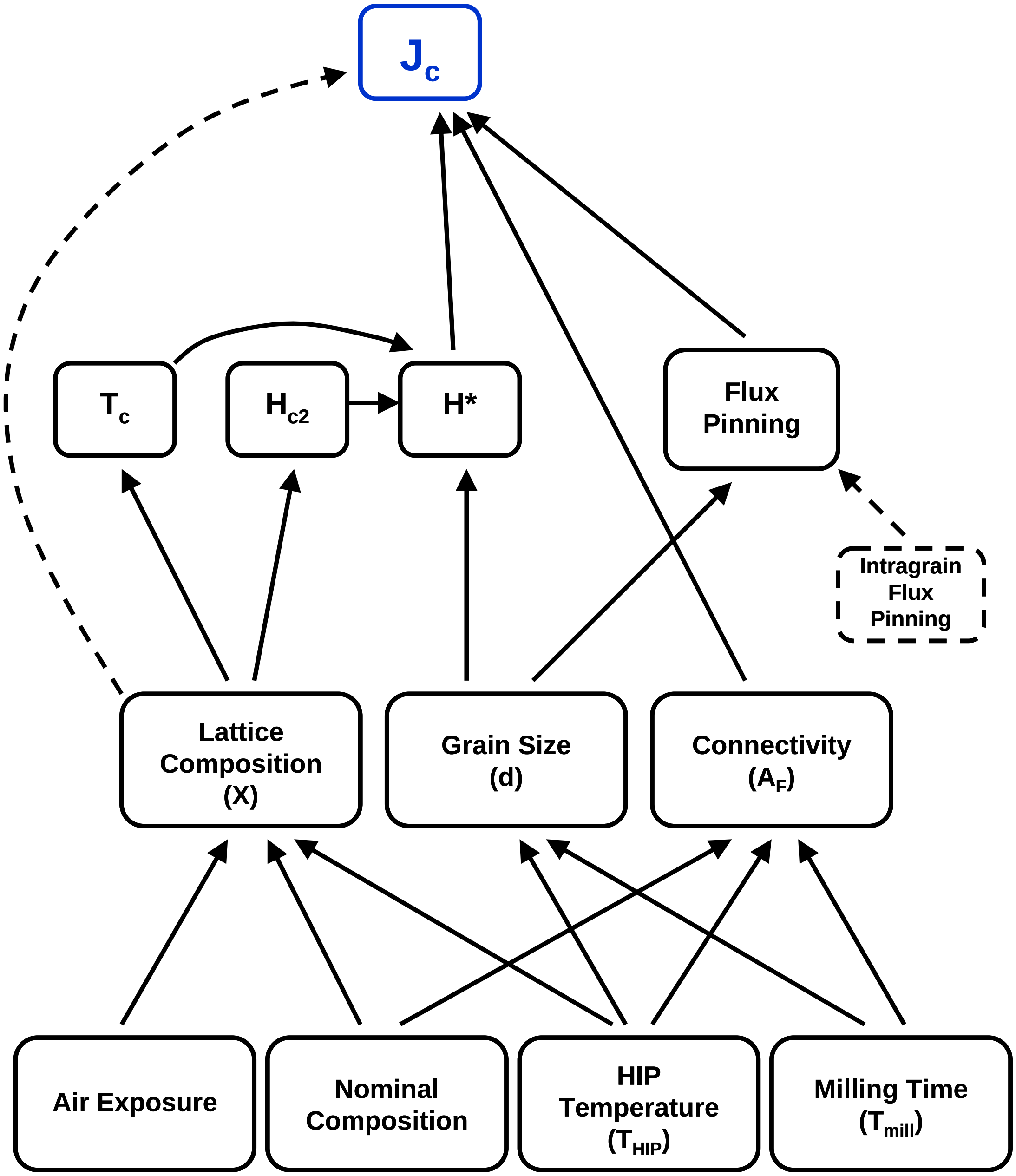

Figure 8.1 – Schematic diagram showing how processing and properties effect J_c – based on information from Ch. 4 – 7. Arrows represent strong effects. Dashed arrow indicates effects identified in this chapter.

In Ch. 4 air exposure resulted in increased lattice carbon content with only weak suppression of connectivity. The result was increased $H_{c2}(T)$ which boosted H*(4.2 K).

Ch. 5 showed that variable nominal composition strongly affects both lattice composition (which was expected) and connectivity. Effects of lattice composition on T_c and H_{c2} were similar to those established in single crystals (see Ch. 2). H_{c2} increase from C-doping strongly increased H*(4.2 K) from ~12 T (nominally undoped) to ~18 T (nominal X ~ 0.05). This was particularly beneficial to high field J_c. Overdoping beyond the C-solubility limit X~0.06 (also established in Ch. 7) decreased connectivity and thus degraded J_c at all temperatures and fields. Optimal C-content was X ~ 0.04 to 0.07. J_c(8 T, 4.2 K) increased from ~$2\text{x}10^4$ A/cm^2 in the nominally undoped case to ~$5\text{x}10^4$ A/cm^2 for X ~ 0.05.

Ch. 6 established the link between fine grains and high H*, and showed that fine (20 – 30 nm) grains could be obtained by long milling times on the order of 600 min. Fine grains were probably stabilized during the heat treatment by finely dispersed second phases. A slow connectivity decrease resulted from increased milling times. The t_{mill} = 3000 min sample had lower J_c at all (T, H) than samples with less milling. Peak J_c(8 T, 4.2 K) ~ 8.5 x 10^4 A/cm^2 was obtained at t_{mill} = 1200 min. A major conclusion of Ch. 5 and 6 was that high J_c results mainly from two factors: fine grains and good connectivity, with fine grains more important at high field.

Ch. 7 established that T_{HIP} strongly determines C-solubility, and therefore maximum lattice C-content. A_F improved rapidly from between ~0.3 (unmilled) and ~ 0.6 (milled undoped) to about 1 as T_{HIP} increased from 900°C to 1000°C. Increased T_{HIP} resulted in exponentially larger grains, but because final grain size also depends on initial grain size, milled samples had about a factor of 5-10 smaller grains than corresponding unmilled samples for T_{HIP} up to 1000°C. Furthermore, particle refinement by milling improved sintering at lower T_{HIP}, allowing reasonable connectivity (A_F~0.5) to be obtained while retaining fine (~20 nm) grains at 900°C.

As a result of these observations, most of the important relationships in Fig 8.1 were determined at least semi-quantitatively. A few important gaps remain in our knowledge. Based on these data, we do not know the quantitative relationship between A_F and J_c. The direct effect (if any) of changing lattice composition on J_c is unknown. The effects (if any) or intragrain flux pinning are unknown. We also do not know whether increase of H* by grain refinement is due to flux pinning, increased H_{c2}(//c), or a combination of both. Our understanding can be increased by comparison of samples between experiments.

8.1 – Comparability (reproducibility) of experiments

Even when air exposure is controlled, MgB_2 is subject to much larger sample-to-sample and set-to-set variation than more mature superconductors such as NbTi and Nb_3Sn. Even basic relationships as T_c(X) are still not well agreed upon (Ch. 2). In this section we will show that set-to-set variation is significant in this work, especially where sets were produced at different facilities. The cause of this variation is not clear, but could be related to surface oxidation of the starting powders. In some cases, samples with nominally identical processing conditions can have significantly different H* and H_{c2} without significant variation in other superconducting and normal state properties. There is an extreme paucity of published results where earlier work was quantitatively reproduced using different facilities, implying unpredictable variation in properties is a common problem in MgB_2. This may be related to uncontrolled and undocumented variation in H_{c2}(H//c-axis).

Eight samples were selected from Ch. 5-7 based on their mutual comparability. Their properties are listed in Table 8.I. These data can be used to evaluate sample to sample variation. For example, Sample 1 from the variable X study (Ch. 5) and Sample 2 from the milling time study (Ch.6) had identical processing parameters. In fact, Sample 2 had more C in the lattice ($X = 0.051$ compared to $X = 0.046$) which resulted in higher H_{c2}(25 K) (7.1 T compared to 6.7 T) and higher H^*(4.2 K) (17.2 T compared to 14.4 T). This variation in X may indicate a poorly controlled process variable such as C-contamination from an unidentified source. It may also result from the fact that Sample 1 and Sample 2 were made from different batches of powder, possibly with different amounts of prior air exposure.

Table 8.1 – Properties of various samples from different experiments. Resistivity values in μΩ-cm. J_c values in kA/cm^2. Magnetic Fields in T.

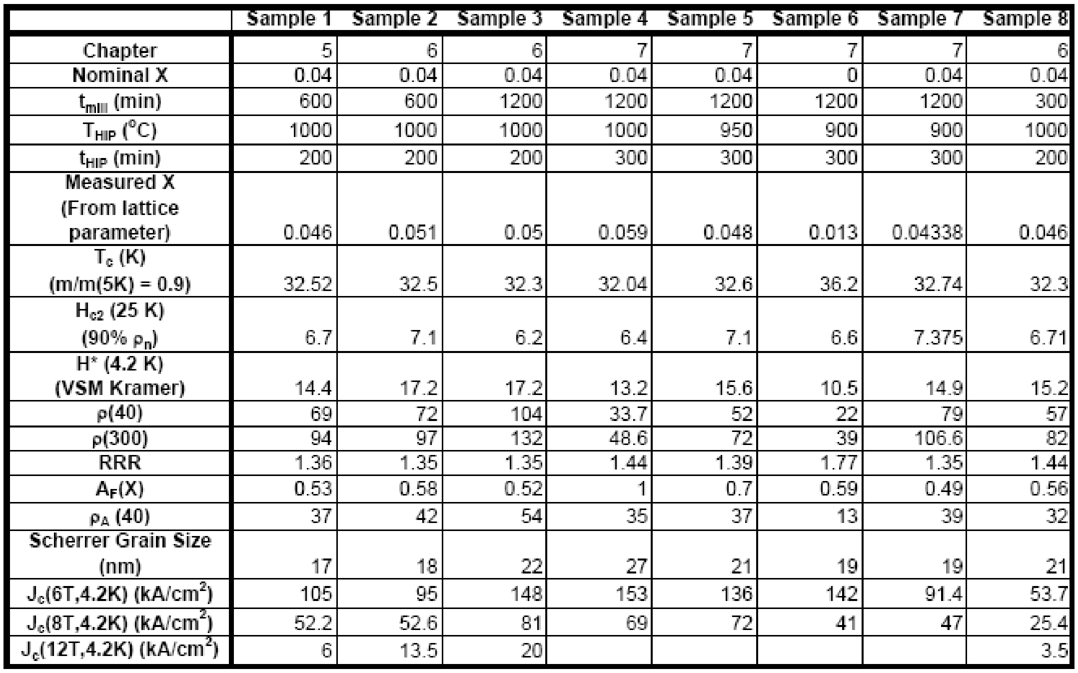

	Sample 1	Sample 2	Sample 3	Sample 4	Sample 5	Sample 6	Sample 7	Sample 8
Chapter	5	6	6	7	7	7	7	6
Nominal X	0.04	0.04	0.04	0.04	0.04	0	0.04	0.04
t_{mill} (min)	600	600	1200	1200	1200	1200	1200	300
T_{HIP} (°C)	1000	1000	1000	1000	950	900	900	1000
t_{HIP} (min)	200	200	200	300	300	300	300	200
Measured X (From lattice parameter)	0.046	0.051	0.05	0.059	0.048	0.013	0.04338	0.046
T_c (K) (m/m(5K) = 0.9)	32.52	32.5	32.3	32.04	32.6	36.2	32.74	32.3
H_{c2} (25 K) (90% ρ_n)	6.7	7.1	6.2	6.4	7.1	6.6	7.375	6.71
H* (4.2 K) (VSM Kramer)	14.4	17.2	17.2	13.2	15.6	10.5	14.9	15.2
ρ(40)	69	72	104	33.7	52	22	79	57
ρ(300)	94	97	132	48.6	72	39	106.6	82
RRR	1.36	1.35	1.35	1.44	1.39	1.77	1.35	1.44
A_F(X)	0.53	0.58	0.52	1	0.7	0.59	0.49	0.56
ρ_A (40)	37	42	54	35	37	13	39	32
Scherrer Grain Size (nm)	17	18	22	27	21	19	19	21
J_c(6T,4.2K) (kA/cm^2)	105	95	148	153	136	142	91.4	53.7
J_c(8T,4.2K) (kA/cm^2)	52.2	52.6	81	69	72	41	47	25.4
J_c(12T,4.2K) (kA/cm^2)	6	13.5	20					3.5

We now compare Sample 3 (Ch. 6) with Sample 4 (Ch.7). The only nominal processing difference between Sample 3 and Sample 4 is that Sample 4 was heat treated for 300 minutes compared to 200 minutes for Sample 3. The 100 min t_{HIP} difference does not account for the significant differences in measured properties. Compared to Sample 3, Sample 4 had much cleaner resistivity properties (ρ_A = 33.7 μΩ-cm compared to 104), larger grains (d = 27 nm compared to 20), vastly improved A_F (1 compared to 0.52), and much lower H*(4.2 K) (13.2 T compared to 17.2). These differences were is spite of Sample 4 containing more C (X = 0.059 compared to 0.05). There were actually a number of subtle processing differences that are note easily quantified. Sample 4 was part of Ch.7, an experiment carried out at the ASC facility in Tallahassee, FL. The experiments presented in Ch. 4-6 were carried out at the ASC facility in Madison, WI. Processing in Tallahassee differed in three main ways. 1) A different lot of MgB_2 powder was used. 2) A different glove box was used for powder preparation. The Tallahassee box had fresh oxygen and water getter materials, and was filled with Ar rather than N_2. 3) HIP cans at Tallahassee were lined with Nb foil, reducing the possibility of contamination due to direct contact between the pellet and the 304 stainless steel tube. 4) The Tallahassee heat treatments were carried out in a different HIP unit, where T_{HIP} may have been slightly different.

Of the four processing differences, the most alarming is the possibility of different T_{HIP}, but comparison of Sample 3 to Sample 5 (heat treated at 950°C) shows many the of same qualitative differences, so any differences in T_{HIP} were probably minor. The most significant factor may have been variation in the starting powder. More oxide contamination in Sample 3 than in Sample 4 could have inhibited sintering and grain growth.

We have therefore identified imperfect process reproducibility. For example, Samples 1-5 all had nominal $X = 0.04$, but measured X varied from 0.046 to 0.059. On the other hand, J_c(H) trends do respond in predictable ways to the secondary properties (such as H*, connectivity) but the effects are sometimes complex, as we will see in the next section.

8.2 - Inter-experiment Comparisons

According to Fig. 8.1 J_c(H) is controlled lattice C-content, grain size, and connectivity. In order to understand how those properties relate, and identify any additional influences on J_c, we can examine J_c(H,T) in groups of samples where only one important property changes.

For example, we can isolate the effect of lattice C-content (X) on H* and J_c(H) for fixed A_F and fixed grain size by comparing Sample 1, Sample 2, and Sample 6 from Table 8.I. First, A_F was very similar (0.53 – 0.59), so field-independent J_c differences due to connectivity should be negligible. Second, all three samples have similar grain size (17-19 nm). Therefore grain boundary flux pinning should be similar for all three samples. The grain size contribution to H* should also be the same for all three samples. Any observed H* differences should therefore be purely compositional. The effect of H* on low-field J_c is negligible. According to the scaling rule $J_c \propto h^{-1/2}(1-h)^2$, where h = H/H^*, H* ~ 14 T and H < 0.2 T gives dJ_c / dH* ~ 5% per Tesla. Figure 8.2 shows J_c(H) for the three samples at 4.2 K and 20 K.

Several observations can be made. At 4.2 K and 7.25 T, the three samples have similar J_c (For Samples 1, 2, and 6 (respectively) J_c(7.25 T, 4.2 K) =68.7, 65.0, and 67.9 KA/cm^2). At H > 8 T, J_c(4.2 K) ranks in order of H* (and C-content), as expected. But for H < 7.5 T, J_c(4.2 K) ranks in *reverse* order of both C-content and H*, even though all three samples have similar A_F. At 20 K all three samples have about the same H* making the differences in J_c very clear. This result suggests a *connectivity and grain size independent* suppression of low-field J_c by increased C-doping.

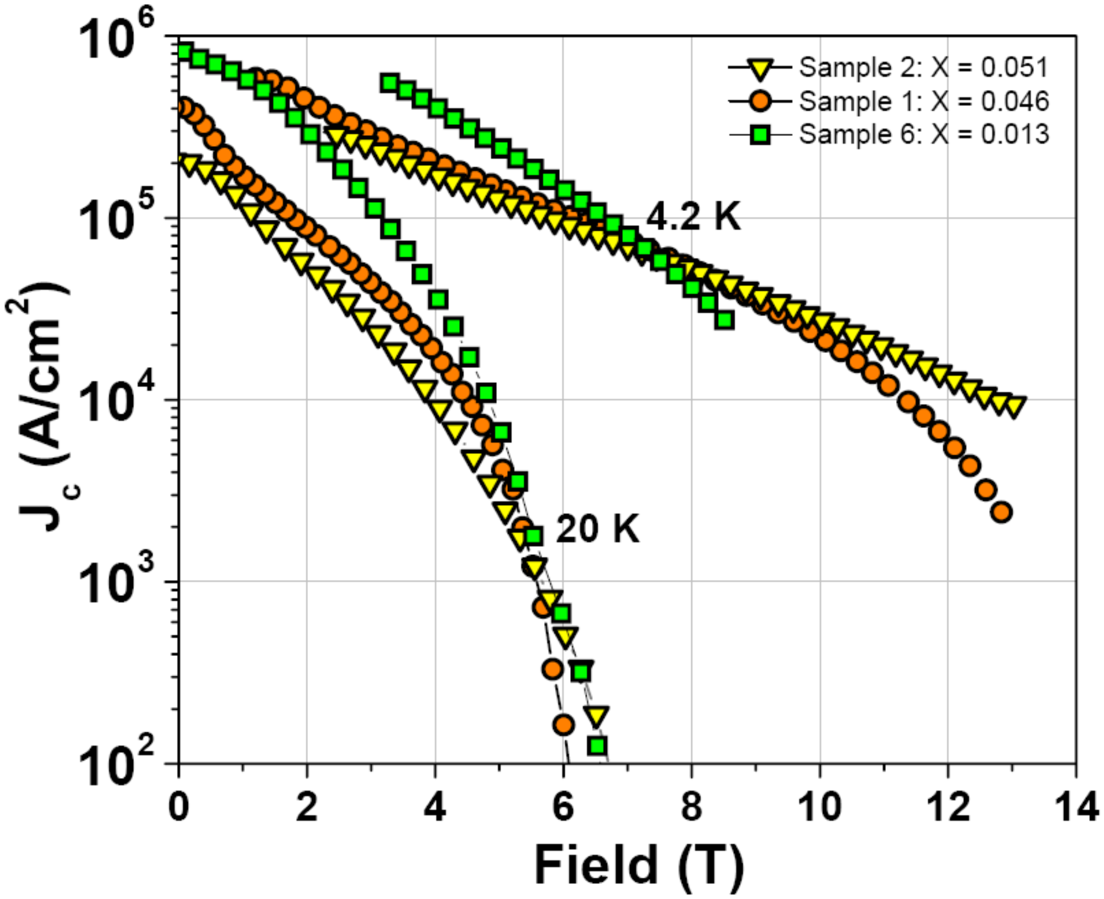

Figure 8.2 – J_c(H) at 4.2 K and 20 K for samples having different H* and (and therefore X) but similar grain size and A_F.

This data is significant because it indicates that to optimizing low-field J_c(H) at any temperature down to and including 4.2 K requires *adding no carbon* to the as-received powder. At 4.2 K, C-doping is only useful because it raises H* and thus high-field (H > 7.5 T) J_c. At 20 K C-doping has no utility whatsoever. This result was not entirely clear in Ch. 5 because J_c(H) comparison was complicated by systematic changes in several parameters, as well as large non-systematic sample to sample variation (particularly in A_F).

Connectivity is now widely recognized[Iwasa01] within the community to be very important to J_c. Imperfect connectivity can arise from two sources: current blockage by non-superconducting phases (such as oxides), or imperfect sintering. In *in situ* work, current blockage due to oxides has a large effect. Jiang et al.[Jiang01] have shown that in-situ MgB_2 can have A_F decreased by a factor of 2 when oxides are present on the surface of B precursor powders. However, connectivity in milled *ex situ* samples is not significantly affected by oxidation of the starting powder surfaces. TEM electron diffraction (By Ye Zhu) from our ex-situ milled samples showed MgO spots (Figure 8.3) from finely dispersed particles, but continuous grain boundary oxides analogous to those found in *in situ* samples[Jiang01] have not been found.

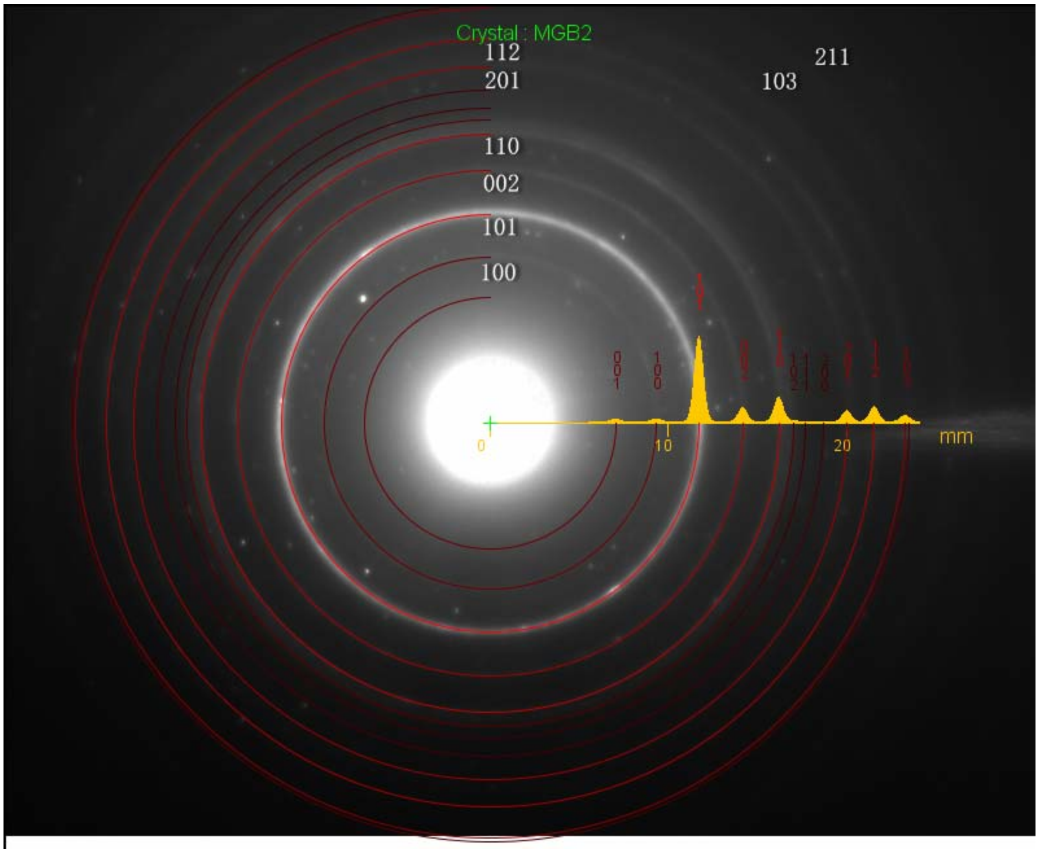

Figure 8.3 - TEM diffraction by Ye Zhu – Small spots are MgO.

In *in situ* processing, B powders have essentially no free surfaces created during processing and therefore continuous oxide layers are present during reaction. These layers 1) inhibit sintering between reacted particles and 2) block supercurrent. In milled ex situ MgB_2, fresh surface is created by particle attrition during milling. Furthermore, we have observed that particle size only decreases significantly during the initial few minutes of milling. This implies that particle cold-welding takes place in the mill. As a result, any oxide phases are not only pulverized, but the pieces are actually milled into particle interiors. Milled powder particles therefore contain a fine dispersion of oxide nano-particles and have fairly clean surfaces. This condition can actually improve performance, as will be discussed later when we compare two samples from the milling time set.

The hypothesis that milling negates the deleterious effects of powder oxidation on connectivity can be tested by deliberately inducing surface oxidation in ex-situ powder prior to milling. The result might be increased J_c coupled with only a small decrease in A_F. On the other hand, oxidation of powders *after* milling might have a strong detrimental effect on sintering behavior and therefore J_c.

Then the most significant obstacle to connectivity in milled, ex-situ material is incomplete sintering. This was shown in Ch. 7 when aggressive heat treatment resulted in $A_F \sim 1$ for each sample set. However, A_F and J_c have not been quantitatively linked in these samples because of other influences changing simultaneously with A_F. By comparing samples with similar non-connectivity properties, we can further establish the link between A_F and J_c.

In order to determine the effect of A_F, four samples were chosen for comparison based on their similar composition ($0.043 \leq X \leq 0.048$), grain size ($17\text{ nm} \leq d \leq 21\text{ nm}$) and H* ($14.4\text{ T} \leq H^* \leq 15.6$). They were Sample 1 ($A_F$=0.53), Sample 5 ($A_F$=0.7), Sample 7 ($A_F$=0.49), and Sample 8 ($A_F$=0.56). J_c(H) curves for those samples appear in Figure 8.4.

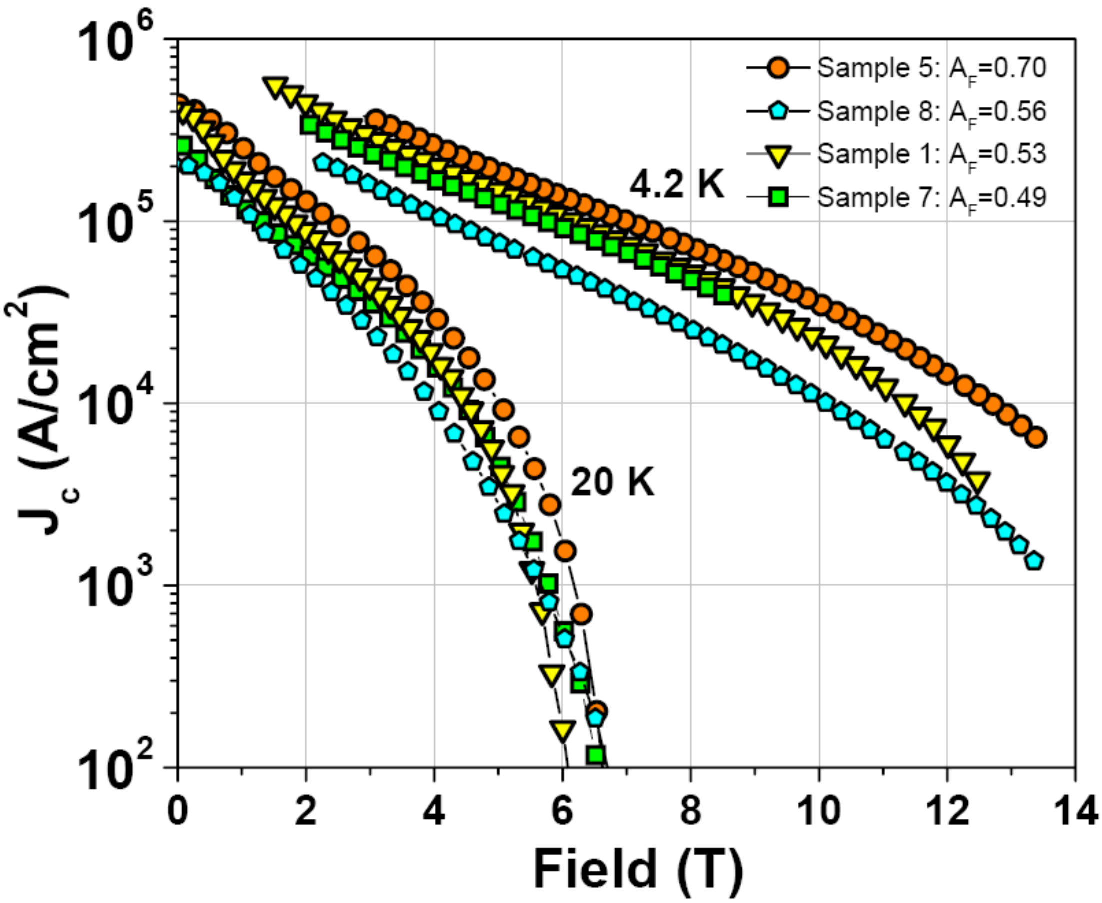

Figure 8.4 – J_c(H) for samples with similar X, d, and H* but different A_F.

Several observations can be made from these data. First, the J_c(H) curves are nearly parallel indicating that the effect of A_F on J_c is field independent. Second, J_c ranks in order of A_F for all but one of the samples. We will postpone discussion of the outlier until later in the section. Third, A_F variation from 0.49 to 0.7 (an increase of 43%) resulted in J_c(H) increases between 50% and 100%, depending on T and H. This is only slightly larger than the expected value based on the idea that J_c should be directly proportional to the active cross sectional area. This result does not necessarily indicate direct proportionality between J_c and A_F over all A_F but does tend to support the work of Yamamoto et al.[Yamamoto02]

The outlier (sample 8) implies that at least one other variable governs the magnitude of J_c(H), besides those fixed in our sample selection. The uncontrolled variable may be intragrain flux pinning. In order to isolate the possible effect of intragrain flux pinning, it is necessary to fix all of the other influences on J_c. Those are (From Fig 8.1) C-content, H*, grain size, and A_F. In our data set, there were only two comparable samples: Sample 2 and Sample 3 from Table 8.I. For the two samples, lattice X was 0.05 – 0.051, H* was 17.2 T, grain size was 18 – 22 nm, and A_F was 0.52 – 0.58. Table 8.I shows that J_c*(Sample 3) ~ 1.5* J_c*(Sample 2)* – A very significant difference! Of the four factors controlling J_c, only flux pinning was not directly fixed in this comparison. We therefore conclude that the difference in J_c between Sample 2 and Sample 3 is a result of a *flux pinning contribution independent of grain size*.

The pinning force curves for Samples 2 and 3 are shown in Figure 8.5 at 10 K – the lowest T for which there exists complete data. The black line is $1.5 \times F_P(Sample2)$. The pinning force curves for Sample 2 and Sample 3 are very similar in shape, with a factor of 1.5 difference in magnitude. This observation suggests that at least half of the pinning force in Sample 3 was provided by some mechanism other than grain boundary pinning. The most likely possibility seems to be intragranular pinning. We suggest (but cannot yet prove) that the intragranular pinning centers are finely dispersed oxide particles generated by the break-up of oxidized particle surface layers during milling. We further suggest that this is the main uncontrolled variable affecting the results in this thesis.

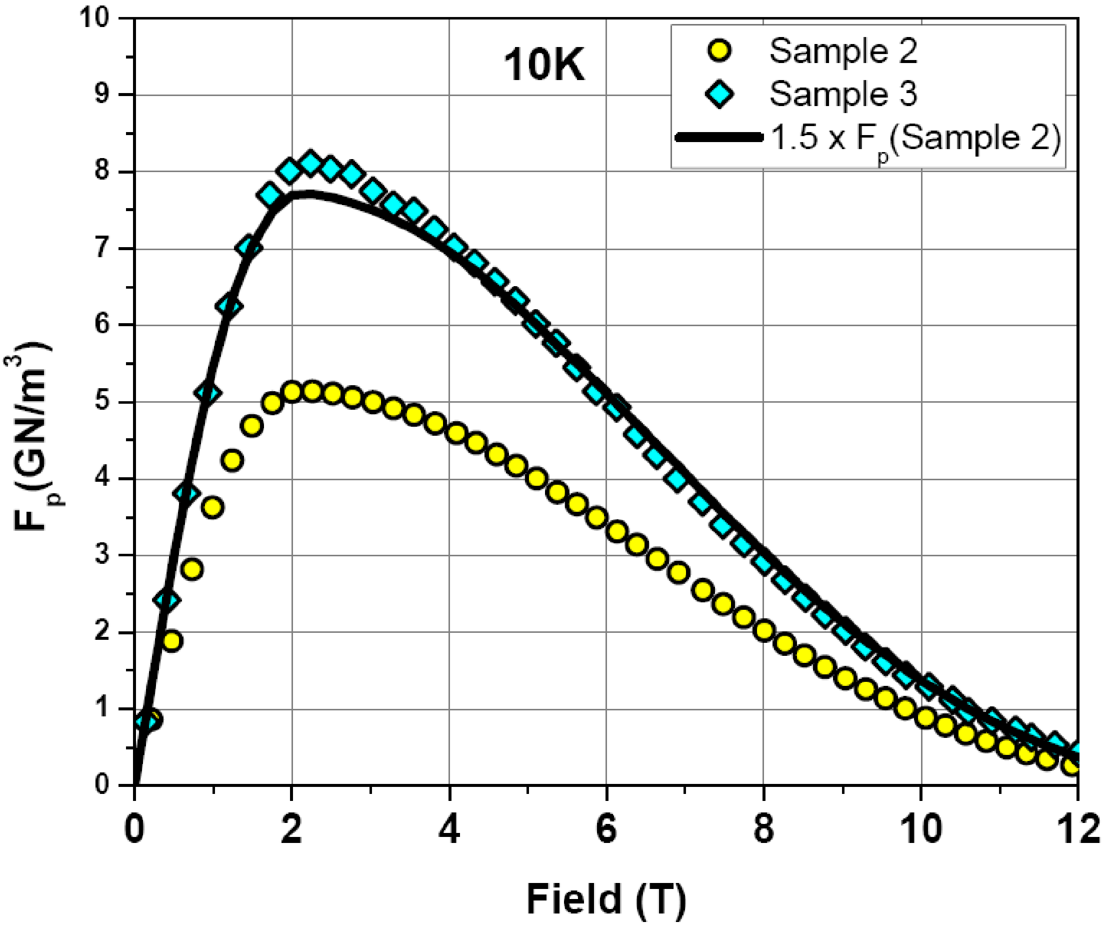

Figure 8.5 – Pinning force curves for two samples with similar X, d, A_F, and H*.

In this section we have reached several interesting conclusions. We discovered that C-doping significantly depresses low-field J_c and argued that C-doping is not beneficial for conductor operation at any T above 20 K, and at 4.2 K C-doping is only beneficial above about 7 T. We showed that J_c is close to directly proportional to A_F, and suggested that oxides on particle surfaces prior to milling do not significantly affect A_F in these samples. We also suggested that intragrain flux pinning is the major source of seemingly random sample to sample J_c variation, and that beneficial intragrain pinning effects may result from oxidation of powder surfaces prior to milling. We therefore suspect that powder oxidation prior to milling is actually beneficial to J_c(H).

8.3 – Summary

As in any material, the properties of MgB_2 are determined by composition and microstructure which in turn depend on processing. In previous chapters we investigated how our three main processing parameters (nominal composition, milling time, and HIP temperature) influenced superconducting and normal state properties, and ultimately J_c(H,T). Our observations allowed us to construct the diagram in Figure 8.1. We identified three primary properties (lattice C-content, grain size, and connectivity) which controlled J_c(H) and were themselves determined by the processing parameters. We also suggested intragrain pinning contributed to J_c(H). Some influences of the primary properties on J_c(H) are indirect, working through secondary properties such as H_{c2}, H*, and flux pinning. Each of those relationships has been outlined in this document.

Because changes in the processing parameters often result in changes to multiple primary and secondary properties, J_c trends observed in previous chapters were often the summation of several effects. By comparing samples between sets in this chapter we were able to effectively vary single properties and explore the effect on J_c(H). In this way we clarified the effect of A_F on J_c, identified a direct effect of lattice C-content on low-field J_c, and identified powder oxidation as a major source of unintended variation in properties.

As a result of this work, we have identified the meaningful variables that influence J_c(H,T) - and how they change as a function of processing parameters. With this knowledge we understand how to get the best J_c for a given H and T. These recommendations follow.

1) Milling is a highly beneficial process. It refines grains, facilitates sintering, breaks up particle surface layers, and introduces flux pinning centers. Milling therefore raises H*, A_F, and J_c. Milling should always be applied in ex-situ powder processing. In C-doped material, the optimum milling time was around 1200 min.

2) C-doping is the most effective way to increase H*(4.2 K) beyond 10 T. Maximum J_c(12 T) can be achieved by X=0.04 - 0.07. However, C should *not* be added if optimizing J_c for any temperature above about 10-15 K or for H < 7.5 T at 4.2 K. At low H or high T, carbon reduces J_c.

3) Grain size is extremely important to J_c because fine grains increase H*. It is not known whether this is strictly a flux pinning phenomenon or if H_{c2}(H//c-axis) is also improved. It is most important to retain fine grains for operation at high fields.

4) Connectivity has a field-independent effect on J_c. It can be indexed by Rowell A_F. For reasonably well-connected samples (A_F~0.5) small changes in A_F appear to cause similar changes in J_c but the scaling relationship is not known for large or small A_F. For low-field operation, good connectivity should be obtained even at the cost of some grain growth. Connectivity in milled ex-situ samples is fairly independent of particle air exposure prior to milling (see Ch. 4), but highly dependent on sintering.

5) Because they are both thermally activated diffusional processes, sintering and grain growth occur simultaneously. However, in undoped milled material it is possible to achieve reasonable connectivity while retaining ~20 nm grains by heat treating at 900-950°C.

6) Intragranular flux pinning is present in at least some samples, and can favorably influence J_c(H). It is believed to result from the pulverized remnants of oxide surface layers originally present on powder particles prior to milling. One way to further improve J_c(H) might be to increase powder oxidation prior to milling or add MgO. Under no circumstances should powders be allowed to oxidize after milling.

These recommendations facilitate co-optimization of several parameters, but J_c is fundamentally limited by the competition between grain size and sintering. It may be possible to pin grain boundary motion to some extent (see 5, above) with second phase nano-dispersions, but in these experiments the effect was limited. While some tactics (see 6, above) might improve J_c beyond the values in this thesis, simple mill-and-sinter processing is unlikely to achieve J_c(8 T, 4.2 K) much greater than that of NbTi. In order to further improve the bulk material one of two breakthroughs must occur. Either H_{c2} must be raised to approximate that of some films, or grain growth must be stagnated at small grain size so that large grain boundary F_p can be combined with full connectivity. The author hopes that the seeds to at least one of those breakthroughs might be sown by this thesis.

References

[Angst01] Angst M, Bud'ko S L, Wilke R H T and Canfield P C (2005) Difference between Al and C doping in anisotropic upper critical field development in MgB_2. *Phys. Rev. B* **71** 144512

[Avdeev01] Avdeev M, Jorgensen J D, Ribeiro R A, Bud'ko S L and Canfield P C (2003) Crystal chemistry of carbon-substituted MgB_2. *Physica C: Superconductivity* **387**, 301

[Bean01] Bean C P (1962) Magnetization of hard superconductors *Phys. Rev. Lett.* **8** 250

[Bellingeri01] Bellingeri E, Malagoli A, MOdica M, Braccini V, Siri A S and Grasso G (2003) Neutron scattering studies of superconducting MgB_2 tapes. *Supercond. Sci. Technol.* **16** 276

[Bhatia01] Bhatia M, Sumption M D, Collings E W, Dregia S (2005) Increases in the irreversibility field and the upper critical field of bulk MgB_2 by ZrB_2 addition. *Applied Physics Letters* **87**, 042505

[Bhatia02] Bhatia M, Sumption M D and Collings E W (2005) Effect of various additions on upper critical field and irreversibility field of in-situ MgB_2 superconducting bulk material *IEEE Trans. Appl. Supercond.* **15** 3204

[Bonney01] Bonney L A, Willis T C and Larbalestier D C (1995) Dependence of critical current density on microstructure in the $SnMo_6S_8$ Chevrel phase superconductor. *J. Appl. Phys.* **77** 6377

[Braccini01] Braccini V, Cooley L D, Patnaik S, Larbalestier D C, Manfrinetti P, Palenzona A, Siri A S, (2002) Significant enhancement of irreversibility field in clean-limit bulk MgB_2. *Applied Physics Letters* **81**, 24

[Braccini02] Braccini V, Nardelli D, Penco R, Grasso G (2007) Development of ex situ processed MgB_2 wires and their applications to magnets *Physica C: Superconductivity* **456**, 209

[Braccini03] Vraccini V, Gurevich A, Giencke J E, Jewell M C, Eom C B, Larbalestier D C, Pogrebnyakove A, Cui Y, Liu B T, Hu Y F, Redwing J M, Li Q, Xi X X, Singh R K, Gandikota R, Kim J, Wilkens B, Newman N, Rowell J, Moeckly B, Ferrando V, Tarantini C, Marre D, Putti M, Ferdeghini C, Vaglio R, Haanappel E (2005) High-field superconductivity in alloyed MgB_2 thin films. *Physical Review B* **71**, 012504

[Braccini04] Braccini V, Nardelli D, Malagoli A, Tumino A, Fanciulli C, Bernini C, Siri A S, and Grasso G (2005) MgB_2 tapes with non-magnetic sheath: effect of sintering temperature on the superconducting properties. *IEEE Trans Appl. Supercond.* **15** 2, 3211

[Budko01] Bud'ko S L, Canfield P C and Kogan V G (2002) Magnesium diboride: Basic physical properties and high upper critical field anisotropy *Physica C: Superconductivity.* **382** 85

[Budko02] Bud'ko S L, Lapertot G, Petrovic C, Cunningham C E, Anderson N and Canfield P C (2001) Boron Isotope Effect in Superconducting MgB_2 *Physical Review Letters* **86**, 1877

[Canfield01] Canfield P C, Crabtree G W, (March 2003) *Physics Today*, 34

[Canfield02] Canfield P C, Bud'ko S L, and Finnemore D K (2003) An overview of the basic physical properties of MgB_2 *Physica C: Superconductivity* **385**, 1

[Canfield03] Canfield P C, Finnemore D K, Bud'ko S L, Ostenson J E, Lapertot G, Cunningham C E and Petrovic C (2001) Superconductivity in dense MgB_2 wires. *Phys. Rev. Let.* **86** 11, 2423

[Chen01] Chen S K, Glowacki B A, MacManus-Driscoll J L, Vickers M E, and Majoros M (2004) Influence of in situ and ex situ ZrO_2 addition to the properties of MgB_2 *Supercond. Sci. Technol.* **17** 243

[Chen02] Chen S K, Yates K A, Blamire M G and MacManus-Driscoll J L (2005) Strong influence of boron precursor power on the critical current density of MgB_2. *Supercond. Sci. Technol.* **18** 1473

[Chen03] Chen S K, Wei M and MacManus-Driscoll J L (2006) Strong pinning enhancement in MgB_2 using very small Dy_2O_3 additions. *Appl. Phys. Let.* **88**, 192512

[Chen04] Chen J, Ferrando V, Orgiani P, Pogrebnyakov A V, Wilke R H T, Betts J B, Mielke C H, Redwing J M, Xi X X, and Li Q (2006) Enhancement of flux pinning and high-field critical current density in carbon-alloyed MgB_2 thin films. *Phys. Rev. B* **74** 174511

[Chiang01] Chiang Y M, Birnie III D, Kingery D W (1997) *Physical Ceramics* (John Wiley & Sons)

[Cooper01] Cooper J R, Carrington A, Meeson P J, Yelland E A, Hussey, N E, Balicas L, Tajima S, Lee S, Kazakov S M, Karpinski J (2003) de Haas-van Alphen effect in MgB_2 crystals. *Physica C: Superconductivity* **385**, 75

[Coble01] Coble R L (1961) Sintering Crystalline Solids. I. Intermediate and Final State Diffusion Models. *J. Appl. Phys* **32** 5, 787

[Cullity01] Cullity B D (1978) *Elements of X-Ray Diffraction 2nd ed.* (Addison-Wesley)

[Dou01] Dou S X, Soltanian S, Yeoh W K and Zhang Y (2005) Effect of nano-particle doping on the upper critical field and flux pinning in MgB2 *IEEE Trans. Appl. Supercond.* **15** 3219

[Eltsev01] Eltsev Y, Nakao K, Lee S, Masui T, Chikumoto N, Tajima S, Koshizuka N, and Murakami M (2002) Anisotropic resistivity and Hall effect in MgB_2 single crystals. *Phys. Rev. B* **66** 150504

[Eom01] Eom C B, Lee M K, Belinky L J, Song X, Cooley L D, Naus M T, Patnaik S, Jiang J, Rikel M, Polyanskii A, Gurevich A, Cai X Y, Bu S D, Babcock S E, Hellstrom E E, Larbalestier D C, Rogado N, Regan K A, Hayward M A, He T, Slusky J S, Inumaru K, Haas M K, and Cava R J (2001) High critical current density and enhanced irreversibility field in superconducting MgB_2 thin films *Nature* **411** 558

[Evetts01] Evetts J (ed) 1992 *Concise Encyclopedia of Magnetic and Superconducting Materials* (Oxford: Pergamon)

[German01] German R M (1984) *Powder Metallurgy Science* (Metal Powder Industies Federation)

[Godeke01] Godeke A (2006) A review of the properties of Nb_3Sn and their variation with A15 composition, morphology, and strain state. *Supercond. Sci. Technol.* **19** R68.

[Goldacker01] Goldacker W, Schlachter S I, Obst B, Liu B, Reiner J and Zimmer S (2004) Development and performance of thin steel reinforced MgB_2 wires and low-temperature in situ processing for further improvements. *Supercond. Sci. Technol.* **17** S363.

[Grasso01] Grasso G, Malagoli A, Ferdeghini C, Roncallo S, Braccini V, Siri A and Cimberle M (2001) Large transport critical currents in unsintered MgB_2 superconducting tapes. *Appl. Phys. Let.* **79** 2, 230

[Gumbel01] Gumbel A, Eckert J, Fuchs G, Nenkov K, Muller K H and Schulz L (2002) Improved superconducting properties in nanocrystalline bulk MgB_2. *Appl. Phys. Lett.* **80** 15, 2725

[Gumbel02] Gumbel A, Perner O, Eckert J, Fuchs G, Nenkov K, Muller K H and Schultz L (2003) High density nanocrystalline MgB_2 bulk superconductors with improved pinning. *IEEE Trans. Appl. Supercond.* **13** 2, 3064

[Gurevich01] Gurevich A, Patnaik S, Braccini V, Kim K H, Mielke C, Song X, Cooley L D, Bu S D, Kim D M, Choi J H, Belenky L J, Giencke J, Lee M K, Tian W, Pan X Q, Siri A, Hellstrom E E, Eom C B, and Larbalestier D C (2004) Very high upper critical fields in MgB_2 produced by selective tuning of impurity scattering *Supercond. Sci. Technol.* **17** 278.

[Gurevich02] Gurevich A (2003) Enhancement of the upper critical field by nonmagnetic impurities in dirty two-gap superconductors *Physical Review B* **67**, 184515

[Gurevich03] Gurevich A (2007) Limits of the upper critical field in dirty two-gap superconductors *Physica C: Superconductivity* **456**, 160

[Gurevich04] Gurevich A (2003) Lectures in superconductivity given to students at University of Wisconsin - Madison

[Hossain01] Hossain M S A, Kim J H, Wang X L, Xu X, Peleckis G, and Dou S X (2007) Enhancement of flux pinning in a MgB_2 superconductor doped with tartaric acid. *Supercond. Sci. Technol.* **20** 112.

[Ibach01] Ibach H and Luth H (1995) *Solid-State Physics 2nd ed.* (Germany: Springer)

[Indrakanti01] Indrakanti S S, Nesterenko V F, Maple M B, Frederick N A, Yuhasz W M and Li S (2001) Hot isostatic pressing of bulk magnesium diboride: mechanical and superconducting properties. *arXiV:cond-mat* 0105485

[Iwasa01] Iwasa Y, Larbalestier D C, Okada M, Penco R, Sumption M D and Xi X (2006) A round table discussion on MgB_2: Toward a wide market or a niche production? – A summary. *IEEE Trans. Appl. Supercond.* **16** 2, 1457

[Jiang01] Jiang J, Senkowicz B J, Larbalestier D C and Hellstrom E E (2006) Boron powder purification and its effects on the connectivity of bulk MgB_2 *Supercond. Sci. Technol.* **19** L33–6

[Karkin01] Karkin A E, Voronin V I, Dyachkova T V, Tyutyunnik A P, Zubkov V G, Zainulin Y G, Goshchitskii B N (2001) Superconducting properties of MgB_2 probed by radiation-induced disordering. *arXiV:cond-mat* 0103344v2

[Karpinski01] Karpinski J, Zhigadlo N D, Katrych S, Puzkiak R, Rogacki K, Gonnelli R, (2007) Single crystals of MgB2: Synthesis, substitutions, and properties. *Physica C: Superconductivity* **456**, 3-13

[Kazakov01] Kazakov S M, Puzniak R, Rogacki K, Mironov A V, Zhigadlo N D, Jun J, Soltmann C, Batlogg B and Karpinski J, (2005) Carbon substitution in MgB2 single crystals: structural and superconducting properties. *Phys.Rev.* B **71** 24533

[Kim01] Kim J H, Zhou S, Hossain A, Pan A V and Dou S X (2006) Carbohydrate doping to enhance electromagnetic properties of MgB_2 superconductors. *Applied Physics Letters* **89** 142505

[Kim02] Kim J H, Dou S X, Wang J L, Shi D Q, Xu X, Hossain M S A, Yeoh W K, Choi S and Kiyoshi T (2007) The effects of sintering temperature on superconductivity in MgB_2/Fe wires. *Supercond. Sci. Technol.* **20** 448

[Kitaguchi01] Kitaguchi H, Matsumoto A, Kumakura H, Doi T, Yamamoto H, Saitoh K, Sosiati H, Hata S (2004) MgB_2 films with very high critical current densities due to strong grain boundary pinning. *Applied Physics Letters* **85** 14, 2842

[Kiuchi01] Kiuchi M, Mihara H, Kimura K, Haraguchi T, Otabe E S, Matsushita T, Yamamoto A, Shimoyama J and Kishio K (2006) Critical current characteristics in MgB_2 bulks. *Physica C* **445** 474

[Kortus01] Kortus J, Maxin I I, Belashchenko K D, Antropov V P, Boyer L L (2001) Superconductivity of metallic Boron in MgB_2 *Physical Review Letters* **86**, 20 4656

[Kramer01] Kramer E J (1973) Sclaing laws for flux pinning in hard superconductors *J. Appl. Phys.* **44** 3, 1360

[Larbalestier01] Larbalestier D C, Rikel M O, Cooley L D, Polyanskii A A, Jiang J Y, Patniak S, Cai X Y, Feldmann D M, Gurevich A, Squitieri A A, Naus M T, Eom C B, Hellstrom E E, Cava R J, Regan K A, Rodago N, Hayward M A, He T, Slusky J S, Khalifah P, Inumaru K and Haas M (2001) Strongly linked current flow in polycrystalline forms of the superconductor MgB_2 *Nature* **410** 186

[Lee01] Lee S, (2003) Crystal growth of MgB_2. *Physica C: Superconductivity* **385**, 31

[Lee02] Lee S, Masui T, Yamamoto A, Uchiyama H, Tajima S (2003) Carbon-substituted MgB_2 single crystals. *Physica C: Superconductivity* **397**, 7

[Li01] Li S Y, Xiong Y M, Mo W Q, Fan R, Wang C H, Luo X G, Sun Z, Zhang H T, Li L, Cao L Z, Chen X H (2001) Alkali metal substitution effects in $Mg_{1-X}A_XB_2$ (A = Li and Na) *Physica C: Superconductivity* **363**, 219

[Liu01] Liu Z K, Schlom D G, Li Q, Xi X X, (2001) Thermodynamics of the Mg-B system: Implications for the deposition of MgB_2 thin films. *Applied Physics Letters* **78**, 23

[Lorentz01] B Lorenz, O Perner, J Eckert, and C W Chu, Superconducting properties of nanocrystalline MgB_2, 2006 *Superconductor Science and Technology.* **19** 912.

[Ma01] Ma Y, Zhang X, Nishijima G, Watanabe K, Awaji S and Bai X (2006) Significantly enhanced critical current densities in MgB_2 tapes made by a scaleable nanocarbon addition route *Appl. Phys. Lett.* **88** 72502

[Masui01] T Masui, S Lee, A Yamamoto, H Uchiyama, S Tajima, Carbon-substitution effect on superconducting properties in MgB_2 single crystals, 2004, *Physica C.* **412-414** 303-306

[Matsumoto01] Matsumoto A, Kumakura H, Kitaguchi H, Senkowicz B J, Jewell M C, Hellstrom E E, Zhu Y, Voyles P M and Larbalestier D C (2006) Evaluation of connectivity, flux pinning, and upper critical field contributions to the critical current density of bulk pure and SiC-alloyed MgB_2 *Appl. Phys. Lett.* **89** 132508

[Matsumoto02] Matsumoto A, Kumakura H, Kitaguchi H, Senkowicz B J, Jewell M C, Hellstrom E E, Zhu Y, Voyles P M and Larbalestier D C 2006 Evaluation of connectivity, flux pinning, and upper critical field contributions to the critical current density of bulk pure and SiC-alloyed MgB2 *Appl. Phys. Lett.* **89** 132508

[Matsumoto03] Matsumoto A, Kumakura H, Kitaguchi H and Hatakeyama H 2003 Effect of SiO_2 and SiC doping on the powder-in-tube processed MgB_2 tapes *Supercond Sci Technol.* **16** 926

[Monni01] Monni M, Ferdeghini C, Manfrinetti P, Palenzona A, Putti M, Affronte M, Postorino P, Lavagnini M, Sacchetti A, Di Castro D, Sacchetti F, Petrillo C and Orecchini A (2005) Co-doped $Mg_{1-X}(AlLi)_XB_2$ compounds: a key system to probe the effect of the charge doping and inter-band scattering. *arXiV:cond-mat* 0506162

[Monni02] Monni M, Ferdeghini C, Putti M, Manfrinetti P, Palenzona A, Affronte M, Postorino P, Lavagnini M, Sacchetti A, Di Castro D, Sacchetti F, Petrillo C and Orecchini A (2006) Role of charge doping and lattice distortions in codoped $Mg_{1-X}(AlLi)_XB_2$ compounds. *Phys. Rev. B* **73** 214508

[Nagamatsu01] J. Nagamatsu, N. Kakagawa, T. Muranaka, Y. Zenitani, J. Akimitsu, *Nature*, **410** (2001) 63

[Newman01] Newman N and Rowell J (2006) personal communication.

[Ohmichi01] Ohmichi E, Masui T, Lee S, Tajima S and Osada T (2004) Enhancement of irreversibility field in carbon-substituted MgB_2 single crystals. *J Phys. Soc. Japan* **73** 8, 2065

[Park01] Park E T (1999) Grain growth of $BaTiO_3$ *J. Mat. Sci. Let.* **18** 163

[Polyanskii01] A Polyanskii, V Beilin, I Felner, MI Tsindlekht, E Yashchin, E Dul'kin, E Galstyan, M Roth, B Senkowicz, E Hellstrom, Magneto-optical and electromagnetic studies of core connectivity and weak-link behaviour in Cu/MgB_2 and Ni/MgB_2 wires and tapes, 2004 *Superconductor Science and Technology.* **17** 363.

[Polyanskii02] AA Polyanskii, DM Feldmann and DC Larbalestier. C3.4 in *Handbook of Superconducting Materials.* Edited by D. Cardwell and D. Ginley. IOP publishing Ltd., 2003.

[Porter01] Porter D A and Easterling K E (1981) *Phase Transformations in Metals and Alloys* (UK: Van Nostrand Reinhold)

[Putti01] Putti M, Vraccini V, Ferdeghini C, Gatti F, Grasso G, Manfrinetti P, Marre D, Palenzona A, Pallecchi I, and Tarantini C (2005) Neutron irradiation of $Mg^{11}B_2$: From the enhancement to the suppression of superconducting properties *Appl. Phys. Lett.* **86** 112503

[Richerson01] Richerson D W (1992) *Modern Ceramic Engineering* (Marcel Dekker Inc.)

[Rodrigues01] Rodrigues Jr D, Foner S and Pinatti D G (1998) Flux pinning mechanisms in superconducting A15 materials and the optimization of their transport properties. *Adv. Cryo. Eng. (Mat.)* **44** 959

[Rodrigues02] Rodrigues Jr D, personal communication

[Rowell01] Rowell J M (2003) The widely variable resistivity of MgB_2 samples *Supercond Sci Technol.* **16** 17

[Rowell02] Rowell J M, Xu S Y, Zeng X H, Pogrebnyakov A V, Li Qi, Xi X X, Redwing J M, Tian W and Pan X (2003) Critical current density and resistivity of MgB_2 films *Appl. Phys. Lett.* **83** 102

[Rowell03] Rowell J, personal communication

[Senkowicz01] Senkowicz B J, Giencke J E, Patnaik S, Eom C B, Hellstrom E E and Larbalestier D C (2005) Improved upper critical field in bulk-form magnesium diboride by mechanical alloying with carbon *Appl. Phys. Lett.* **86** 202502

[Senkowicz02] Senkowicz B J, Polyanskii A, Mungall R J, Zhu Y, Giencke J E, Voyles P M, Eom C B, Hellstrom E E, and Larbalestier D C (2007) Understanding the route to high critical current density in mechanically alloyed $Mg(B_{1-X}C_X)_2$ *Supercond. Sci. Technol.* **20** 650

[Senkowicz03] Senkowicz B J, Perez Moyet R, Mungall R J, Hedstrom J, Uwakweh O N C, Hellstrom E E and Larbalestier D C (2006) Atmospheric conditions and their effect on ball-milled magnesium diboride. *Supercond. Sci. Technol.* **19** 1173

[Serquis01] Serquis A, Civale L, Hammon D L, Liao X Z, Coulter J Y, Zhu Y T, Jaime M, Peterson D E, Mueller F M (2003) Hot isostatic pressing of powder in tube MgB_2 wires. *Appl. Phys. Lett.* **82** 17, 2847

[Serquis02] Serquis A, Civale L, Coulter J Y, Hammon D L, Liao X Z, Zhu Y T, Peterson D E, Mueller F M, Nesterenko V F and Indrakanti S S (2004) Large field generation with a hot isostatically pressed powder-in-tube MgB_2 coil at 25 K. *Supercond. Sci. Technol.* **17** L35

[Serquis03] Serquis A, Serrano G, Moreno S M, Civale L, Maiorov B, Balakirev F and Jaime M (2007) Correlated enhancement of H_{c2} and Jc in carbon nanotube doped MgB_2. *Supercond. Sci. Technol.* **20** L12

[Shen01] Shen T M, Li G, Cheng C H, and Zhao Y (2006) Doping effects of carbon and titanium on the critical current density of MgB_2. *Supercond. Sci. Technol.* **19** 1219

[Song01] Song X, Braccini V, Larbalestier D C (2004) Inter- and introgranular nanostructure and possible spoinodal decomposition in lon-resistivity bulk MgB_2 with varying critical fields. *J. Mat. Res.* **19** 8, 2245

[Sumption01] Sumption M D, Bhatia M, Rindfleisch M, Tomsic M, Collings E W (2005) Transport and magnetic J_c of MgB_2 strands and small helical coils. *Appl. Phys. Lett.* **86** 102501

[Sumption02] Sumption M D and Collings E W (1995) Chromium diffusion into plated Nb_3Sn strands deduced form electrical resistivity measurement. *IEEE Trans. Appl. Supercond.* **5** 2, 1925

[Sumption03] Sumption M D, Bhatia M, Buta F, Bohnensteihl S, Tomsic M, Rindfleisch M, Yue J, Phillips J, Kawabata S and Collings E W (2005) Solenoidal coils made from monofilamentary and multifilamentary MgB_2 strands. *Supercond. Sci. Technol.* 18 961

[Sun01] Sun Y, Yu D, Liu Z, Wang T, He J, Xiang J, Zheng D, Tian Y (2007) Structural and superconducting properties of Ca-doped MgB_2 superconductors. *Supercond. Sci. Technol.* **20** 261

[Wamg01] Wang X L, Cheng Z X and Dou S X (2007) Silicon oil: A cheap liquid additive for enhancing in-field critical current density in MgB_2. *Appl. Phys. Lett.* **90** 042501

[Wilke01] Wilke R H T, Bud'ko S L, Canfield P C, Farmer J, Hannahs S T (2006) Systematic study of the superconducting and normal-state properties of neutron-irradiated MgB_2 *Physical Review B* **73**, 134512

[Wilke02] Wilke R H T, Bud'ko S L, Canfield P C, Farmer J, Hannahs S T (2006) Effects of neutron irradiation on carbon doped MgB_2 wire segments. *Supercond. Sci. Technol.* **19** 556

[Wilke03] Wilke R H T, Bud'ko S L, Canfield P C, Finnemore D K, Suplinskas R J and Hannahs S T (2005) Synthesis and optimization of $Mg(B_{1-x}C_x)_2$ wire segments *Physica* C **424** 1

[Wilke04] Wilke R H T, personal communication.

[Wilke05] Wilke R H T, Bud'ko S L, Canfield P C, Finnemore D K, Hannahs S T (2005) Synthesis of $Mg(B_{1-X}C_X)_2$ powders. *Physica C* **432** 193

[Wilke06] Silke R H T, Bud'ko S L, Canfield P C, Kramer M J, Wu Y Q, Finnemore D K, Suplinskas R J, Marzik J V, Hannahs S T (2005) Superconductivity in MgB_2 doped with Ti and C. *Physica C* **418** 160

[Wu01] Wu Y F, Lu Y F, Yan G, Li J S, Feng Y, Tang H P, Chen S K, Xu H L, Li C S and Zhang P X (2006) Improved superconducting properties in bulk MgB_2 prepared by high-energy milling of Mg and B powders. *Supercond. Sci. Technol.* **19** 1215

[Xu01] Xu HL, Feng Y, Zhao Y, Xu Y D, Wu X J, Pu M H, Yan G, Lu Y F, Li C S, Ji P, Shen Z H and Xu Z (2006) Effects of polycarbosilane doping on the superconductivity and microstructure of MgB_2. *Supercond. Sci. Technol.* **19** 68

[Xu02] Xu X, Kim J H, Yeoh W K, Zhang Y, Dou S X (2006) Improved Jc of MgB_2 superconductor by bal milling using different media. *Supercond. Sci. Technol.* **19** L47

[Yamada01] Yamada H, Hirakawa M, Kumakura H and Kitaguchi H (2006) Effect of aromatic hydrocarbon addition on in situ powder in tube processed MgB_2. *Supercond. Sci. Technol.* **19** 175

[Yamamoto01] Yamamoto A, Shimoyama J, Ueda S, Katsura Y, Iwayama I, Horii Shigeru, Kishio K (2005) Effect of sintering conditions on critical current properties and microstructures of MgB_2 bulks. *Physica C* **426** 1220

[Yamamoto02] Yamamoto A, Shimoyama J, Kishio K and Matsushita T (2007) Limiting factors of normal-state conductivity in superconducting MgB_2: an application of mean-field theory for a site percolation problem. *Supercond. Sci. Technol.* **20** 658

[Yeoh01] Yeoh W K and Dou S X (2007) Enhancement of Hc2 and Jc by carbon-based chemical doping. *Physica* C **456** 170

[Zhetmayer01] Zhetmayer M, Eisterer M, Jun J, Kazakov S M, Karpoinski J, Weber H W (2004) Magnetic field dependence of the reversible mixed-state properties of superconducting MgB_2 single crystals and the influence of artificial defects. *Physical Review B* **70**, 214516

[Zhu01] Zhu Y, Larbalestier D C, Voyles P M, Pogrebnyakov A V, Xi X X and Redwing J M (2007) Nanoscale disorder in high critical field carbon-doped MgB_2 hybrid physical vapor deposition thin films. *Unpublished.*

[Zhu02] Zhu Y, Matsumoto A, Senkowicz B J, Kumakura H, Kitaguchi H, Jewell M C, Hellstrom E E, Larbalestier D C, Voyles P M (2007) Microstructures of SiC nanoparticle-doped MgB_2/Fe tapes. *Accepted by JAP*